

Dissertation zur Erlangung des Doktorgrades
der Fakultät für Chemie und Pharmazie
der Ludwig-Maximilians-Universität München

Two-dimensional Covalent Organic Frameworks as Platforms for Renewable Energy and Environmental Applications

Linus Martin Stegbauer

aus

Mannheim

2016

Erklärung

Diese Dissertation wurde im Sinne von § 7 der Promotionsordnung vom 28. November 2011 von Frau Prof. Dr. Bettina Lotsch betreut.

Eidesstattliche Versicherung

Diese Dissertation wurde eigenständig und ohne unerlaubte Hilfe erarbeitet.

München, den 12.4.2016

gez. Linus Stegbauer

Dissertation eingereicht am 8. Januar 2016

1. Gutachterin: Prof. Dr. Bettina V. Lotsch

2. Gutachter: Prof. Konstantin Karaghiosoff

Mündliche Prüfung am 8. Februar 2016

“Every era has always found a way to explain, failing to understand.”

OSCAR WILDE

Acknowledgements

I would like to thank first of all my dear Friederike Hög, who supported me all through my phd. Mäx, my best friend, helped me a lot in dark phd times. Thank you! Also I would like to thank my mum and my dad for financial and moral support through my time of study.

More of all thanks go to my boss Prof. Bettina Lotsch, who gave me a lot of freedom in my science. Sincere thanks to Prof. Konstantin Karaghiosoff, Prof. Hendrik Zipse, Prof. Hans Böttcher, Prof. Christian Ochsenfeld and Dr. Henry Dube for being part of the board of examiners. Special thanks go to Prof. Christian Ochsenfeld for the good collaboration and mentorship.

Experiments in this thesis were heavily supported by staff and equipment of the Max-Planck Institut of Solid State Research, Stuttgart.

The whole Lotsch group in MUC and S is acknowledged with special view on Albi, not only for being the best conference mate I met so far, but also for his ongoing helpfulness. Drinking coffee is always a pleasure with you, Albi. Freddi, the second best conference mate ;), hope he will handle the tough time he is facing at the moment. Stebbo, Erik and Basti J. gave me a lot of advice during the start and Chris at the end of my PhD journey, thanks guys you helped a lot. Chris especially helped keeping up my motivation during writing in the AFM room. Katha gets specials thx because of her will to collaborate during the last three years. Vio, the god master of TEM: I owe you a lot. Thanks also to all my students (Kerstin Sigl, Jenny Teichert, Matthias Schmid, Li Gao, Lara Weisheit, Stefania Saßnink, Hendrik Schlomberg) especially Basti, the Organic magician and Kerstin Gottschling, the princess of layers. My lunch mates Ellen and Iacovos often made my day!

At this point, I would like to send lots of thanks to Stuttgart: Claudi, you often made my day, and helped a lot in many cases. Roland, it is always a pleasure for me to have you for a good chat in S. Dan, scientific and personal discussions were always fruitful with you. Unfortunately, I did not make it with you to SE Asia. Marie-Luise, you helped me a lot in synthesis of TFPT, thank you so much for this. Filip, you work so hard, be careful to keep your motivation.

The spectroscopic guys and girls at LMU are also specially acknowledged: Brigitte Breitenstein, the queen of MS, you made my molecules fly ;), Peter Mayer & Christine Neumann, you micro-waved my liquid NMR samples, Christian Minke, you did the same with the solid NMR samples and also shot electrons on them by SEM. Thanks a lot, you are such a nice guy, Christian! Jana Obel for ICP-AES, R. Eicher for elemental analysis (special thx for measuring toxic samples). In MPI FKF Christine Stefani and Helga Hoier are specially acknowledged, because of their steady motivation to measure my nearly amorphous samples in XRD.

Special PL thanks go to my cooperation partners in other groups: Florian Ehrat and the Feldmann group. You guys have the best equipment. Thanks to my one-year lab mate Nicole Braml and the Schnick group: We had a nice time in Mühlheim and our project is published! Max Hahn of the

Lercher Group helped me a lot with my second paper: Thanks for that, you were a very motivated collaborator. Gökçen Savasci and the Ochsenfeld group: You guys did such nice calculations for me. Thank you so much.

I would like to thank CENS and NIM for supporting my projects and providing funding for my stay at SF for ACS. Thanks to Christoph Hohmann, who nicely designed one of my TOCs.

meiner Familie

SUMMARY

Covalent organic frameworks (COFs) have recently emerged as a new generation of porous polymers combining molecular functionality with the robustness and structural definition of crystalline solids. Drawing on the recent development of tailor-made semiconducting COFs, we here report on a new COF capable of visible-light driven hydrogen generation in the presence of Pt as proton reduction catalyst (PRC) with quantum efficiencies up to 2.2% at 400 nm. The COF, TFPT-COF, is based on hydrazone-linked functionalized triazine and phenyl building blocks and adopts a layered structure with a honeycomb-type lattice featuring mesopores of 3.8 nm and the highest surface area among all hydrazone-based COFs reported to date. When illuminated with visible light, the Pt-doped COF continuously produces hydrogen from water without signs of degradation up to 92 h. With their precise molecular organization and modular structure combined with high porosity, photoactive COFs represent well-defined model systems to study and adjust the molecular entities central to the photocatalytic process. It could be shown that TFPT-COF, although losing its long-range order after sonication in water, can be reconverted to the crystalline form by subjecting it to the initial synthesis conditions. This approach has also been used to post-synthetically introduce functionalized linkers in TFPT-COF and provides a new generally applicable way for functionalization of COFs. Studies on the exfoliation and crystalline order as well as grain sizes of TFPT-COF revealed the disc-shape form of the crystallites: The thickness of the crystals along the stacking direction is smaller than in the lateral directions, although all sizes are on the nanometer scale and therefore not suitable for single-crystal structure determination.

Based on this initial work, further studies were conducted on four 2D azine-linked COFs from hydrazine and triphenylarene aldehydes with a varying number of nitrogen atoms (N0, N1, N2 and N3-COF), in collaboration with Vijay Vyas. The electronic and steric variations in the precursors are transferred to the resulting frameworks, thus leading to a progressively enhanced light-induced hydrogen evolution with increasing nitrogen content in the frameworks.

Building on these insights, three new microporous, pyrene-containing COFs were developed, based on the azine linkage (ATEXPY-COFs), which vary in the number of nitrogen atoms in the peripheral aromatic units. The COFs show high surface areas of up to $921 \text{ m}^2 \text{ g}^{-1}$ and low optical band gaps ($<1.92 \text{ eV}$). Regarding their photocatalytic activity, they show an effect which contrasts to the previous findings: The COFs are all capable of photocatalytic hydrogen production from water with increasing efficiency upon decreasing the number of nitrogen atoms in the peripheral aromatic units. Further photoluminescence experiments about these phenomena are on the way.

The use COFs in environmental settings such as atmospheric water capture or CO_2 separation under realistic pre- and post-combustion conditions is largely unexplored to date. Herein, we present two isostructural azine-linked COFs based on 1,3,5-triformyl benzene (AB-COF) and 1,3,5-triformylphloroglucinol (ATFG-COF) and hydrazine building units, respectively, whose sorption characteristics are precisely tunable by the rational design of the chemical nature of the pore walls. This effect is particularly pronounced for atmospheric water harvesting, which is explored for the first time using COFs as adsorbents. We demonstrate that the less polar AB-COF acts as

a reversible water capture and release reservoir, featuring among the highest water vapor uptake capacity at low pressures reported to date (28 wt% at $<0.3 p p_0^{-1}$). Furthermore, we show tailored CO₂ sorption characteristics of the COFs through polarity engineering, demonstrating high CO₂ uptake at low pressures (< 1 bar) under equilibrium (sorption isotherm) and kinetic conditions (flow TGA, breakthrough) for the more polar ATFG-COF, and very high CO₂ over N₂ (IAST: 88) selectivity for the apolar AB-COF. In addition, the pore walls of both COFs were modified by doping with metal salts (lithium and zinc acetate), revealing an extremely high CO₂ uptake of 4.68 mmol g⁻¹ at 273 K for the zinc-doped AB-COF.

Further proof-of-concept studies on water sorption on covalent triazine frameworks (CTFs), developed by Stephan Hug, revealed their potential as a more polar replacement for activated carbon due to the high number of nitrogen atoms incorporated into their carbon backbone. These systems therefore offer a higher water vapor uptake at low pressures (10 wt% water vapor uptake at 10% abs. humidity/298 K), confirming the highly hydrophilic nature of CTFs with high nitrogen content.

In the search for new reversible bond-forming reactions for the development of new COFs, a new triazine-containing polymer has been synthesized by the pyrolysis of tris(1-propynyl)-1,3,5-triazine in collaboration with Nicole Braml and Wolfgang Schnick. This polymer has been characterized in detail for its structural features and sorption properties. Spectroscopic methods show that the polymer contains mesitylene units, which were formed during pyrolysis probably by a Reppe-like [2+2+2] cyclotrimerization of the alkyne moieties. Sorption revealed its ultramicroporous nature (360 m² g⁻¹) and a reasonable CO₂ uptake (1.59 mmol g⁻¹ at 1 bar/273 K).

TABLE OF CONTENTS

1	INTRODUCTION.....	1
1.1	Broader Context.....	1
1.1.1	Porous Materials.....	1
1.2	Covalent Organic Frameworks.....	2
1.2.1	COFs Based on B-O Bond Formation.....	4
1.2.2	COFs Based on C-N Bond Formation.....	11
1.2.3	Highlights of COF Chemistry: Towards Applications.....	20
1.3	Photocatalytic Hydrogen Generation with Light-Element Photocatalysts.....	21
1.4	Adsorbents for Post- and Pre-Combustion CO ₂ Capture.....	24
1.5	Water Vapor Sorbents as New Field of Application.....	26
1.5.1	Water Sorption-based Thermally Driven Heat Pumps.....	26
1.5.2	Fresh Water Generation by Atmospheric Water Capture.....	27
1.6	Objectives.....	27
1.7	References.....	28
2	METHODS.....	40
2.1	Physisorption.....	40
2.1.1	Physisorption Isotherms.....	41
2.1.2	Heats of Adsorption.....	44
2.1.3	Pore Size Distribution Analysis.....	44
2.1.4	Water Vapor Sorption.....	45
2.1.5	Experimental Details.....	46
2.1.6	Experimental Considerations.....	47
2.2	Powder X-Ray Diffraction.....	48
2.3	Materials Studio.....	49
2.4	Infrared Spectroscopy.....	51
2.5	Ultraviolet-Visible Spectroscopy.....	51
2.6	Electron Microscopy.....	52
2.7	Nuclear Magnetic Resonance Spectroscopy.....	53
2.8	Mass Spectrometry.....	54
2.9	References.....	54
3	NEW COVALENT ORGANIC FRAMEWORKS FOR PHOTOCATALYTIC APPLICATIONS.....	57
3.1	A Hydrazone-based Covalent Organic Framework for Photocatalytic Hydrogen	

Production	57
3.1.1 Introduction	58
3.1.2 Results and Discussion	59
3.1.3 Conclusion	65
3.1.4 Bibliography	65
3.1.5 Supporting Information	69
3.2 A Tunable Azine Covalent Organic Framework Platform for Visible Light-Induced Hydrogen Generation	92
3.3 Tunable Azine-based Covalent Organic Frameworks with Pyrene Chromophors for Visible-Light Photocatalytic Hydrogen Generation.	93
3.3.1 Introduction	93
3.3.2 Results and Discussion	94
3.3.3 Conclusion	102
3.3.4 Bibliography	102
3.3.5 Supporting Information	105
4 COVALENT ORGANIC FRAMEWORKS AS SORBENTS FOR WATER VAPOR AND CARBON DIOXIDE SORPTION	129
4.1 Tunable Water and CO ₂ Sorption Properties in Isostructural Azine-based Covalent Organic Frameworks through Polarity Engineering.....	129
4.1.1 Introduction	130
4.1.2 Results and Discussion	132
4.1.3 Conclusion	142
4.1.4 Bibliography	142
4.1.5 Supporting Information	147
4.2 Synthesis of Triazine-Based Materials by Functionalization with Alkynes	191
4.3 Nitrogen-rich Covalent Triazine Frameworks as High-Performance Platforms for Selective Carbon Capture and Storage.	192
5 DESIGN PRINCIPLES, FUNCTIONALIZATION AND SCREENING OF COFs - UNPUBLISHED RESULTS	193
5.1 Doping of Photocatalytically-active TFPT-COF by Perylene Moieties.....	193
5.2 Crystallite and Particle sizes of TFPT-COF & Exfoliation	196
5.3 Preparing Covalent Organic Frameworks for <i>Click</i> Reactions	200
5.3.1 Modification of DETH with Alkyne and Azide Moieties.	200
5.3.2 Synthesis of Modified TFPT-COF Derivatives	201
5.3.3 Functionalization of TFPT-COF by Reconversion	205
5.3.4 Conclusion and Outlook	206
5.3.5 Experimental Data	207

5.4	Towards Implementing new Chromophoric Moieties in COFs and Polymers.....	212
5.4.1	Conclusions: The Art of Building Block Synthesis	217
5.5	On the Way to Highly Porous COFs.....	220
5.5.1	Screening of TFPT-COF.....	220
5.5.2	Screening of AB-COF	227
5.5.3	Conclusions of Conventional Screening	231
5.5.4	Microwave synthesis of TFPT-COF	232
5.6	References	235
6	CONCLUSION AND OUTLOOK.....	238
6.1	References	240
7	APPENDIX.....	242
7.1	Table of Abbreviations	242
7.2	List of publications	244
7.3	Contributions to conferences.....	245

1 INTRODUCTION

1.1 Broader Context

During the past three hundred years, anthropogenic effects have considerably influenced the the global environment. Due to these man-made emissions of carbon dioxide and methane, global climate will significantly differ from its natural state for the next thousands of years. According to the latest estimates by the Intergovernmental Panel on Climate Change (IPCC), the Earth will warm up by 5.8°C during this century. For this human-dominated geological epoch the term “Anthropocene”¹ has been introduced, as a clear statement of the intrusion of humans and their impact on the Earth. This process has sped up dramatically during the last hundred years since invention of artificial nitrogen fixation for the synthesis of fertilizers in 1908 and the consequent exponential growth of the world population from 1.5 billion up to expected 10 billion in this century, leading to a yet unknown gigantic demand for food, electricity and fuel. A challenging task lies ahead for scientists to search for environmentally sustainable energy generation for the era of the Anthropocene. Present objectives are wide-spread and urge the development of new materials which are molecularly tailorable to fit the targeted purpose. Porous materials, especially those based on cheap and abundant organic building blocks may play a key role in this process, offering applications in the field of energy and possibly also in the field of fuel generation.

The introduction to this thesis will give a short overview on porous materials, with an in-depth focus on covalent organic frameworks. Then several applications which are covered by this thesis, will be introduced, by a closer look on photocatalytic water splitting, CO₂ capture and water vapor sorption and their task-specific challenges. Finally, this introduction will close with the objectives of this thesis.

1.1.1 Porous Materials

The porosity is a measure of the void (“empty”) space in the material, and is a fraction of the void volume over the total volume of the material. For a more detailed definition of porous materials the reader is referred to the Methods section (2.1 Physisorption). Porous materials are crucial in established processes such as catalysis and molecular separations and in emerging energy and health technologies. While still being developed, zeolites, which are porous aluminosilicates also known as molecular sieves, have so far made the largest contribution to society, e.g. in separation of aromatic hydrocarbons or even in self-cooled beer barrels.² More porous materials have evolved during the last ten years, such as metal-organic frameworks (MOFs), covalent organic frameworks (COFs) and porous polymers. While MOFs are already commercialized by BASF on the ton scale, the other materials have so far not been successfully introduced to the market, besides some examples in the fine chemicals market.³ Having such great variety of porous mate-

rials in our hands, it is apparent that there is no single class fitting ideally for all purposes. For an overview of recent advances in porous materials, the reader is referred to a recent review.⁴ To further push these new classes of porous materials into real applications certain criteria, such as scalability, long-term stability, appropriate adsorption kinetics and selectivity, and processability, all within a reasonable budget, need to be met. All these criteria represent a major challenge of design and therefore involve the control of structure and deep understanding of structure-property relationships. Extended conjugated structures, which are not available in zeolites and MOFs, as found in microporous polymers composed of aromatic building blocks and some COFs have led to a plethora of new electronic applications, previously only accessible in semiconductors. The crystal engineering approaches developed for crystalline porous MOFs and COFs cannot be applied to amorphous porous polymers, but similar strategies have allowed for controlling their properties such as porosity and electronic band gap, by carefully choosing appropriate molecules as building blocks. Additionally, the development of new porous materials is further promoted by rapid advances in computational chemistry.

1.2 Covalent Organic Frameworks

In this introduction the main focus is not on applications but rather on the extraction of all COF building blocks since the two COF reviews of 2013 until September 2015.^{5,6} Nevertheless, some outstanding applications are mentioned. Note that this introduction does not cover covalent organic frameworks only synthesized as single layers for scanning tunneling microscopy (STM) purposes⁷ and theoretical COF publications.⁸

After the initial publication about covalent organic frameworks (COFs) by Yaghi in 2005,⁹ a decade has passed and the emerging scientific field of COFs is blooming and has already lead to a plethora of possible applications for this new type of materials. A widely accepted definition describes COFs as porous and crystalline two-dimensional or three-dimensional polymers, constructed with organic building units via strong covalent bonds,^{5,6} although the term “COF” is sometimes misused for porous polymers without long-range order.^{10,11}

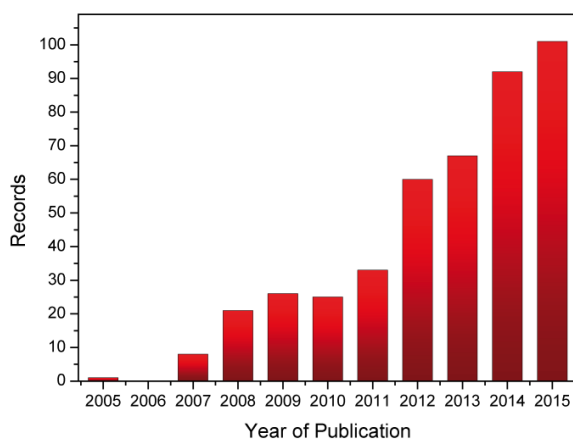


Figure 1.1: Publications per year based on the search topic “covalent organic framework AND COF” in the CAS Scifinder™ database. Accessed: 23/09/2015.

In comparison with other porous crystalline materials like zeolites, COFs possess the advantages of low density, very large surface area, tunable pore size and structure as well as easily tailorable functionality. Besides the *Yaghi* group, starting from 2005, the *Jiang* group, (since 2007) and the *Dichtel* group (since 2010) published major contributions on the field of COFs. These three groups account for one quarter of all COF related publications.

COFs are built up from molecular, symmetric and rigid building blocks in a reversible COF-forming reaction. More synthetic aspects can be found in the following chapters. According to the type of COF-forming reaction, the frameworks can be generally divided into i) Boron-Oxygen (B-O) and ii) Carbon-Nitrogen (C-N) bond formation, besides two exceptions utilizing N-N and B-N bond formation.^{12,13} As visualized by Figure 1.2, depending on the symmetry of the building blocks (C_2 , C_3 , C_4 and T_d), COFs can be categorized into either 2D (hexagonal or tetragonal) or 3D frameworks. In hexagonal and tetragonal COFs, the covalently bound framework is restricted to two-dimensional sheets, which stack further in different modes, held together by van der Waals forces. The *Dichtel* group and co-workers firstly investigated these interlayer stacking energies by means of *ab-initio* and molecular mechanics calculations.¹⁴ These calculations predicted a lateral offset of 1.7 Å between two adjacent layers of the hexagonal sheets of boronate ester COFs. Later work of the same group explored several other B-O linkers and stated offsets between 1.4 and 2.8 Å as stable, depending on the linkers of the COF.¹⁵

The combination of two C_4 linkers to build a tetragonal COF has also been realized (not shown in Figure 1.2).¹⁶ The size and the appearance of the resulting empty space - the pore - can be predicted by knowledge of the size and symmetry of the building blocks. This concept is known as *reticular chemistry*, a term coined by Michael O’Keeffe, and has already been successfully applied to MOFs.^{17–22} Furthermore, 3D COFs can also be prepared by combination of a T_d and a C_3 symmetric building block (not shown in Figure 1.2).^{23,24} A triangular topology has been realized by

combination of a C_6 (coronene **77** or **78**, see Figure 1.10) and a C_2 linker (terephthalaldehyde **34**, see Figure 1.7).²⁵

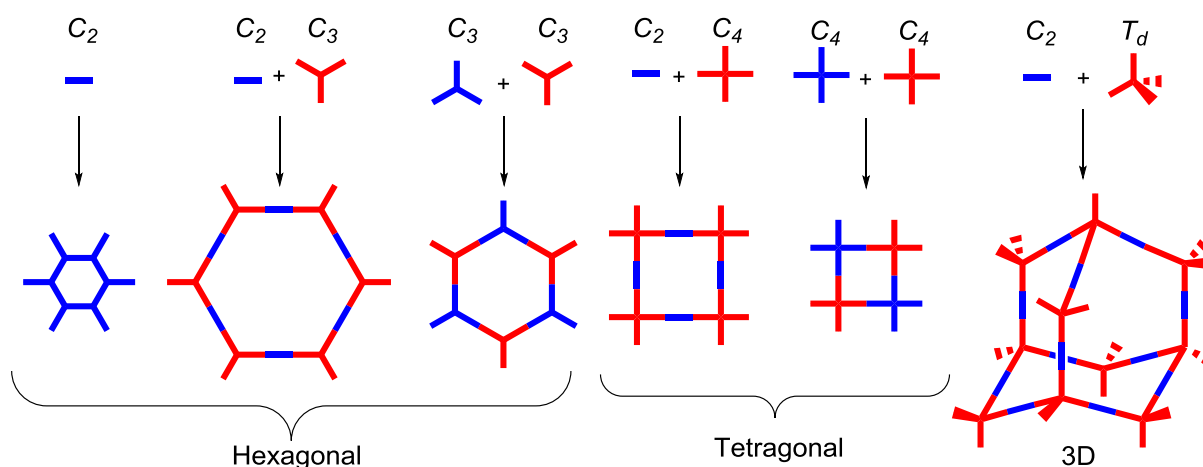


Figure 1.2: Different symmetries of building blocks lead to different framework morphologies.

1.2.1 COFs Based on B-O Bond Formation

Linkages Based on B-O Bond Formation

The by far most prominent COFs are based on B-O formation, a condensation reaction involving a boronic acid as starting material. The first COF (COF-1) was based on the boroxine formation by self-condensation of benzenediboronic acid (Figure 1.3 top). A combination of this ditopic C_2 symmetric building block and the C_3 symmetric boroxine linkage leads to a hexagonal “honeycomb” network. A boronate ester is formed, if the boronic acid is combined with a polyalcohol (polyol) (see Figure 1.3 middle)⁹ and a combination of a boronic acid with a silanol results in borosilicate linkages (see Figure 1.3 bottom). Despite being thermally robust, the B-O bond is easily hydrolyzed by water vapor in the air and therefore, corresponding B-O based COFs lose their crystallinity by storage under air. The speed of decomposition depends on their hydrophobicity²⁶ and layer-layer interactions.²⁷

B-O bond formation

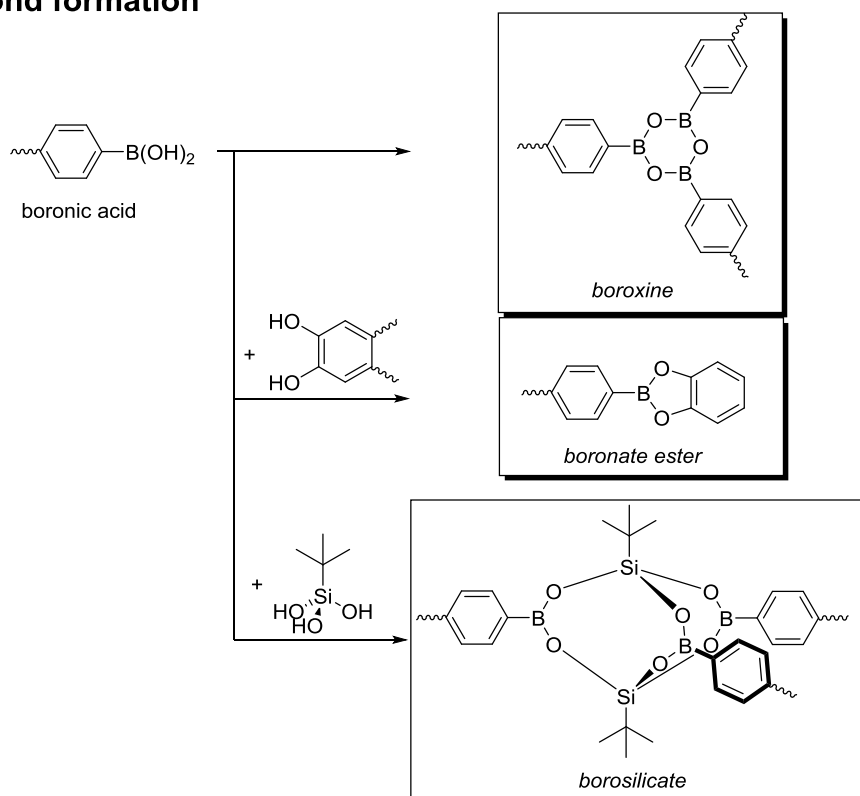


Figure 1.3: Different COF linkages based on B-O bond formation.

B-O Building Blocks Utilized in COFs

Most of the concepts of *reticular chemistry* have been applied to B-O based COFs. By utilization of building blocks with the same symmetry, but differing in length (compare **19** and **20** extended by a phenyl ring in Figure 1.4) *Yaghi* showed for 2D and 3D COFs an expansion of the resulting pore size as the result.^{23,24,28} Not many 3D COFs have been published so far. A 3D COF (tetraphenylmethane **22a** + tetraol **24a**) has been used for natural gas separation by sieving due to its 6.4 Å small pore size.²⁹ COF-102 (**22a**) has been modified by metallocenes³⁰ and platinum nanoparticles,³¹ which lead to increased hydrogen uptake compared to the unmodified framework. Some 3D COFs have been functionalized by a “truncation” method: The tetrahedral building block **22a** has been “truncated” to building block **18a** to attach organic residues such as allyl-groups (**18b**),^{32,33} which were used as target for postsynthetic attachment by thiol-ene chemistry.³⁴ Another truncation strategy has been pursued by integration of a monotopic boronic acid into the COF.³⁵

The pore size of honeycomb 2D COFs was further extended by variation of the C_2 symmetric linker while keeping the C_3 symmetric linker **23**, from 2.7 nm (benzene-di(1,4)boronic acid (**1**), see Figure 1.4),⁹ via 3.4 nm (bisphenyl **11**),²⁸ 4.0 nm (benzothiadiazole **12**)³⁶ and 4.7 nm (alkyne **13**)¹⁴ to 5.3 nm (naphthalene **15**).³⁷ A similar expansion of pore size from 2.7 nm (pyrene **10**), via 3.4 nm (pyromellitic imide **14**), 3.6 nm (alkyne **13**), 4.0 nm (perylene imide **17**) to 4.4 nm (with alkyne **16**) with increasing length of the linker has been shown for tetragonal phthalocyanine

(**27b-27d**, see Figure 1.5) containing networks, while keeping the size of the C_4 symmetric linker.^{38,39}

Further tailoring has been done by integration of hetero-atoms containing moieties with interesting electronic properties into the building blocks, known from organic solar cells. Examples for this strategy involved moieties such as pyrene **10**,^{40,41} phthalocyanine **27a-d**,^{42,43} benzothiazole **12**,⁴⁴ naphthalenedimide **15**,³⁷ perylenediimide **17**,³⁹ thienothiophene **4**,⁴⁵ benzodithiophene **5a**⁴⁶ including its heavier chalcogen analogues **5b** and **5c**,⁴⁷ thiophene **6**, bithiophene **7**,⁴⁸ and porphyrin as C_2 (**9**)^{49,50} and C_4 building block **21a-c**.^{51,52} A naphthalenedimide based B-O COF (**15** + triphenylene **23**) has been used to use the COF as electrode material in Li batteries.⁵³

Boronic acids

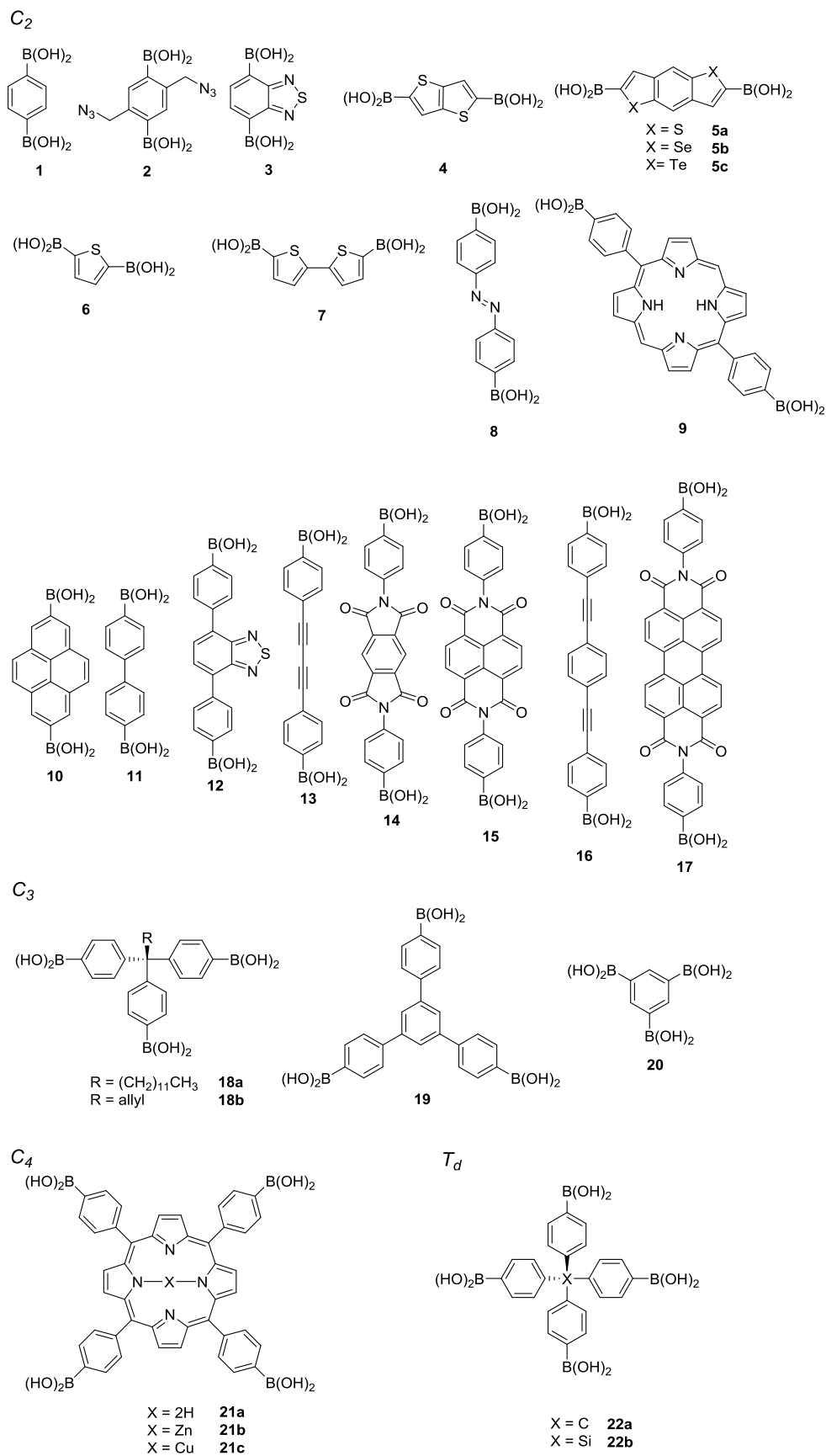


Figure 1.4: Previously employed molecular boronic acids as building blocks for B-O based COFs.

Influences on the pore size of the resulting COF were shown for variation of the length of the alkylchain of polyol (compare **24a-d**)⁵⁴ and by introduction of azide moieties (benzyl azide **2**, see Figure 1.4) for subsequent *click* chemistry,⁵⁵ which enabled covalent attachment of fullerene derivatives to the COF pore wall.⁵⁶

Photoinduced isomerization/reactions of the COF framework itself have been applied in two examples: *Cis/trans* isomerization of the azo benzene **8** containing COF under UV light results in amorphization but not in the expected change of the pore size.⁵⁷ The isomerization of the azo-benzene building block in the COF is accompanied by a change of geometry, which was thought to result in a different pore size, but resulted only in amorphization of the COF. Anthracene based tetraols (**26b**, see Figure 1.5) have also been used as C₂ linker in a COF (**19 + 26b**).⁵⁸ Irradiation of the anthracene based COF (**26a + 20**) gave interlayer [4π+4π] cycloaddition, which changed gas sorption and electronic properties compared to the parent COF.⁵⁹

For most boronate ester based COFs the commercially available C₃ symmetric 2,3,6,7,10,11-hexahydroxytriphenylene (HHTP, **23**, see Figure 1.5) is used as building block, accompanied by C₂ symmetric boronic acids. More exotic C₃ polyols include triptycene **29**,⁶⁰ cyclotricatechylene **28**,⁶¹ dehydrobenzoannulenes **32** and **33**,⁶² phenanthrene cyclotrimer **31**⁶³ and extended phenanthrene cyclotrimer **30** moieties.⁶⁴

Polyols

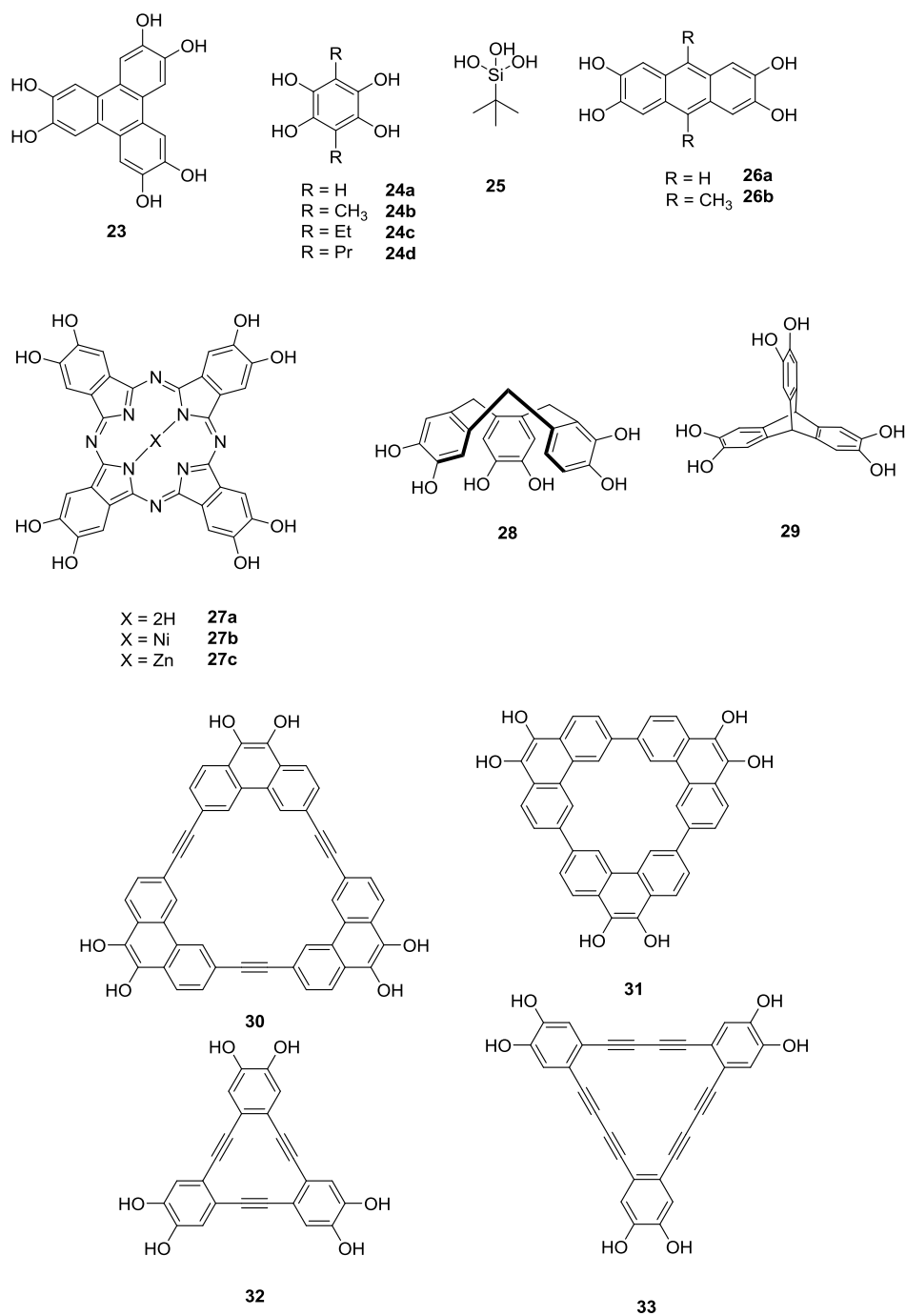


Figure 1.5: Previously employed molecular polyols as building blocks for B-O based COFs.

Synthetic Aspects of B-O COFs

Most COFs are usually synthesized under solvothermal conditions in a glass ampoule sealed under vacuum, although syntheses of B-O COFs under reflux conditions⁶⁵ or in a pressure bomb were reported.⁴⁸ For this a solvent mixture in a varying ratio of mesitylene/dioxane is applied in most cases. Finding the right solvent mixture is crucial for both crystallinity and porosity. In-depth studies on COF-1 (**1**, see Figure 1.4) revealed the crucial role of mesitylene in crystalline and porous COF formation.⁶⁶ IR spectroscopy shows to be a useful tool for diagnostic characterization during synthesis.⁶⁷ COF-1, which is boroxine based, has been synthesized under vapor diffusion⁶⁸ and sonication conditions.⁶⁹ Sonication conditions at room temperature have also been used to synthesize COF-5 (**1** and **23**) on carbon nanotubes and graphene.⁷⁰

Solid state NMR assisted mechanistic studies on the influence of pyridine on boroxine COF-1 (**1**) or boronate ester based COF-10 (**11** + **23**) and COF-5 (**1** + **23**) revealed an irreversible decomposition of the COFs, if boronate ester linked, and a reversible phase change in COF-1.^{71,72} Resistance of COF-1 (**1**) against humid air can be achieved by combination with (3-aminopropyl)triethoxysilane.⁷³ Studies on O-protected polyols employed in COF-synthesis showed that COF formation underlies a complex, not yet fully understood mechanism.⁷⁴ COF-5 (**1** + **23**) prepared from homogenous conditions showed improved crystallinity to COF-5 synthesized under conventional heterogeneous conditions, which is further enhanced by addition of stoichiometric amounts of water.⁷⁵ Further investigation of the mechanism revealed an activation energy of boronate ester formation in COFs of 22-27 kcal mol⁻¹ (92-113 kJ mol⁻¹).⁷⁵ Two factors had a huge influence on the growth rates and stabilities. On the one hand the growth rates of boronate ester COFs revealed its large dependence on the pore size: the larger the slower the rate. On the other hand, if pore sizes of two COFs are similar, the interlayer stacking interactions seem to be the rate limiting step: The better the interlayer stacking of the building blocks involved, as in pyrene building block **10** compared to bisphenyl **11**, the faster the COF formation.²⁷ The speed of COF formation can be improved by microwave-assisted synthesis down to 20 minutes.⁷⁶

Solvothermal methods provide COFs as insoluble powders, which limits their application in devices. Films of B-O COFs have been prepared by synthetic deposition under solvothermal/microwave conditions first on graphene,⁷⁷ then on various other substrates such as FTO/glass⁴⁵ and silicon,⁴⁶ sometimes by employing a special substrate holder.⁴⁶ In some cases, growth is only possible if the substrate has been modified on its surface (grafting).⁷⁸ A 3D COF has been synthesized as film on a surface modified alumina substrate.⁷⁹ A closer look at COF film formation on graphene revealed that certain solvent combinations during synthesis enabled selective and/or oriented growth of the 2D COFs.⁸⁰ Non-oriented films of the B-O COF (**5a** + **23**) were grown by vapor-assisted conversion.⁸¹

1.2.2 COFs Based on C-N Bond Formation

Linkages Based on C-N Bond Formation

A combination of aldehyde building blocks with the simplest nitrogen containing building block hydrazine results in an azine linkage (see Figure 1.6 top). This linkage has first been published by *Jiang*⁸² and was simultaneously synthesized in our group (pyrene **51** + hydrazine (**53**)). Combination of the aldehyde with a hydrazide yields a hydrazone (see Figure 1.6 upper center), which has been firstly realized in COF-42 (**44** + **54b**) and COF-43 (**49** + **54b**).⁸³ In another C-N connection, amines condense with aldehydes to imines (see Figure 1.6 lower center).⁸⁴ A variation of imine condensation by utilization of 1,3,5-triformylphloroglucinol (**45**, see Figure 1.7) as linker leads to enamine formation.⁸⁵ The chemically stable imide formation is achieved by condensation of a cyclic anhydride with amines at high temperatures.⁸⁶ Trimerization of aromatic nitriles leads to the formation of 1,3,5-triazines. This reaction has first been utilized by the *Antonietti* group to obtain CTF-1, a network isoelectronic to COF-1 (see Figure 1.6 bottom).⁸⁷

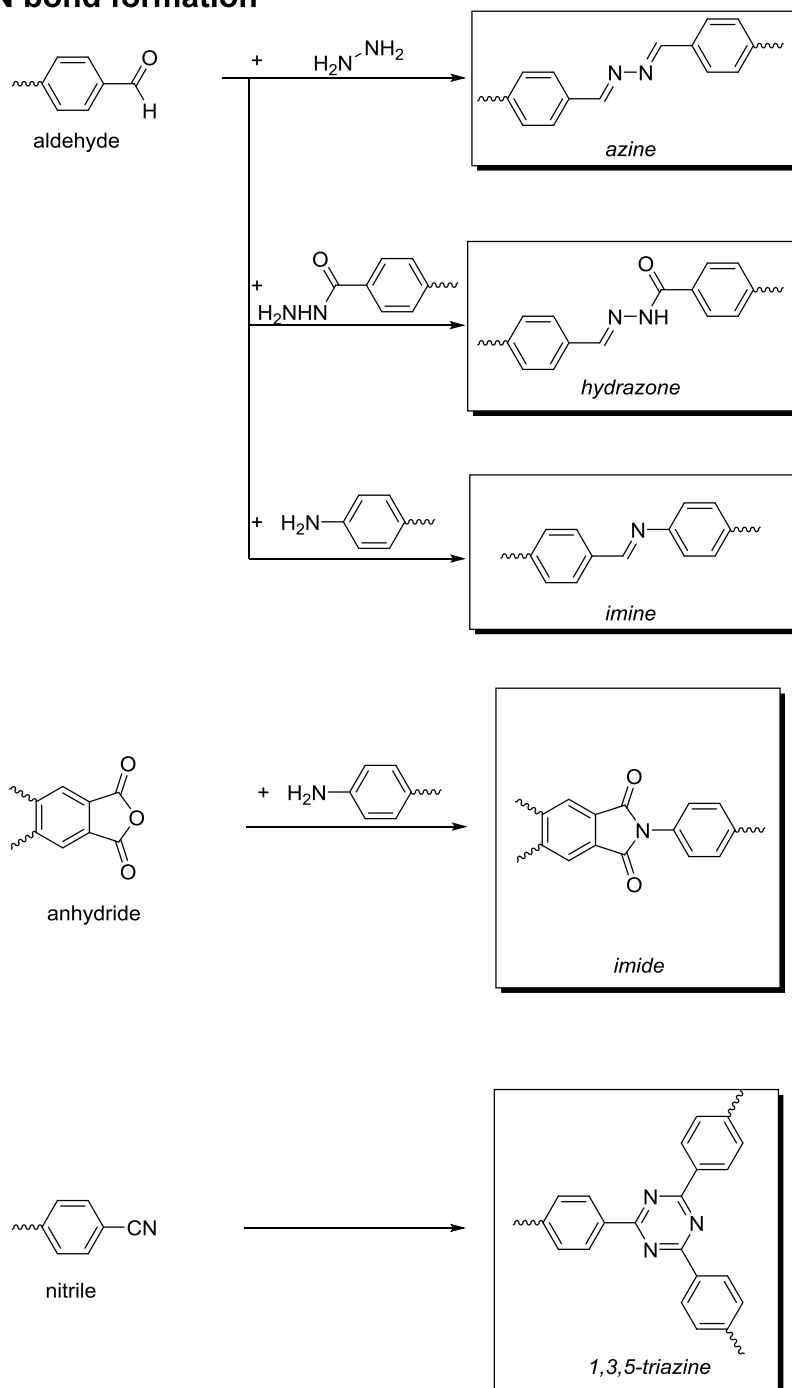
C-N bond formation

Figure 1.6: Different linkages of COFs based on C-N bond formation.

C-N Building Blocks Utilized in COFs

C-N COF formation is less widely spread in the community than B-O based COFs, although C-N bonds are less prone to hydrolysis.⁵ The first imine COF, COF-300, (3D, tetraphenylmethane **68** + **34**) was synthesized by the *Yaghi* group,⁸⁴ offering a high methane uptake capacity.⁸⁸ Later, this COF was modified by a heteropolyacid to introduce catalytic activity for the epoxidation of alkenes.⁸⁹ An in-depth insight into the structure of COFs was obtained recently the electron mi-

croscopy assisted solution of a single crystal structure of the related 3D COF-320 (tetraphenylmethane **68** + bisphenyl **37**).⁹⁰

B-O COFs and C-N COFs have partly different chemical and material properties. Electronic properties such as local photoconduction seem to benefit from the imine connection compared to boronate ester connection as studied on porphyrine COFs (**65a** + **34** and **21a** + **26a**, see Figures 1.4-1.5 and 1.7-1.8).⁵¹ This finding led to the development of a solar cell with 0.9% efficiency with the phenazine based CS-COF (pyrene **40** + triphenylene **76**) in combination with fullerene by the *Jiang* group.⁹¹ The semiconducting properties of a tetrathiafulvalene moiety in COFs (**52** + **55a** and **52** + pyrene **66**) could be changed by oxidative doping by tetracyanoquinone⁹² or iodine^{16,93} which lead to improved electric conductivities, also in films.⁹² Interesting optical properties have been found for some imine-based COFs. Significant visible-light absorption has been achieved by use of triazatruxene **48** as a linker in a COF (**48** + **55a**).⁹⁴ Combination of the two C_3 building blocks (trialdehyde **49** + triamine **70**) in a COF allowed sensing of nitroaromatics by fluorescence quenching.⁹⁵

Although first examples of C-N COFs showed reduced porosity compared to B-O COFs, recently very high porosity ($2700 \text{ m}^2 \text{ g}^{-1}$) has been achieved in a tetragonal framework by utilization of pseudo- C_4 pyrene **51** with 1,4-phenylenediamine (**55a**).⁹⁶ For the first time, uniform mesopores and micropores both present in one single framework have been synthesized in a COF (**34** + **67**) by use of the pseudo C_4 symmetric amine **67** as building block, leading to star-of-david-like structures.⁹⁷

Several imine-based COFs incorporated the porphyrin unit **65a-d** as building block. A combination with C_2 linkers such as catechols **41a-b**,⁹⁸ or squaric acid (**42**) lead to a whole class of COFs.⁹⁹ With this C_4 node (**65c**), a C_2 mixed-linker (combination of **34** and fluorinated **35**) approach lead to an improvement in porosity due to improved stacking interactions in the imine-COFs.¹⁰⁰ Hydrogen bonds between the C_2 hydroxy-decorated aldehyde (such as *o*-dihydroxyterephthalaldehyde **36a**) and the imine of the C_4 symmetric porphyrin tetraamine (**65a**, **c**, **d**, see Figure 1.8) leads to improved crystallinity and porosity in comparison to the methylated **36b**, as a result of in-plane hydrogen bonding.^{101,102} Functionalization of linker **36a** with an alkyne bearing moiety (**36c**) enabled postfunctional *click* chemistry in C-N COFs.¹⁰³ Suitable *click* chemistry enabled the introduction of free amine or carboxylic acid moieties into these kinds of COFs to investigate their influence on CO_2 adsorption.¹⁰⁴ This investigation was expanded by postfunctionalization of the hydroxyl group of linker **36a** in the COF (**36a** + **65a**) with several anhydrides, leading to introduction of carboxylic acid residues in the pore.¹⁰⁵ *Click* chemistry has been also employed to covalently attach the persistent radical 2,2,6,6-tetramethyl-1-piperidinyloxy (TEMPO) to the COF (**65d** + alkyne **36c**) in different amounts. The resultant COF has been used as a pseudocapacitor.¹⁰⁶ Palladium has been immobilized on an imine-based porphyrin containing COF (**65a** + bisphenyl **37**) to catalyze the *Suzuki* reaction.¹⁰⁷ A cobalt-porphyrin containing COF (**65e** + **34**) has been used as precursor to a cobalt containing carbon electrocatalyst via pyroly-

sis.¹⁰⁸ A similar porphyrin containing COF (**65e** + bisphenyl **37**) showed high activity in electrocatalytic CO₂ reduction to CO in its pristine crystalline form.¹⁰⁹

Aldehydes

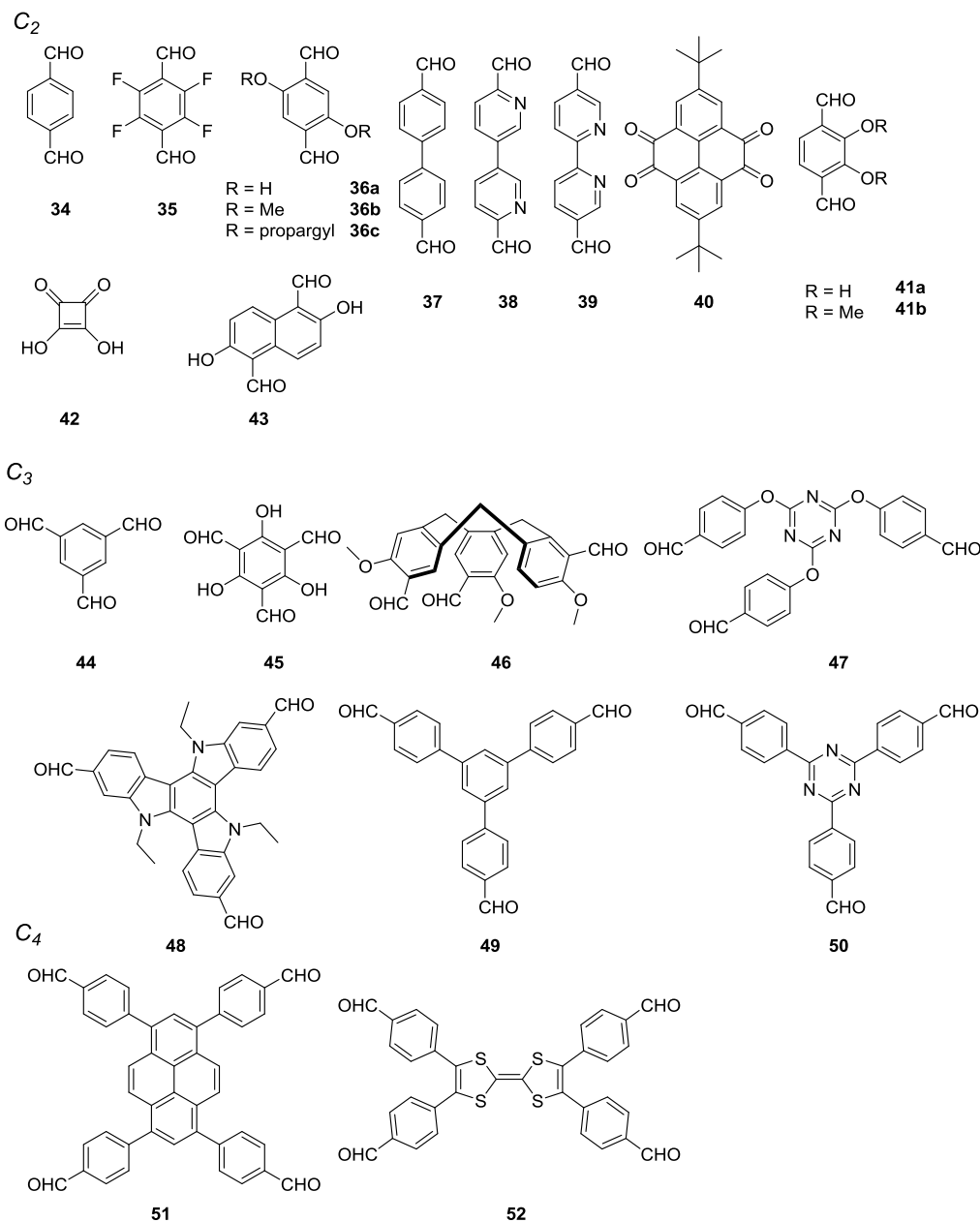


Figure 1.7: Previously employed aldehyde-bearing building blocks for C-N based COFs.

The pseudo C₄ symmetric pyrene **66** containing amine functionality has been employed with different C₂ linkers (**36a**, catechol **41a**, bipyridines **38** and **39**) offering docking sites for e.g. metals like vanadium.¹¹⁰

Due to their higher chemical stability, several COFs have been used as catalysts in different reactions: The imine-based COF LZU-1 (1,3,5-triformylbenzene (TFB, **44**) + diamine **55a**) in combination with palladium acetate can act as a catalyst for *Suzuki* couplings as demonstrated by the Wang group.¹¹¹ Enantioselective *Michael* additions have been catalyzed by an imine-based COF

system (triamine **70** + dialdehydes **36b** + different equivalents of alkyne **36c**), functionalized by *click* chemistry with a proline derivative, showing that a higher degree of functionalization of the pore wall with the catalyst leads to decreased catalytic activity.¹¹² The Brønsted-basic properties of 3D BF-COF-1 (adamantane **69** + **44**) and 2 (**69** + **45**) were used for size-selective organocatalysis of a *Knoevenagel* condensation.¹¹³ Introduction of an anthracene moiety **58** in a COF (**58** + pyrene **51**) improved the speed of *Diels-Alder* reactions in the pore.¹¹⁴

The triazine moiety is a molecular motif of carbon nitrides and covalent triazine frameworks. Besides these networks, integration of this moiety into a COF, TFPT-COF (**50** + **54b**) was accomplished for the first time in this work (see Chapter 3).¹¹⁵ In the meantime, other triazine containing COFs appeared: An imine-based COF was introduced with a triazine moiety (diamine **55a** + trialdehyde **47**).¹¹⁶ Depending on the solvothermal synthesis conditions such as temperature and solvent combination, the resulting COF (**55a** + **47**) has the same structure but different porosities.^{116,117} Two other C₃-triazine containing imine COFs (triazine **71** + TFB (**44**) and **71** + **34**) have good CO₂ adsorption capacities.^{118,119}

Hydrazine/Hydrazides/Amines

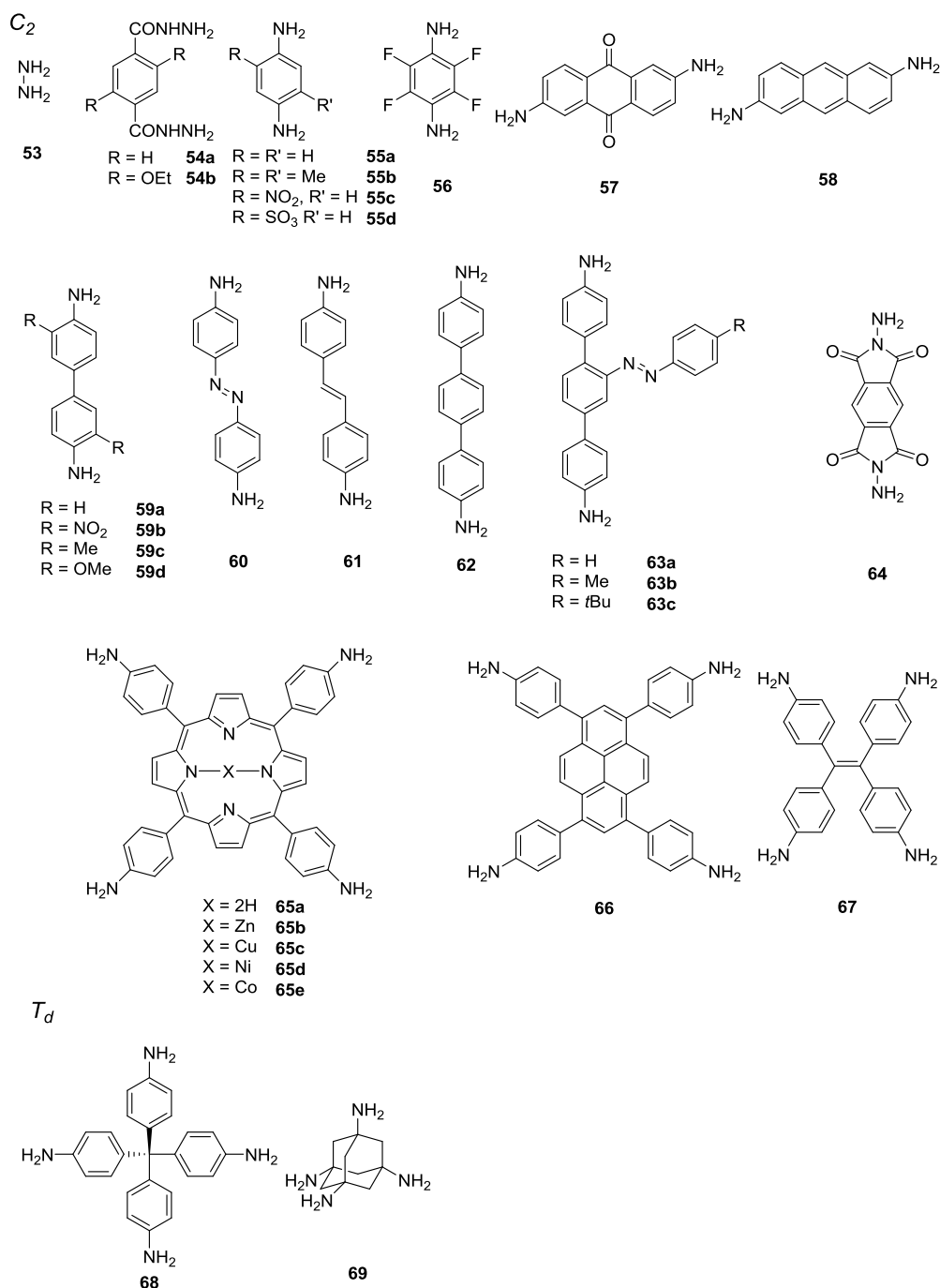


Figure 1.8: Previously employed C_2 and C_4 amine/hydrazide bearing building blocks for C-N based COFs.

The rather exotic linker **46** was also employed in two COFs (**46** + **55a**, **46** + **59a**).¹²⁰ Imine-based COFs have not only been synthesized as bulk material, but were also coated on aramid (**43** + triamine **72**),¹²¹ decorated with gold nanoparticles¹²² and synthesized on graphene (anthraquinone **57** + TFB (**44**)) for capacitor purposes.¹²³ The LZU1-COF (TFB (**44**) + **55a**) has been used in combination with graphite oxide to build a supercapacitor electrode.¹²⁴

Related enamine linked COFs are all based on 1,3,5-triformylphloroglucinol (TFG, **45**) as C_3 linker, which was first introduced by *Banerjee's* group.⁸⁵ When condensed with an amine this unique molecular building unit can undergo a keto-enol/imine-enamine tautomerism (see Figure 1.9), which occurs both in molecules (monotopic amine as reactant)¹²⁵ and in COFs (ditopic amine as reactant).⁸⁵

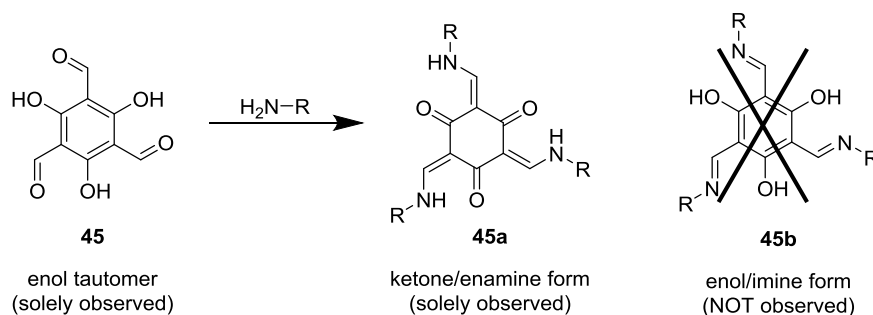


Figure 1.9: Reaction of 1,3,5-triformylphloroglucinol **45** and an amine resulting in an enamine as condensed product.

Initially synthesized by the *Banerjee* group,⁸⁵ the TFG-based COFs can also be expanded in lattice size by linker extension (diamines **55a-c** + TFG (**45**)) and bisphenyls **59a-d** + TFG (**45**)) and exfoliated mechanically.¹²⁶ In combination with the redox-active anthraquinone **57**, the resulting COF (**57** + **45**) has been used in pseudocapacitors.¹²⁷ Introduction of a basic azo moiety through the C_2 building block **60** in a COF (**60** + **45**) enabled high proton conductivity when loaded with phosphoric acid.¹²⁸ The corresponding stilbene-based COF (**61** + **45**) did not show such high proton conductivities. Different azo-benzene moieties (**63a-c**) have been attached to a linear terphenyl diamine core **62** in a COF (**63a-c** + **45**). Photoswitching of the pore adjacent azo moiety in these COFs from *trans* to *cis*-isomer had great impact on gas sorption and optical properties of COFs.¹²⁹ The outstanding chemical resistance of the enamine linkage enabled the usage of those COFs for catalysis purposes. These COFs have been decorated with palladium nanoparticles to catalyze *Sonogashira* and *Heck* couplings,¹³⁰ with molybdenum ions to catalyze epoxidation,¹³¹ and with cadmium sulfide to co-catalyze photocatalytic hydrogen production.¹³² The application of a COF as photocatalyst for hydrogen evolution has firstly been shown in the present work (see chapter 3).¹¹⁵ Sulfonate functionalized C_2 diamine **55d** was utilized in the enamine COF (**55d** + **45**) to catalyze fructose conversion.¹³³

Combination of the two C_3 building blocks (triamine **70** + TFG (**45**)) in a COF lead to high CO_2 uptake capacity.⁹⁵ Liquid phase exfoliated covalent organic nanosheets (CONs) of an enamine COF (pyromellitic hydrazide **64** + **45**) and a hydrazone COF (**64** + **49**) were prepared by immersion in isopropanol and used for sensing purposes.¹³⁴ The enamine-based COF (**59a** + **45**) has been used as stationary phase in gas chromatography.¹³⁵

After the initial publication by *Yaghi*,⁸³ COF-43 (**49** + **54b**) was exfoliated in a solvent mediated exfoliation.¹³⁶ The related azine-based Py-azine COF (pyrene **51** + hydrazine **53**) offers fluorescence based detection of nitroaromatics and stability under acidic/basic aqueous conditions.⁸²

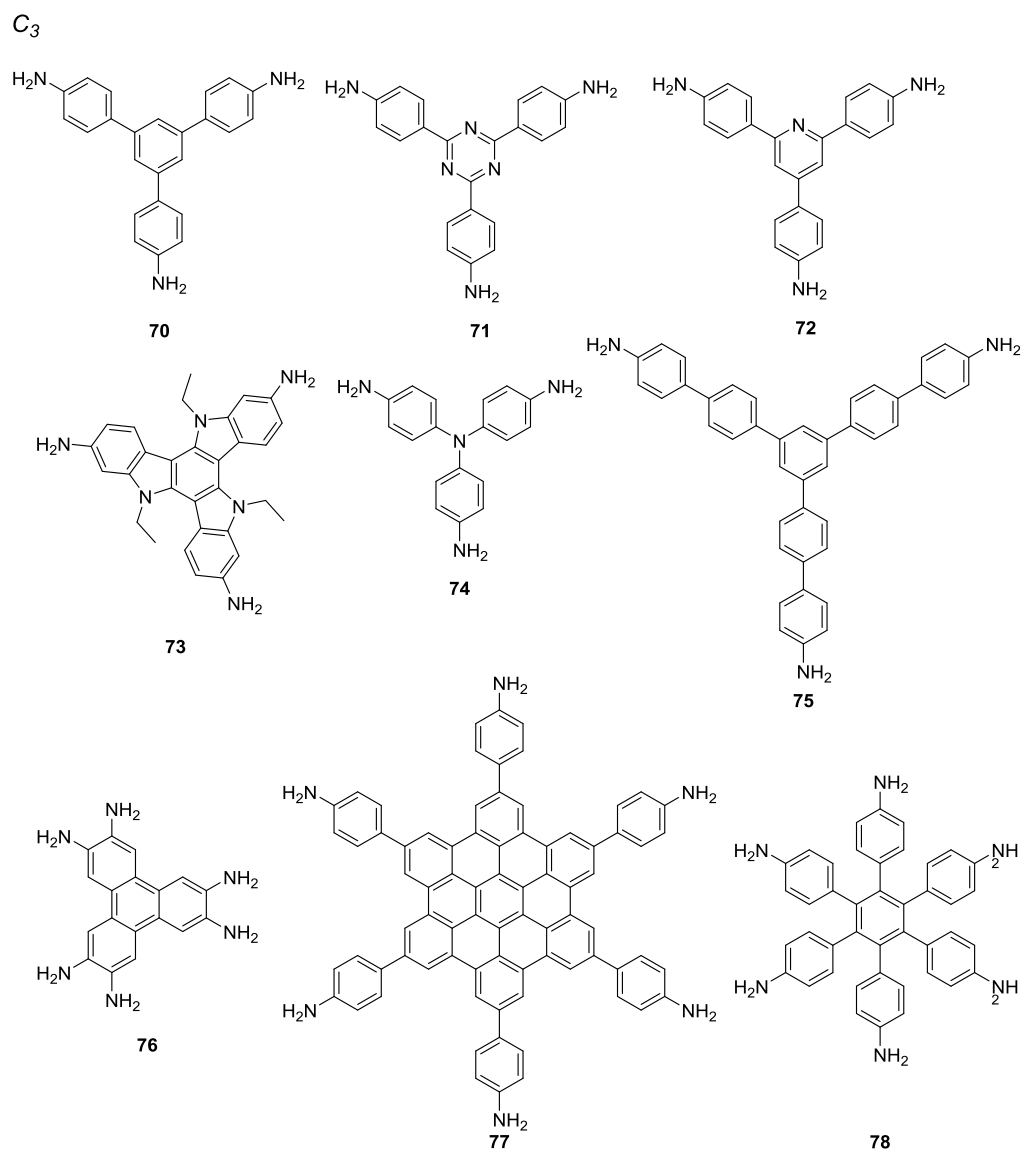


Figure 1.10: Previously employed C_3 amine bearing building blocks for C-N based COFs.

Imide-based COFs by the *Yan* group are the most recent subclass of C-N COFs, offering superior chemical stability also under oxidizing conditions.⁸⁶ So far all imide-based COFs have only employed pyromellitic dianhydride (**79**, see Figure 1.11) as anhydride building block.

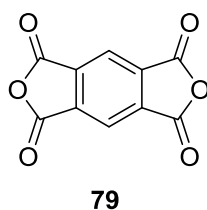


Figure 1.11: Pyromellitic anhydride as C_2 building block for imide COFs.

Isorecticular lattice expansion can also be applied on imide COFs (all with **79**) by employing the triamines **74** as well as extended **70** and double extended **75**. Polyimide 3D COFs are feasible by use of T_d symmetric linkers **68** and **69 + 79**.¹³⁷

C-N based COFs involving the triazine ring formation during polymerization are also called covalent triazine frameworks (CTFs). While there are many CTFs synthesized so far, there are only two examples of both crystalline and porous CTFs involving **80** and **81** as linkers (see Figure 1.12),^{87,138} both were synthesized under ionothermal conditions in a $ZnCl_2$ salt melt.

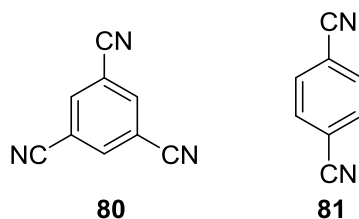


Figure 1.12: Aromatic nitriles employed for the formation of crystalline covalent triazine frameworks (CTFs).

Synthetic Aspects of C-N COFs

The general approach for synthesis of C-N COFs is also the solvothermal method (see above). This section describes further approaches specially developed for C-N COFs. Enamine-based COFs have been synthesized by mortar and pestle, although with low crystallinity and porosity,¹³⁹ in a solvent assisted mechanochemical approach with increased crystallinity, albeit still low porosity.¹⁴⁰ Stability of imine COFs was increased by introduction of a hydroxyl group in the aldehyde bearing linker (**36a + 65a**, see also Figure 1.13).¹⁰²

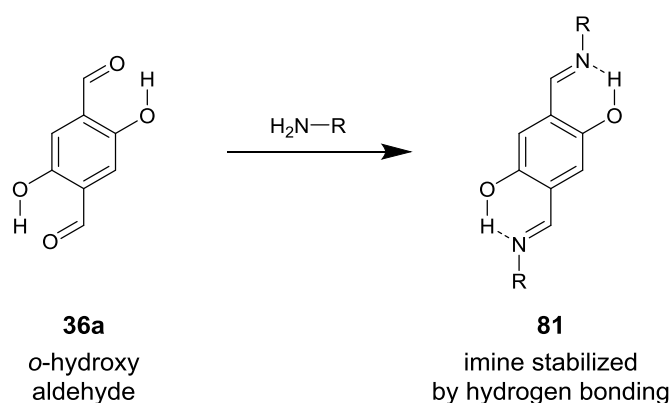


Figure 1.13: Stabilization of imine-based COFs by hydrogen bonding.

Investigation of an imine COF (**36a + 70**) with a hollow spherical morphology shows indications for an Ostwald ripening process during COF formation and the important role of the mesitylene content in the synthesis solvent mixture.¹⁴¹ The conventional solvothermal synthesis of COFs was varied in a vapor-solid approach,¹⁴² although the resulting COF (**43 + 72**) shows lower crystallinity than the parent one which was synthesized by solvothermal methods.¹²¹ The imine-based COF

(TFB (**44**) + triamine **70**) has been printed in laminar columns as a film.¹⁴³ Also microwave heating has been employed for the synthesis of the enamine COF (TFG (**45**) + diamine **55a**), which showed a 35% increased surface area compared to the COF prepared by the conventional solvothermal synthesis.¹⁴⁴ A homogenous solution approach gave promising results with regard to both high surface area and crystallinity in the imine-based COF (TFB (**44**) + **55a**).¹⁴⁵ ZnO nanorods act as template in the conventional solvothermal synthesis of an enamine-based COF (**45** + **55a**). The ZnO nanorods were dissolved after COF synthesis.¹⁴⁶ The enamine-based COF (**45** + **57**) has been grown on gold by slow addition of one of the starting materials (TFG (**45**)) over 1 h, which resulted in oriented COF film growth.¹⁴⁷ The material has been applied as pseudocapacitor. Imine-linking has been used in a MOF-COF combination, although synthesized in two steps.¹⁴⁸ An orthogonal combination of both C-N and B-O bond formation in two steps has been applied in COF synthesis, resulting in mixed imine/boronate ester framework.¹⁴⁹

1.2.3 Highlights of COF Chemistry: Towards Applications

Porosity and Gas Storage

With their high porosity (the BET surface area of the 3D COF-103 (**22b**) is $4210 \text{ m}^2 \text{ g}^{-1}$)²³ and low density (as low as 0.17 g cm^{-3} for the 3D COF-108 (**22b** + HHTP (**23**))), B-O based COFs hold the records in comparison to any other organic porous material. The high surface area and pore volume (up to $1.66 \text{ cm}^3 \text{ g}^{-1}$)²³ predestine 3D COFs for gas storage applications, although recently higher pore volumes (up to $1.85 \text{ cm}^3 \text{ g}^{-1}$) have been achieved in 2D imine-based COFs.¹¹⁰ COF-102 (**22a**) does indeed offer one of the highest H_2 uptake of 7.24 wt% at 77 K / 1 bar and a reasonable methane uptake of 187 mg g^{-1} at 298 K/35 bar,¹⁵⁰ exceeding the US Department of Energy (DoE) target of 129 mg g^{-1} . The imine-based 2D COF (pyrene **51** + diamine **55a**) with the highest surface area of $2700 \text{ m}^2 \text{ g}^{-1}$ lacks behind in gas storage capacity.⁹⁶ A 3D COF (**22a** + **24a**) offers a sorption-measured pore size of 6.4 \AA , which is the smallest pore ever measured of all COFs, although zeolites do offer smaller pores.²⁹ The largest pore of 5.3 nm has been measured in a B-O based COF (**15** + **23**), hence COFs offer homogeneous pore sizes differing by an order of magnitude.

Electronic Properties

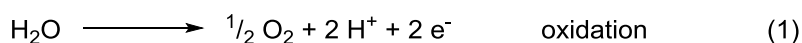
With their conjugated systems 2D COFs are good candidates for electronic applications in devices. Their modular character allows tuning of their semiconducting properties into ambipolar,¹⁵¹ p- or n-type⁴⁴ conduction.¹⁵² The semiconducting properties could even be switched between ambipolar, p- and n-type by changing the metal coordinating to the porphyrin unit in the COF.⁵² First measurements⁴¹ of the local hole photoconductivity of a porphyrin containing C-N COF revealed values of $8 \text{ cm}^2 (\text{Vs})^{-1}$,⁵¹ thus exceeding amorphous silicon. A first organic solar cell based on a fullerene@COF gave rather low efficiencies,⁴⁵ although the solar cell based on the phenazine CS-COF (**76** + **40**) combined with a fullerene approached 1%.⁹¹ On porphyrin containing imine

COFs, the photocatalytic singlet oxygen generation⁹⁹ was shown to be faster than in comparable molecular porphyrins, and within the COFs this reaction is faster with non-metal containing porphyrin **65a** than with Cu@porphyrin **65d**. This has also been underlined by time-resolved fluorescence spectroscopy.¹⁰¹ An in-depth view on this topic would go beyond the scope of this introduction, and the reader is therefore referred to a recent review.¹⁵³

1.3 Photocatalytic Hydrogen Generation with Light-Element Photocatalysts.

In consideration of an inevitable steady decay of fossil fuels, along with the concerns over storage and economic aspects, the research in novel techniques for energy generation plays a decisive role. One of the most promising ideas for a renewable energy source is the concept of photocatalytic water splitting. Hydrogen and oxygen provided by such a process can be used either to generate electricity in various types of fuel cells, or to produce heat when combusted in appropriate reactors. In both cases, the starting product is regenerated without the formation of toxic byproducts, making water and the sun a highly desirable, environmentally friendly and nearly inexhaustible alternative for non-renewable resources.¹⁵⁴

The key to success is to find a material suitable for catalyzing the highly endergonic (+237.2 kJ/mol under standard conditions at pH = 0) reaction shown in equation 3.



Since the seminal work of titanium dioxide (anatase) on photoelectrical water splitting in the early 1970s,¹⁵⁵ research interest has mainly focused on inorganic solids having semiconducting properties.¹⁵⁶ The principle process of heterogeneous photocatalytic water splitting,¹⁵⁷ involving such a semiconducting catalyst, is illustrated in Figure 1.14.

Absorption of incident photons, possessing sufficient energy to overcome the semiconductor band gap, excites an electron in the photocatalyst from the valence band (VB) to the conduction band (CB) (step 1 in Figure 1.14). The band designations (conduction band and valence band, respectively) are taken from classical semiconductors, although some photocatalysts have only very limited semiconducting properties. In other words, such systems may rather be viewed in the more localized picture of molecular systems where the valence band should be replaced by highest occupied molecular orbital (HOMO) and the conduction band by the lowest unoccupied molecular orbital (LUMO), respectively. The second step (step 2 in Figure 1.14) involves charge separation and migration of charge carriers towards the solid-liquid interface. Finally, the actual

redox reactions between holes, electrons and aqueous species occur on the solid surface (equation 1 and 2), which results in evolution of oxygen and hydrogen (step 3 in Figure 1.14).

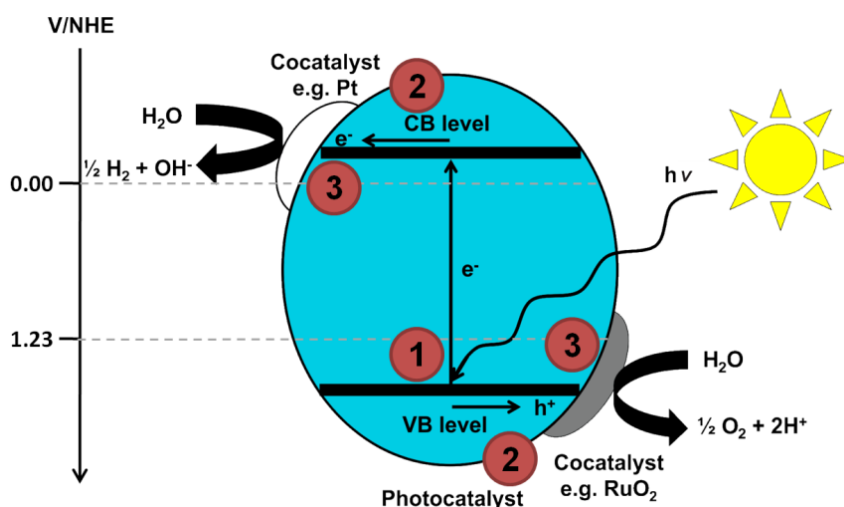


Figure 1.14: Process scheme of photocatalytic water splitting. NHE refers to standard hydrogen electrode (pH = 0, 1013 hPa).

In order to reduce protons to hydrogen, the promoted electrons in the CB have to exhibit a more negative potential than the H⁺/H₂ redox potential (0 V vs. NHE at pH = 0, see dashed line), whereas the holes are only able to oxidize water to oxygen, if the top level of the catalysts VB is more positive than the corresponding redox potential of O₂/H₂O (+1.23 V vs. NHE at pH = 0, see dashed line).¹⁵⁸ In the ideal theoretical case, the required energy for successful water splitting equals the difference between the potentials of the participating redox species, that is 1.23 eV. Due to inevitable resistive and recombination losses, along with kinetic barriers (overpotential), and the demand for transferring more than one electron, the actual minimum energy needed to effectively drive water splitting is significantly higher.^{159,160} In order to lower such overpotentials and to improve the overall catalytic performance of a semiconducting material, additional cocatalysts, possessing exceptional low activation barriers towards one of the two half reactions, are usually employed. For the water oxidation reaction (equation 1), precious metals and metal oxides like ruthenium(IV), iridium(IV) oxide or cobalt(II,III) oxide are commonly predominant,^{161–163} whereas in the case of hydrogen evolution (equation 2) pristine noble metals, such as platinum and rhodium, are best suited because they exhibit the weakest hydrogen adsorption energies and the highest exchange currents owing to their low Fermi levels.^{164–166} All these catalysts also accelerate the back reaction of hydrogen and oxygen to water, if the evolution of both gases is not spatially separated.

For evaluating purpose, it is advisable to focus on only one of the two half reactions to show whether a certain system satisfies the thermodynamic and kinetic needs for hydrogen or oxygen evolution, respectively.¹⁶⁷ In such cases, sacrificial electron donors/acceptor reagents are added in excess to suppress undesired recombination reactions by rapid quenching of photogenerated charge carriers. Herein, reducing agents, like alcohols such as methanol or amines such as tri-

ethanolamine, work well as sacrificial donor for investigating hydrogen evolution, since they are more readily oxidized than water. In contrast, oxidizing agents such as silver(I), iron(III) or peroxodisulfate ions effectively consume electrons in the conduction band as sacrificial acceptor for closer look on the oxygen evolution half reaction.

The ultimate photocatalyst for water splitting, which is yet not available, has the following features: i) natural abundant ingredients, ii) simultaneous evolution of hydrogen and oxygen at high quantum yield, iii) excellent long-term stability under sunlight irradiation as well as iv) chemical inertness against oxidation and reduction in the presence of an aqueous electrolyte. Nevertheless, big strides have been made in the last decades towards the development of photocatalyst based on more or less complex structured inorganic solids, including transition metal oxides, (oxy)nitrides and (oxy)sulfides.^{168,169} While most photocatalysts known to date are metal-containing compounds, there are some exceptions containing only light elements. Only the classes of light-element photocatalysts are reviewed here; for a more detailed overview the reader is referred to other literature.¹⁷⁰

The first “organic” heterogeneous photocatalyst for photocatalytic hydrogen generation in the presence of a sacrificial donor was short chain (7-11 units) poly(*p*-phenylene) (PPP, see Figure 1.15), which initially only provided hydrogen production under UV-light irradiation without any co-catalyst added.¹⁷¹ This catalyst has been improved in efficiency by addition of a noble metal co-catalyst, so that hydrogen is produced under visible-light irradiation.¹⁷² Switching to the more coplanar poly(pyridine-2,5-diyl) (PPy, see Figure 1.15) offered enhanced quantum yields in photocatalytic hydrogen generation.^{173,174} Further investigations concentrated on oligomeric poly(pyridine-2,5-diyls) as photocatalysts.¹⁷⁵ A bipyridine unit has also been introduced in the polymer, and the chelating platinum (PBpy, see Figure 1.15) offers enhanced hydrogen evolution.¹⁷⁶

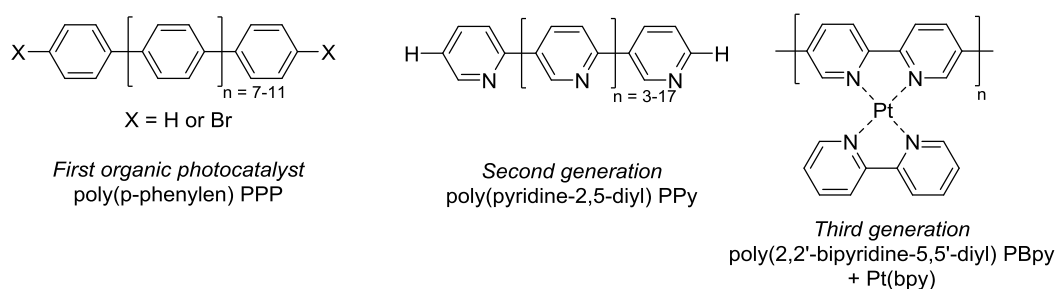


Figure 1.15: First three organic photocatalysts for hydrogen generation based upon polyaromatics.

Full water splitting has so far been achieved only by carbon nitrides under visible-light irradiation,^{177,178} although in two separated experiments with either a suitable sacrificial donor (hydrogen evolution) or acceptor (oxygen evolution). This finding paved the way to a whole range of carbon-nitride based photocatalysts.¹⁷⁰ Although the field of carbon nitride photocatalysis has undergone a tremendous development since its beginning in 2009, these systems still lack molecular tunability due to the limited choice of building units (triazines or heptazines).¹⁷⁹ For a closer look on car-

bon nitrides the reader is referred to the thesis of Katharina Schwinghammer. A few amorphous 2D polyimines have also been shown to be photocatalytically active towards hydrogen evolution.¹⁸⁰ Structurally comparable to COFs, these polyimines combine the C_3 triamine **70** with different C_2 dialdehydes (**45**, **82-84**, see Figure 1.16). The polyimines consisting of the building blocks **70** + **82** or **84** showed the highest photocatalytic activity for hydrogen generation, compared to the other two polyimines (**70** + **81**, **70** + **83**), although these systems are by a factor of 5 slower than standard carbon nitride photocatalysts.

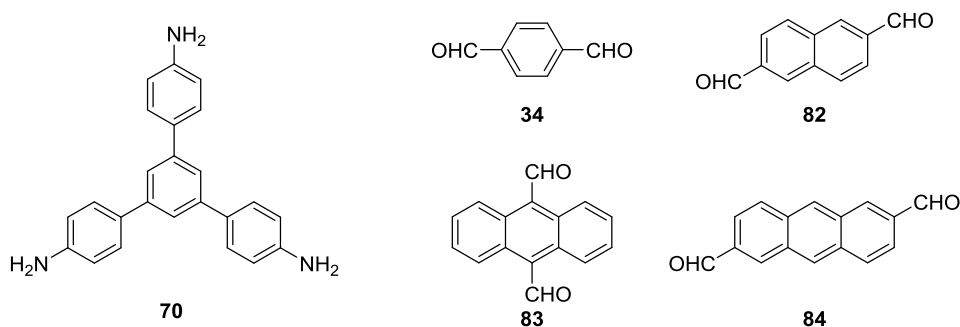


Figure 1.16: Building blocks of 2D polyimines used as photocatalysts.

Boron carbide¹⁸¹ and amorphous 2D carbon doped boron nitride-systems¹⁸² also show moderate hydrogen generation under visible-light irradiation, in part even both half-reactions are possible in the presence of suitable sacrificial agents.

1.4 Adsorbents for Post- and Pre-Combustion CO₂ Capture

The global warming is mainly caused by carbon dioxide resulting from industrial processes and burning of fossil fuels for energy production, heating and transportation.¹⁸³ CO₂ capture and storage (CCS) is one of the key technologies to reduce anthropogenic CO₂ emissions, and the least developed, when compared to other key technologies such as increasing the efficiency in industrial and energy production. This technology has the potential to reduce the emissions of CO₂ up to 20%.¹⁸⁴ The carbon dioxide capture can be accomplished before combustion (pre-combustion) or after combustion (post-combustion). For a more detailed explanation of CCS the reader is referred to.^{185,186} Depending on the process parameters of CO₂ capture in fossil fuel-fired power plants, a high selectivity towards CO₂ over H₂ at high pressures (>10 atm) (pre-combustion capture) or over N₂ at low pressures (post-combustion capture) is desirable.^{185,187}

CO₂/H₂ separation as used in pre-combustion capture is already well-developed due to the tremendous scale of H₂ production (50 million tons per year worldwide) and is primarily accomplished by the application of zeolites or activated carbons for selectively and reversibly adsorbing CO₂ and other impurities in the presence of H₂ at high pressures.¹⁸⁸⁻¹⁹²

The CO₂/N₂ separation as applied in post-combustion capture is a more pretentious challenge to master.

The key requirements for physisorbents for both capture processes are: high capture capacities, high selectivity and stability towards water vapor, which is a part of the emitted process gasses. Literature provides different strategies to fulfill the first two requirements: i) Increase the surface area, thus providing more interaction sites. ii) Increase the average interaction energy between CO₂ and the sorbent. iii) Engineering of the pore size, providing a molecular gas sieving effect.¹⁹³ The CO₂ molecule provides a comparably large quadrupole moment, which results in partial Lewis acid and base properties.¹⁹⁴ The Lewis acidic carbon atom of CO₂ can easily interact with nucleophilic moieties in nitrogen rich compounds such as amines, which provide a basic free electron pair. The Lewis basic oxygen atoms of CO₂ prefer interaction with Lewis acidic sites like uncoordinated metal ions as in zeolites (see Figure 1.17).

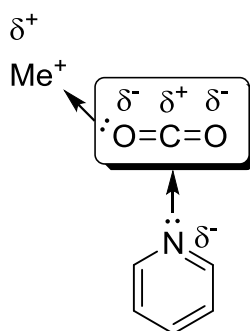


Figure 1.17: Attractive interactions of CO₂ with metals-ions and nitrogen rich compounds.

Their polar surfaces render them as good candidates (2-3 mmol g⁻¹ at 0.1 bar at RT for zeolite 13X) for CO₂ capture¹⁸⁵, although, in the presence of water vapor, the capacity of CO₂ vanishes.¹⁹⁵

Because of their molecular versatility, MOFs are in principal able to fulfill all three requirements. Big efforts in basic research have led to the record holding Mg-MOF-74, which shows exceptionally high uptakes of 8.61 mmol g⁻¹ (298 K, 1bar) and high CO₂/N₂ selectivities (195). For an exhausting overview of carbon dioxide capture in MOFs and porous non-crystalline polymers the reader is referred to.^{186,196} The drawbacks are comparable to zeolites: In the presence of water, some MOFs lose their structure, other their high CO₂ uptake capacity.¹⁹⁷

1.5 Water Vapor Sorbents as New Field of Application

1.5.1 Water Sorption-based Thermally Driven Heat Pumps

Space and water heating accounts for more than 70% of the EU households' energy consumption, provided primarily by the combustion of fossil fuels.¹⁹⁸ Therefore this is one of the major contributions to climate warming. Water sorption-based thermally driven heat pumps can significantly help to minimize primary energy consumption and carbon dioxide emissions generated by industrial or domestic heating and cooling applications.

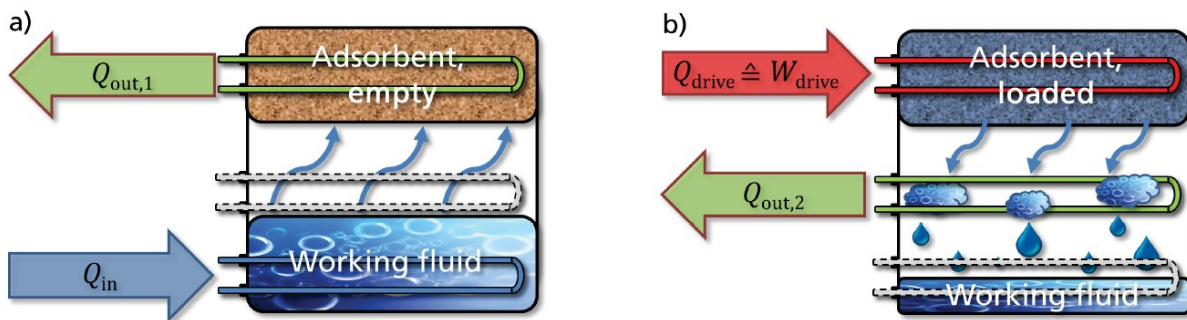


Figure 1.18: Working scheme of a sorption heat pump during (a) the working step and (b) the regeneration step. Temperature levels of the arrows are transliterated using different colors (blue: cold, green: intermediate, and red: hot). U-formed pipes refer to heat exchanger. Adapted from ref¹⁹⁹ by permission of the Royal Society of Chemistry

Figure 1.18 shows the typical 2-step process of sorption-based heat pumps/chillers:²⁰⁰

1. *Working step:* During this step, heat is transferred (“pumped”) from a low temperature level to an intermediate temperature level. In a closed vessel (volume) the working fluid is vaporized by consumption of the heat of vaporization Q_{in} . This heat is taken from the environment from a low temperature level. The sorbent with high affinity towards the vapors of the working fluid will remove the vapor from the gas phase, releasing heat $Q_{out,1}$ defined by the heat of adsorption at an intermediate temperature level. At one point the sorbent is saturated, the vapor pressure of the working fluid will build up in the chamber and the process ceases.
2. *Regeneration step:* Driving energy W_{drive} is applied to the saturated sorbent in form of high-temperature heat. The working fluid is released and is conducted towards a condenser, releasing another part of intermediate temperature heat $Q_{out,2}$, defined by the heat of condensation. The condensed working fluid is re-fed to the evaporator for the repeated initiation of the working step.

The economic and ecological efficiency, power density and operating temperature of this reliable and silent technology directly relate to the properties of the available sorbent. Plain water is the ideal non-toxic working fluid with the unsurpassed high evaporation enthalpy of 2440 kJ/L

(298 K).²⁰¹ During the last years the development of water sorption technologies has progressed due to utilization of low-grade thermal (waste heat) or solar thermal energy. Currently, microporous materials (pore size < 2 nm) such as silica gel and zeolites²⁰² are widely applied commercially in domestic heat pumps (e.g. *Vaillant zeoTHERM*[®])²⁰³ but these specific sorbents must be heated to 150°C for the regeneration step (desorption), so they are far from ideal for the rather low temperatures generated by solar irradiation or waste heat. Potential sorbents need to provide a high uptake of water vapor in a well-defined pressure window.

1.5.2 Fresh Water Generation by Atmospheric Water Capture

Fresh water generation is an ongoing problem in countries with arid climates, as it requires large amounts of energy for processes such as desalination. For this task sorbents which possess high uptakes at low relative humidity (RH) around 30% (the global average vapor content in the atmosphere is 1 vol%, which corresponds to 32% RH at 25°C)²⁰⁴ are most relevant for atmospheric water capture. The sorbents “charge” water vapor in arid climates at night (high humidity, low temperature) and discharge with the help of solar heat at day. A condenser reliquifies the concentrated water vapor and provides fresh water.

1.6 Objectives

The first objective of this thesis is to establish appropriate conditions for the synthesis of new COFs, obeying the two crucial requirements of crystallinity and porosity, and their in-depth characterization by applying state-of-the-art synthesis and analytical tools,

Promising results in photocatalysis of carbon nitrides and other polymers show, that this topic is not restricted to inorganic semiconductors. Therefore the production of non-toxic, lightweight and affordable materials, which do not rely on rare metals, seems feasible.

Besides their promising performance, all these light-element photocatalysts face similar problems, like poor crystallinity, low charge carrier mobility and limited variety for chemical modifications. Covalent organic frameworks (COFs) – could potentially overcome these constraints. With their modular and tunable structure, COFs are predestined for the use as photocatalysts in visible-light driven hydrogen generation, which had not been realized prior to this thesis. All B-O based COFs are moisture sensitive to a certain degree, and all of them decompose in water. Hence, the first objective is the synthesis of a new COF showing both crystallinity and porosity, which are key features for a photocatalytically active framework. For the purpose of photocatalytic water splitting the linkage of the new COF has to be stable in water, but the COF should also offer visible-light absorption. For this task it will be beneficial to introduce molecular building blocks such as triazine into COFs, which is familiar from carbon nitrides, the most important class of non-metal photocatalysts.

COFs are ideal platforms for studying the impact of pore wall polarity and pore size on the gas selectivity. Both of these properties can be tailored by the appropriate selection of the molecular building blocks resulting in a long-range ordered crystalline scaffold. With their high surface areas and pore volumes, gas storage is considered as application for COFs since the early years,¹⁵⁰ although their use in gas separation is only investigated recently. In contrast to MOFs, COFs provide strong covalent bonds such as C-N as linkage type, which are in principal stable against hydrolytic cleavage - a crucial requirement for both pre- and post-combustion CO₂ capture and water vapor adsorption. Their porous nature and intrinsic coordination sites allow modification with metal salts, which may result in beneficial CO₂ capture capacity as predicted by theoretical calculation.^{205–208} As crystalline, modular materials on the level of MOFs COFs surpass all classical adsorbents in terms of structural variability and chemical versatility and are hence expected to supplement established porous materials such as zeolites, activated carbons or silica gels in many technical applications in the future.

The pore wall polarity and pore size may play a crucial role in water vapor sorption as well. For future applications a proof-of-concept work is missing, demonstrating the potential application of COFs as high-performance water sorbents with engineered pore wall polarity. This has been achieved for metal-organic frameworks during the last few years.^{197,209–212} Besides initial experiments by Banerjee and co-workers,^{98,139,141} COFs have not been investigated as potential water sorbents in detail so far.

1.7 References

1. P. J. Crutzen, *Nature*, 2002, **415**, 23.
2. Zeo-Tech GmbH, *Das Selbstkühlende Bierfass*. <http://www.zeo-tech.de/index.php/entwicklungen/mobile-kuehlung/selbstkuehlendes-bierfass-coolkeg> (last accessed September 2015).
3. Valco Instruments Company Inc., *HayeSep® Porous Polymers*. http://www.vici.com/profiles/prof_hay.php (last accessed September 2015).
4. A. G. Slater and A. I. Cooper, *Science*, 2015, **348**.
5. S.-Y. Ding and W. Wang, *Chem. Soc. Rev.*, 2013, **42**, 548–568.
6. X. Feng, X. Ding and D. Jiang, *Chem. Soc. Rev.*, 2012, **41**, 6010–6022.
7. X.-H. Liu, C.-Z. Guan, D. Wang and L.-J. Wan, *Adv. Mater. (Weinheim, Ger.)*, 2014, **26**, 6912–6920.
8. R. L. Martin, C. M. Simon, B. Medasani, D. K. Britt, B. Smit and M. Haranczyk, *J. Phys. Chem. C*, 2014, **118**, 23790–23802.

9. A. P. Côté, A. I. Benin, N. W. Ockwig, M. O'Keeffe, A. J. Matzger and O. M. Yaghi, *Science*, 2005, **310**, 1166–1170.
10. Hausoul, Peter J. C., T. M. Eggenhuisen, D. Nand, M. Baldus, B. M. Weckhuysen, Klein Gebbink, Robertus J. M. and Bruijninx, Pieter C. A., *Catal. Sci. Technol.*, 2013, **3**, 2571–2579.
11. J. Li, X. Yang, C. Bai, Y. Tian, B. Li, S. Zhang, X. Yang, S. Ding, C. Xia, X. Tan, L. Ma and S. Li, *J. Colloid Interface Sci.*, 2015, **437**, 211–218.
12. K. T. Jackson, T. E. Reich and H. M. El-Kaderi, *Chem. Commun.*, 2012, **48**, 8823–8825.
13. D. Beaudoin, T. Maris and J. D. Wuest, *Nat. Chem.*, 2013, **5**, 830–834.
14. E. L. Spitler, B. T. Koo, J. L. Novotney, J. W. Colson, F. J. Uribe-Romo, G. D. Gutierrez, P. Clancy and W. R. Dichtel, *J. Am. Chem. Soc.*, 2011, **133**, 19416–19421.
15. B. T. Koo, W. R. Dichtel and P. Clancy, *J. Mater. Chem.*, 2012, **22**, 17460–17469.
16. S. Jin, T. Sakurai, T. Kowalczyk, S. Dalapati, F. Xu, H. Wei, X. Chen, J. Gao, S. Seki, S. Irle and D. Jiang, *Chem. - Eur. J.*, 2014, **20**, 14608–14613.
17. M. O'Keeffe, *Chem. Soc. Rev.*, 2009, **38**, 1215–1217.
18. O. M. Yaghi, M. O'Keeffe, N. W. Ockwig, H. K. Chae, M. Eddaoudi and J. Kim, *Nature*, 2003, **423**, 705–714.
19. M. O'Keeffe, M. A. Peskov, S. J. Ramsden and O. M. Yaghi, *Acc. Chem. Res.*, 2008, **41**, 1782–1789.
20. M. O'Keeffe and O. M. Yaghi, *Chem. Rev.*, 2012, **112**, 675–702.
21. D. J. Tranchemontagne, J. L. Mendoza-Cortes, M. O'Keeffe and O. M. Yaghi, *Chem. Soc. Rev.*, 2009, **38**, 1257–1283.
22. N. W. Ockwig, O. Delgado-Friedrichs, M. O'Keeffe and O. M. Yaghi, *Acc. Chem. Res.*, 2005, **38**, 176–182.
23. H. M. El-Kaderi, J. R. Hunt, J. L. Mendoza-Cortes, A. P. Cote, R. E. Taylor, M. O'Keeffe and O. M. Yaghi, *Science*, 2007, **316**, 268–272.
24. J. R. Hunt, C. J. Doonan, J. D. LeVangie, A. P. Côté and O. M. Yaghi, *J. Am. Chem. Soc.*, 2008, **130**, 11872–11873.
25. S. Dalapati, M. Addicoat, S. Jin, T. Sakurai, J. Gao, H. Xu, S. Irle, S. Seki and D. Jiang, *Nat. Commun.*, 2015, **6**, Art. No. 7786.
26. L. M. Lanni, R. W. Tilford, M. Bharathy and J. J. Lavigne, *J. Am. Chem. Soc.*, 2011, **133**, 13975–13983.

27. B. J. Smith, N. Hwang, A. D. Chavez, J. L. Novotney and W. R. Dichtel, *Chem. Commun.*, 2015, **51**, 7532–7535.
28. A. P. Côté, H. M. El-Kaderi, H. Furukawa, J. R. Hunt and O. M. Yaghi, *J. Am. Chem. Soc.*, 2007, **129**, 12914–12915.
29. H. Ma, H. Ren, S. Meng, Z. Yan, H. Zhao, F. Sun and G. Zhu, *Chem. Commun.*, 2013, **49**, 9773–9775.
30. S. B. Kalidindi, K. Yussenko and R. A. Fischer, *Chem. Commun.*, 2011, **47**, 8506–8508.
31. S. B. Kalidindi, H. Oh, M. Hirscher, D. Esken, C. Wiktor, S. Turner, G. Van Tendeloo and R. A. Fischer, *Chem.--Eur. J.*, 2012, **18**, 10848–10856.
32. D. N. Bunck and W. R. Dichtel, *Angew. Chem., Int. Ed.*, 2012, **51**, 1885–1889.
33. D. N. Bunck and W. R. Dichtel, *Chem.--Eur. J.*, 2013, **19**, 818–827.
34. D. N. Bunck and W. R. Dichtel, *Chem. Commun.*, 2013, **49**, 2457–2459.
35. Spencer D. Brucks, David N. Bunck and William R. Dichtel, *Polymer*, 2014, **55**, 330–334.
36. M. Dogru, A. Sonnauer, S. Zimdars, M. Doblinger, P. Knochel and T. Bein, *CrystEngComm*, 2013, **15**, 1500–1502.
37. S. Jin, K. Furukawa, M. Addicoat, L. Chen, S. Takahashi, S. Irle, T. Nakamura and D. Jiang, *Chem. Sci.*, 2013, **4**, 4505–4511.
38. E. L. Spitler, J. W. Colson, F. J. Uribe-Romo, A. R. Woll, M. R. Giovino, A. Saldivar and W. R. Dichtel, *Angew. Chem., Int. Ed.*, 2012, **51**, 2623–2627.
39. S. Jin, M. Supur, M. Addicoat, K. Furukawa, L. Chen, T. Nakamura, S. Fukuzumi, S. Irle and D. Jiang, *J. Am. Chem. Soc.*, 2015, **137**, 7817–7827.
40. S. Wan, J. Guo, J. Kim, H. Ihee and D. Jiang, *Angew. Chem., Int. Ed.*, 2008, **47**, 8826–8830.
41. S. Wan, J. Guo, J. Kim, H. Ihee and D. Jiang, *Angew. Chem., Int. Ed.*, 2009, **48**, 5439–5442.
42. E. L. Spitler and W. R. Dichtel, *Nat. Chem.*, 2010, **2**, 672–677.
43. V. S. P. K. Neti, X. Wu, M. Hosseini, R. A. Bernal, S. Deng and L. Echegoyen, *CrystEngComm*, 2013, **15**, 7157–7160.
44. X. Ding, L. Chen, Y. Honsho, X. Feng, O. Saengsawang, J. Guo, A. Saeki, S. Seki, S. Irle, S. Nagase, V. Parasuk and D. Jiang, *J. Am. Chem. Soc.*, 2011, **133**, 14510–14513.
45. M. Dogru, M. Handloser, F. Auras, T. Kunz, D. Medina, A. Hartschuh, P. Knochel and T. Bein, *Angew. Chem., Int. Ed.*, 2013, **52**, 2920–2924.

46. D. D. Medina, V. Werner, F. Auras, R. Tautz, M. Dogru, J. Schuster, S. Linke, M. Döblinger, J. Feldmann, P. Knochel and T. Bein, *ACS Nano*, 2014, **8**, 4042–4052.
47. S. Duhović and M. Dincă, *Chem. Mater.*, 2015, **27**, 5487–5490.
48. G. H. V. Bertrand, V. K. Michaelis, T.-C. Ong, R. G. Griffin and M. Dincă, *Proceedings of the National Academy of Sciences*, 2013, **110**, 4923–4928.
49. V. S. P. K. Neti, X. Wu, S. Deng and L. Echegoyen, *CrystEngComm*, 2013, **15**, 6892–6895.
50. M. Calik, F. Auras, L. M. Salonen, K. Bader, I. Grill, M. Handloser, D. D. Medina, M. Dogru, F. Löbermann, D. Trauner, A. Hartschuh and T. Bein, *J. Am. Chem. Soc.*, 2014, **136**, 17802–17807.
51. S. Wan, F. Gándara, A. Asano, H. Furukawa, A. Saeki, S. K. Dey, L. Liao, M. W. Ambrogio, Y. Y. Botros, X. Duan, S. Seki, J. F. Stoddart and O. M. Yaghi, *Chem. Mater.*, 2011, **23**, 4094–4097.
52. X. Feng, L. Liu, Y. Honsho, A. Saeki, S. Seki, S. Irle, Y. Dong, A. Nagai and D. Jiang, *Angew. Chem., Int. Ed.*, 2012, **51**, 2618–2622.
53. F. Xu, S. Jin, H. Zhong, D. Wu, X. Yang, X. Chen, H. Wei, R. Fu and D. Jiang, *Sci. Rep.*, 2015, **5**, Article No. 8225.
54. R. W. Tilford, S. J. Mugavero, P. J. Pellechia and J. J. Lavigne, *Adv. Mater. (Weinheim, Ger.)*, 2008, **20**, 2741–2746.
55. A. Nagai, Z. Guo, X. Feng, S. Jin, X. Chen, X. Ding and D. Jiang, *Nat. Commun.*, 2011, **2**, Art. No. 536.
56. L. Chen, K. Furukawa, J. Gao, A. Nagai, T. Nakamura, Y. Dong and D. Jiang, *J. Am. Chem. Soc.*, 2014, **136**, 9806–9809.
57. J. Zhang, L. Wang, N. Li, J. Liu, W. Zhang, Z. Zhang, N. Zhou and X. Zhu, *CrystEngComm*, 2014, **16**, 6547–6551.
58. M. Dogru, A. Sonnauer, A. Gavryushin, P. Knochel and T. Bein, *Chem. Commun.*, 2011, **47**.
59. N. Huang, X. Ding, J. Kim, H. Ihee and D. Jiang, *Angew. Chem., Int. Ed.*, 2015, **54**, 8704–8870.
60. Z. Kahveci, T. Islamoglu, G. A. Shar, R. Ding and H. M. El-Kaderi, *CrystEngComm*, 2013, **15**, 1524–1527.
61. J.-T. Yu, Z. Chen, J. Sun, Z.-T. Huang and Q.-Y. Zheng, *J. Mater. Chem.*, 2012, **22**, 5369–5373.
62. L. A. Baldwin, J. W. Crowe, M. D. Shannon, C. P. Jaroniec and P. L. McGrier, *Chem. Mater.*, 2015, **27**, 6169–6172.

63. X. Feng, Y. Dong and D. Jiang, *CrystEngComm*, 2013, **15**, 1508–1511.
64. H. Yang, Y. Du, S. Wan, G. D. Trahan, Y. Jin and W. Zhang, *Chem. Sci.*, 2015, **6**, 4049–4053.
65. R. W. Tilford, W. R. Gemmill, H.-C. Zur Loye and J. J. Lavigne, *Chem. Mater.*, 2006, **18**, 5296–5301.
66. Y. Du, D. Calabro, B. Wooler, Q. Li, S. Cundy, P. Kamakoti, D. Colmyer, K. Mao and P. Ravikovitch, *J. Phys. Chem. C*, 2013, **118**, 399–407.
67. M. K. Smith and B. H. Northrop, *Chem. Mater.*, 2014, **26**, 3781–3795.
68. S. B. Kalidindi, C. Wiktor, A. Ramakrishnan, J. Weßing, A. Schneemann, G. van Tendeloo and R. A. Fischer, *Chem. Commun.*, 2013, **49**, 463–465.
69. S.-T. Yang, J. Kim, H.-Y. Cho, S. Kim and W.-S. Ahn, *RSC Adv.*, 2012, **2**, 10179–10181.
70. J. Yoo, S. Lee, S. Hirata, C. Kim, C. K. Lee, T. Shiraki, N. Nakashima and J. K. Shim, *Chem. Lett.*, 2015, **44**, 560–562.
71. Y. Du, K. Mao, P. Kamakoti, P. Ravikovitch, C. Paur, S. Cundy, Q. Li and D. Calabro, *Chem. Commun.*, 2012, **48**, 4606–4608.
72. Y. Du, K. Mao, P. Kamakoti, B. Wooler, S. Cundy, Q. Li, P. Ravikovitch and D. Calabro, *J. Mater. Chem. A*, 2013, **1**, 13171–13178.
73. Y. Du, D. Calabro, B. Wooler, P. Kortunov, Q. Li, S. Cundy and K. Mao, *Chem. Mater.*, 2015, **27**, 1445–1447.
74. E. L. Spitler, M. R. Giovino, S. L. White and W. R. Dichtel, *Chem. Sci.*, 2011, **2**, 1588–1593.
75. B. J. Smith and W. R. Dichtel, *J. Am. Chem. Soc.*, 2014, **136**, 8783–8789.
76. N. L. Campbell, R. Clowes, L. K. Ritchie and A. I. Cooper, *Chem. Mater.*, 2009, **21**, 204–206.
77. J. W. Colson, A. R. Woll, A. Mukherjee, M. P. Levendorf, E. L. Spitler, V. B. Shields, M. G. Spencer, J. Park and W. R. Dichtel, *Science*, 2011, **332**, 228–231.
78. D. Hao, J. Zhang, H. Lu, W. Leng, R. Ge, X. Dai and Y. Gao, *Chem. Commun.*, 2014, **50**, 1462.
79. H. Lu, C. Wang, J. Chen, R. Ge, W. Leng, B. Dong, J. Huang and Y. Gao, *Chem. Commun.*, 2015.
80. J. W. Colson, J. A. Mann, C. R. DeBlase and W. R. Dichtel, *J. Polym. Sci. A Polym. Chem*, 2015, 378–384.
81. D. D. Medina, J. M. Rotter, Y. Hu, M. Dogru, V. Werner, F. Auras, J. T. Markiewicz, P. Knochel and T. Bein, *J. Am. Chem. Soc.*, 2015, **137**, 1016–1019.

82. S. Dalapati, S. Jin, J. Gao, Y. Xu, A. Nagai and D. Jiang, *J. Am. Chem. Soc.*, 2013, **135**, 17310–17313.
83. F. J. Uribe-Romo, C. J. Doonan, H. Furukawa, K. Oisaki and O. M. Yaghi, *J. Am. Chem. Soc.*, 2011, **133**, 11478–11481.
84. F. J. Uribe-Romo, J. R. Hunt, H. Furukawa, C. Klöck, M. O’Keeffe and O. M. Yaghi, *J. Am. Chem. Soc.*, 2009, **131**, 4570–4571.
85. S. Kandambeth, A. Mallick, B. Lukose, M. V. Mane, T. Heine and R. Banerjee, *J. Am. Chem. Soc.*, 2012, **134**, 19524–19527.
86. Q. Fang, Z. Zhuang, S. Gu, R. B. Kaspar, J. Zheng, J. Wang, S. Qiu and Y. Yan, *Nat. Commun.*, 2014, **5**, Art. No. 4503.
87. P. Kuhn, M. Antonietti and A. Thomas, *Angew. Chem., Int. Ed.*, 2008, **47**, 3450–3453.
88. J. L. Mendoza-Cortés, S. S. Han, H. Furukawa, O. M. Yaghi and W. A. Goddard, *J. Phys. Chem. A*, 2010, **114**, 10824–10833.
89. W. Gao, X. Sun, H. Niu, X. Song, K. Li, H. Gao, W. Zhang, J. Yu and M. Jia, *Microporous Mesoporous Mater.*, 2015, **213**, 59–67.
90. Y.-B. Zhang, J. Su, H. Furukawa, Y. Yun, F. Gándara, A. Duong, X. Zou and O. M. Yaghi, *J. Am. Chem. Soc.*, 2013, **135**, 16336–16339.
91. J. Guo, Y. Xu, S. Jin, L. Chen, T. Kaji, Y. Honsho, M. A. Addicoat, J. Kim, A. Saeki, H. Ihee, S. Seki, S. Irle, M. Hiramoto, J. Gao and D. Jiang, *Nat. Commun.*, 2013, **4**, Art. No. 2736.
92. S.-L. Cai, Y.-B. Zhang, A. B. Pun, B. He, J. Yang, F. M. Toma, I. D. Sharp, O. M. Yaghi, J. Fan, S.-R. Zheng, W.-G. Zhang and Y. Liu, *Chem. Sci.*, 2014, **5**, 4693–4700.
93. H. Ding, Y. Li, H. Hu, Y. Sun, J. Wang, C. Wang, C. Wang, G. Zhang, B. Wang, W. Xu and D. Zhang, *Chem. - Eur. J.*, 2014, **20**, 14614–14618.
94. Y.-F. Xie, S.-Y. Ding, J.-M. Liu, W. Wang and Q.-Y. Zheng, *J. Mater. Chem. C*, 2015.
95. D. Kaleeswaran, P. Vishnoi and R. Murugavel, *J. Mater. Chem. C*, 2015, **3**, 7159–7171.
96. M. G. Rabbani, A. K. Sekizkardes, Z. Kahveci, T. E. Reich, R. Ding and H. M. El-Kaderi, *Chem.--Eur. J.*, 2013, **19**, 3324–3328.
97. T.-Y. Zhou, S.-Q. Xu, Q. Wen, Z.-F. Pang and X. Zhao, *J. Am. Chem. Soc.*, 2014, **136**, 15885–15888.
98. D. B. Shinde, S. Kandambeth, P. Pachfule, R. R. Kumar and R. Banerjee, *Chem. Commun.*, 2015, **51**, 310–313.
99. A. Nagai, X. Chen, X. Feng, X. Ding, Z. Guo and D. Jiang, *Angew. Chem., Int. Ed.*, 2013, **52**, 3770–3774.

100. X. Chen, M. Addicoat, S. Irle, A. Nagai and D. Jiang, *J. Am. Chem. Soc.*, 2012, **135**, 546–549.
101. X. Chen, M. Addicoat, E. Jin, L. Zhai, H. Xu, N. Huang, Z. Guo, L. Liu, S. Irle and D. Jiang, *J. Am. Chem. Soc.*, 2015, **137**, 3241–3247.
102. S. Kandambeth, D. B. Shinde, M. K. Panda, B. Lukose, T. Heine and R. Banerjee, *Angew. Chem., Int. Ed.*, 2013, **52**, 13052–13056.
103. D. Jiang, H. Xu, X. Chen, J. Gao, J. Lin, M. Addicoat and S. Irle, *Chem. Commun.*, 2013.
104. N. Huang, R. Krishna and D. Jiang, *J. Am. Chem. Soc.*, 2015, **137**, 7079–7082.
105. N. Huang, X. Chen, R. Krishna and D. Jiang, *Angew. Chem., Int. Ed.*, 2015, **54**, 2986–2990.
106. F. Xu, H. Xu, X. Chen, D. Wu, Y. Wu, H. Liu, C. Gu, R. Fu and D. Jiang, *Angew. Chem., Int. Ed.*, 2015, **54**, 6814–6818.
107. Y. Hou, X. Zhang, J. Sun, S. Lin, D. Qi, R. Hong, D. Li, X. Xiao and J. Jiang, *Microporous Mesoporous Mater.*, 2015, **214**, 108–114.
108. Wenjie Ma, Ping Yu, Takeo Ohsaka and Lanqun Mao, *Electrochem. Commun.*, 2015, **52**, 53–57.
109. S. Lin, C. S. Diercks, Y.-B. Zhang, N. Kornienko, E. M. Nichols, Y. Zhao, A. R. Paris, D. Kim, P. Yang, O. M. Yaghi and C. J. Chang, *Science*, 2015, **349**, 1208–1213.
110. X. Chen, N. Huang, J. Gao, H. Xu, F. Xu and D. Jiang, *Chem. Commun.*, 2014, 6161–6163.
111. S.-Y. Ding, J. Gao, Q. Wang, Y. Zhang, W.-G. Song, C.-Y. Su and W. Wang, *J. Am. Chem. Soc.*, 2011, **133**, 19816–19822.
112. H. Xu, J. Gao and D. Jiang, *Nat. Chem.*, 2015, **7**, 905–912.
113. Q. Fang, S. Gu, J. Zheng, Z. Zhuang, S. Qiu and Y. Yan, *Angew. Chem., Int. Ed.*, 2014, **53**, 2878–2882.
114. Y. Wu, H. Xu, X. Chen, J. Gao and D. Jiang, *Chem. Commun.*, 2015, **51**, 10096–10098.
115. L. Stegbauer, K. Schwinghammer and B. V. Lotsch, *Chem. Sci.*, 2014, **5**, 2789.
116. S. Lin, Y. Hou, X. Deng, H. Wang, S. Sun and X. Zhang, *RSC Adv.*, 2015, **5**, 41017–41024.
117. D. Mullangi, S. Nandi, S. Shalini, S. Sreedhala, C. P. Vinod and R. Vaidhyanathan, *Sci. Rep.*, 2015, **5**, 10876 EP -.
118. Q. Gao, L. Bai, X. Zhang, P. Wang, P. Li, Y. Zeng, R. Zou and Y. Zhao, *Chin. J. Chem.*, 2015, **33**, 90–94.
119. R. Gomes, P. Bhanja and A. Bhaumik, *Chem. Commun.*, 2015, **51**, 10050–10053.

120. J.-R. Song, J. Sun, J. Liu, Z.-T. Huang and Q.-Y. Zheng, *Chem. Commun.*, 2014, 788–791.
121. W. Huang, Y. Jiang, X. Li, X. Li, J. Wang, Q. Wu and X. Liu, *ACS Appl. Mater. Interfaces*, 2013, **5**, 8845–8849.
122. P. Pachfule, S. Kandambeth, D. Diaz Diaz and R. Banerjee, *Chem. Commun.*, 2014, **50**, 3169–3172.
123. Z. Zha, L. Xu, Z. Wang, X. Li, Q. Pan, P. Hu and S. Lei, *ACS Appl. Mater. Interfaces*, 2015, **7**, 17837–17843.
124. P. Wang, Q. Wu, L. Han, S. Wang, S. Fang, Z. Zhang and S. Sun, *RSC Adv.*, 2015, **5**, 27290–27294.
125. J. H. Chong, M. Sauer, B. O. Patrick and M. J. MacLachlan, *Org. Lett.*, 2003, **5**, 3823–3826.
126. S. Chandra, S. Kandambeth, B. P. Biswal, B. Lukose, S. M. Kunjir, M. Chaudhary, R. Babarao, T. Heine and R. Banerjee, *J. Am. Chem. Soc.*, 2013, **135**, 17853–17861.
127. C. R. DeBlase, K. E. Silberstein, T.-T. Truong, H. D. Abruña and W. R. Dichtel, *J. Am. Chem. Soc.*, 2013, **135**, 16821–16824.
128. S. Chandra, T. Kundu, S. Kandambeth, R. Babarao, Y. Marathe, S. M. Kunjir and R. Banerjee, *J. Am. Chem. Soc.*, 2014, **136**, 6570–6573.
129. Y. Zhu and W. Zhang, *Chem. Sci.*, 2014, 4957–4961.
130. P. Pachfule, M. K. Panda, S. Kandambeth, Shivaprasad, S. M., D. D. Diaz and R. Banerjee, *J. Mater. Chem. A*, 2014, **2**, 7944–7952.
131. W. Zhang, P. Jiang, Y. Wang, J. Zhang, Y. Gao and P. Zhang, *RSC Adv.*, 2014, **4**, 51544–51547.
132. J. Thote, H. B. Aiyappa, A. Deshpande, D. Díaz Díaz, S. Kurungot and R. Banerjee, *Chem. - Eur. J.*, 2014, **20**, 15961–15965.
133. Y. Peng, Z. Hu, Y. Gao, D. Yuan, Z. Kang, Y. Qian, N. Yan and D. Zhao, *ChemSusChem*, 2015, **8**, 3208–3212.
134. G. Das, B. P. Biswal, S. Kandambeth, V. Venkatesh, G. Kaur, M. Addicoat, T. Heine, S. Verma and R. Banerjee, *Chem. Sci.*, 2015, **6**, 3931–3939.
135. C.-X. Yang, C. Liu, Y.-M. Cao and X.-P. Yan, *Chem. Commun.*, 2015, **51**, 12254–12257.
136. D. N. Bunck and W. R. Dichtel, *J. Am. Chem. Soc.*, 2013, **135**, 14952–14955.
137. Q. Fang, J. Wang, S. Gu, R. B. Kaspar, Z. Zhuang, J. Zheng, H. Guo, S. Qiu and Y. Yan, *J. Am. Chem. Soc.*, 2015, **137**, 8352–8355.
138. P. Katekomol, J. Roeser, J. Weber and A. Thomas, *Chem. Mater.*, 2013, **9**, 1542–1548.

139. B. P. Biswal, S. Chandra, S. Kandambeth, B. Lukose, T. Heine and R. Banerjee, *J. Am. Chem. Soc.*, 2013, 5328–5331.
140. R. Banerjee, S. G K, G. Das, D. B. Shinde and B. Biswal, *Chem. Commun.*, 2014, 12615–12618.
141. S. Kandambeth, V. Venkatesh, D. B. Shinde, S. Kumari, A. Halder, S. Verma and R. Banerjee, *Nat. Commun.*, 2015, **6**, Art. No. 6786.
142. Y. Jiang, W. Huang, J. Wang, Q. Wu, H. Wang, L. Pan and X. Liu, *J. Mater. Chem. A*, 2014, **2**, 8201.
143. A. Ruigómez, D. Rodríguez-San-Miguel, K. C. Stylianou, M. Cavallini, D. Gentili, F. Liscio, S. Milita, Roscioni, Otello Maria, M. L. Ruiz-González, C. Carbonell, D. MasPOCH, R. Mas-Ballesté, J. L. Segura and F. Zamora, *Chem. - Eur. J.*, 2015, **21**, 10666–10670.
144. H. Wei, S. Chai, N. Hu, Z. Yang, L. Wei and L. Wang, *Chem. Commun.*, 2015, **51**, 12178–12181.
145. T. Shiraki, G. Kim and N. Nakashima, *Chem. Lett.*, 2015, DOI: 10.1246/cl.150678.
146. P. Pachfule, S. Kandmabeth, A. Mallick and R. Banerjee, *Chem. Commun.*, 2015, **51**, 11717–11720.
147. C. R. DeBlase, K. Hernández-Burgos, K. E. Silberstein, G. G. Rodríguez-Calero, R. P. Bisbey, H. D. Abruña and W. R. Dichtel, *ACS Nano*, 2015, **9**, 3178–3183.
148. A. Dutta, K. Koh, A. G. Wong-Foy and A. J. Matzger, *Angew. Chem., Int. Ed.*, 2015, **54**, 3983–3987.
149. Y. Zeng, R. Zou, Z. Luo, H. Zhang, X. Yao, X. Ma, R. Zou and Y. Zhao, *J. Am. Chem. Soc.*, 2015, **137**, 1020–1023.
150. H. Furukawa and O. M. Yaghi, *J. Am. Chem. Soc.*, 2009, **131**, 8875–8883.
151. X. Feng, L. Chen, Y. Honsho, O. Saengsawang, L. Liu, L. Wang, A. Saeki, S. Irle, S. Seki, Y. Dong and D. Jiang, *Adv. Mater. (Weinheim, Ger.)*, 2012, **24**, 3026–3031.
152. X. Feng, L. Chen, Y. Dong and D. Jiang, *Chem. Commun.*, 2011, **47**.
153. M. Dogru and T. Bein, *Chem. Commun.*, 2014, **50**, 5531–5546.
154. J. A. Turner, *Science*, 1999, **285**, 687–689.
155. A. Fujishima and K. Honda, *Nature*, 1972, **238**, 37–38.
156. A. Kudo and Y. Miseki, *Chem. Soc. Rev.*, 2009, **38**, 253–278.
157. E. Borgarello, J. Kiwi, E. Pelizzetti, M. Visca and M. Gratzel, *Nature*, 1981, **289**, 158–160.
158. M. F. Weber and M. J. Dignam, *Journal of The Electrochemical Society*, 1984, **131**, 1258–1265.

159. J. R. Bolton, S. J. Strickler and J. S. Connolly, *Nature*, 1985, **316**, 495–500.
160. J. Liu, Y. Liu, N. Liu, Y. Han, X. Zhang, H. Huang, Y. Lifshitz, S.-T. Lee, J. Zhong and Z. Kang, *Science*, 2015, **347**, 970–974.
161. Y. Matsumoto and E. Sato, *Materials Chemistry and Physics*, 1986, **14**, 397–426.
162. P. Rasiyah and Tseung, A. C. C., *Journal of The Electrochemical Society*, 1984, **131**, 803–808.
163. S. Trasatti, *Journal of Electroanalytical Chemistry and Interfacial Electrochemistry*, 1980, **111**, 125–131.
164. B. E. Conway and B. V. Tilak, *Electrochimica Acta*, 2002, **47**, 3571–3594.
165. R. Parsons, *Trans. Faraday Soc.*, 1958, **54**, 1053–1063.
166. S. Trasatti, *Journal of Electroanalytical Chemistry and Interfacial Electrochemistry*, 1972, **39**, 163–184.
167. T. Hisatomi, J. Kubota and K. Domen, *Chem. Soc. Rev.*, 2014, **43**, 7520–7535.
168. X. Chen, S. Shen, L. Guo and S. S. Mao, *Chem. Rev.*, 2010, **110**, 6503–6570.
169. H. Kisch, *Angew. Chem., Int. Ed.*, 2013, **52**, 812–847.
170. S. Cao, J. Low, J. Yu and M. Jaroniec, *Adv. Mater. (Weinheim, Ger.)*, 2015, **27**, 2150–2176.
171. S. Yanagida, A. Kabumoto, K. Mizumoto, C. Pac and K. Yoshino, *J. Chem. Soc., Chem. Commun.*, 1985, 474–475.
172. T. Shibata, A. Kabumoto, T. Shiragami, O. Ishitani, C. Pac and S. Yanagida, *J. Phys. Chem.*, 1990, **94**, 2068–2076.
173. S. Matsuoka, T. Kohzuki, A. Nakamura, C. Pac and S. Yanagida, *J. Chem. Soc., Chem. Commun.*, 1991, 580–581.
174. S. Matsuoka, T. Kohzuki, Y. Kuwana, A. Nakamura and S. Yanagida, *J. Chem. Soc., Perkin Trans. 2*, 1992, 679–685.
175. S. Yanagida, T. Ogata, Y. Kuwana, Y. Wada, K. Murakoshi, A. Ishida, S. Takamuku, M. Kusaba and N. Nakashima, *J. Chem. Soc., Perkin Trans. 2*, 1996, 1963–1969.
176. T. Maruyama and T. Yamamoto, *J. Phys. Chem. B*, 1997, **101**, 3806–3810.
177. X. Wang, K. Maeda, A. Thomas, K. Takanabe, G. Xin, J. M. Carlsson, K. Domen and M. Antonietti, *Nat. Mater.*, 2009, **8**, 76–80.
178. K. Maeda, X. Wang, Y. Nishihara, D. Lu, M. Antonietti and K. Domen, *J. Phys. Chem. C*, 2009, **113**, 4940–4947.

179. K. Schwinghammer, B. Tuffy, M. B. Mesch, E. Wirthier, C. Martineau, F. Taulelle, W. Schnick, J. Senker and B. V. Lotsch, *Angew. Chem.*, 2013, **125**, 2495–2499.
180. M. G. Schwab, M. Hamburger, X. Feng, J. Shu, H. W. Spiess, X. Wang, M. Antonietti and K. Mullen, *Chem. Commun.*, 2010, **46**, 8932–8934.
181. J. Liu, S. Wen, Y. Hou, F. Zuo, G. J. O. Beran and P. Feng, *Angew. Chem., Int. Ed.*, 2013, **52**, 3241–3245.
182. C. Huang, C. Chen, M. Zhang, L. Lin, X. Ye, S. Lin, M. Antonietti and X. Wang, *Nat. Commun.*, 2015, **6**.
183. T. Stocker, L. Alexander and M. Allen, *Climate change 2013: The physical science basis ; Working Group I contribution to the fifth assessment report of the Intergovernmental Panel on Climate Change*, WMO IPCC, Geneva, 2014.
184. International Energy Agency, *Energy Technology Perspectives 2008*.
www.iea.org/media/etp/etp2008.pdf (last accessed September 2015).
185. M. E. Boot-Handford, J. C. Abanades, E. J. Anthony, M. J. Blunt, S. Brandani, N. Mac Dowell, J. R. Fernandez, M.-C. Ferrari, R. Gross, J. P. Hallett, Haszeldine, R. Stuart, P. Heptonstall, A. Lyngfelt, Z. Makuch, E. Mangano, Porter, Richard T. J., M. Pourkashanian, G. T. Rochelle, N. Shah, J. G. Yao and P. S. Fennell, *Energy Environ. Sci.*, 2014, **7**, 130–189.
186. S. Hug, *Covalent Triazine Frameworks: Structure, Properties and Applications in Gas Storage and Energy Conversion*, Dissertation, München, 2014.
187. D. M. D'Alessandro, B. Smit and J. R. Long, *Angew. Chem., Int. Ed.*, 2010, **49**, 6058–6082.
188. S. Sircar and T.C Golden, *Separation Science and Technology*, 2000, **35**, 667–687.
189. S. Sircar, *Ind. Eng. Chem. Res.*, 2002, **41**, 1389–1392.
190. N. W. Ockwig and T. M. Nenoff, *Chem. Rev.*, 2007, **107**, 4078–4110.
191. Ritter, James A. and Ebner, Armin D., *Separation Science and Technology*, 2007, **42**, 1123–1193.
192. S.-I. Yang, D.-Y. Choi, S.-C. Jang, S.-H. Kim and D.-K. Choi, *Adsorption*, 2008, **14**, 583–590.
193. R. Dawson, A. I. Cooper and D. J. Adams, *Polym. Int.*, 2013, **62**, 345–352.
194. K. D. Vogiatzis, A. Mavrandonakis, W. Klopper and G. E. Froudakis, *ChemPhysChem*, 2009, **10**, 374–383.
195. G. Li, P. Xiao, P. Webley, J. Zhang, R. Singh and M. Marshall, *Adsorption*, 2008, **14**, 415–422.

196. K. Sumida, D. L. Rogow, J. A. Mason, T. M. McDonald, E. D. Bloch, Z. R. Herm, T.-H. Bae and J. R. Long, *Chem. Rev.*, 2012, **112**, 724–781.
197. N. C. Burtch, H. Jasuja and K. S. Walton, *Chem. Rev.*, 2014, **114**, 10575–10612.
198. European Environment Agency, *Household energy consumption by end-use in the EU-27*. <http://www.eea.europa.eu/data-and-maps/figures/households-energy-consumption-by-end-uses-4> (last accessed April 2015).
199. F. Jeremias, A. Khutia, S. K. Henninger and C. Janiak, *J. Mater. Chem.*, 2012, **22**, 10148–10151.
200. F. Jeremias, *Synthesis and characterization of metal-organic frameworks for heat transformation applications*, Dissertation, Düsseldorf, 2014.
201. K. N. Marsh, *Recommended reference materials for the realization of physicochemical properties*, Blackwell Scientific Publications, Oxford, 1987.
202. E.-P. Ng and S. Mintova, *Microporous Mesoporous Mater.*, 2008, **114**, 1–26.
203. Vaillant, *zeoTHERM Systemkombination*. http://www.vaillant.de/heizung/produkte/zeotherm-systemkombination-1088.de_de.html (last accessed September 2015).
204. NASA, *Earth Fact Sheet*. <http://nssdc.gsfc.nasa.gov/planetary/factsheet/earthfact.html> (last accessed April 2015).
205. F. Gao, Z. Ding and S. Meng, *Sci. Rep.*, 2013, **3**, 1882.
206. J.-H. Guo, H. Zhang, M. Gong and X.-L. Cheng, *Struct. Chem.*, 2013, **24**, 691-703.
207. J.-H. Guo, H. Zhang and Y. Miyamoto, *Phys. Chem. Chem. Phys.*, 2013, **15**, 8199–8207.
208. J.-H. Guo, H. Zhang, Z.-P. Liu and X.-L. Cheng, *J. Phys. Chem. C*, 2012, **116**, 15908–15917.
209. F. Jeremias, V. Lozan, S. K. Henninger and C. Janiak, *Dalton Trans.*, 2013, **42**, 15967–15973.
210. P. Küsgens, M. Rose, I. Senkovska, H. Fröde, A. Henschel, S. Siegle and S. Kaskel, *Microporous Mesoporous Mater.*, 2009, **120**, 325–330.
211. K. László, O. Czakkel, G. Dobos, P. Lodewyckx, C. Rochas and E. Geissler, *Carbon*, 2010, **48**, 1038–1048.
212. J. K. Brennan, T. J. Bandosz, K. T. Thomson and K. E. Gubbins, *Colloids Surf., A*, 2001, **187–188**, 539–568.

2 METHODS

Standard COF Characterization

Suitable large single crystals for x-ray structure determination have so far not been obtained for COFs, although a structure solution based on electron diffraction was reported recently.¹ Therefore, powder x-ray diffraction (PXRD) supported by structure simulation by the program *Materials Studio*² is currently the main method to determine the structure of a COF. Additionally, the porosity is checked and the pore size is determined by physisorption analysis. A COF should show essentially the same pore size in physisorption and PXRD; otherwise either the modeled structure is incorrect or the COF phase is accompanied by an amorphous porous phase having a different pore size. To characterize the local order and the as-formed chemical bonds, IR spectroscopy and solid-state NMR spectroscopy have proven as valuable tools. All these methods are shortly introduced here.

2.1 Physisorption

A plethora of experimental methods for the characterization of pore sizes and the surface of porous materials is available including gas (ad)sorption, small angle x-ray and neutron scattering, mercury porosimetry, electron microscopy, thermoporometry and nuclear magnetic resonance methods.³ Each method has distinct limitations in applicability for porosity characterization, regarding accuracy, pore size resolution and sample interaction and handling. Gas (ad)sorption is a widespread method, because it can describe a range of pore sizes comprising more than two orders of magnitude (0.35-100 nm, practically 0.6-100 nm with Ar at 87 K) in combination with simple handling and low costs.⁴ By definition, adsorption is the increase in concentration of one or more components in an interfacial layer, e.g. the interface between a gaseous and a condensed phase in gas adsorption.⁵ The gas is called the *adsorptive*, while the solid is called the *adsorbent* and the gas in the adsorbed state the *adsorbate*.⁵ Two types of adsorption can be distinguished, namely chemical and physical adsorption. The former is called chemisorption and consists of an activated, specific chemical reaction between the surface and the adsorptive, mostly in line with a higher adsorption enthalpy as compared to physisorption.⁴ The process of chemisorption is often irreversible, entails the formation of bonds with the surface and is therefore necessarily confined to single layer adsorption. In contrast, physical adsorption or physisorption, is a fully reversible and spontaneous, nonspecific process. Compared to chemisorption, the adsorption enthalpies are generally lower (e.g. between 4 and 50 kJ/mol)⁴ and multi-layer adsorption at higher relative pressures is possible. In this manner physisorption allows full surface coverage and complete pore filling of pores up to 100 nm in a nondestructive measurement. This gives physisorption analysis the advantages of analyzing both pore sizes and surface areas of porous materials.

2.1.1 Physisorption Isotherms

In a typical isotherm the relative pressure of the adsorptive is plotted against the amount of adsorbed gas. The shape of physisorption isotherms depends on the interaction of the adsorptive and the adsorbent (monolayer formation) as well as on the adsorbate-adsorptive interactions (multilayer formation). The majority of vapor isotherms (i.e. at sub-critical temperatures) may be divided into eight groups in an extended IUPAC classification (see Figure 2.19). Any isotherm which cannot be classified in these eight groups is most likely a combination of several types.

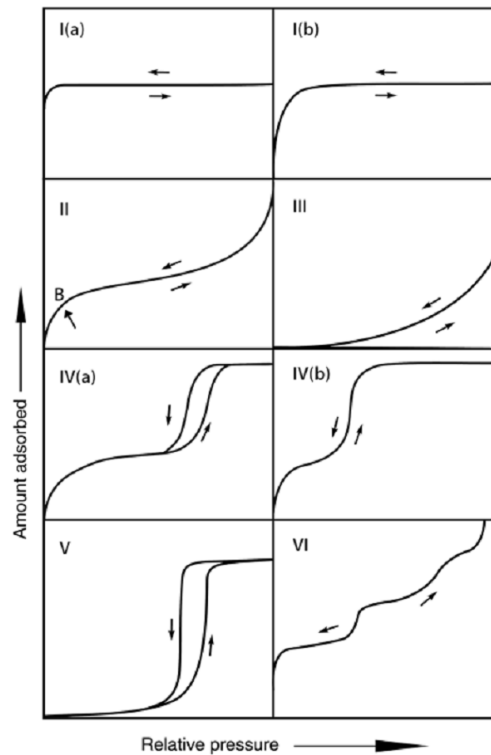


Figure 2.19: Types of physisorption isotherms as classified by the IUPAC.⁶ All types are explained in more detail in the text. ©IUPAC 2015

In microporous materials (pore diameter in molecular dimensions, < 2 nm), however, the adsorption potentials of the opposed pore walls overlap, resulting in strong adsorbate-adsorbent interactions, and consecutive pore filling at low pressures. The smaller the micropore diameter, the lower the relative pressure at which micropore filling takes place (e.g. type Ia with smaller pore diameter < 1 nm and Ib with larger diameter < 2.5 nm). Type I isotherms reach a nearly horizontal plateau with increasing relative pressures, indicating a lack of textural surface area (e.g. between nanoparticles).

In macroporous materials (pore diameter > 50 nm), the adsorption process is comparable to that on planar surfaces with weak adsorbate-adsorbent interactions which only leads to reasonable uptake of adsorptive at high relative pressures (e.g. type II). Type II isotherms have a concave shape until complete monolayer formation (point B) where it transits to a linear increase and concludes with a convex shape typical for textural pore filling. This shape is usually obtained for non-

porous or macroporous materials such as pigments or cements. Type II isotherms show completely reversible desorption over the whole pressure range.

The uncommon type III isotherm, featuring a convex shape, indicates weak adsorbate-adsorbent interactions and pronounced inter-adsorptive interactions, e. g. nitrogen adsorption on polyethylene or water on apolar charcoal.⁵

In mesoporous materials the adsorption process depends on both, the adsorbate-adsorbent and the inter-adsorbate interactions. Type IV isotherms, which are usually obtained from mesoporous materials, show initially a type II behavior with monolayer formation, followed by multilayer formation. At a critical relative pressure, capillary condensation, a phenomenon where gas molecules adsorb into a liquid-like state in the pores, commences with a sudden large uptake of adsorptive before reaching a limiting value at $p/p_0 < 1$. A characteristic feature of the type IVa isotherm is the hysteresis loop, which typically occurs in pores >4 nm in diameter.^{4,7,8} The rarer type IVb isotherm shows completely reversible ad- and desorption behavior over the whole pressure range, which is given in materials with smaller mesopores than 4 nm, such as MCM-41.⁹

In the process of capillary condensation the adsorptive goes through a phase transition from a gas state to a liquid state in a pore at pressures below the condensation pressure of the bulk liquid.^{10,7} This process is controlled by intermolecular forces in the pore fluid and can be described in a macroscopic thermodynamic approach for cylindrical pores by the Kelvin equation:

$$\ln\left(\frac{p}{p_0}\right) = \frac{-2\gamma}{rRT\rho}$$

where γ is the surface tension, ρ the molar density of the fluid, r the pore radius, R the gas constant and T the temperature. This provides a correlation between pore radius and pore condensation pressure, where pore filling starts in pores with smaller diameters, while in the desorption process the evaporation from the pores will occur primarily in larger pores.⁴ Although the phase transition of capillary condensation is a much more complex process involving metastable states (e.g. nucleation) of the pore fluid in a manner analogous to superheating/cooling of a bulk liquid,^{11,12} especially temperature dependence of the capillary condensation can reliably be described by the Kelvin equation.¹³ The desorption stage, however, as observed in systems with ordered pore architectures, is equivalent to a regular liquid-vapor transition in thermodynamic equilibrium.^{7,8,10}

The shape of the type V isotherm is very similar to type III and this can be attributed to very weak adsorbent-adsorbate interactions. At higher relative pressures, molecular clustering is followed by pore filling. Type V isotherms are rarely observed, but found for example for the adsorption of water on hydrophobic macroporous and mesoporous materials.

The type VI isotherm describes highly uniform non-porous surfaces where each step reflects the formation of a new layer in multilayer adsorption.

The most commonly used gas for sorption measurements of porous powder samples is nitrogen (N₂) at 77 K, although argon (Ar) at 87 K offers various advantages, especially if micropores are present. Firstly, the binuclear nitrogen molecule has a quadrupole moment and can thus interact with the adsorbent to a larger extent than the completely apolar, spherical Ar atom. This can lead to a reduction of nitrogen's molecular cross sectional area $\sigma(\text{N}_2)$ by up to 20%, and therefore may falsify determined surface areas (**surface area aspect**).⁹ Secondly, as a consequence of this additional adsorbate-adsorbent interaction, N₂ at boiling temperature fills micropores at lower relative pressures ($<10^{-7}$ mbar) compared to argon, leading to longer equilibration times (ultra-low pressure \rightarrow low diffusion rate)⁶ compared to Ar (**time aspect**). Lastly, Ar has a smaller kinetic diameter (3.4 Å vs. 3.6 Å) and therefore smaller molecular cross sectional area (14.2 Å² vs. 16.2 Å²) compared to nitrogen, which allows the access to smaller micropores (**size aspect**).⁶ All these reasons have led to a recent revision of IUPAC recommendations advocating for the use of Ar as standard sorptive for micropore sorption analysis.⁶

Associated with the low pressures is (as indicated above) the well-known problem of restricted diffusion, which prevents nitrogen molecules and also argon molecules from entering the narrowest micropores (i.e. ultramicropores in the range of ~ 2 kinetic diameters of the corresponding gas). This may lead to erroneous sorption isotherms and underestimated pore volumes. A possibility to overcome these problems exists: the use of CO₂ as adsorptive at temperature close to room temperature. For example, the saturation pressure at 273 K is ca. 26400 torr, i.e. in order to achieve the low relative pressures (down to $p/p_0^{-1} < 10^{-7}$) a turbomolecular pump vacuum is not necessary. With CO₂ adsorption up to 1 bar pores from the narrowest micropores up to ca. 1.5 nm can be evaluated and accessed. At these comparably "high" temperatures and pressures compared to cryogenic conditions, significant diffusion limitations no longer exist. This leads to an accelerated equilibration compared to N₂ and Ar adsorption at 77 K and 87 K, respectively. Typically, a micropore analysis with N₂ as adsorptive requires ca. 24 h or more, whereas in contrast an adequate micropore analysis using CO₂ can typically be completed in less ca. 3 h. The larger quadrupole moment of CO₂ compared to N₂ results in a stronger interaction (such as quadrupole – dipole) of the CO₂ molecules with the pore wall, highly dependent on the pore wall's polarity. Standard models for pore size calculations, such as Monte Carlo methods implemented in different sorption software packages, are based on a unique simulation in one or two pore-systems with a certain polarity such as carbon. The error of this assumption can be very high in more polar real systems such as COFs. Therefore the CO₂ derived pore size distribution must be regarded as error-prone instrument for pore size analysis.

2.1.2 Heats of Adsorption

The process of adsorption is exothermic. Heat is released, when a gas molecule adsorbs on a surface. The heat of adsorption gives information of the affinity of the surface towards the adsorptive. In most adsorbents, the specific heat of adsorption varies considerably in relation to the adsorbed amount (surface coverage θ), which is due to changing adsorption mechanisms. The differential heat of adsorption Q_{st} is defined as the heat released by adding a small amount of adsorbate to the surface in a constant gas volume.¹⁴ It can be calculated by calorimetric means or from at least two isotherms measured at different temperatures, according to the Clausius-Clapeyron equation:⁹

$$Q_{st} = R \cdot \left(\frac{\partial \ln(p)}{\partial \frac{1}{T}} \right)_{\theta}$$

where R is the gas constant, p the pressure and T the temperature.

For determination of the differential heat of adsorption, a dataset of n ($n \geq 2$) isotherms is acquired at n different temperatures T_n . For any surface coverage θ , Q_{st} can now be calculated from the pressure p_n required to reach this specific coverage θ at the temperature T_n . In a plot of $\ln(p_n)$ against $1/T_n$, the slope will be Q_{st}/R for each specific surface coverage θ .

2.1.3 Pore Size Distribution Analysis

In order to calculate the pore size from the sorption isotherms different microscopic models, such as molecular dynamics, density functional theory (DFT) or Monte Carlo simulations can be used. These methods lead to realistic results by using statistical molecular mechanics, which allow the calculation of equilibrium density profiles of a fluid near the adsorbent surface. The calculated fluid-solid interaction potential depends on the pore model, and for this purpose different pore shapes (cylindrical, spherical, slit) for different materials (carbon, silica) are available. By this approach a whole series of theoretical isotherms $N(p/p_0, W)$ for a particular adsorbent/adsorptive are calculated for different pore widths W in a given pore shape (e.g. cylinder), leading to the so called *kernel*, which can be regarded as a theoretical reference for a given class of adsorbent/adsorptive system. The calculation of the PSD is done by correlating the kernel with the experimental isotherm based on the Generalized Adsorption Isotherm equation:

$$N\left(\frac{p}{p_0}\right) = \int_{W_{min}}^{W_{max}} N\left(\frac{p}{p_0}, W\right) f(W) dW$$

where $N(p/p_0)$ is the experimental adsorption isotherm data, W the pore width, $N(p/p_0, W)$ the kernel of theoretical isotherms with pores of different widths and $f(W)$ the PSD function.⁶ This bottom-up statistical molecular mechanics approach has several advantages to classical macroscop-

ic thermodynamic approaches like the Dubinin-Radushkevich (DR) method. No assumptions about pore filling are necessary, because the theoretical $N(p/p_0, W)$ isotherms for different pore sizes are derived by DFT or Monte Carlo for the whole microporous and mesoporous range.⁴

There are various commercially available kernels which take different pore shapes into account and can be used with the adsorptives argon, nitrogen and carbon dioxide. Nonetheless, the main disadvantage of the often used non-local DFT (NLDF) method is the assumption of a smooth and homogenous adsorbent surface.¹⁵ As a consequence the calculated isotherm exhibits multiple steps which are related to the formation of subsequent layers. Because these kinds of isotherms are only observed for smooth surfaces like e.g. zeolites or silicas, the theoretical isotherms cause artificial gaps on the calculated PSD.¹⁶ A new approach is the quenched solid DFT (QSDFT) model in which the adsorbate atoms are considered as quenched components of the adsorptive-adsorbate system.¹⁷ Taking into account surface heterogeneity significantly improves the reliability of the pore size analysis of heterogenous nanoporous carbons. As a conclusion, the application of advanced microscopic methods based on DFT and Monte Carlo can lead to reasonably accurate description of the PSD as long as a given nanoporous system is compatible with the chosen DFT/MC kernel, otherwise the derived PSD may be significantly incorrect.⁶

2.1.4 Water Vapor Sorption

While argon and nitrogen sorption is a valuable tool for assessment of the physical geometry, such as size and appearance, of the pores, water vapor sorption is more sensitive to surface heterogeneity and can act as a probe to characterize surface chemistry.^{18–21}

While polar ionic zeolites like NaA (see Figure 1.6) show typical type I behaviour, decreasing polarity in adsorbents such as silica gel leads to decreased uptake at low relative pressures. The steepness of the isotherm at low pressures is a good indication of the hydrophilicity of the employed sorbents with a similar pore size. In microporous, hydrophilic sorbents pores are filled at low pressure as a consequence of the strong water-sorbent interaction.²² Therefore the isotherms are of type I, which is also typical for microporous materials, adsorbing cryogenic Ar/N₂. The mechanism of adsorption of water in hydrophilic microporous sorbents is similar to Ar/N₂ at cryogenic temperatures: i) monolayer formation, ii) complete filling of the pore.

Hydrophobic and weakly hydrophilic materials like activated carbons – though microporous – and amorphous silicas such as MCMs show type V behavior with a pronounced steep slope at intermediate ($p/p_0 > 0.3$) relative pressures,²³ which is ascribed to capillary condensation. Uptake of hygroscopic salts (chemisorbents) like CaCl₂ show an ongoing growth in uptake with increasing relative pressures until uptake capacity is depleted and the stoichiometric hydrate is formed.

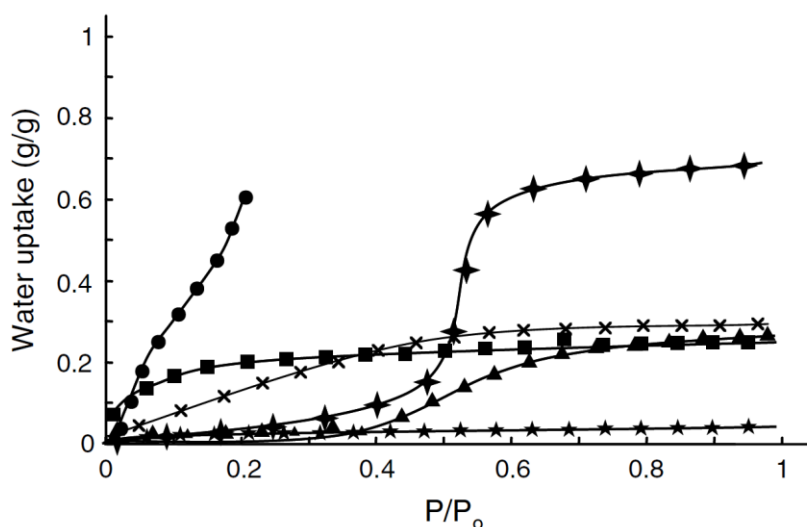


Figure 2.20: Water sorption isotherms of different sorbents: -▲- commercial activated carbon (CMS), -×- commercial silica gel (SiGel 10–40), -■- commercial zeolite NaA, -◆- AIMCM-41 (hydrothermal synthesis with Si/Al = 30), -★- silicalite-1, and -●- CaCl₂ salt. Reproduced with permission of Elsevier from.²²

The main underlying differences for hydrophobic sorbents compared to hydrophilic/hygroscopic sorbents stem from the comparably strong water-water interactions, in contrast to weak water-sorbent, e.g. dispersion, interactions and the formation of hydrogen bonds with polar groups on the surface.²⁴ Therefore, the understanding of the behavior of simple fluids, like argon, nitrogen or carbon dioxide such as monolayer formation, in confined pores cannot be applied to water in hydrophobic adsorbents.²¹ While in these simple fluids adsorbate-adsorbent interactions contribute to most of the overall interactions, in water, especially as sorptive in hydrophobic sorbents, the sorptive-sorptive interactions predominate. The mechanism of water adsorption in porous hydrophobic sorbents such as carbons proceeds in the four following steps: (i) the adsorption of single water molecules on polar sites (ii) the adsorption of water on previously adsorbed water molecules and subsequent cluster formation;^{25,26} (iii) pore filling which allows connection of the previously unconnected clusters; (iv) a plateau is reached when all pores are filled. A more detailed study shows that the relative pressure at which pore filling of water on similar hydrophobic porous carbons occurs is highly dependent on the pore size (e.g. 0.7 nm vs. 1.1 nm pore size results in a difference of relative pressure of pore filling of $\Delta p/p_0^{-1} > 0.2$).^{27,28} The whole process is yet not fully understood, and hence the reader is referred to a recent presentation on water adsorption in confined carbon space for further reading.²⁹

2.1.5 Experimental Details

In this thesis argon, carbon dioxide, nitrogen and water vapor adsorption/desorption measurements were performed at 87, 273, 287, 298 or 313 K with an Autosorb-iQ surface analyzer with vapor option (Quantachrome Instruments, USA). The static measurement temperature was controlled by boiling argon (87 K) in a dewar, or a refrigerated – heating circulator Julabo F12 (273,

287, 298 or 313 K) combined with a magnetically stirred dewar beaker. Samples were outgassed in vacuum to a final pressure of 10^{-7} mbar at 90-120°C for 12 h to remove all guest molecules. Pore-size distributions were determined using the calculation model for Ar at 87 K on carbon (cylindrical pore, QSDFT equilibrium model) of the ASiQwin software (v3.01) from Quantachrome. For multipoint BET calculations pressure ranges of the Ar isotherms were chosen with the help of the BET Assistant in the ASiQwin software, which chooses BET tags equal or below the maximum in $V \cdot (1 - P/P_0)$ in accordance with IUPAC.⁶ The isosteric heats of adsorption were calculated from the water vapor/CO₂ adsorption isotherms using the AsiQwin software.

2.1.6 Experimental Considerations

Sample Mass

The precision of BET surface area measurements is highly dependent on the porosity of the material in combination with the mass of the sample. If BET surface areas as small as $10 \text{ m}^2 \text{ g}^{-1}$ are considered, sample masses were used exceeding 250 mg. Otherwise, dosing of the ultrasmall volumes involved can be error-prone.⁹ When measuring highly porous materials with BET surface areas $>500 \text{ m}^2 \text{ g}^{-1}$, the sample mass was reduced to 15 mg, as long as a reliable balance is used with an acceptable error in mass. For new samples a mass of 50 mg has been used in this thesis.

Measuring at or Near Ambient Temperature

Sorption isotherm measurements at/near ambient temperature mainly involve N₂ (for gas selectivity calculations) CO₂ and water vapor as adsorptives at 273 K, 288 K, 298 K and 313 K. To this end, the *Autosorb IQ* has been modified with a thermostat using water/glycol mixtures as coolant, allowing a temperature control between -10°C and 60°C. A dewar vessel, filled with distilled water to the edge (bath), is equipped with magnetic stirring to ensure sufficient heat exchange. The stir rate had to be set to low values to avoid inhomogeneous turbulent mixing (whirl), which may lead to temperature discrepancies. The thermostat had to be run for at least 1 h to equilibrate at the desired temperature. There is a small temperature drop between the dewar vessel and the thermostat, therefore the thermostat temperature had to be selected a bit higher/lower ($\pm 0.3^\circ\text{C}$). The temperature in the dewar vessel was checked by a temperature logger. For precise measurements, the bath temperature was kept at the desired temperature with a maximum deviation of 0.1°C.

Water Vapor Isotherms

The AutosorbIQ is equipped with a vapor option allowing the acquisition of vapor isotherms. All the (standard) fittings of the device are compatible for water and isopropanol vapor. Before starting the measurement, the standard procedure for the change between physisorption/vapor sorption has to be run (heat manifold, equip sorption with vapor storage vessel, switch on gas ballast

of membrane pump, see sorption manual). For temperatures close to room temperature and above heating mantle was used to heat the sample glass tube outside of the bath above room temperature (usually up to 50°C-60°C at set point “1” of the control device) to avoid water vapor condensation on the cooler parts of the glass tube. The manifold was usually heated to 50°C, limiting the maximum temperature of measurement to <50°C.

2.2 Powder X-Ray Diffraction

X-rays are a form of electromagnetic radiation with typical wavelengths between 1 pm and 100 pm, ranging between UV rays and gamma rays. In general, x-rays are generated when a metal target (anode) is hit by focused electrons. This collision of high energetic electrons with the electron shell results in emission of i) a continuous “white” spectrum of “Bremsstrahlung” and ii) characteristic spikes of x-ray emission (K, L etc lines). There are three basic interactions of x-rays with matter: a) absorption, b) reflection, and c) scattering. For structural information about the lattice and atomic positions in solids elastic scattering is used in the technique of powder x-ray diffraction by monitoring diffraction maxima caused by constructive interference of the x-rays. The right conditions for constructive interference can be described by the *Bragg equation*.³⁰

$$\sin\theta = \frac{n \cdot \lambda}{2d_{hkl}}$$

where θ is the scattering angle, d_{hkl} the lattice plane distances, λ the wavelength of incident x-rays and n the order of interference (see Figure 2.21).

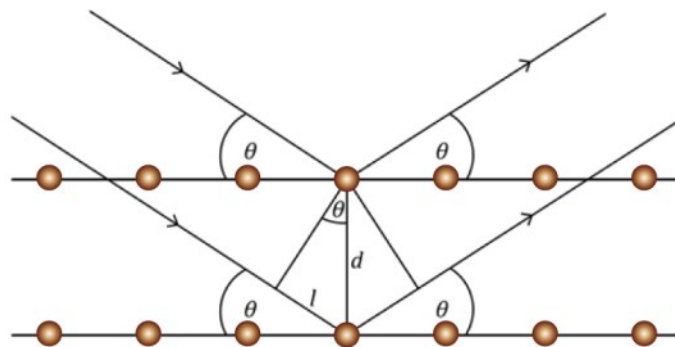


Figure 2.21: Simplified visualization of the Bragg equation for educational purposes (atoms depicted in brown).

The angle θ is the so-called *Bragg angle* and describes the angle at which constructive interference occurs. This constructive interference is only observed if the length l is an integer multiple of the wavelength λ .

Measuring at different diffraction angles θ while keeping the incident wavelength fixed, allows calculation of the distances d_{hkl} . When using polycrystalline samples in powder diffraction, ideally

showing statistical orientation of the microcrystals, reflections of all three spatial directions d_h , d_k and d_l are projected onto one or two dimensions in concentric cones (*Debye-Scherrer* cones) around the primary beam.

While the reflection positions depend on the lattice parameters, the intensity is determined by the structure factor, which in turn is correlated to the atomic form factor. This form factor is strongly dependent on the number of electrons (z) of an atom. Therefore, powder x-ray diffraction of materials with solely light elements gives less intense reflections than materials based on heavy elements.

The shape and broadness (appearance) of the reflections is dependent on several further factors such as differences in strain in microcrystals and the size of the crystallites. Hence, further information can be obtained from the diffraction pattern.

The size of crystallites or crystalline domains can be determined by application of the Scherrer equation:³²

$$L_{hkl} = \frac{k \cdot \lambda}{\beta \cdot \cos\theta}$$

with L_{hkl} : volume averaged crystallite size in the direction perpendicular to the lattice planes,³¹ k : Scherrer constant (usually set to 0.9), λ : wavelength of the x-ray radiation, β : integral breadth,^{32,34} and θ : angular peak position.

For a Gaussian reflection profile, the integral breadth β is calculated by:

$$\beta = \sqrt{\frac{\pi}{4 \cdot \ln 2}} \cdot FWHM$$

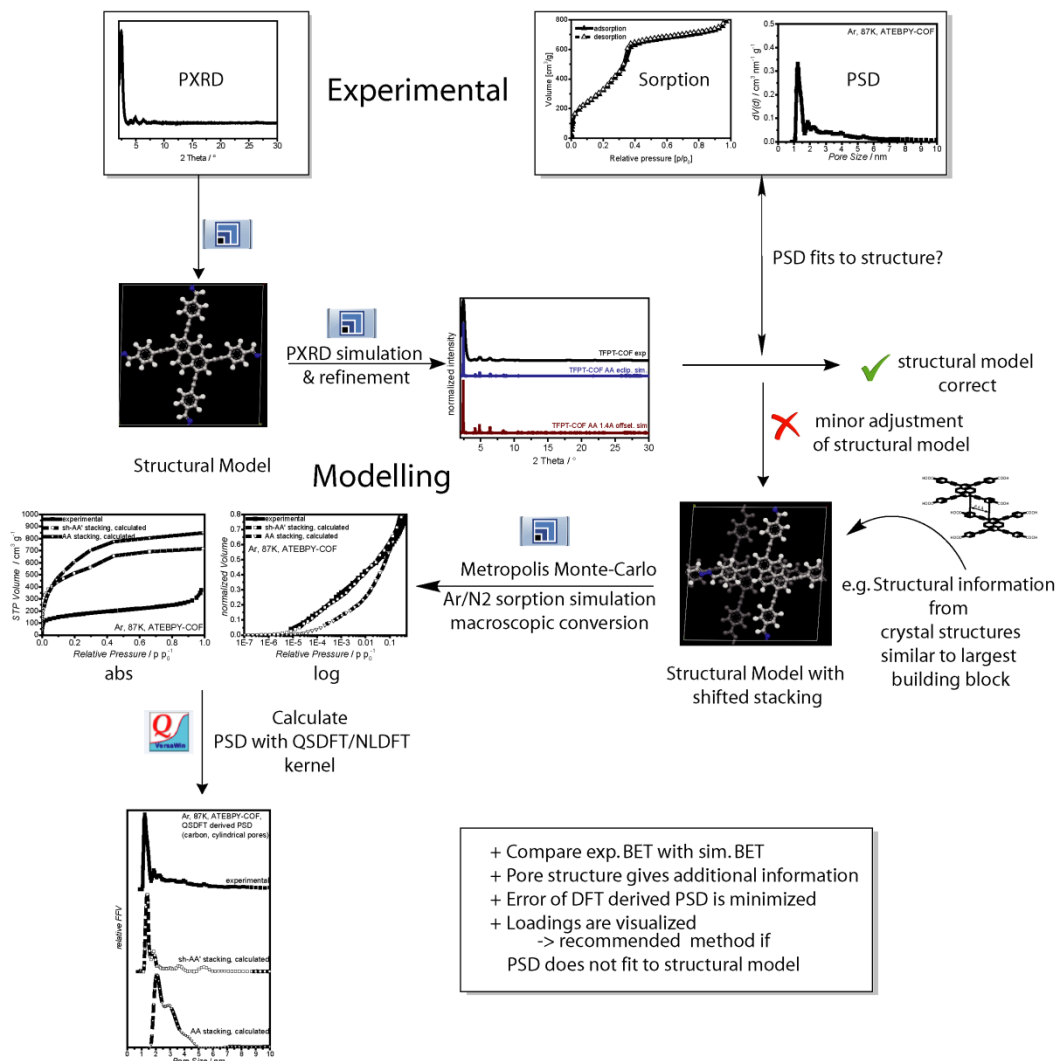
with FWHM is the full width at half maximum. For further reading about the Scherrer-equation the reader is referred to.³⁴

Powder diffraction patterns were measured on a BRUKER D8 Avance (Bruker AXS, USA) in Bragg-Brentano geometry or on a STOE Stadi P in Debye-Scherrer geometry. Acquisition parameters are given in the respective parts of the thesis. The measurements were either done by Tina Reuter (AK Bein, LMU Munich), Kerstin Gottschling, Christine Stefani (Max Planck Institute for Solid State Research, Stuttgart).

2.3 Materials Studio

Covalent organic frameworks have the unique feature of being a long-range ordered crystalline porous polymer. Although their crystallinity can be high, the typical crystallite size of typically less than 100 nm in all dimensions is too small to allow single crystal x-ray diffraction.

All of the COF materials obtained so far were produced as nanocrystalline powders and analyzed by powder x-ray diffraction; their theoretically predicted structures were then correlated with the experimentally obtained diffraction patterns and—if the two agreed—a structure was assigned. Therefore, powder x-ray diffraction is a valuable tool in structure determination of COFs, but so far only in combination with structure modelling with the help of *Accelrys Materials Studio*.² *Materials Studio*, together with its predecessor *Cerius*², is a molecular and crystal modeling package which is used for COF structure simulation. Sorption isotherm simulation can give further information about the pore structure and help to set up a COF structural model if the experimental pore size does not fit to the standard AA/AB packing pore size of the corresponding COF as visualized in Figure 2.22.



Materials Studio
Quantachrome VersaWin

Figure 2.22: Flow chart of COF structure determination by powder pattern simulation and isotherm simulation.

2.4 Infrared Spectroscopy

Infrared spectroscopy provides vibrational information generally about chemical bonding and specifically in the case of this thesis on functional organic moieties in molecules and polymers, typically in the mid-IR range between 4000 and 400 cm^{-1} . Molecular units absorb infrared light if their dipole moment changes during the vibration process.

Infrared spectra are a valuable tool in the characterization of COFs and their corresponding molecular building blocks. While C=O stretch vibrations of aromatic aldehyde moieties appear in the carbonyl region between 1650 and 1700 cm^{-1} , the Fermi double resonance of the O=C-H deformation and stretch vibration between 2700 and 2900 cm^{-1} is a specific feature of aldehyde moieties.³³ IR spectra of azine and hydrazone COFs show a – compared to the original carbonyl stretch vibration – less intense C=N stretch vibration between 1600 and 1700 cm^{-1} .³⁵

Infrared measurements were performed on a Perkin Elmer Spektrum BX II (Perkin Elmer, USA) with an attenuated total reflectance (ATR) unit or on a JASCO FT/IR-4100 spectrometer equipped with a diamond ATR unit in a range of 600–4000 cm^{-1} . Data was background corrected and processed with JASCO's proprietary software Spectra Manager II. All measurements were conducted by Linus Stegbauer or Sebastian Zech.

2.5 Ultraviolet-Visible Spectroscopy

Ultraviolet-visible light spectroscopy probes the absorption of materials in the visible and ultraviolet range. The absorption is caused by excitation of electrons from occupied to unoccupied orbitals or bands in the material. In this thesis, only optical diffuse reflectance spectra of solid powders were recorded, photoluminescence spectra were recorded in the optical laboratory of the *Feldmann* group by Florian Ehrat on a Horriba Fluorolog 3. The spectra were collected at room temperature with a UV-Vis-NIR diffuse reflectance spectrometer Cary 5000 (Agilent Technologies, USA) at a photometric range of 350–800 nm. Powders were prepared in a sample carrier with a quartz glass window at the edge of the integrating sphere. Further data was collected on a JASCO V650 double-beam spectrophotometer equipped with a photomultiplier tube detector. Solid samples were loaded into a special designed holder and pressed against a quartz disc at the edge of the integrating sphere. BaSO₄ is used as the optical standard. Data was processed with JASCO's proprietary software *Spectra Manager II*. Kubelka-Munk plots were calculated from the reflectance data. All measurements were conducted by Linus Stegbauer or Sebastian Zech.

2.6 Electron Microscopy

Electron microscopy relies on similar basic principles as light microscopy but uses an electron beam instead of light. Since the resolution of a microscope is mainly limited by the wavelength of the irradiation source, the utilization of electrons with much shorter wavelengths enhance the magnification from approximately 2000× (200 nm resolution) for a light microscope to 1000000× (0.1 nm resolution) for an electron microscope. The electrons, generated by a field emission gun (FEG) or a tungsten filament, are accelerated to 40-300 kV and collimated by changing magnetic and electric fields (electrostatic and electromagnetic lenses). Besides the better resolution, which can give important information about the morphology of the samples, also electron diffraction can be applied on selected parts of the specimen to obtain distances of the crystal lattice.

In transmission electron microscopy (TEM) the electron beam is focused on very thin (< 100 nm) specimen, allowing transmittance of the electrons, and the transmitted beam is detected. The electrons interact with the sample, which gives information about the internal structure by imaging and electron diffraction. TEM was operated on a Philips CM30 ST, 300 kV S/TEM (FEI, USA) with a Si/Li EDX-detector (Thermo Fischer, USA) by Viola Duppel (Max Planck Institute for Solid State Research, Stuttgart).

The topographic images obtained by Scanning Electron Microscopy (SEM) exhibit a much better resolution and a sharper depth of focus than light microscopes. A set of condenser lenses focuses the electrons to a typical spot of a few nm before the beam impacts on the sample surface and interacts. Deflection coils move the electron beam in a grid fashion over the sample (scanning). Several detectors are available for i) secondary and ii) backscattered electrons. While secondary electrons are inelastically scattered electrons with which the morphology of the surface of the specimen can be imaged, backscattered electrons are elastically scattered electrons yielding information on the elemental composition of the sample: the brighter the image, the heavier the observed element. Additionally, the electron beam can eject an electron from the inner shell of the observed atom, leaving an electron hole which is immediately filled by an electron from an outer shell under emission of element-specific x-ray fluorescence. This principle is applied in energy-dispersive x-ray (EDX) SEM. EDX measurements were performed using either a JEOL JSM-6500F electron microscope (JEOL, Japan) with a field emission source equipped with an EDX detector (model 7418, Oxford Instruments, UK) by Christian Minke (Ludwig-Maximilians-Universität, Munich), a TESCAN Vega TS 5130MM electron microscope equipped with a Si/Li EDX detector (Oxford Instruments, UK) or a ZEISS Merlin microscope, using either a secondary electron or energy selective back-scattered electron detector by Viola Duppel (Max Planck Institute for Solid State Research, Stuttgart).

2.7 Nuclear Magnetic Resonance Spectroscopy

Nuclear magnetic resonance (NMR) has become a standard tool for determination of local order and molecular structure in organic chemistry, chemical biology and material science and furthermore allows studying dynamics in and between manifold systems. Nuclei with an odd number of protons, neutrons, or both, have an intrinsic nuclear spin and a corresponding spin quantum number I (e.g. $I(^1\text{H}) = \frac{1}{2}$), which is a crucial requirement for NMR. This nuclear spin, a rotating carrier of charge, has a magnetic dipole moment, which can only have discrete orientations in a magnetic field. The number of possible orientations is given by $2I+1$. The possible orientations split in different energy levels when an external magnetic field is applied (Zeeman splitting). The resonance condition between the energy levels is fulfilled when the used frequency of radiation meets the following equation:

$$\nu_0 = \frac{\gamma B_0}{2\pi}$$

Where ν_0 is the resonance frequency (*Larmor* frequency), γ the nucleus-specific gyromagnetic ratio and B_0 is the external magnetic field.

Frequencies for meeting the resonance conditions are usually in the radio frequency range (1-900 MHz).

Small differences between the local and applied magnetic field leading to a slightly different resonance frequency are caused by various electronic surroundings of each nucleus (shielding and deshielding). This subtle difference is called the *chemical shift* (in ppm deviation from standard Larmor frequency of the observed nucleus), which provides very valuable information about the local molecular structure and interaction between molecules. In contrast to liquids where Brownian motion leads to an averaging of anisotropic effects, supported by additional spinning of the sample tube at low frequencies, internuclear dipole-dipole interactions, the anisotropy of the chemical shift, quadrupolar coupling and spin-spin coupling result in the broadening of the signal in solid-state NMR (ssNMR). The dipolar coupling can be suppressed to a large extent by spinning of the sample at an angle of 54.74° (*Magic Angle Spinning, MAS*). The spinning frequency is around 1000 times faster than in solution state NMR to avoid overlap of spinning side bands with the spectrum. Cross-polarization (CP) can be used to increase the signal strength of nuclei with low gyromagnetic ratio such as ^{13}C and ^{15}N , by transferring the polarization of a nucleus with a higher gyromagnetic ratio, usually ^1H , to the rare nucleus. As a consequence of this, the relaxation times decrease and signal intensity increases up to the ratio $\gamma_{\text{H}}/\gamma_{\text{Nuc}}$.^{36,37}

MAS ssNMR spectra were recorded at ambient temperature on a BRUKER DSX500 Avance NMR spectrometer (Bruker Biospin, Germany) by Christian Minke (Ludwig-Maximilians-Universität, Munich), with an external magnetic field of 11.75 T. The operating frequencies are 500.1 MHz, 125.7 MHz and 50.7 MHz for ^1H , ^{13}C and ^{15}N respectively, and the spectra were ref-

erenced relative to TMS (^1H , ^{13}C) and nitromethane (^{15}N). The samples were contained either in 1.3, 2.4, 3.2 or 4 mm ZrO_2 rotors. For the ^{13}C and ^{15}N CP-MAS spectra, a ramped cross-polarization sequence was employed where the ^1H pulse amplitude was decreased linearly by 50%; typical contact times between 2 ms and 20 ms were chosen. For 1D CP-MAS experiments, a spinning frequency of typically 10 kHz was applied;

NMR spectra in solution were recorded on BRUKER Avance and JOEL Eclipse devices operating at 270 MHz or 400 MHz in deuterated solvents at room temperature, respectively, unless otherwise stated. The chemical shifts (δ) for ^1H - and ^{13}C nuclei refer to tetramethylsilane as an internal standard. Splitting patterns are indicated as *s* (singlet), *d* (doublet), *t* (triplet), *q* (quartet), *m* (multiplet) and *br* (broad).

2.8 Mass Spectrometry

Both the relative molecular weights and even the elemental composition can be determined by high resolution mass spectrometry (MS). Depending on the polarity and solubility of the sample it is ionized by different available methods, like electron impact ionization (EI), chemical ionization (CI), electrospray ionization (ESI), fast atom bombardment (FAB). EI may result in molecular fragmentation, which can assist in functional group determination. The reader is referred to the “Best Practice Guide for Generating Mass Spectra”, which is especially useful for an in-depth comparison of the different methods.³⁸

EI-MS was performed on a JOEL JMS-700 MStation equipped with a double-focusing sector field detector by Brigitte Breitenstein (Ludwig-Maximilians-Universität, Munich). Samples were deposited on a platinum filament and heated from 20°C to 1600°C at a rate of 120°/min.

2.9 References

1. Y.-B. Zhang, J. Su, H. Furukawa, Y. Yun, F. Gándara, A. Duong, X. Zou and O. M. Yaghi, *J. Am. Chem. Soc.*, 2013, **135**, 16336–16339.
2. Accelrys Software Inc, *Materials Studio*, Accelrys Software Inc., 2011.
3. J. Rouquerol, D. Avnir, C. W. Fairbridge, D. H. Everett, J. M. Haynes, N. Pernicone, J. D. Ramsay, K. S. Sing and K. K. Unger, *Pure Appl. Chem.*, 1994, **66**, 1739–1758.
4. S. Lowell, J. E. Shields, M. A. Thomas and M. Thommes, *Characterization of porous solids and powders: surface area, pore size and density*, Springer Science & Business Media, Dordrecht, Netherlands, 2012.
5. K. S. Sing, D. H. Everett, R. A. Haul, L. Moscou, R. A. Pierotti, J. Rouquerol and T. Siemieniowska, *Pure Appl. Chem.*, 1985, **57**, 603–619.

6. M. Thommes, K. Kaneko, A. V. Neimark, J. P. Olivier, F. Rodriguez-Reinoso, J. Rouquerol and K. S. W. Sing, *Pure Appl. Chem.*, 2015, **87**, 1051–1069.
7. M. Thommes and K. Cychosz, *Adsorption*, 2014, **20**, 233-250.
8. J. Landers, G. Y. Gor and A. V. Neimark, *Characterization of Porous Materials: From Angstroms to Millimeters A Collection of Selected Papers Presented at the 6th International Workshop, CPM-6 April 30 – May 2nd, 2012, Delray Beach, FL, USA Co-sponsored by Quantachrome Instruments*, 2013, **437**, 3–32.
9. F. Rouquerol, *Adsorption by powders and porous solids principles, methodology and applications*, 2nd edn., Academic Press, Amsterdam, 2014.
<http://www.sciencedirect.com/science/book/9780080970356>.
10. P. A. Monson, *Microporous Mesoporous Mater.*, 2012, **160**, 47–66.
11. A. V. Neimark and P. I. Ravikovitch, *Microporous Mesoporous Mater.*, 2001, **44–45**, 697–707.
12. P. I. Ravikovitch, A. Vishnyakov and A. V. Neimark, *Phys. Rev. E*, 2001, **64**, 011602.
13. M. Thommes, J. Morell, K. A. Cychosz and M. Fröba, *Langmuir*, 2013, **29**, 14893–14902.
14. M. Nič, J. Jirát, B. Košata, A. Jenkins and A. McNaught, *IUPAC Compendium of Chemical Terminology*, IUPAC, Research Triangle Park, NC, 2009.
15. G. Y. Gor, M. Thommes, K. A. Cychosz and A. V. Neimark, *Carbon*, 2012, **50**, 1583–1590.
16. A. V. Neimark, Y. Lin, P. I. Ravikovitch and M. Thommes, *Carbon*, 2009, **47**, 1617–1628.
17. P. I. Ravikovitch and A. V. Neimark, *Langmuir*, 2006, **22**, 11171–11179.
18. C. Fan, V. Nguyen, Y. Zeng, P. Phadungbut, T. Horikawa, D. D. Do and D. Nicholson, *SI: Characterization of Porous Solids X*, 2015, **209**, 79–89.
19. T. J. Bandoz, J. Jagiełło, J. A. Schwarz and A. Krzyzanowski, *Langmuir*, 1996, **12**, 6480–6486.
20. M. Thommes, C. Morlay, R. Ahmad and J. P. Joly, *Adsorption*, 2011, **17**, 653-661.
21. J. K. Brennan, T. J. Bandoz, K. T. Thomson and K. E. Gubbins, *Colloids Surf., A*, 2001, **187–188**, 539–568.
22. E.-P. Ng and S. Mintova, *Microporous Mesoporous Mater.*, 2008, **114**, 1–26.
23. K. Kaneko, Y. Hanzawa, T. Iiyama, T. Kanda and T. Suzuki, *Adsorption*, 1999, **5**, 7-13.
24. P. B. Balbuena and K. E. Gubbins, *Langmuir*, 1993, **9**, 1801–1814.
25. M. Bellissent-Funel, R. Sridi-Dorbez and L. Bosio, *J. Chem. Phys.*, 1996, **104**, 10023–10029.

26. T. Iiyama, K. Nishikawa, T. Otowa and K. Kaneko, *J. Phys. Chem.*, 1995, **99**, 10075–10076.
27. T. Ohba and K. Kaneko, *Journal of Physics: Conference Series*, 2009, **177**, 012001.
28. T. Ohba, S. Yamamoto, T. Kodaira and K. Hata, *Langmuir*, 2015, **31**, 1058–1063.
29. T. Iiyama, *Structural Understanding of Water Confined in Hydrophobic Nanopores*, Les Houches, 2013.
30. W. H. Bragg and W. L. Bragg, *Proceedings of the Royal Society of London A: Mathematical, Physical and Engineering Sciences*, 1913, **88**, 428–438.
31. U. Holzwarth and N. Gibson, *Nat. Nano.*, 2011, **6**, 534.
32. P. Scherrer, *Nachr. Ges. Wiss. Göttingen*, 1918, **26**, 98–100.
33. M. Hesse, H. Meier and B. Zeeh, *Spektroskopische Methoden in der organischen Chemie*, Georg Thieme Verlag, 2005.
34. C. Weidenthaler, *Nanoscale*, 2011, **3**, 792–810.
35. L. D. Frederickson, *Anal. Chem.*, 1964, **36**, 1349–1355.
36. A. Pines, M. G. Gibby and J. S. Waugh, *The Journal of Chemical Physics*, 1973, **59**, 569–590.
37. A. Pines, M. G. Gibby and J. S. Waugh, *The Journal of Chemical Physics*, 1972, **56**, 1776–1777.
38. V. Barwick, J. G. Langley, A. I. Mallet, B. K. Stein and K. Webb, *LGC, London, UK*, 2006.

3 NEW COVALENT ORGANIC FRAMEWORKS FOR PHOTOCATALYTIC APPLICATIONS

3.1 A Hydrazone-based Covalent Organic Framework for Photocatalytic Hydrogen Production

Linus Stegbauer, Katharina Schwinghammer, Bettina V. Lotsch

published in *Chem. Sci.* **2014**, 5, 2789-2753

DOI: 10.1039/C4SC00016A

<http://pubs.rsc.org/en/Content/ArticleLanding/2014/SC/c4sc00016a>

Formatting and numbering of figures were changed.

Adapted with permission from The Royal Society of Chemistry

Abstract

Covalent organic frameworks (COFs) have recently emerged as a new generation of porous polymers combining molecular functionality with the robustness and structural definition of crystalline solids. Drawing on the recent development of tailor-made semiconducting COFs, we here report on a new COF capable of visible-light driven hydrogen generation in the presence of Pt as proton reduction catalyst (PRC). The COF is based on hydrazone-linked functionalized triazine and phenyl building blocks and adopts a layered structure with a honeycomb-type lattice featuring mesopores of 3.8 nm and the highest surface area among all hydrazone-based COFs reported to date. When illuminated with visible light, the Pt-doped COF continuously produces hydrogen from water without signs of degradation. With their precise molecular organization and modular structure combined with high porosity, photoactive COFs represent well-defined model systems to study and adjust the molecular entities central to the photocatalytic process.

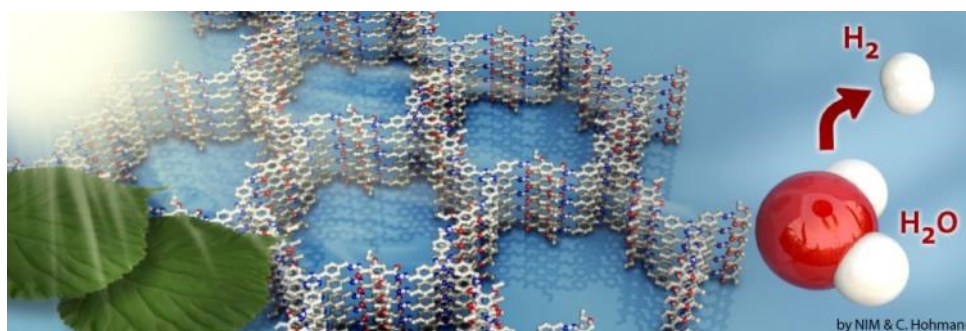


Table of Content

3.1.1 Introduction

The last decade has seen a continuous rise in activity revolving around the development of potent photocatalytic systems, which are capable of transforming solar energy into chemical fuels.¹ Whilst most photocatalysts are based on inorganic semiconductors,² there are a few examples of materials composed solely of light elements.³ These systems, prominently represented by carbon nitride polymers, are moderately active in hydrogen generation from water,⁴ however their performance can be significantly enhanced by morphology tuning and structural modifications, including doping.^{5,6} The major downside of these polymers, however, is their lack of crystallinity and generally low surface areas, which are inherently hard to control. In addition, carbon nitrides are invariably composed of heptazine or triazine units, thus offering only limited chemical variety and they are only little susceptible to systematic post-modification. A closely related class of organic polymers, dubbed covalent organic frameworks (COFs), is apt to overcome these inherent weaknesses of carbon nitrides by combining chemical versatility and modularity with potentially high crystallinity and porosity.⁷⁻¹¹ Recently, unique 2D COFs with interesting optoelectronic properties have emerged, representing ideal scaffolds for exciton separation and charge percolation within self-sorted, nanoscale phase-separated architectures. Whereas most COFs rely on the formation of water-labile boronate ester linkages,¹² a few other examples based on imine¹³⁻¹⁷ and hydrazone¹⁸ linkage have been synthesized recently. For example, the imine-based COF-LZU1 in combination with Pd has been used as catalyst in Suzuki couplings.¹⁹ Surprisingly, after the pioneering work by Yaghi hydrazone formation has not been used again for the synthesis of COFs, although hydrazones are typically much less prone to hydrolysis than imines.²⁰ This chemoselective type of bond formation between a substituted acyl hydrazine and an aldehyde is highlighted by its use in labeling modified proteins²¹ and for drug delivery purposes.²²

Although big strides towards photoactive COFs with light-harvesting and charge separation capability have already been made,^{15,23-27} COFs have not yet been explored as photosensitizers in photocatalytic systems for the production of solar fuels. A first indication of the underlying potential of COFs as photoactive material has been the light-induced activation of oxygen by a squaraine-based COF reported recently by Jiang and co-workers.¹³

Herein, we report the first COF which is active in visible light induced hydrogen evolution in the presence of Pt as proton reduction catalyst (PRC). Our hydrazone-based COF (TFPT-COF) is constructed from 1,3,5-*tris*-(4-formyl-phenyl)triazine (TFPT) and 2,5-diethoxy-terephthalohydrazide (DETH) building blocks (Fig. 3.1), featuring mesopores of 3.8 nm in diameter and the highest surface area among all hydrazone-based COFs reported so far.

3.1.2 Results and Discussion

TFPT-COF: Synthesis and Characterization

Triazine-based molecules offer high electron mobilities, an electron withdrawing character²⁸ and are hence widely used in synthetic chemistry²⁹ and optoelectronics.²⁸ TFPT has a much smaller dihedral angle between the phenyl and triazine unit ($\sim 7.7^\circ$) compared to its benzene centered analogue (38.3°) (Fig. 3.S1, ESI†).³⁰ As a consequence, the use of TFPT should facilitate the formation of a planar COF with an extended, π -system compared to the monomers and enhanced crystallinity. Indeed, the TFPT-COF turns out to be crystalline and at the same time stable in methanol and other solvents (Fig. 3.S15, ESI†).

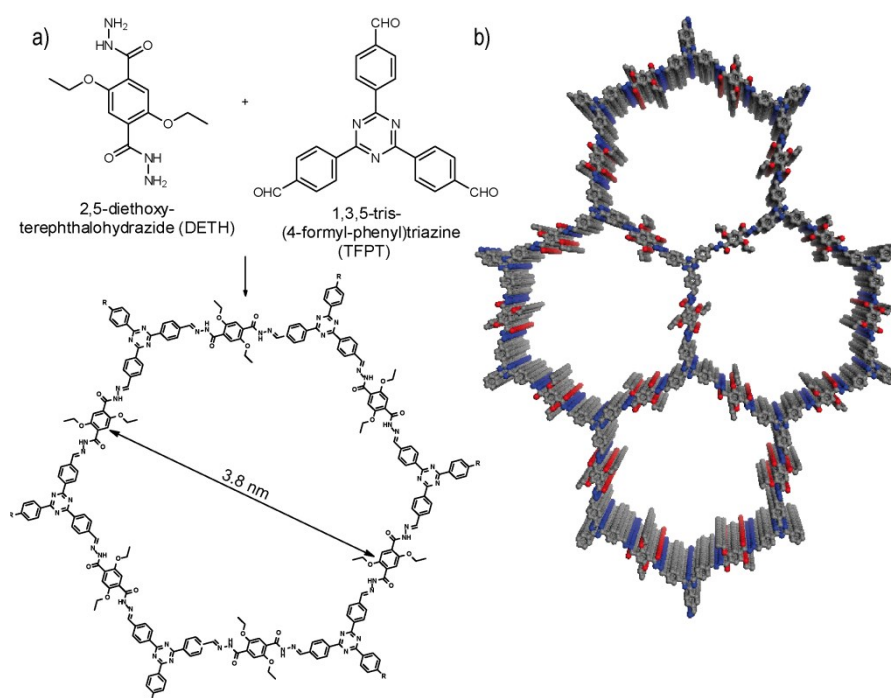


Figure 3.1: Acetic acid catalysed hydrazone formation furnishes a mesoporous 2D network with a honeycomb-type in plane structure. (a) Scheme showing the condensation of the two monomers to form the TFPT-COF. (b) TFPT-COF with a cofacial orientation of the aromatic building blocks, constituting a close-to eclipsed primitive hexagonal lattice (grey: carbon, blue: nitrogen, red: oxygen).

TFPT-COF was synthesized by the acetic acid catalysed reversible condensation of the building blocks in dioxane/mesitylene (1:2 v/v) at 120°C in a sealed pressure vial under argon atmosphere for 72 hours. The product was obtained as a fluffy pale-yellow nanocrystalline solid. To remove any starting material or solvent contained in the pores, TFPT-COF was centrifuged, washed with DMF and THF, soaked in DCM for 3 hours, and subsequently heated to 120°C in high dynamic vacuum for 12 h (10^{-7} mbar).

It is worth mentioning that TFPT-COF could also be synthesized by in situ deprotection and subsequent condensation in a one-pot procedure (see Scheme S6, ESI†). Using this reaction scheme, the acetal protected TFPT is deprotected by treatment with a catalytic amount of

camphersulfonic acid in the solvent mixture. The COF formation is then started by adding the corresponding catalytic amount of sodium acetate to the reaction mixture. After 72 h, we obtained a material chemically and structurally identical to TFPT-COF (Fig. 3.S2, ESI†). This protocol opens the door to a new variety of acetal-protected building blocks and at the same time enhances the solubility of otherwise insoluble building blocks due to the aliphatic protection group.

ATR-IR data of TFTP-COF show stretching modes in the range $1670 - 1660 \text{ cm}^{-1}$ and $1201 - 1210 \text{ cm}^{-1}$, which are characteristic of C=N moieties. The lack of the aldehyde Fermi double resonance at 2824 and 2721 cm^{-1} , as well as the aldehyde carbonyl stretching vibration at 1700 cm^{-1} of the TFPT monomer clearly suggests the absence of any starting material. Furthermore, the triazine moiety is still present in the TFTP-COF as ascertained by the triazine semicircle stretch vibration at 806 cm^{-1} (Fig. 3.S3).

^1H solid-state NMR MAS spectroscopy shows the presence of the ethoxy group through signals at 1.39 ppm ($\text{CH}_3\text{-CH}_2\text{-O}$) and 3.29 ppm ($\text{CH}_3\text{-CH}_2\text{-O}$) (Fig. 3.2e). The aromatic region is represented by a broadened signal at 6.5 ppm . Furthermore, the ^{13}C CP-MAS spectrum clearly supports the formation of a hydrazone bond corresponding to the signal at 148.9 ppm , and confirms the presence of the triazine ring (167.9 ppm) (Fig. 3.2d). All other signals were also unambiguously assigned to the corresponding carbon atoms (Fig. 3.2c).¹⁸

Powder X-Ray diffraction (PXRD) measurements confirm the formation of a crystalline framework with metrics being consistent with the structure model shown in Figure 3.1. Comparison of the experimental data with the simulation³¹ reveal a hexagonal structure with $P6/m$ symmetry and an eclipsed AA layer stacking, which is in line with most COF structures reported to date (Fig. 3.2a).⁷⁻¹¹ Nevertheless, we assume that slight offsets with respect to the ideal cofacial layer stacking have to be taken into account as recently delineated by Heine,³² Dichtel and co-workers.³³ Subtle layer offsets which are not resolvable by XRD result in the minimization of repulsive electrostatic forces between the layers with respect to the energetically less favorable, fully eclipsed structures. Nevertheless, whether the same situation holds true also for hydrazone COFs has yet to be demonstrated.

Pawley refinement (including peak broadening) of the experimental powder pattern gave lattice parameters of $a = b = 41.90 \text{ \AA}$ (Figs. 3.2a and 3.S5, ESI†). The theoretical powder pattern of the related staggered conformation derived from the *gra* net with $P63/m$ symmetry does not reproduce the observed intensity distribution and was therefore discarded (Figs. 3.2a and 3.S8, ESI†). The 001 diffraction peak at $2\theta = 26.6$ corresponds to an interlayer distance of 3.37 \AA (Fig. 3.2b), suggesting a typical van der Waals contact between the aromatic layers. Interestingly, the presence of the ethoxy groups protruding into the pores does not notably increase the interlayer distance, thus indicating a predominantly coplanar arrangement with the plane of the honeycomb lattice.

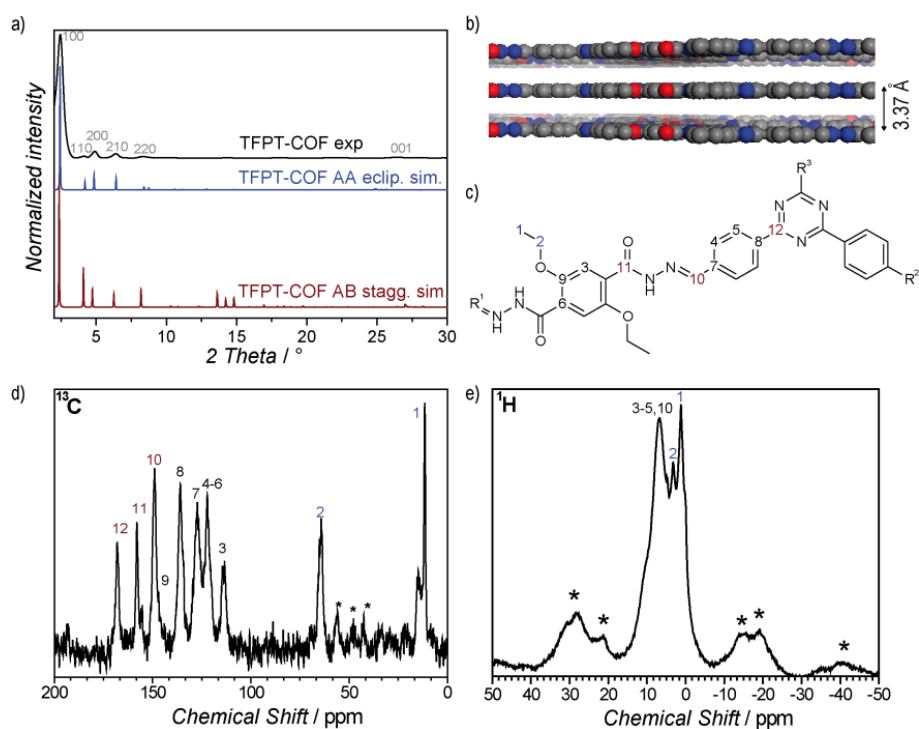


Figure 3.2: Characterization of the TFPT-COF by PXRD and MAS solid-state NMR spectroscopy. (a) and (b) PXRD suggests a (close to) eclipsed layer stacking as confirmed by Pawley refinement of the AA-stacked structure model. (c) Assignment of ^{13}C and ^1H NMR data. (d) ^{13}C CP-MAS NMR spectrum, asterisks mark spinning side bands. (e) ^1H MAS NMR spectrum with a group of signals centered between 1 and 8 ppm; asterisks mark spinning side bands.

According to the above theoretical studies and other predictions for the stacking of triazines by Gamez et al.,³⁴ we have also simulated a parallel displaced structure (displacement vector 1.4 Å) with an AA'A-type stacking sequence (Figs. 3.S9 and 3.S10, ESI†). As expected, the simulated PXRD is very similar to both the experimental PXRD as well as the PXRD calculated for the perfectly eclipsed structure (Fig. 3.S11, ESI†).

Argon sorption measurements at 87 K clearly show the formation of mesopores as indicated by a typical type IV adsorption isotherm (Fig. 3.3a). The Brunauer-Emmett-Teller (BET) surface area was calculated to be $1603 \text{ m}^2 \text{ g}^{-1}$ (total pore volume is $1.03 \text{ cm}^3 \text{ g}^{-1}$, Fig. 3.S12, ESI†), which the highest measured surface area among all hydrazone COFs reported to date.^{13–18,35} Comparing these values with those of COF-43, derived from a benzene-centered trigonal building block with the same pore size,¹⁸ the surface area has more than doubled, probably as a consequence of the smaller dihedral angle of the triazine-centered TFPT and the resulting more favorable stacking interactions, or due to the more complete activation of the material. The pore size distribution (PSD) was evaluated with non-local density functional theory (NLDFT). The experimental PSD exhibits a maximum at 3.8 nm, thereby verifying the theoretical pore diameter of 3.8 nm (Fig. 3.S13, ESI†) which is the same pore size found by Yaghi and co-workers for their benzene-centered COF.¹⁸ Transmission electron microscopy images confirm the data derived from PXRD

and sorption measurements. The hexagonal pore arrangement with pore distances of ≈ 3.4 nm is clearly visible, as well as the layered nanomorphology (Fig. 3.3b).

The diffuse reflectance UV/Vis spectrum of the yellow powder exhibits an absorption edge around 400 nm (the spike at 380 nm is due to a change of the light source), with the absorption tail extending well beyond 600 nm (Fig. 3.4a). We estimate an optical band gap of roughly 2.8 eV from the absorption edge, based on the Kubelka–Munk function (Fig. 3.S14, ESI†). The TFPT-COF shows a pronounced red-shift of the absorption edge by 33 nm in comparison with the individual building blocks. A similar broadened and red-shifted absorption of the COF with respect to the monomers has been found by Jiang and co-workers for several COF systems.^{13,23–27} In principle, the observed HOMO-LUMO gap of the TFPT-COF is large enough to enable water splitting through band gap excitation and at the same time small enough to harvest a significant portion of the visible light spectrum.

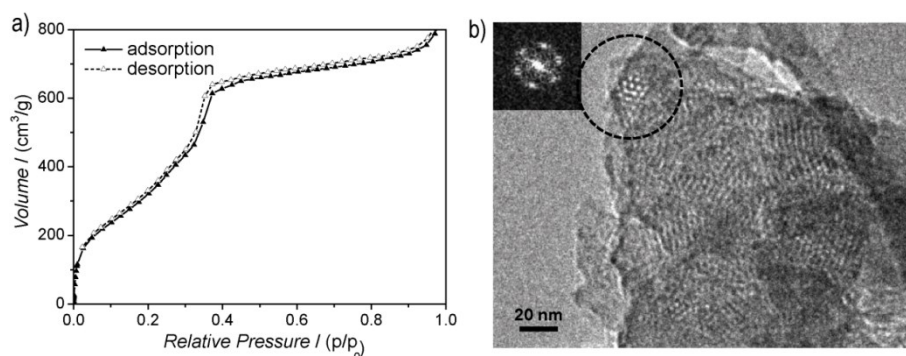


Figure 3.3: Structural characterization of TFPT-COF by physisorption and TEM. (a) Argon-sorption isotherms show the formation of mesopores, consistent with the predicted size based on the structure model. The reversible type IV isotherm (adsorption: black triangles, desorption: white triangles) gives a BET surface of $1603 \text{ m}^2 \text{ g}^{-1}$. (b) TEM images showing the formation of hexagonal pores.

To investigate this possibility, we studied the light-induced hydrogen evolution mediated by Pt-modified TFPT-COF in the presence of a sacrificial electron donor as the photocatalytic system under visible light irradiation. While TFPT-COF primarily acts as a photosensitizer for exciton generation, Pt functions as PRC. We previously demonstrated that the Pt-modified triazine-based carbon nitride poly(triazine imide) (PTI) shows substantial photocatalytic activity, despite its amorphous character.⁶ Therefore, the presence of triazine moieties in the TFPT-COF, along with a moderate band gap, renders this crystalline COF an excellent candidate to study hydrogen-evolution and possible structure-property relations.

Photocatalytic hydrogen evolution

Hydrogen evolution was studied under standardized conditions and measured in the presence of the PRC Pt, using sodium ascorbate as sacrificial electron donor (see ESI† for details). In fact, TFPT-COF/Pt is a potent photocatalytic system, showing continuous and stable hydrogen production of $230 \mu\text{mol h}^{-1} \text{g}^{-1}$ (Figs. 3.4b and 3.S22, ESI†). The total amount of hydrogen produced after 52 h (with sodium ascorbate) exceeds the total amount of hydrogen incorporated in the material ($97.6 \mu\text{mol}$), which adds evidence that hydrogen evolution is in fact catalytic and does not result from stoichiometric decomposition of the COF itself. Measurements in the dark (Fig. 3.S22, ESI†) show no hydrogen evolution, confirming that the evolution of hydrogen is a photoinduced effect. The monomer TFPT alone does not show photocatalytic activity under these conditions either. The long-time stability was tested by catalyst cycling, i.e. centrifugation of the reaction mixture, washing of the precipitate and addition of fresh sodium ascorbate solution. Even after three cycles the hydrogen evolution does not decrease (Fig. 3.S23, ESI†). Small fluctuations are due to small concentration differences of the COF/aqueous sodium ascorbate suspensions.

Using a 10 vol% aqueous triethanolamine (TEoA) solution as sacrificial donor, an even higher hydrogen evolution rate was detected, with the amount of hydrogen evolved in the first five hours being as high as $1970 \mu\text{mol h}^{-1} \text{g}^{-1}$, corresponding to a quantum efficiency of 2.2%, while maximum QEs of up to 3.9% were obtained for individual batches (Fig. 3.4b). However, this high rate comes along with a quicker deactivation of the photocatalytic system. By reducing the amount of triethanolamine (1 vol%) and adjusting the suspension to pH = 7, stable hydrogen evolution for a longer time range (24 hours) was detected.

The observed high amount of hydrogen evolved under standard basic conditions ($1970 \mu\text{mol h}^{-1} \text{g}^{-1}$) suggests that TFPT-COF/Pt is superior to Pt-modified amorphous melon, *g*- C_3N_4 (which was synthesized according to Zhang et al.⁵ at 600 °C) and crystalline poly(triazine imide) ($720 \mu\text{mol h}^{-1} \text{g}^{-1}$, $840 \mu\text{mol h}^{-1} \text{g}^{-1}$ and $864 \mu\text{mol h}^{-1} \text{g}^{-1}$, respectively),⁶ which were tested under similar conditions for three hours with TEoA as sacrificial donor. We also studied oxygen evolution to probe whether full water splitting is possible with the TFPT-COF. However, no O_2 could be detected under the conditions used (see ESI†).

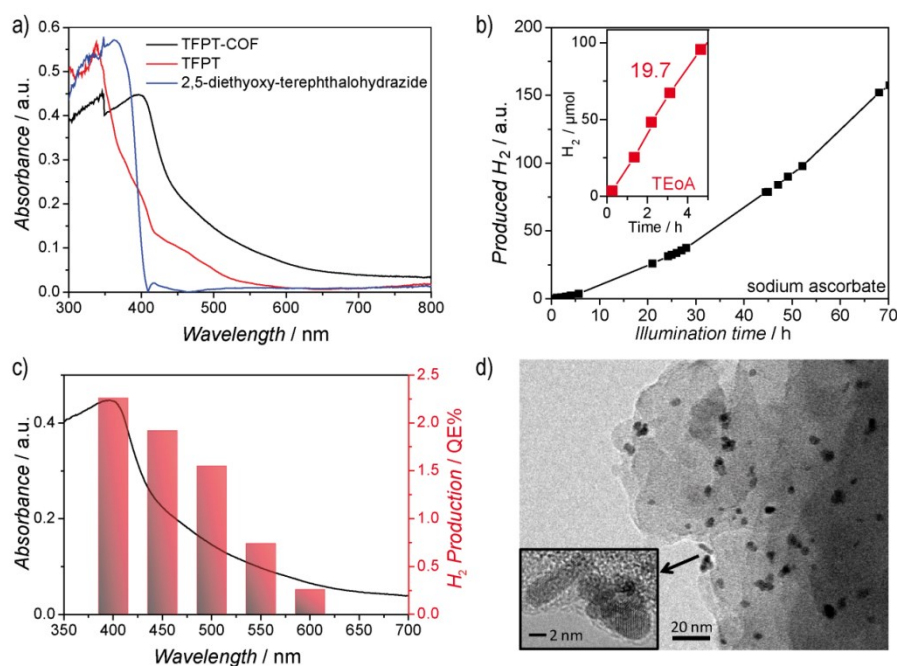


Figure 3.4: Optical properties of the TFPT-COF and photocatalytic hydrogen evolution. (a) UV/Vis diffuse reflectance spectra of TFPT-COF (black) and its monomers (blue and red). (b) Time course of hydrogen evolution from an aqueous sodium ascorbate solution by the Pt-modified TFPT-COF under visible light irradiation ($\lambda > 420$ nm). The inset shows the hydrogen evolution rate ($19.7 \mu\text{mol h}^{-1}$) from 10 vol% aqueous triethanolamine solution over 5 h (red). (c) Overlay of UV/Vis absorption of TFPT-COF and wavelength-specific hydrogen production of Pt-modified TFPT-COF in a 10 vol% aqueous triethanolamine solution using 40 nm FWHM band-pass filters. (d) TEM image of TFPT-COF/Pt after illumination for 84 h showing the formation of Pt nanoparticles (5 nm).

Reconversion of TFPT-COF

After photocatalysis, the amorphous material is coated with dispersed Pt nanoparticles, formed in situ (Fig. 3.4d). The TEM images suggest that the material loses its long-range order during photocatalysis (Fig. 3.4d), which is supported by XRD measurements (Figs. 3.5 and 3.S16, ESI†). This loss of long-range order has also been observed by Dichtel and co-workers and has been assigned to exfoliation of the COF in water.²⁰ To test this hypothesis, we carried out sorption measurements and PXRD after photocatalysis (95 h of irradiation in sodium ascorbate solution). TFPT-COF/Pt was filtered off as a greenish solid (Fig. 3.5, inset picture, see ESI† for more images). A DCM extract of the solid catalyst did not contain any molecular material, which suggests that the as-obtained powder did not decompose and no monomers were released. At the same time, however, crystallinity was lost (Fig. 3.S16, ESI†) and the BET surface area was reduced to $410 \text{ m}^2 \text{ g}^{-1}$ (Fig. 3.S18, ESI†). Nevertheless, we found that the amorphous product can easily be reconverted into the crystalline and porous TFPT-COF with a BET surface area of $1185 \text{ m}^2 \text{ g}^{-1}$ (Fig. 3.5 and ESI†) by subjecting it to the initial synthesis conditions. Further experiments revealed that the TFPT-COF already loses its long-range order during sonication in water. Overall,

this observation strengthens the hypothesis that the COF is exfoliated in water,²⁰ thereby losing its long-range order, while the connectivity and photoactivity is retained.

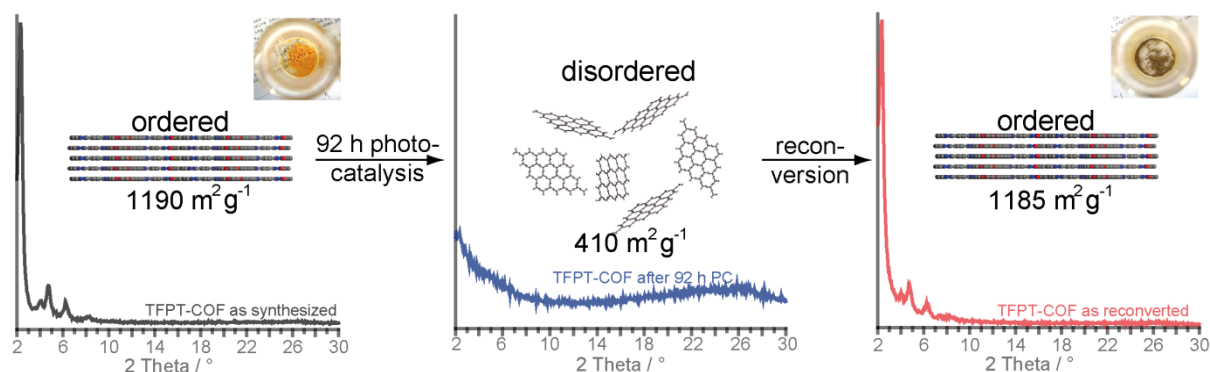


Figure 3.5: Transformation of TFPT-COF during photocatalysis and subsequent recovery by re-conversion (see SI for details). Inset photographs show colour change from yellow (TFPT-COF) to green (TFPT-COF/Pt).

3.1.3 Conclusion

In conclusion, we have developed a new crystalline hydrazone-based TFPT-COF, which is the first COF to show photocatalytic hydrogen evolution under visible light irradiation in the presence of Pt as PRC. This framework is competitive with the best non-metal photocatalysts for hydrogen production and represents a lightweight, well-ordered model system, which in principle can be readily tuned – by replacement, expansion or chemical modification of its building blocks – to further study and optimize the underlying mechanism of hydrogen evolution mediated by the framework and to enhance its light harvesting capability. The triazine moieties in the TFPT-COF, which are likewise present in the recently developed triazine-based carbon nitride photocatalytic system PTI/Pt may point to an active role of the triazine unit in the photocatalytic process.

The development of COFs as tunable scaffolds for photocatalytic hydrogen evolution enables a general bottom-up approach toward designing tailor-made photosensitizers and photocatalysts with tunable optical and electronic properties, a goal we are currently pursuing in our lab. We expect this new application of COFs in photocatalysis to open new avenues to custom-made heterogeneous photocatalysts, and to direct and diversify the ongoing development of COFs for optoelectronic applications.

3.1.4 Bibliography

Author contributions

Linus Stegbauer wrote the manuscript, edited the figures, designed and did the synthesis of the COFs, carried out the sorption measurements, simulated the COF structure and PXRDs, and did

the spectral characterization. Katharina Schwinghammer did the photocatalysis experiments, calculated the quantum efficiencies and carried out the long-term experiments.

Acknowledgements

We thank S. Hug for help with sorption measurements, C. Stefani for PXRDs, V. Duppel for TEM measurements, D. Weber for general assistance, C. Minke for ssNMR measurements and M.-L. Schreiber for syntheses. Financial support by the Fonds the Chemischen Industrie (scholarship for L.S.), the cluster of excellence “Nanosystems Initiative Munich” (NIM, and the Center for NanoScience (CeNS) is gratefully acknowledged.

References

- 1 X. Chen, S. Shen, L. Guo and S. S. Mao, *Chem. Rev. (Washington, DC, U. S.)*, 2010, **110**, 6503–6570.
- 2 H. Tong, S. Ouyang, Y. Bi, N. Umezawa, M. Oshikiri and J. Ye, *Adv. Mater. (Weinheim, Ger.)*, 2012, **24**, 229–251.
- 3 a) S. Yanagida, A. Kabumoto, K. Mizumoto, C. Pac and K. Yoshino, *J. Chem. Soc., Chem. Commun.*, 1985, 474–475. b) J. Liu, S. Wen, Y. Hou, F. Zuo, G. J. O. Beran and P. Feng, *Angew. Chem. Int. Ed.*, 2013, **52**, 3241–3245. c) X. Wang, K. Maeda, A. Thomas, K. Takanaabe, G. Xin, J. M. Carlsson, K. Domen and M. Antonietti, *Nat. Mater.*, 2009, **8**, 76–80.
- 4 K. Maeda, X. Wang, Y. Nishihara, D. Lu, M. Antonietti and K. Domen, *J. Phys. Chem. C*, 2009, **113**, 4940–4947.
- 5 J. Zhang, X. Chen, K. Takanabe, K. Maeda, K. Domen, J. D. Epping, X. Fu, M. Antonietti and X. Wang, *Angew. Chem. Int. Ed.*, 2010, **49**, 441–444.
- 6 K. Schwinghammer, B. Tuffy, M. B. Mesch, E. Wirnhier, C. Martineau, F. Taulelle, W. Schnick, J. Senker and B. V. Lotsch, *Angew. Chem. Int. Ed.*, 2013, **52**, 2435–2439.
- 7 A. P. Côté, A. I. Benin, N. W. Ockwig, M. O’Keeffe, A. J. Matzger and O. M. Yaghi, *Science (Washington, DC, United States)*, 2005, **310**, 1166–1170.
- 8 H. M. El-Kaderi, J. R. Hunt, J. L. Mendoza-Cortes, A. P. Cote, R. E. Taylor, M. O’Keeffe and O. M. Yaghi, *Science (Washington, DC, United States)*, 2007, **316**, 268–272.
- 9 A. P. Côté, H. M. El-Kaderi, H. Furukawa, J. R. Hunt and O. M. Yaghi, *J. Am. Chem. Soc.*, 2007, **129**, 12914–12915.
- 10 S.-Y. Ding and W. Wang, *Chem. Soc. Rev.*, 2013, **42**, 548–568.
- 11 X. Feng, X. Ding and D. Jiang, *Chem. Soc. Rev.*, 2012, **41**, 6010–6022.
- 12 Y. Du, K. Mao, P. Kamakoti, P. Ravikovitch, C. Paur, S. Cundy, Q. Li and D. Calabro, *Chem. Commun. (Cambridge, U. K.)*, 2012, **48**, 4606–4608.
- 13 A. Nagai, X. Chen, X. Feng, X. Ding, Z. Guo and D. Jiang, *Angew. Chem. Int. Ed.*, 2013, **52**, 3770–3774.

- 14 X. Chen, M. Addicoat, S. Irle, A. Nagai and D. Jiang, *J. Am. Chem. Soc.*, 2012, **135**, 546–549.
- 15 S. Wan, F. Gándara, A. Asano, H. Furukawa, A. Saeki, S. K. Dey, L. Liao, M. W. Ambrogio, Y. Y. Botros, X. Duan, S. Seki, J. F. Stoddart and O. M. Yaghi, *Chem. Mater.*, 2011, **23**, 4094–4097.
- 16 F. J. Uribe-Romo, J. R. Hunt, H. Furukawa, C. Klöck, M. O’Keeffe and O. M. Yaghi, *J. Am. Chem. Soc.*, 2009, **131**, 4570–4571.
- 17 M. G. Rabbani, A. K. Sekizkardes, Z. Kahveci, T. E. Reich, R. Ding and H. M. El-Kaderi, *Chem.–Eur. J.*, 2013, **19**, 3324–3328.
- 18 F. J. Uribe-Romo, C. J. Doonan, H. Furukawa, K. Oisaki and O. M. Yaghi, *J. Am. Chem. Soc.*, 2011, **133**, 11478–11481.
- 19 S.-Y. Ding, J. Gao, Q. Wang, Y. Zhang, W.-G. Song, C.-Y. Su and W. Wang, *J. Am. Chem. Soc.*, 2011, **133**, 19816–19822.
- 20 D. N. Bunck and W. R. Dichtel, *J. Am. Chem. Soc.*, 2013, **135**, 14952–14955.
- 21 T. P. King, S. W. Zhao and T. Lam, *Biochemistry*, 1986, **25**, 5774–5779.
- 22 C. C. Lee, E. R. Gillies, M. E. Fox, S. J. Guillaudeu, J. M. J. Fréchet, E. E. Dy and F. C. Szoka, *Proceedings of the National Academy of Sciences*, 2006, **103**, 16649–16654.
- 23 S. Jin, X. Ding, X. Feng, M. Supur, K. Furukawa, S. Takahashi, M. Addicoat, M. E. El-Khouly, T. Nakamura, S. Irle, S. Fukuzumi, A. Nagai and D. Jiang, *Angew. Chem. Int. Ed.*, 2013, **52**, 2017–2021.
- 24 E. L. Spitler and W. R. Dichtel, *Nat. Chem.*, 2010, **2**, 672–677.
- 25 X. Ding, X. Feng, A. Saeki, S. Seki, A. Nagai and D. Jiang, *Chem. Commun. (Cambridge, U. K.)*, 2012, **48**, 8952–8954.
- 26 X. Ding, J. Guo, X. Feng, Y. Honsho, J. Guo, S. Seki, P. Maitarad, A. Saeki, S. Nagase and D. Jiang, *Angew. Chem. Int. Ed.*, 2011, **50**, 1289–1293.
- 27 X. Ding, L. Chen, Y. Honsho, X. Feng, O. Saengsawang, J. Guo, A. Saeki, S. Seki, S. Irle, S. Nagase, V. Parasuk and D. Jiang, *J. Am. Chem. Soc.*, 2011, **133**, 14510–14513.
- 28 T. Ishi-i, K. Yaguma, T. Thiemann, M. Yashima, K. Ueno and S. Mataka, *Chem. Lett.*, 2004, **33**, 1244–1245.
- 29 D. Sun, S. Ma, Y. Ke, D. J. Collins and H.-C. Zhou, *J. Am. Chem. Soc.*, 2006, **128**, 3896–3897.
- 30 a) Z.-S. Li, J.-X. Chen, Y.-B. Huang, G.-R. Chen and T.-Y. Lan, *Acta Cryst. Sect. E*, 2006, **62**, 777–779. b) V. Volkis, E. Nelkenbaum, A. Lisovskii, G. Hasson, R. Semiat, M. Kapon, M. Botoshansky, Y. Eishen and M. S. Eisen, *J. Am. Chem. Soc.*, 2003, **125**, 2179–2194.
- 31 *Material Studio v 5.5.0.0*, Accelrys Software Inc., 2011.
- 32 B. Lukose, A. Kuc and T. Heine, *Chem.–Eur. J.*, 2011, **17**, 2388–2392.

- 33 B. T. Koo, W. R. Dichtel and P. Clancy, *J. Mater. Chem.*, 2012, **22**, 17460–17469.
- 34 a) S. Grimme, *Angew. Chem. Int. Ed.*, 2008, **47**, 3430–3434. b) J. Antony, B. Alameddine, T. A. Jenny and S. Grimme, *J. Phys. Chem. A*, 2012, **117**, 616–625. c) T. J. Mooibroek and P. Gamez, *Inorg. Chim. Acta*, 2007, **360**, 381–404. d) W. Pisula, H. Tsao, D. Dudenko, D. Cho, S. Puniredd, Y. Zhao, A. Mavrinskiy, J. Shu, M. Hansen, M. Baumgarten and K. Müllen, *Polymers*, 2013, **5**, 833–846.
- 35 a) S. Chandra, S. Kandambeth, B. P. Biswal, B. Lukose, S. M. Kunjir, M. Chaudhary, R. Barbarao, T. Heine and R. Banerjee, *J. Am. Chem. Soc.*, 2013, **135**, 17853–17861. b) S. Kandambeth, D. B. Shinde, M. K. Panda, B. Lukose, T. Heine and R. Banerjee, *Angew. Chem. Int. Ed.*, 2013, **52**, 13052–13056. c) S. Kandambeth, A. Mallick, B. Lukose, M. V. Mane, T. Heine and R. Banerjee, *J. Am. Chem. Soc.*, 2012, **134**, 19524–19527.

3.1.5 Supporting Information

Materials and Instruments

All reagents were purchased from commercial sources and used without further purification. The starter 2,5-diethoxy-terephthalohydrazide^{S1} was prepared according to ref. S1, the NMR data being consistent with those given in the literature.

The synthesis of the second starting material TFPT^{S2} is described below.

Infrared spectra were recorded on a Perkin Elmer Spektrum BX II FT-IR equipped with an ATR unit (Smith Detection Dura-Sample IIR diamond). The spectra were background-corrected.

The ¹³C and ¹⁵N MAS NMR spectra were recorded at ambient temperature on a Bruker Avance 500 solid-state NMR spectrometer, operating at frequencies of 500.1 MHz, 125.7 MHz and 50.7 MHz for ¹H, ¹³C and ¹⁵N, respectively. The sample was contained in a 4 mm ZrO₂ rotor (Bruker) which was mounted in a standard double resonance MAS probe. The ¹³C and ¹⁵N chemical shifts were referenced relative to TMS and nitromethane, respectively.

The ¹H-¹⁵N and ¹H-¹³C cross-polarization (CP) MAS spectra were recorded at a spinning speed of 10 kHz using a ramped-amplitude (RAMP) CP pulse on ¹H, centered on the $n = +1$ Hartmann-Hahn condition, with a nutation frequency ν_{nut} of 55 kHz (¹⁵N) and 40 kHz (¹³C). During a contact time of 7 ms the ¹H radio frequency field was linearly varied about 20%.

UV/Vis optical diffuse reflectance spectra were collected at room temperature with a Varian Carry 500 UV/Vis diffuse reflectance spectrometer. Powders were prepared between two quartz discs at the edge of the integrating sphere with BaSO₄ as the optical standard. Absorption spectra were calculated from the reflectance data with the Kubelka-Munk function.

Argon sorption measurements were performed at 87 K with a Quantachrome Instrument Autosorb iQ. Samples of 20 mg were preheated in vacuum at 120 °C for 12 h. For BET calculations pressure ranges were chosen between 0.20-0.34 p/p₀.

The pore size distribution was calculated from Ar adsorption isotherms by non-local density functional theory (NLDFT) using the “Ar-zeolite/silica cylindrical pores at 87 K” kernel (applicable pore diameters 3.5 Å – 1000 Å) for argon data as implemented in the AUTOSORB data reduction software.

Powder x-ray diffraction data were collected using a Bruker D8-advance diffractometer in reflectance Bragg-Brentano geometry employing Cu filtered CuK α -monochromator focused radiation (1.54059 Å) at 1600 W (40 kV, 40 mA) power and equipped with a Lynx Eye detector (fitted at 0.2 mm radiation entrance slit). Samples were mounted on Ge (111) sample holders after dispersing the powders with ethanol and letting the slurry dry to form a conformal film on the holder. The

samples were measured with a 2θ -scan from 2° to 30° as a continuous scan with 3046 steps and 5 s/step (acquisition time 4 h 47 min 45 s).

Transmission electron microscopy data were obtained with a Philips CM30/ST microscope with LaB₆ cathode, at an acceleration voltage of 300 kV. The powder was dispersed in *n*-Butanol. One drop of the suspension was placed on a holey carbon/copper grid.

Scanning electron microscopy images were obtained with a Zeiss Merlin at 1.5 kV. The TEM grids were deposited onto a sticky carbon surface.

Synthetic Procedures

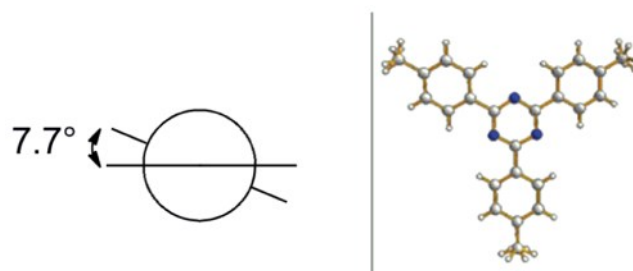
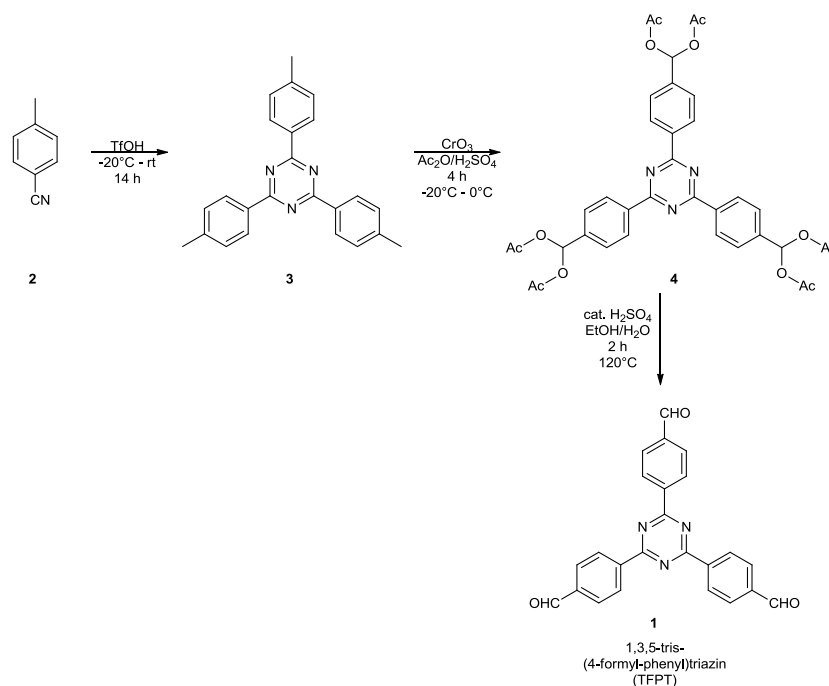
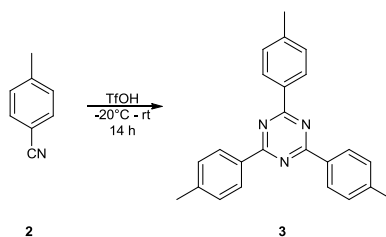


Figure 3.S1. Molecular structure of 1,3,5-(4-methylphenyl)triazine. Newman projection on the single bond connecting triazine and phenyl ring (left) and structure derived from crystal data (right).^{S3}



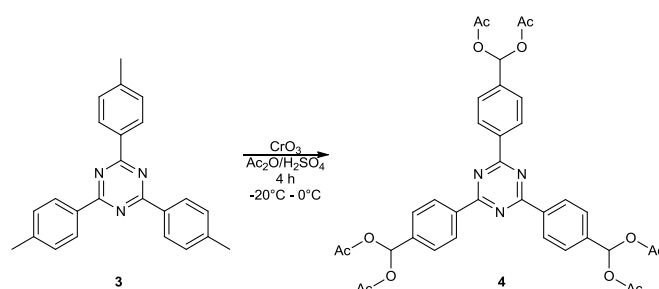
Scheme 3.S1. Synthesis of 1,3,5-*tris*-(4-formyl-phenyl)triazine (TFPT) (**1**) by a three-step modified literature procedure.^{S2}



Scheme 3.S2. Synthesis of 1,3,5-*tris*-(4-methyl-phenyl)triazine (**3**) by super-acid catalyzed trimerization of *p*-tolunitrile (**2**) according to a literature procedure.^{S2}

1,3,5-*tris*-(4-methyl-phenyl)triazine (**3**)

p-**(2)** (98%, Sigma Aldrich) was liquefied by putting the storage vessel in a 60 °C drying oven for 30 min. To a 25 ml round-bottom Schlenk flask with stir bar 5.0 ml (8.24 g, 53.8 mmol, 2.15 eq.) of triflic acid (AlfaAesar, 98%) were added and cooled to -20 °C in a dewar with salt/ice bath (1:3 v/v) under stirring. By syringe 3.1 mL (2.99 g, 25.0 mmol, 1.0 eq.) of **2** were added dropwise with help of a syringe pump over 1 h. The solution turned into a slurry solid over time and was left for 24 h. The cake was scratched off and transferred in ice water under stirring. This solution was neutralized with 4-5 mL 25% ammonia. The off-white precipitate was filtered off, washed with acetone (3 x 5 mL) and dried in vacuum to yield the title compound **3** (2.56 g, 7.29 mmol, 88%). ¹³C and ¹H NMR data were consistent with the literature.



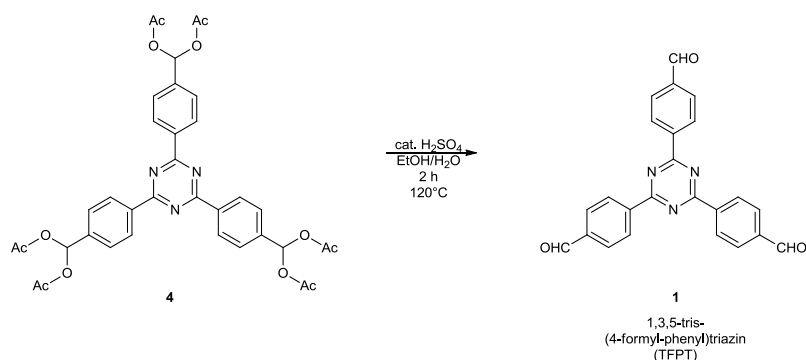
Scheme 3.S3. Synthesis of [4,4',4''-(1,3,5-triazine-2,4,6-triyl)tris(4,1-phenylene)]-tris(methanetriyl)hexaacetate (**4**) by threefold benzylic oxidation of **3** by CrO₃ based on a modified literature procedure.^{S2}

[4,4',4''-(1,3,5-Triazine-2,4,6-triyl)tris(4,1-phenylene)]-tris(methanetriyl)hexaacetate (**4**)

To a 25 ml round-bottom flask with stir bar and rubber septum 100 mg (0.285 mmol, 1.0 eq.) of **3** and 1.00 mL of acetic anhydride were added and cooled down to -20 °C in a salt/ice bath. After addition of 0.2 ml 98% sulfuric acid, to the yellowish solution was added dropwise by syringe a solution of chromium(VI)oxide (250 mg, 92.6 mmol, 325 eq.) in 1.25 mL acetic anhydride over a period of 3.5 h under stirring. The temperature was kept below 0 °C. The greenish solution was stirred for another hour and then added dropwise to 12.5 mL stirred ice water. The yellowish precipitate was filtered off, washed with dest. water (3 x 3 mL) until neutral and dried in vacuum. The

subsequent further purification by column chromatography (50:1 DCM/EtOAc) on silica gel yielded the title compound **4** (75 mg, 0.107 mmol, 38%).

^{13}C and ^1H NMR data were consistent with the literature.

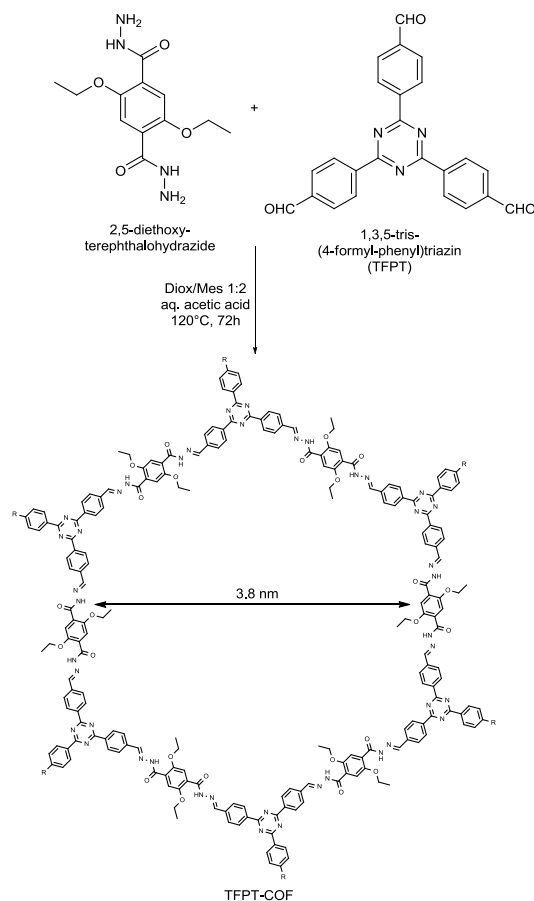


Scheme 3.S4. Synthesis of 1,3,5-*tris*-(4-formyl-phenyl)triazine (TFPT) (**1**) by a microwave-assisted acid catalyzed deprotection based on a modified literature procedure.^{S2}

1,3,5-*tris*-(4-formyl-phenyl)triazine (TFPT) (**1**)

To a stirred suspension of compound **4** (460 mg, 0.66 mmol, 1.0 eq) in 5.25 mL of dest. water and 4.20 mL of ethanol in a Biotage® 20 mL microwave vial was added 98% sulfuric acid (0.53 mL, 14.7 eq.). The vial was sealed and the resulting mixture was heated under microwave irradiation to 120°C under stirring for 3 h. The resulting off-white precipitate was filtered, washed with water and dried under vacuum to yield title compound **1** (230 mg, 0.59 mmol, 89%).

^1H NMR data were consistent with the literature.



Scheme 3.S5. Synthesis of TFPT-COF by acid catalyzed hydrazone formation.

TFPT-COF

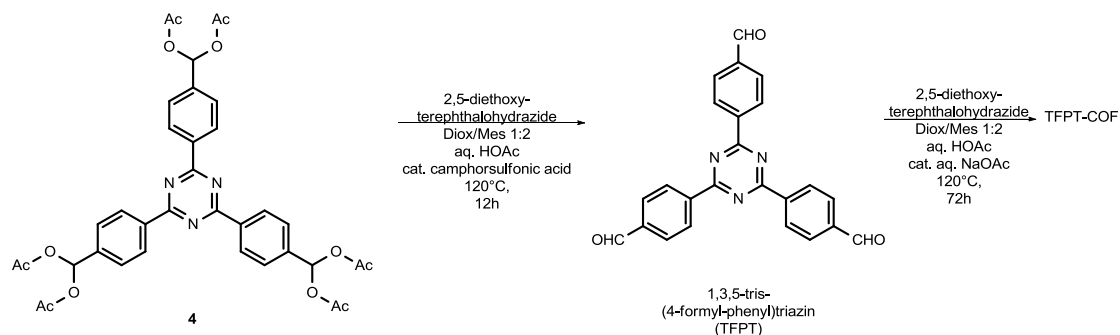
To a Biotage® 5 mL microwave vial 17.7 mg (0.044 mmol, 2.0 eq.) of TFPT (**1**) and a stir bar was added. Then 18.6 mg (0.066 mmol, 3.0 eq.) of 2,5-diethoxy-terephthalohydrazide was added and the vial was temporarily sealed with a rubber septum. Subsequently, the vial was flushed three times in argon/vacuum cycles. To the mixture 0.66 mL of mesitylene and 0.33 mL of 1,4-dioxane were added and again degassed three times in argon/vacuum cycles. In one shot 100 μ L aqueous 6M acetic acid was added, the vial was sealed and heated in a stirred oil bath with 120 °C (preheated) on a heating stirrer for 72 h. After slow cooling to room temperature the vial was opened and the whole mixture was centrifuged (3 x 15 min, 20000 rpm) while being washed with DMF (1 x 7 mL) and THF (2 x 7 mL). The resulting yellow precipitate was transferred to a storage vial with DCM, dried at room temperature, then in vacuum and characterized by powder x-ray diffraction.

Alternative workup: The vial was opened and the slurry suspension was transferred by a polyethylene pipette to a Büchner funnel and filtered. The filter cake was scratched off and transferred to an Erlenmeyer flask, washed with DMF (1 x 10 mL) and THF (2 x 10 mL) and again filtered off.

IR (FT, ATR): 3277 (w), 2966 (w), 2888 (w), 1674 (s), 1567 (m), 1515 (s), 1415 (m), 1356 (s), 1203 (vs), 1145 (m), 806 (s) cm^{-1} .

For elemental analysis the COF was wrapped in filter paper and then washed with THF in a microwave oven with THF (100 °C, 3 x 20 mL). Then the COF was activated in high-vacuum for 12 h at 120 °C at 10⁻⁷ mbar and kept under an inert atmosphere until elemental analysis was performed.

Anal. Calcd. for (C₈₄H₇₄N₁₈O₁₂)_n: C, 66.04; H, 4.88; N, 16.50. Found: C, 64.17; H, 4.96; N, 15.48.



Scheme 3.S6. Synthesis of TFPT-COF by acid catalyzed in situ deprotection and subsequent hydrazone formation, carried out in one reaction vessel.

TFPT-COF from protected TFPT ([4,4',4''-(1,3,5-Triazine-2,4,6-triyl)tris(4,1-phenylene)]-tris(methanetriyl)hexaacetate (4))

To a Biotage® 5 mL microwave vial 30.8 mg (0.044 mmol, 2.0 eq.) of **4** and a stir bar was added. Then 18.6 mg (0.066 mmol, 3.0 eq.) of 2,5-diethoxy-terephthalohydrazide was added and the vial was temporarily sealed with a rubber septum. Subsequently, the vial was flushed three times in argon/vacuum cycles. To the mixture 0.66 mL of mesitylene and 0.23 mL of 1,4-dioxane were added and again degassed three times in argon/vacuum cycles. In one shot 100 μL aqueous 6M acetic acid was added. To this vial, 0.10 mL ($c = 20 \text{ mg mL}^{-1}$, 0.008 mmol, 0.38 eq.) of a solution of *rac*-camphorsulfonic acid in 1,4-dioxane was added, the vial was sealed and heated in a stirred oil bath with 120 °C (preheated) on a heating stirrer for 12 h. After cooling to room temperature, to the vial was added 0.02 mL ($c = 35 \text{ mg mL}^{-1}$, 0.008 mmol, 0.38 eq.) of an aqueous solution of sodium acetate by a micro syringe. The vial was then reheated again on the preheated oil bath for 72 h at 120 °C. After slow cooling to room temperature the vial was opened and the whole mixture was centrifuged (3 x 15 min, 20000 rpm) while being washed with DMF (1 x 7 mL) and THF (2 x 7 mL). The resulting yellow precipitate was transferred to a storage vial with DCM, dried at room temperature, then in vacuum and characterized by powder x-ray diffraction.

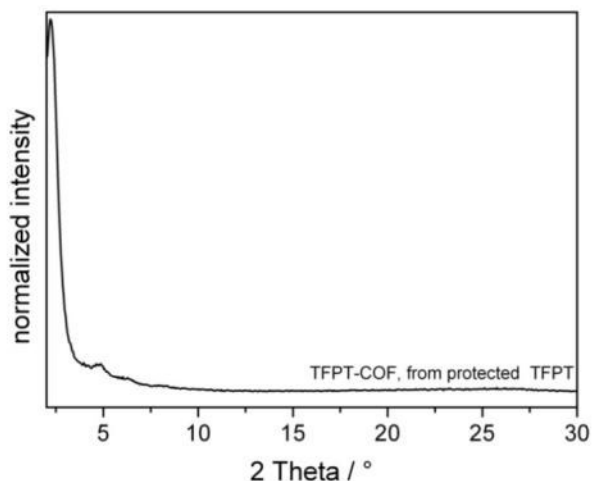


Figure 3.S2. PXRD of the TFPT-COF from protected TFPT.

TFPT-COF reconverted after sonication in water/photocatalysis

To a Biotage® 5 mL microwave vial 20 mg of amorphous TFPT-COF and a stir bar were added. The vial was temporarily sealed with a rubber septum. Subsequently, the vial was flushed three times in argon/vacuum cycles. To the mixture 0.66 mL of mesitylene and 0.33 mL of 1,4-dioxane were added and again degassed three times in argon/vacuum cycles. In one shot 100 μ L aqueous 6M acetic acid was added. The vial was sealed and heated in a stirred oil bath with 120 °C (preheated) on a heating stirrer for 72 h. After slow cooling to room temperature the vial was opened and the whole mixture was centrifuged (3 x 15 min, 20000 rpm) while being washed with DMF (1 x 7 mL) and THF (2 x 7 mL). The resulting yellow precipitate was transferred to a storage vial with DCM, dried at room temperature, then in vacuum and characterized by powder x-ray diffraction and BET surface area determination.

FT-IR Spectra

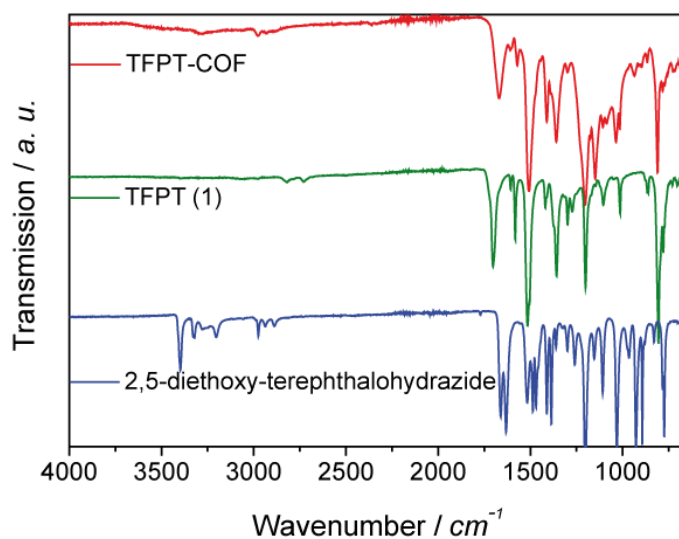


Figure 3.S3. Stack plot FT-IR spectra of TFPT-COF and starting materials.

Table 3.S1. IR assignments for TFPT (green), DETH (blue) and TFPT-COF (red).

Wavenumber [cm^{-1}]	Band Assignment
2824, 2721	Fermi double peak, aldehyde C-H (specific)
>3200	N-H stretching
1700	Aldehyde C=O stretching
1632, 1660, 1670-1660, 1201	C=O stretching, C=N
806, 806	triazine ring breath

CP-MAS NMR Measurements

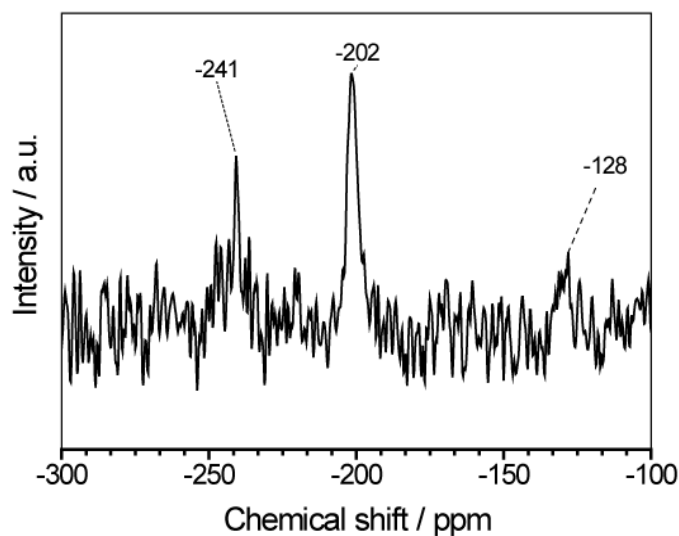


Figure 3.S4. ^{15}N CP-MAS spectrum of TFTP-COF.

The ^{15}N CP-MAS NMR spectrum exhibits a peak at -241 ppm, which we assign to the tertiary nitrogen of the hydrazone moiety, the peak at -202 ppm to the hydrazine secondary nitrogen, and the peak at -128 ppm to the nitrogen of the triazine ring.

Powder X-Ray Diffraction Data and Structure Simulation

Molecular modeling of the COF was carried out using the *Materials Studio* (5.5) suite of programs by *Accelrys*.

The unit cell was defined by two TFPT molecules bonded via six hydrazone linkages to 2,5-diethoxy-terephthalohydrazide. The initial structure was geometry optimized using the MS Forcite molecular dynamics module (Universal force fields, Ewald summations), and the resultant distance between opposite formyl carbon atoms in the structure was used as the *a* and *b* lattice parameters (initially 43 Å) of the hexagonal unit cell with *P6/m* symmetry (*bnn* net). The interlayer spacing *c* was chosen as 3.37 Å according to the 001 stacking reflection of the powder at $2\theta = 26.6^\circ$, and the crystal structure was geometry optimized using Forcite (resulting in $a = b = 43.164$ Å).

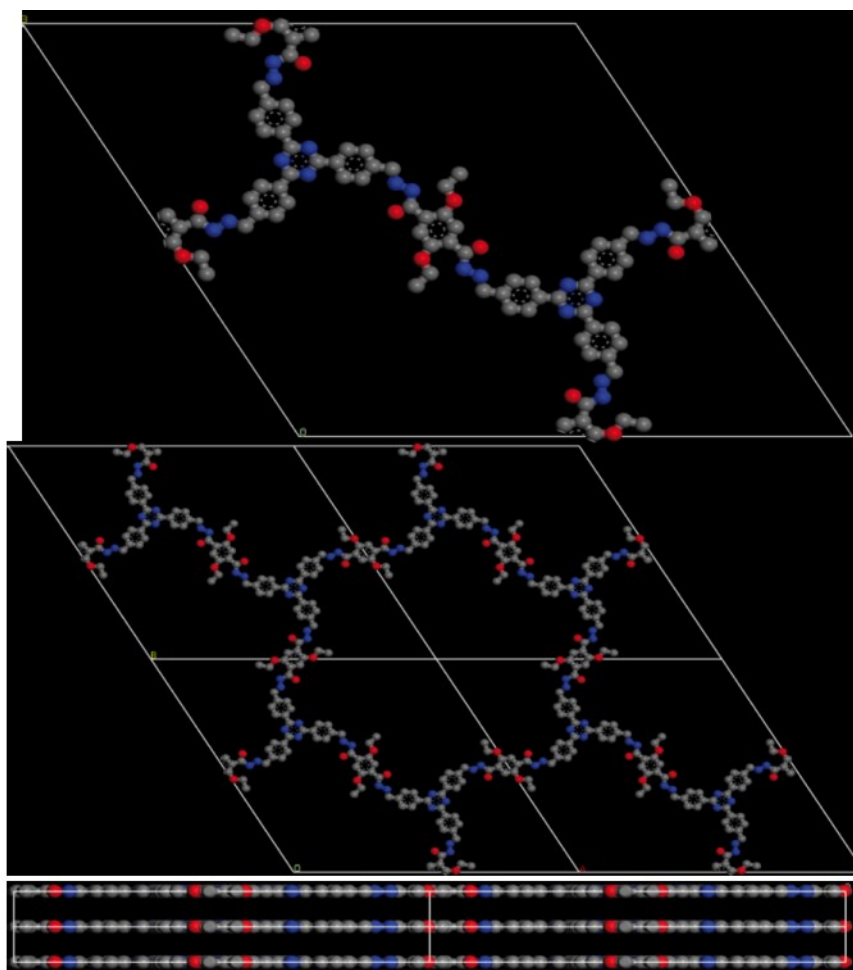


Figure 3.S5. Simulation of the unit cell content calculated in an eclipsed arrangement: top view onto the ab -plane and view perpendicular to the c -axis.

The MS Reflex Plus module was then used to calculate the PXRD pattern, which matched the experimentally observed pattern closely in both the positions and intensity of the reflections. The observed diffraction pattern was subjected to Pawley refinement wherein reflection profile and line shape parameters were refined using the crystallite size broadening (one size was extracted from the exp. PXRD with the help of the Scherrer equation \rightarrow crystal size: $c = 35$ nm, kept fixed) and background in the 20th polynomial order.

The refinement was applied to the calculated lattice, producing the refined PXRD profile with lattice parameters $a = b = 41.895$ Å and $c = 3.37$ Å. wRp and Rp values converged to 3.30% and 6.73%, respectively. The resulting refined crystallite size (149 nm in each lateral direction) is in reasonable agreement with the SEM and TEM data. Overlay of the observed and refined profiles shows good correlation (Figure 3.S6).

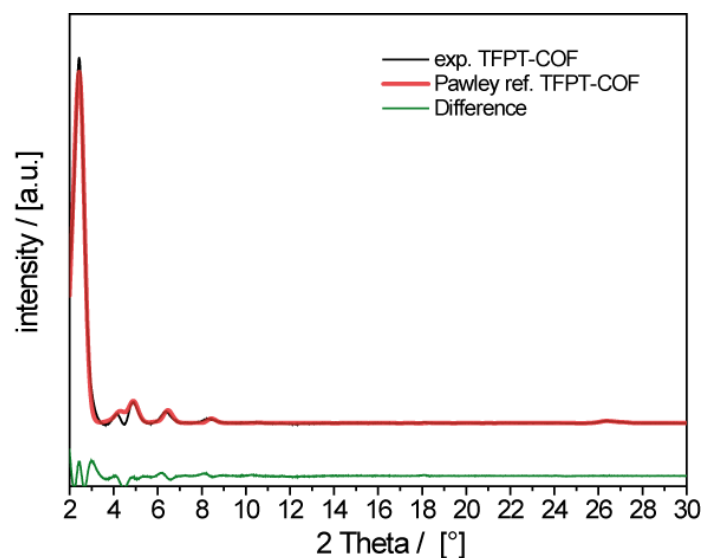


Figure 3.S6. Experimental powder pattern and Pawley refined pattern based on $P6/m$ symmetry.

Table 3.S2. Atom coordinates of optimized $P6/m$ structure.

Atomic parameters					
Atom	Ox.	Wyck.	x/a	y/b	z/c
C1		6j	4.46484	0.49326	0
C2		6j	4.46961	0.46288	0
C3		6j	4.50666	0.46983	0
C7		6j	4.47874	0.55594	0
O8		6j	4.56434	0.57050	0
C10		6j	4.43337	0.39480	0
C11		6j	4.39330	0.36475	0
O14		6j	4.44518	0.54253	0
N15		6j	4.50051	0.59501	0
N19		6j	4.52013	0.38747	0
C21		6j	4.49094	0.64722	0
C23		6j	4.53965	0.34528	0

C25	6j	4.46512	0.69023	0
C26	6j	4.43386	0.69438	0
C27	6j	4.39837	0.66301	0
C28	6j	4.39415	0.62805	0
C29	6j	4.42460	0.62405	0
C30	6j	4.36484	0.66515	0
N31	6j	4.36636	0.69806	0

Even lower wRp and Rp values (1.94% and 3.94%) could be achieved by lowering the symmetry to $P1$ (Figure 3.S7) but keeping the angles α , β and $\gamma = 90^\circ$, 90° and 120° . The resulting lattice parameters a and b were = 42.055 Å and 45.074 Å.

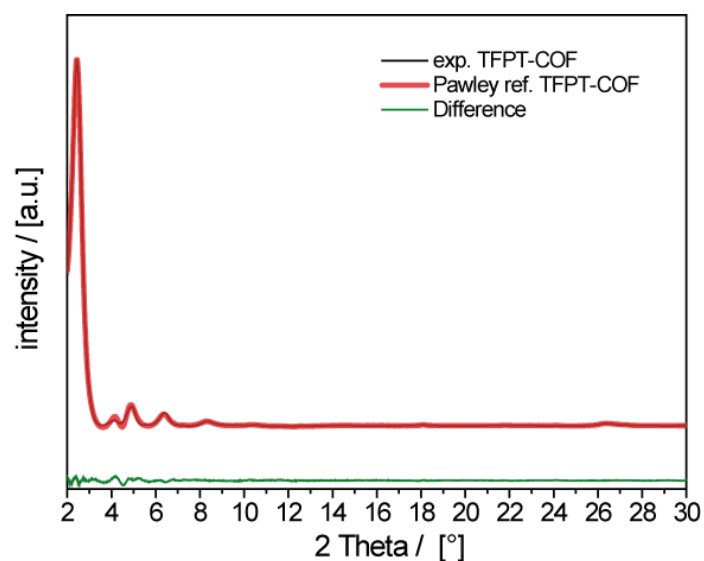


Figure 3.S7. Experimental powder pattern and Pawley refined pattern based on $P1$ symmetry.

An alternative staggered COF arrangement was examined wherein $P63/m$ symmetry was used (*gra* net). Comparison of the calculated PXRD pattern with the observed pattern shows less agreement with the experimental data (see Fig. 3.2), thus ruling out this type of packing arrangement.

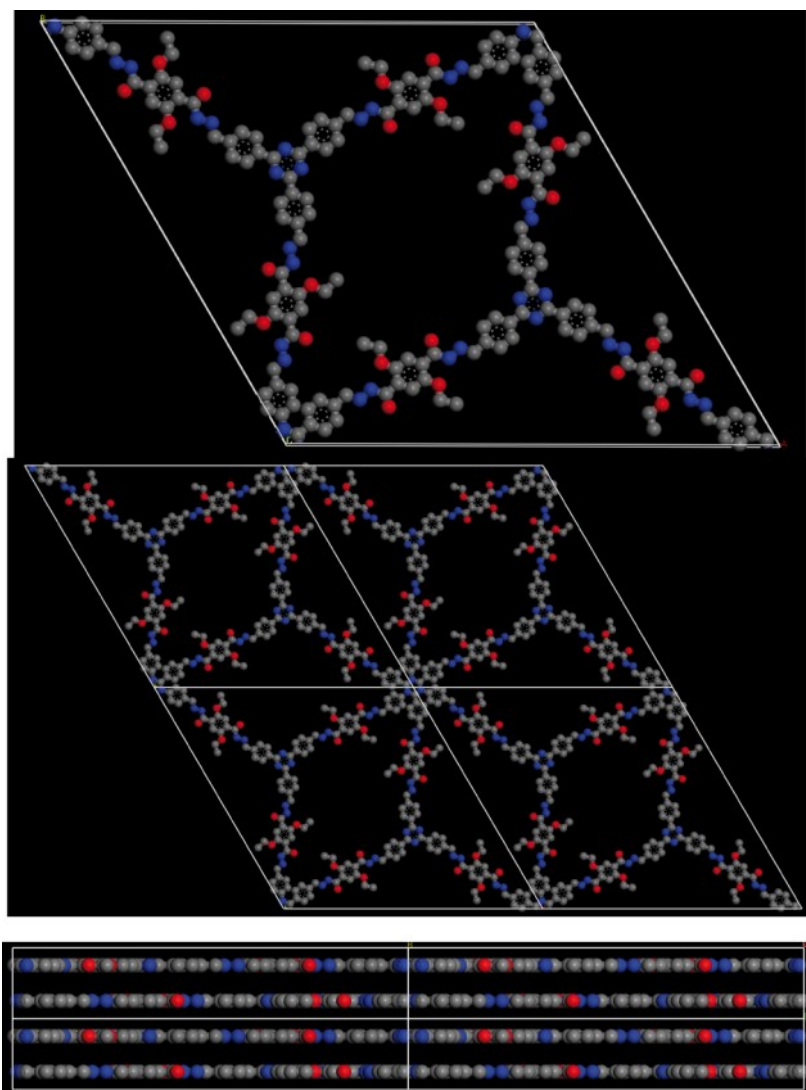


Figure 3.S8. Simulation of the crystal structure with staggered arrangement of adjacent layers: Top view onto the *ab*-plane and view perpendicular to the *c*-axis showing the doubled stacking period due to the staggered AB layer arrangement.

In a recent theoretical study on boronate COFs, Dichtel *et al.* (ref. 42) and Heine (ref. 41) pointed out that two adjacent layers in a COF are not expected to be aligned in a perfectly eclipsed manner, but shifted between $\approx 1.3 - 1.8 \text{ \AA}$ in any direction parallel to the layer (parallel displacement).

We therefore simulated (using the software package *Materials Studio*) an AA'A-structure of TFPT-COF where adjacent layers are offset by 1.4 \AA , such that each partly positively charged carbon atom of triazine is situated beneath a partly negatively charged triazine nitrogen atom, which was found to be a likely structure for triazine units. The structure was simulated in *P1* symmetry with lattice parameters $a = b = 42.16 \text{ \AA}$ and $c = 6.74 \text{ \AA}$ (*c* axis doubled due to symmetry reasons).

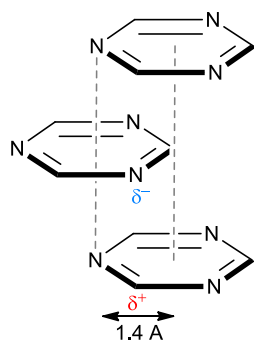


Figure 3.S9. Shift (parallel displacement) in a zig-zag manner to minimize electrostatic repulsion between adjacent layers.

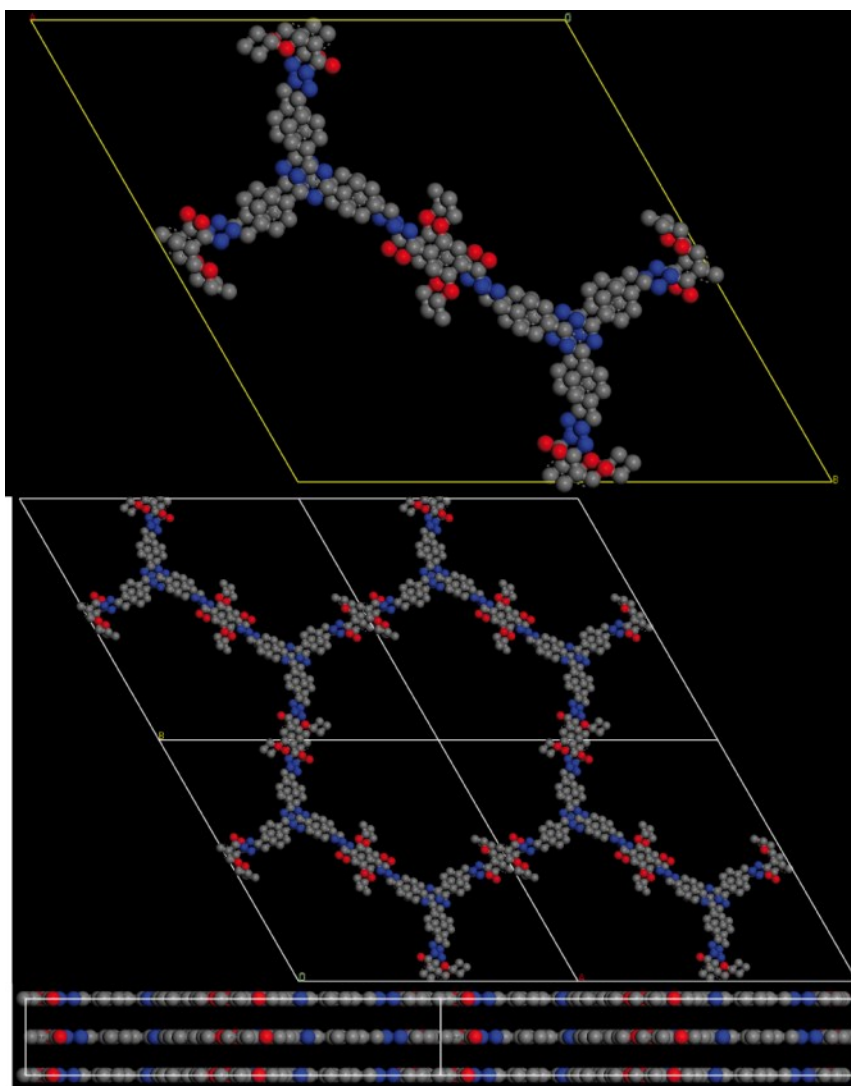


Figure 3.S10. Simulation of the unit cell content calculated in an eclipsed arrangement with 1.4 Å offset and zig-zag-arrangement of the layers: View onto the *ab*-plane (top) and view perpendicular to the *c*-axis (bottom).

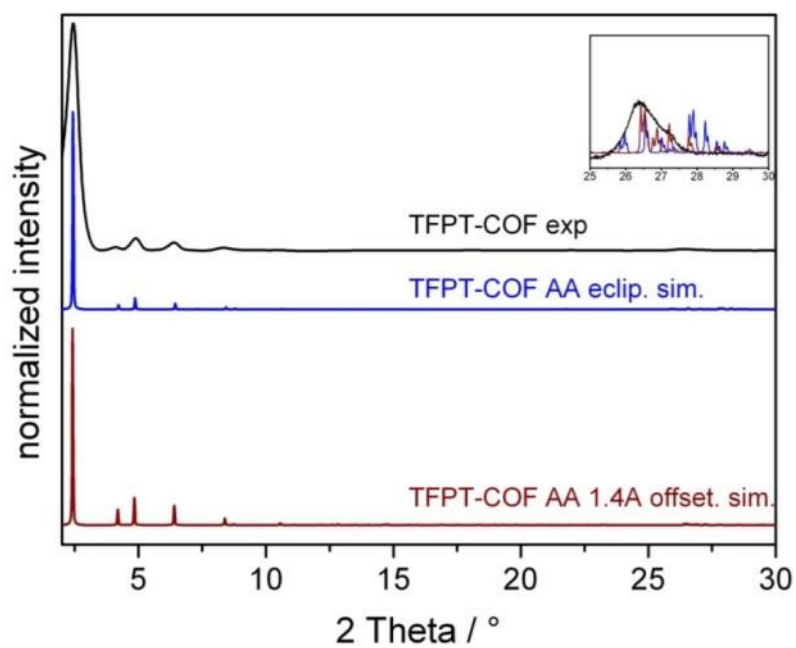


Figure 3.S11. Experimental powder pattern (black), simulated PXRD of perfectly eclipsed TFPT-COF (blue) and simulated PXRD of TFPT-COF with 1.4 Å parallel layer displacement (red).

Sorption Measurements and Pore Size Distribution

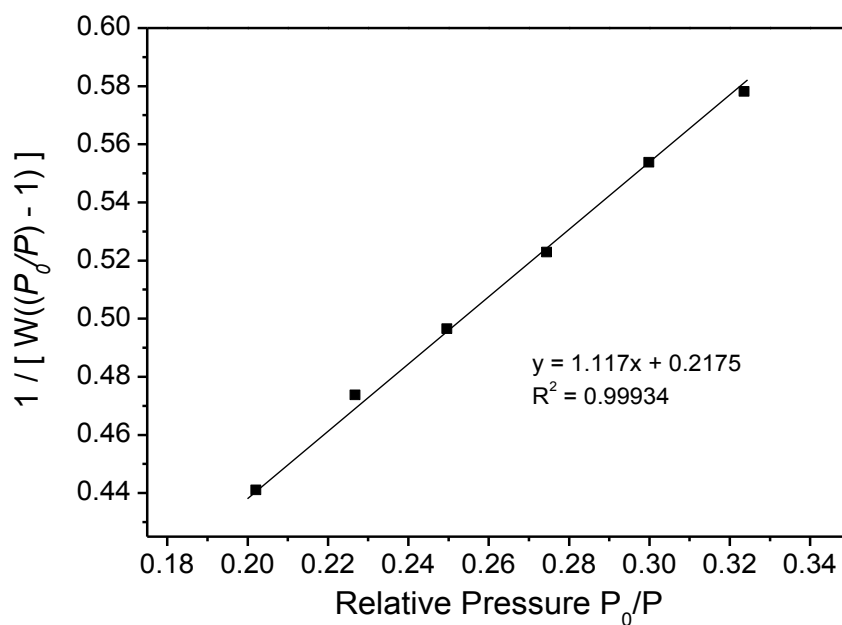


Figure 3.S12. Linear BET plot of TFPT-COF as obtained from Ar adsorption data at 87 K.

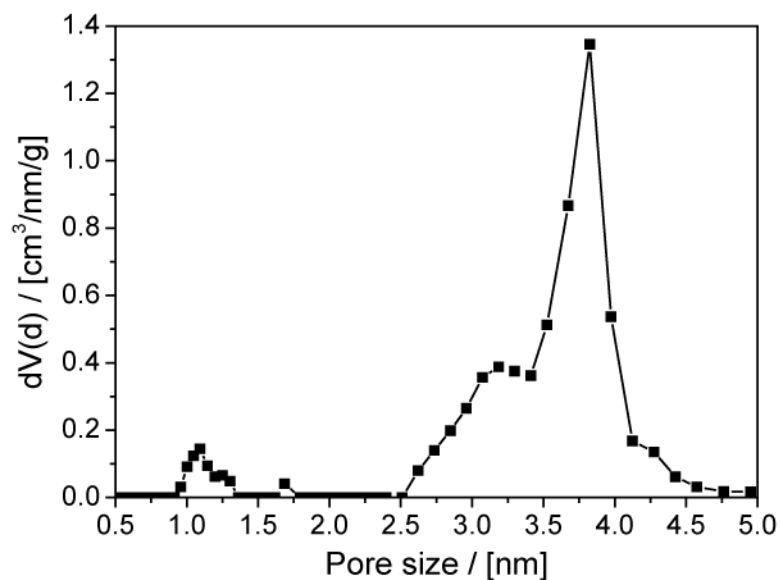


Figure 3.S13. Pore size distribution calculated based on NLDFT using the “Ar-zeolite/silica cylindrical pores at 87 K kernel.

The Brunauer-Emmett-Teller (BET) surface area was calculated to be $1603 \text{ m}^2 \text{ g}^{-1}$ (linear extrapolation between 0.20-0.32 p/p_0).

Plot of the Kubelka-Munk Function

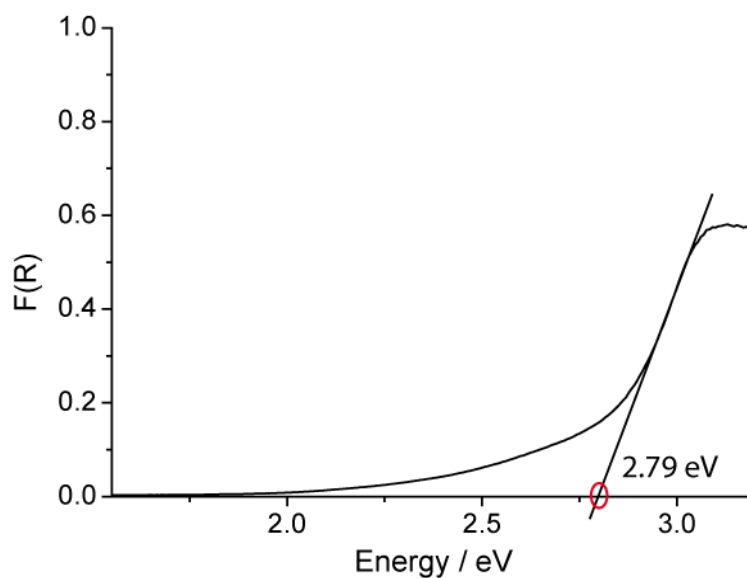


Figure 3.S14. Plot of Kubelka-Munk function used for band gap extraction.

Stability of TFPT-COF in Organic Solvents and Water

Stability in different organic solvents (DCM, DMF and MeOH) has been tested by soaking TFPT-COF (5 mg) in the corresponding solvent for 3 h at room temperature. A PXRD was recorded after filtration and drying in vacuum overnight.

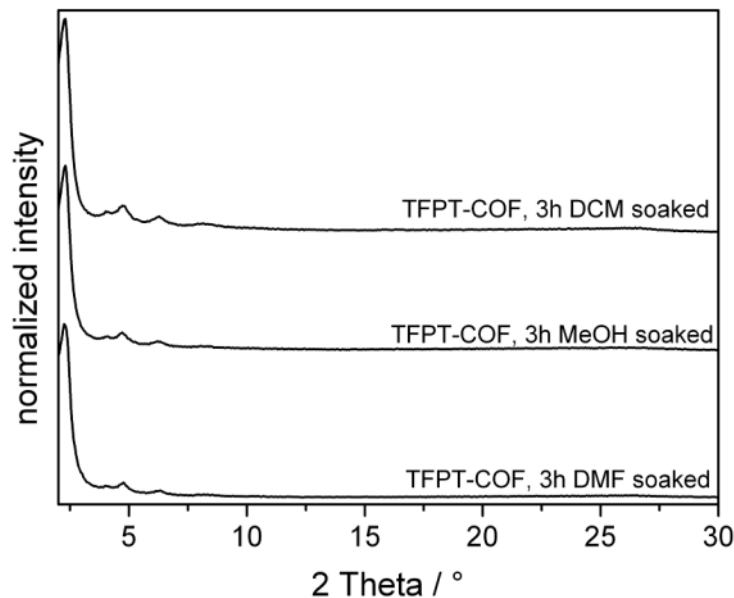


Figure 3.S15. PXRD measurements showing the retention of crystallinity after treatment with different solvents.

Reconversion of TFPT-COF after photocatalysis

20 mg of crystalline TFPT-COF (BET surface area = $1190 \text{ m}^2\text{g}^{-1}$) was used for photocatalytic hydrogen production as described below. After irradiation with visible light for 95 h the TFPT-COF/Pt was filtered off as a green and amorphous solid (Fig. 3.S21) and washed with water, DMF (2 x 7 mL) and THF (2 x 7 mL). The organic filtrates were checked for any formed monomers (e.g. TFPT or DETH), but no traces of monomeric species were detected. The TFPT-COF/Pt has lost its crystallinity after photocatalysis as shown in Fig. 3.S16, and has a BET surface area of $410 \text{ m}^2\text{g}^{-1}$ (Fig. 3.S18). The vacuum-dried powder can be reconverted (see “Synthetic Procedures”) to recover crystalline TFPT-COF with its original PXRD pattern (Fig 3.S16) and a high BET surface area of $1184 \text{ m}^2\text{g}^{-1}$ (Fig. 3.S18) (yield: 14 mg, 70%) by resubjecting it to the initial synthesis conditions. An Ar sorption isotherm of TFPT-COF/Pt_{reconv.} was recorded and is shown in Fig. 3.S19. The corresponding pore size distribution is depicted in Fig. 3.S20, having a maximum at 3.7 nm. Further experiments revealed that the TFPT-COF has already lost its long-range order after sonication in water (Fig. 3.S16). However, the FTIR spectrum shows the characteristic bands of the polymer (C=N at 1603 cm^{-2}), while no additional peaks appear and no bands corresponding to the TFPT or DETH monomers are observed (Fig. 3.S17). The vacuum-dried powder can also be reconverted (see section B) to recover TFPT-COF with its original PXRD pattern (Fig 3.S16).

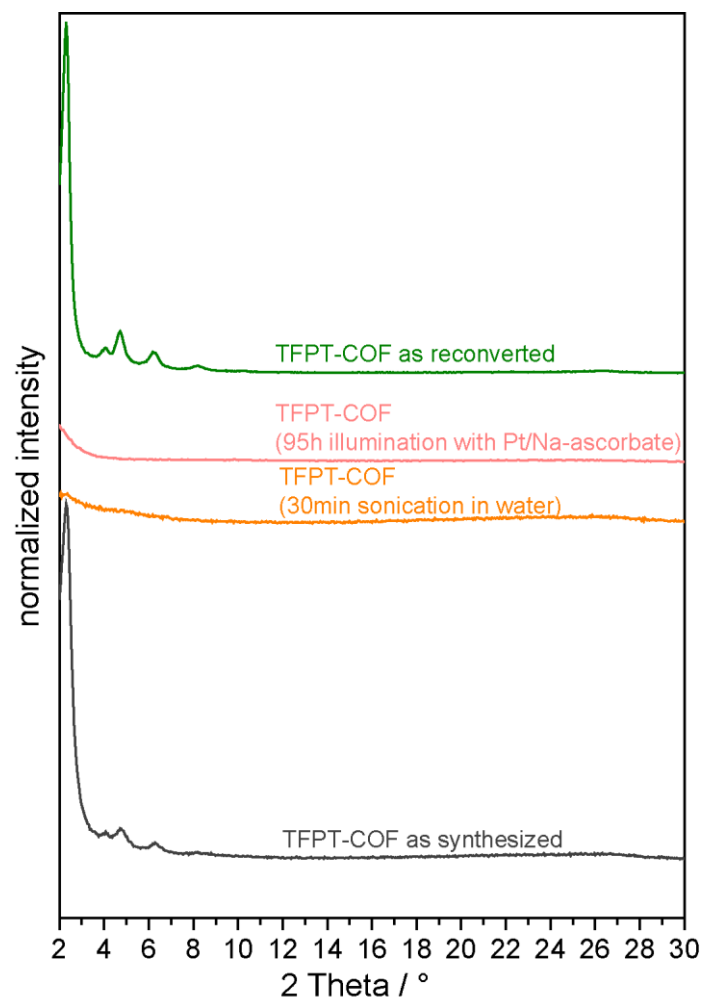


Figure 3.S16. PXRD patterns of TFPT-COF, showing loss of crystallinity after water exposure and photocatalysis. The crystalline TFPT-COF can be obtained by reversion by subjecting it to the initial crystallization conditions.

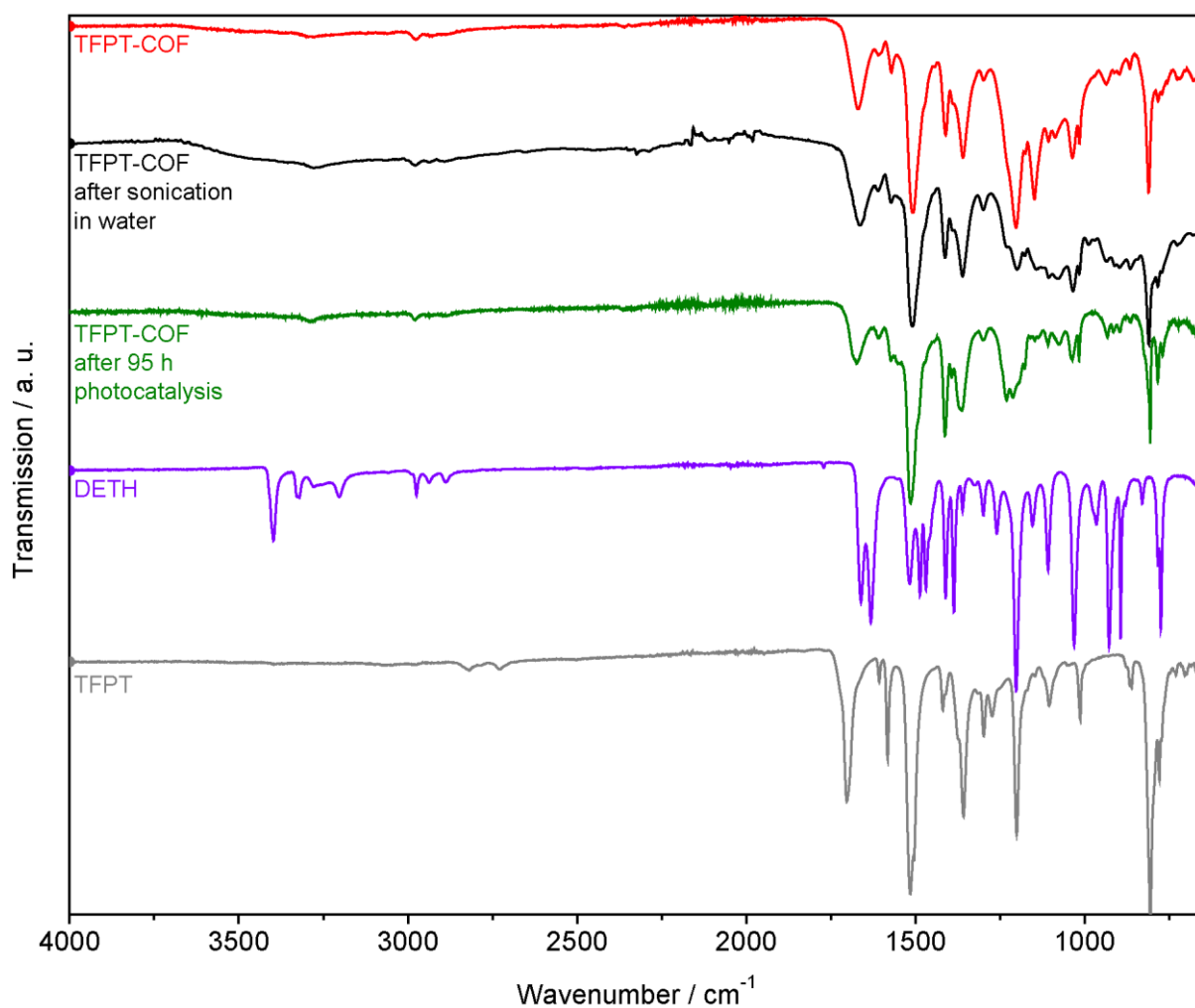


Figure 3.S17. FT-IR spectra showing the vibrational patterns of TFPT-COF before and after water exposure/photocatalysis.

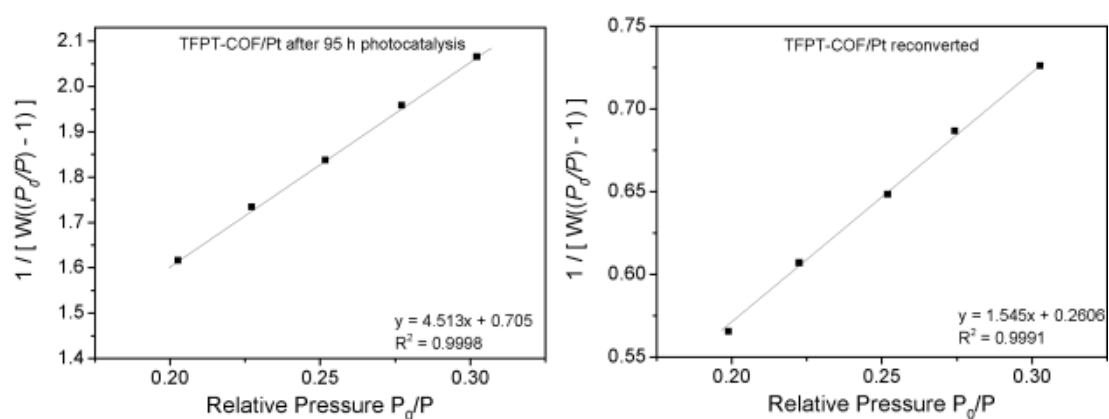


Figure 3.S18. Linear BET plot of TFPT-COF/Pt after 95 h photocatalysis and TFPT-COF/Pt (reconverted) as obtained from Ar adsorption data at 87 K.

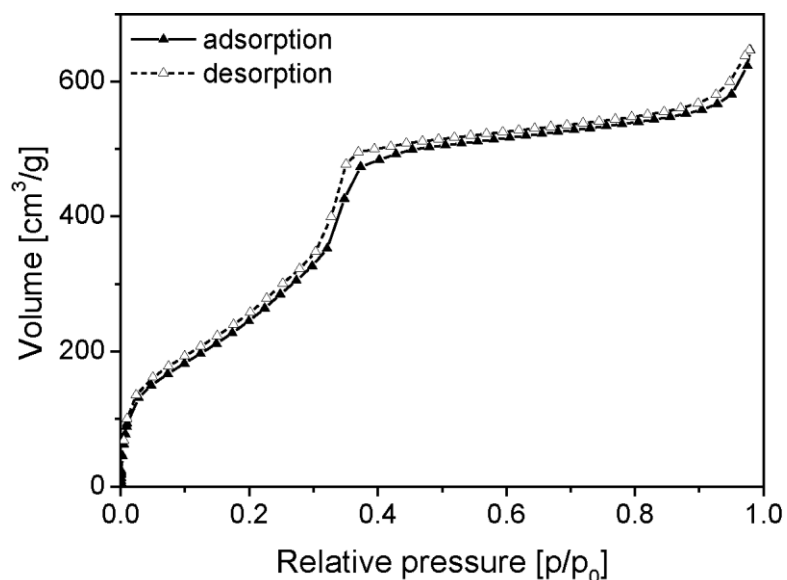


Figure 3.S19. Ar sorption isotherm recorded at 87 K.

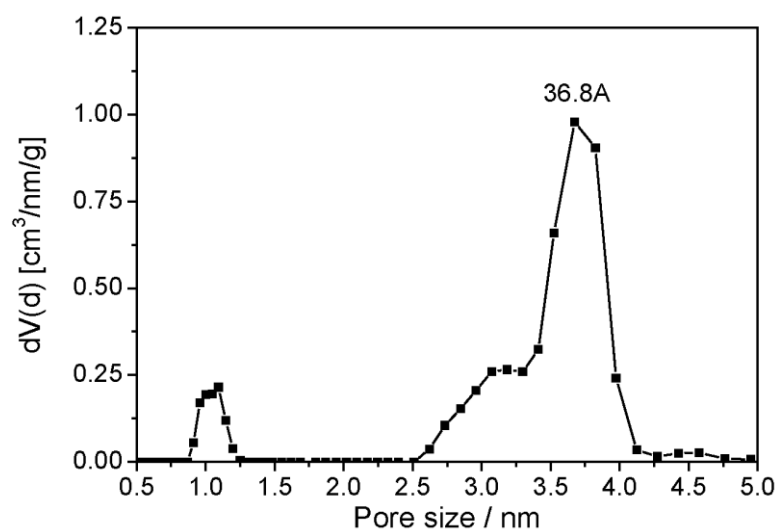


Figure 3.S20. Pore size distribution of TFPT/Pt after reconversion calculated based on NLDFT using the “Ar-zeolite/silica cylindrical pores at 87 K” kernel.



Figure 3.S21. Photographs showing TFPT-COF as-synthesized (left, yellow) and TFPT-COF/Pt after reconversion (right, green).

TFPT-COF/Pt before reconversion is green, as well.

Photocatalysis

For long-time hydrogen evolution experiments in triethanolamine, the TFPT-COF catalyst (4 mg) was suspended in water (9 mL) and dispersed in an ultrasonic bath for 30 min. The sacrificial electron donor (1 mL) triethanolamine (TEoA, Alfa Aesar) and H_2PtCl_6 (2.4 μL of 8 wt% in H_2O , Sigma-Aldrich, ≈ 2.2 wt% Pt) as precursor for the in situ formation of the Pt cocatalyst was added. For long-time hydrogen evolution experiments in sodium ascorbate, the TFPT-COF catalyst (10 mg) was suspended in water (10 mL) and dispersed in an ultrasonic bath for 30 min. Sodium ascorbate as sacrificial electron donor (100 mg) (Sigma-Aldrich, $\geq 98\%$) and H_2PtCl_6 (6.0 μL of 8 wt% in H_2O , Sigma-Aldrich, ≈ 2.2 wt% Pt) was added. The first cycle represents the first three hours of the long-term measurement – the induction time period – where Pt nanoparticles are formed by the photoreduction of H_2PtCl_6 . For each cycle the photocatalyst (Pt-doped COF) was separated from its suspension (for the photocatalytic measurements) by centrifugation and was washed several times with water. The dried photocatalyst was redispersed with a fresh sodium ascorbate solution (10 mL of water and 100 mg of sodium ascorbate) and illuminated for 3 hours (< 420 nm) for each cycle.

For visible light and UV experiments the suspensions were illuminated at a distance of 26 cm from the light source in a 230 mL quartz glass reactor with a PTFE septum under argon atmosphere. The flask was evacuated and purged with argon to remove any dissolved gases in the solution. Samples were simultaneously top-illuminated (top surface = 15.5 cm^2) with a 300 W Xenon lamp with a water filter and dichroic mirror blocking wavelengths < 420 nm for visible light measurements while stirring. For wavelength-specific measurements, the full spectrum of the Xenon lamp coupled with a band-pass filter (400, 450, 500, 550 or 600 nm; bandwidth ± 20 nm) and an 1.5 AM filter was used. Here, an aqueous triethanolamine suspension with 10 mg of Pt-doped catalyst was illuminated for three hours and the concentration of evolved hydrogen was determined by gas chromatography. The intensity of the light was measured for each wavelength, enabling the conversion of produced hydrogen values into quantum efficiencies. For oxygen evolution measurements photodeposition of IrO_2 nanoparticles as oxygen-evolving cocatalyst was carried out before the photocatalytic reaction following a literature procedure.^{S4,5} To this end, 40 mg of the catalyst was dispersed in a reactant solution containing $\text{K}_2[\text{IrCl}_6]$ (1.8 mg, ≈ 2 wt%, Alfa Aesar) and 40 mL of a 5 mM aqueous KNO_3 solution. The suspension was irradiated as described above for 2 h using the full spectrum of the Xenon lamp. The TFPT-COF catalyst loaded with the cocatalyst was isolated from the aqueous KNO_3 solution, washed several times with water, and then dried at 100 $^\circ\text{C}$ in a stream of argon. The IrO_2 -loaded catalyst (10 mg) was dispersed in phosphate buffer solution (10 mL, 0.1 M, pH = 11 or pH = 7). $\text{Na}_2\text{S}_2\text{O}_8$ (110 mg, Sigma-Aldrich) or AgNO_3 (16 mg) was added as electron acceptor. The headspace of the reactor was periodically sampled with an online injection system and the gas components were quantified by gas chromatography (thermal conductivity detector, argon as carrier gas).

The quantum efficiency of the photocatalysts, under irradiation with the band-pass filter 500 ± 20 nm, was determined as follows. The power of the incident light was measured with a thermo power sensor (Thorlabs) to be 14 mW cm^{-2} , which is equivalent to a photon flux of $701 \mu\text{mol h}^{-1}$. Quantum efficiency was calculated using the equation:

$$\text{QE} = 2 \cdot [\text{H}_2] / I$$

where I is the photon flux in $\mu\text{mol h}^{-1}$ and $[\text{H}_2]$ is the average rate of H_2 evolution in $\mu\text{mol h}^{-1}$.

Stability of TFPT-COF during photocatalysis

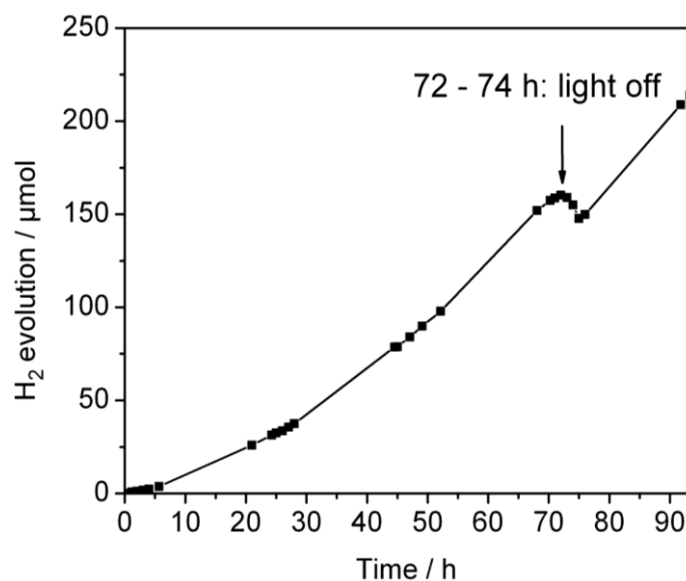


Figure 3.S22. Stability measurements of TFPT-COF for 95 h with ascorbate as sacrificial donor. Between the 72th and 74th hour the light source was turned off to show no hydrogen evolution in the dark (the amount of hydrogen concentration decreased during these hours due to the fact that sampling was performed, i.e. removing sample volume during detection).

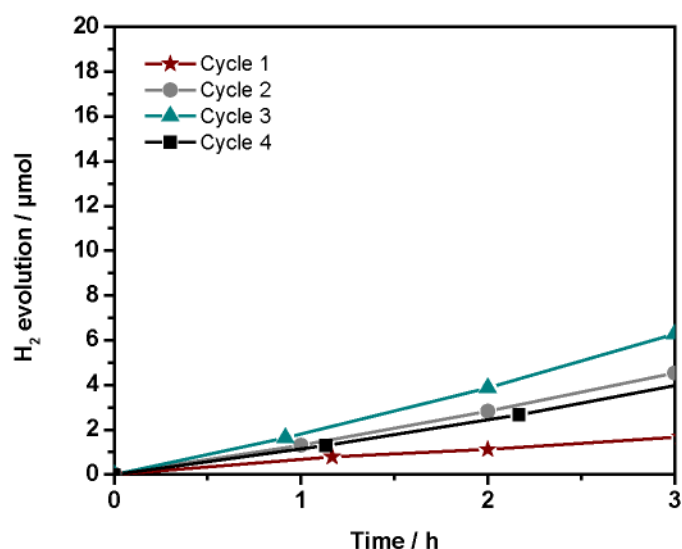


Figure 3.S23. Cycle measurements of TFPT-COF/Pt with sodium ascorbate as sacrificial donor. The first cycle (Cycle 1) corresponds to the first three hours of the long-term stability measurements (95 h) and shows decreased rates due to formation of Pt nanoparticles (induction period). The other cycles were carried out after centrifugation of the photocatalyst, washing with water and resuspending it in a fresh aqueous sodium ascorbate solution.

References

- S1 F. J. Uribe-Romo, C. J. Doonan, H. Furukawa, K. Oisaki, O. M. Yaghi, *J. Am. Chem. Soc.* **2011**, *133*, 11478–11481.
- S2 S.-H. Li, H.-P. Huang, P. Enis, S.-Y. Yu, X.-P. Li, *Chin. J. Chem.* **2006**, *24*, 1225–1229.
- S3 V. Volkis, E. Nelkenbaum, A. Lisovskii, G. Hasson, R. Semiat, M. Kapon, M. Botoshansky, Y. Eishen, M. S. Eisen, *J. Am. Chem. Soc.* **2003**, *125*, 2179–2194.
- S4 T. Ikeda, A. Tsuda, N. Aratani, A. Osuka, *Chem. Lett.* **2006**, *35*, 946–947.
- S5 E. M. Sabio, R. L. Chamousis, N. D. Browning, F. E. Osterloh, *J. Phys. Chem. C.* **2012**, *116*, 3161–3170.

3.2 A Tunable Azine Covalent Organic Framework Platform for Visible Light-Induced Hydrogen Generation

Vijay Vyas, Frederik Haase, Linus Stegbauer, Gökçen Savasci, Filip Podjaski, Christian Ochsenfeld, and Bettina V. Lotsch

published in *Nature Comm. 2015, Art. No. 8508*

DOI: 10.1038/ncomms9508

<http://www.nature.com/ncomms/2015/150930/ncomms9508/full/ncomms9508.html>

Reproduced with permission from Nature Publishing Group.

Abstract

Hydrogen evolution from photocatalytic reduction of water holds promise as a sustainable source of carbon-free energy. Covalent organic frameworks (COFs) present an interesting new class of photoactive materials, which combine three key features relevant to the photocatalytic process, namely crystallinity, porosity and tunability. Here we synthesize a series of water- and photostable 2D azine-linked COFs from hydrazine and triphenylarene aldehydes with varying number of nitrogen atoms. The electronic and steric variations in the precursors are transferred to the resulting frameworks, thus leading to a progressively enhanced light-induced hydrogen evolution with increasing nitrogen content in the frameworks. Our results demonstrate that by the rational design of COFs on a molecular level, it is possible to precisely adjust their structural and optoelectronic properties, thus resulting in enhanced photocatalytic activities. This is expected to spur further interest in these photofunctional frameworks where rational supramolecular engineering may lead to new material applications.

Author Contributions

V.S.V., F.H. and B.V.L. proposed the idea and designed the experiments. V.S.V. and B.V.L. wrote the manuscript. V.S.V. carried out the synthesis and photocatalysis experiments. F.H. helped in synthesis, photocatalysis and structure simulation of the COFs. L.S. performed the sorption experiments and discussed theoretical results. F.P. performed electrochemistry for determining the band potential of COFs. G.S. and C.O. performed the theoretical calculations. All authors discussed the results and commented on the manuscript.

3.3 Tunable Azine-based Covalent Organic Frameworks with Pyrene Chromophors for Visible-Light Photocatalytic Hydrogen Generation.

Linus Stegbauer, Sebastian Zech, Katharina Schwinghammer, Florian Ehrat, Gökçen Savasci, Christian Ochsenfeld, Jochen Feldmann, Bettina V. Lotsch

To be submitted

Abstract

We report on three isostructural azine-linked COFs based on pyrene building units, which vary in the number of nitrogen atoms in the peripheral aromatic units. The COFs show high surface areas up to $921 \text{ m}^2 \text{ g}^{-1}$ and are capable of photocatalytic hydrogen production from water with increasing efficiency, while decreasing the number of nitrogen atoms. Photoluminescence studies indicate a water-induced exfoliation and energy/photon transfer between the resulting nanosheets and the bulk COF.

3.3.1 Introduction

During the past ten years Covalent Organic Frameworks (COFs) have emerged as a new class of crystalline, porous 2D and 3D polymers, formed by reversible condensation reactions and featuring precisely tunable framework topologies with adjustable pore dimensions.¹ Through the flexible choice of lightweight building blocks and their high surface areas, COFs show potential for gas separation and storage, as catalysts and for sensing. The semiconducting properties inherent to most COFs make them interesting candidates for applications in optoelectronics where ordered charge percolation pathways are key,²⁻⁶ including photovoltaics^{7,8} and visible-light driven photocatalysis.⁹⁻¹¹ COFs based on pyrene building units show local photoconductivity,¹² and their fluorescent backbone has been used for chemosensing by means of analyte selective fluorescence quenching.¹³ In addition pyrene's extended pi system offers a unique basis for visible-light absorption as demonstrated by pyrene-derived dyes such as pyranine.¹⁴ COFs based on pyrene units have been synthesized with out-of-plane 4-formylphenyl or 4-aminophenyl substituents on the 1,3,6,8 positions;^{13,15,16} here, we present three completely planar pyrene-COFs which are modulated by peripheral heteroaromatic building units, for the first time. As suggested in our previous work, a planar COF backbone, resulting in an extended pi-system, favourable interlayer interactions through pi-pi-stacking and smaller band gaps, may play a key role in enhancing pho-

tocatalytic activity.¹¹ As a result, we propose to extend both the planarity and the pi-system¹⁰ by integrating alkyne moieties into the building blocks.

3.3.2 Results and Discussion

Starting from 1,3,6,8-tetrabromopyrene¹⁷ the corresponding tetraalkyne 1,3,6,8-tetraethynylpyrene can be synthesized in two steps.^{18,19} Subsequent fourfold Sonogashira coupling with either 4-bromobenzaldehyde or 6-bromonicotinaldehyde or 2-chloropyrimidine-5-carbaldehyde yields three new building blocks, namely 1,3,6,8-tetrakis(4-ethynylbenzaldehyde)-pyrene (**TEBPY**), 1,3,6,8-tetrakis(6-ethynylnicotinaldehyde)-pyrene (**TENPY**) and 1,3,6,8-tetrakis(2-ethynylpyrimidin-5-carb-aldehyde)pyrene (**TEPPY**) (see ESI for experimental details) as red powders, which are hardly soluble in common organic solvents. Their identity has been proven by means of solid-state NMR (ssNMR) and mass spectroscopy.

COF Synthesis and Characterization

These building blocks were designed so as to show an increasing nitrogen content in their peripheral aromatic units, entailing an increase in electron withdrawing character. In an acetic acid catalyzed polycondensation in different aromatic solvent mixtures with hydrazine hydrate (120 °C, 3 days, see ESI for details), either of the **TEXPY** (X = B(enzaldehyde), N(icotinaldehyde), P(yrimidine-5-carbaldehyde) monomers yielded an azine (A) connected COF: A-**TEBPY**-COF, A-**TENPY**-COF and A-**TEPPY**-COF (Figure 3.6, see ESI for details and solvent screening). The A-**TEXPY**-COFs were synthesized under optimal conditions regarding surface area and crystallinity (see below) after an extensive screening (see ESI for details). To remove any starting material or high-boiling solvent contained in the pores, the A-**TEXPY**-COFs were filtered, washed with DMF and THF, soaked in DCM for 3 hours, and subsequently heated to 90 °C in high dynamic vacuum for 12 h (10^{-7} mbar). All A-**TEXPY**-COFs were obtained as red to brown fluffy powders. Compared to the corresponding aldehydes, the A-**TEXPY**-COFs lack the characteristic aldehyde C-H and C=O vibrations (see ESI Fig. 3.S28) in their FT-IR spectra and show the appearance of a C=N^{13,20,21} band at 1620 cm^{-1} (see ESI Fig. 3.S29, highlighted by blue color). The CC triple bond vibration at 2200 cm^{-1} suggests that the alkyne moiety in A-**TEXPY**-COFs is preserved (see ESI Fig. 3.S29, highlighted by red color).

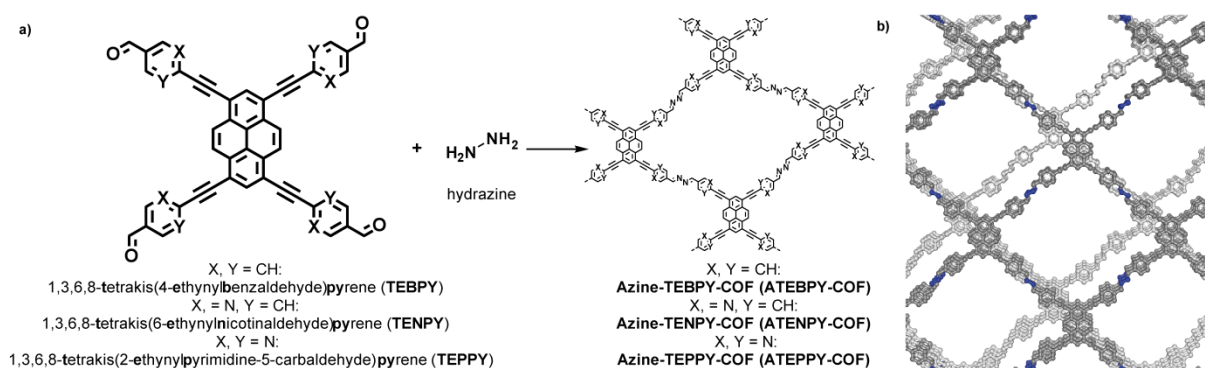


Figure 3.6: a) Synthesis of azine-linked COFs by the acetic acid catalyzed condensation reaction between the pyrene-based aldehyde linkers and hydrazine. b) Ball-and-stick model of the shifted AA' arrangement of A-TEBPY-COF. The other COFs adopt similar stackings.

The local structures of the A-TEXPY-COFs were further confirmed by ^{13}C cross-polarization magic angle-spinning (CP-MAS) solid-state NMR (ssNMR) spectroscopy. The disappearance of the characteristic aldehyde carbonyl ^{13}C resonance located at ≈ 190 ppm in the precursor aldehydes is observed, along with the appearance of the azine C=N signal at ≈ 160 ppm (ESI, see highlighted regions by blue color in Figs. 3.S30-33), thereby attesting the conversion of the precursors into the respective COFs. The local molecular structure of the building blocks remains intact during COF formation, as evidenced by the largely unchanged chemical shifts of the peripheral phenyl rings and the internal alkyne (≈ 85 -95 ppm) (ESI, see regions highlighted by red color in Figs. 3.S30-33). By increasing the nitrogen content in the A-TEXPY-COF series, new downfield shifted peaks arise next to the aromatic region indicating the carbon atoms situated next to the nitrogen atom in the heterocycles (≈ 140 ppm) (ESI, see regions highlighted by green color in Figs. 3.S30, 3.S31-33).

Argon sorption isotherms at 87 K reveal the porous nature of all A-TEXPY-COFs showing BET surface areas of $681\text{ m}^2\text{ g}^{-1}$ for A-TEBPY-COF, $470\text{ m}^2\text{ g}^{-1}$ for A-TENPY-COF and $920\text{ m}^2\text{ g}^{-1}$ for A-TEPPY-COF. All compounds show type I isotherms characteristic of microporous materials (see ESI Fig. 3.S35, and Fig. 3.8a).

The pore size distribution (PSD) was evaluated with quenched-solid density functional theory (QSDFT, cylindrical pores, carbon) for each material, applying the fit with the lowest error. The lower surface area of A-TENPY-COF may be a result of the lower thermal stability of the TENPY monomer, which starts decomposing at $150\text{ }^\circ\text{C}$ (see ESI Fig. 3.S36 for DTA measurement). The experimental PSD exhibits a maximum at 1.2 nm for A-TEBPY-COF, 1.3 nm for A-TEPPY-COF and 1.4 nm for A-TENPY-COF (see ESI Fig. 3.S35).

Investigation of the COF Structure

Powder X-Ray diffraction (PXRD) reveals limited crystallinity for the all-carbon A-TEBPY-COF with reflexes at $2\theta = 4^\circ$ and 8° (see Fig. 3.7a). Due to the resulting limited information content of

the XRD pattern, priority was given to the PSD while developing a structural model. Looking at the possible stacking modes of pseudo square-planar COFs, eclipsed AA-type stacking (space group $P2/m$) is most commonly employed, as an idealized structure model. Here, we consider the single-crystal x-ray structure of the related molecular building block (4-[2-[3,6,8-tris[2-(4-carboxyphenyl)-ethynyl]-pyren-1-yl]ethynyl]-benzoic acid), L_4H ,²² as a starting point to derive a plausible stacking model. In the structure of L_4H the electron rich pyrene core of one molecule is shifted by 6.5 Å so as to interact with the peripheral EWG-substituted phenyl ring of the neighbouring molecule (see Fig. 3.7b). This AA' (shifted(sh-AA')) stacking mode was then used to model the A-TEBPY-COF crystal structure by introducing a 6.5 Å shift between adjacent layers (see Figs. 3.7c and d). Adjacent layers are packed in a zigzag pattern in the unit cell and between two unit cells.²³ A helical pattern, which has been proposed elsewhere,²³ is not considered here. However, similar relative intensity distributions of the two stacking modes in the simulated PXRD patterns (see Fig. 3.7a) suggest that owing to the low quality of the observed powder diffraction data the AA and AA'-models cannot be distinguished experimentally.²⁴

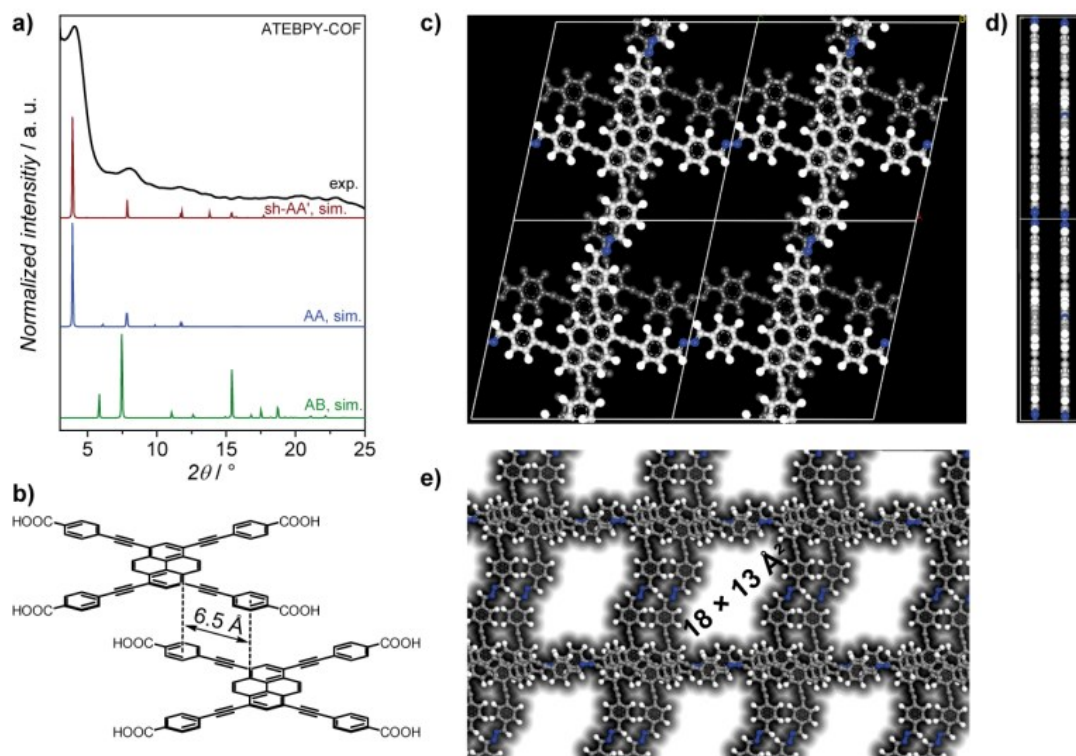


Figure 3.7: Characterization of A-TEBPY-COF by PXRD. a) PXRD suggests a shifted AA' or AA layer stacking. b) shifted stacking of pyrene units in L_4H , extracted from crystal structure.²² c) and d) shifted-AA' stacking of A-TEBPY-COF (grey: carbon, white: hydrogen, blue: nitrogen, background layer in dark grey for better visibility). e) accessible surface of sh-AA' layer stacking with a probe diameter of 3.6 Å (kinetic diameter of Ar) showing the formation of micropores.

While idealized AA stacking results in the formation of mesoporous pore windows of $22 \times 22 \text{ \AA}^2$, sh-AA' stacking results in microporous windows of $18 \times 13 \text{ \AA}^2$ (see Fig. 3.7 e). On the first glance, this microporous pore window of sh-AA' is counter-intuitive. Therefore, we visualized the argon-

accessible surface in a movie by 0.2 Å steps along the stacking axis (see ESI for movie). Careful comparison of the simulated isotherms^{5,25} and the experimental ones reveals that A-TEXPY-COFs are indeed microporous (see Figs. 3.8a and b), in agreement with the sh-AA' stacking mode. With the simulated isotherms in our hand, the next step was comparison of their extracted pore size distributions. As we applied the same QSDFT-based kernel to the simulated and experimental isotherms, potential kernel-related errors such as vague pore potentials were avoided.²⁶ QSDFT (Ar, 87 K, carbon, cylindrical pores) simulations were then performed on the simulated sorption isotherms to extract the PSD. In fact, the calculated PSD is similar to that extracted from the experimental isotherms, thus corroborating the dominant sh-AA' stacking mode (see Fig. 3.8c, see chapter 2.3 for details). Extracting stacking information from the PSD is more applicable to less crystalline COFs suffering from low quality PXRDs as compared to the more traditional method of comparing the modelled and experimental PXRDs. We note that especially layer off-sets in microporous COF systems can have a significant impact on the pore size distribution. Therefore, stacking information may be obtained from the PSD even in cases where PXRD cannot distinguish between different stacking modes as is often the case with low quality XRD data.

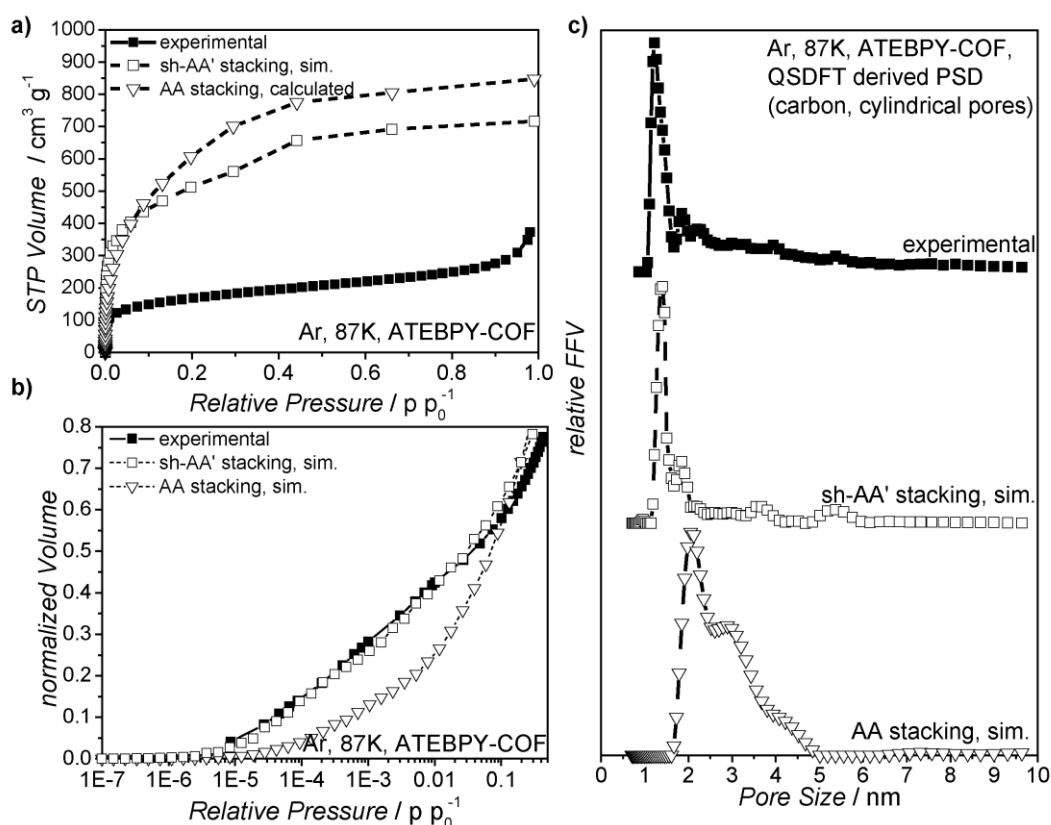


Figure 3.8: a) Ar isotherms at 87 K of A-TEBPY-COF, experimental (filled squares) and theoretical for AA (empty triangle) and sh-AA' stacking (empty square), b) logarithmic representation (relative pressure $<0.5 p p_0^{-1}</math>) of experimental and simulated isotherms with normalized volumes revealing microporous behavior of the experimental isotherm. c) QSDFT-derived pore size distributions of experimental and simulated Ar isotherms (carbon, cylindrical pores).$

Photocatalytic Hydrogen Generation

The diffuse reflectance UV/Vis spectrum of the A-TEXPY-COFs exhibit an absorption edge around 600 nm (the spike at 340 nm is due to a change of the light source), with the absorption tail extending well beyond 800 nm (Fig. 3.9a), corresponding very well to solar irradiation. We estimate an optical band gap of 1.92 eV for A-TEBPY-COF, 1.87 eV for A-TENPY-COF, and 1.83 eV for A-TEPPY-COF from the absorption edge, based on the Kubelka–Munk function (see ESI, Fig. 3.S37). This is consistent with the increasing nitrogen content in the peripheral aromatic rings, leading to an increase in electron-withdrawing character, which in turn results in a stronger push-pull effect and, hence, a decrease in the optical band gap. In principle, the observed HOMO-LUMO gap of the A-TEXPY-COF is large enough to enable water splitting through band gap excitation and at the same time small enough to harvest a significant portion of the solar spectrum.

A-TEXPY-COFs represent an excellent model platform for photocatalysis experiments, as their relative activities will be dominated by their composition and electronic rather than by their geometrical structures, although factors such as morphology and surface area will likely also play a role. We studied light-induced hydrogen evolution by suspending the COF in phosphate buffered saline (PBS) at pH 7. The mixture was irradiated with simulated sunlight (AM 1.5, 100 mW cm⁻²) in the presence of *in situ* generated platinum nanoparticles as co-catalyst for reducing the overpotential of hydrogen evolution and using 10 vol% triethanolamine (TEOA) as sacrificial electron donor (see ESI for details).^{27,28}

Figure 3.9c shows a plot of the amount of hydrogen produced during a test period of 22 h for all samples (Fig. 3.9b). All A-TEXPY-COFs steadily produce hydrogen under these conditions. While A-TEBPY-COF produces hydrogen at the rate of 98 $\mu\text{mol h}^{-1} \text{g}^{-1}$, A-TENPY-COF with 22 $\mu\text{mol h}^{-1} \text{g}^{-1}$ falls short by a factor of 4. A-TEPPY-COF with the highest nitrogen content produced only 6 $\mu\text{mol h}^{-1} \text{g}^{-1}$ hydrogen.

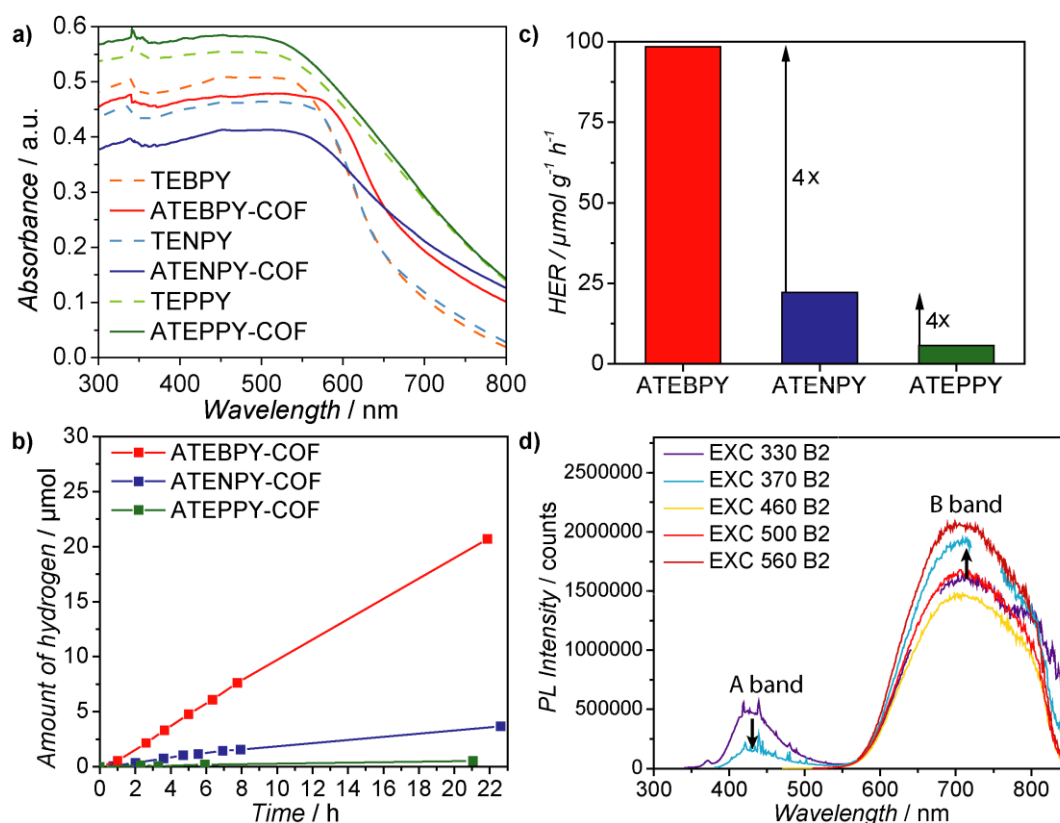


Figure 3.9: Optical properties of A-TEXPY-COFs and photocatalytic hydrogen evolution: a) UV/VIS diffuse reflectance spectra of A-TEXPY-COFs (red, blue, green, solid lines) and their corresponding starting materials (light red, light blue, light green, dotted lines). b) Time course of photocatalytic hydrogen evolution from a 10 vol% aqueous TEOA suspension by the Pt-modified A-TEXPY-COFs. c) Comparison of the hydrogen evolution rates of A-TEXPY-COFs exhibiting a fourfold enhancement with decreasing nitrogen content in the peripheral aromatic unit of the system. d) Photoluminescence spectra excited at the indicated wavelengths for A-TEBPY-COF in PBS buffer suspension with TEOA added (B2), showing two distinct emission peaks and their evolution as a function of excitation (EXC) wavelength.

As shown in schematically Figure 3.10a, preliminary results indicate that excited electrons in A-TEBPY-COF have an increased thermodynamic driving force for hydrogen evolution compared to ATEPPY-COF (1.6 eV against 1.3 eV).^{29,30} To further confirm this theory, experimental determination of HOMO levels by electrochemical analysis and photo-electron spectroscopy have to be obtained. In combination with computational investigations of HOMO/LUMO levels of the A-TEXPY-COF system, this can lead to a deeper understanding of the impact of electronic factors on the photocatalytic activity.

An increase in surface area may play a key role in the photocatalytic activity by providing a greater number of exposed active sites. However, in the present case, no correlation can be established regarding the surface area of the A-TEXPY-COFs (see Fig. 3.10b). As an example A-TEPPY-COF, having double the BET surface area compared to A-TENPY-COF, shows a smaller hydrogen evolution rate (HER) by a factor of four. We suggest that surface area is not the key

factor determining the photocatalytic activity, while a more straightforward correlation can be drawn between the optical band gap and the HER (see Fig. 3.10c).

Photoluminescence Measurements

To better understand the connection between the optical properties and the HER, steady-state were conducted. To this end, PL-spectra were subsequently measured for all three A-TEXPY-COFs as i) powder ii) in PBS buffer, iii) in PBS buffer + TEOA, and iv) in PBS buffer + TEOA + Pt. PL emission of A-TEXPY-COFs in powder form shows increasing intensity with decreasing nitrogen content (see ESI, Fig. 3.S38). This finding is also valid for PL measurements in suspension. In contrast to the powder PL spectrum (see ESI, Fig. 3.S38), the PL emission (EM) spectrum of A-TEBPY-COF in suspension shows two distinct emission bands centred at 425 nm (A band) and 711 nm (B band see Fig. 3.10d). Surprisingly, excitation at ≤ 380 nm leads to emission of both bands. In this excitation window (≤ 380 nm), a decrease of intensity in the A band coincides with an increase of intensity in the B band (see black arrows and compare purple and light-blue spectra, Fig. 3.10d). By addition of TEOA, quenching occurs at the A and B bands, which lose intensity by 50% and 47%, respectively (excitation (EXC) at 360 nm). This quench is intensified even further by adding the Pt precursor solution, leading to a further decrease in intensity by 25% at 425 nm and 12% at 711 nm (see Fig. 3.S39). Excitation spectra at EM = 420 nm (A band) shows its maximum at 330 nm excitation. The overall intensity drops with increasing emission wavelength (compare EM=420 with EM=500 nm and see black arrow in Figs. 3.S40-41), which is consistent with vanishing intensity of the A band at 500 nm in the PL spectra (see Fig. 3.9d). Monitoring the emission at 560 nm up to 600 nm, both located in the B band, clearly shows an increasing intensity at blue excitation wavelengths, the local maximum being at EXC = 360 nm. This feature relates to an energy/photon transfer up to around EXC ≤ 380 nm into the B band (see black arrows, Fig. 3.S41).

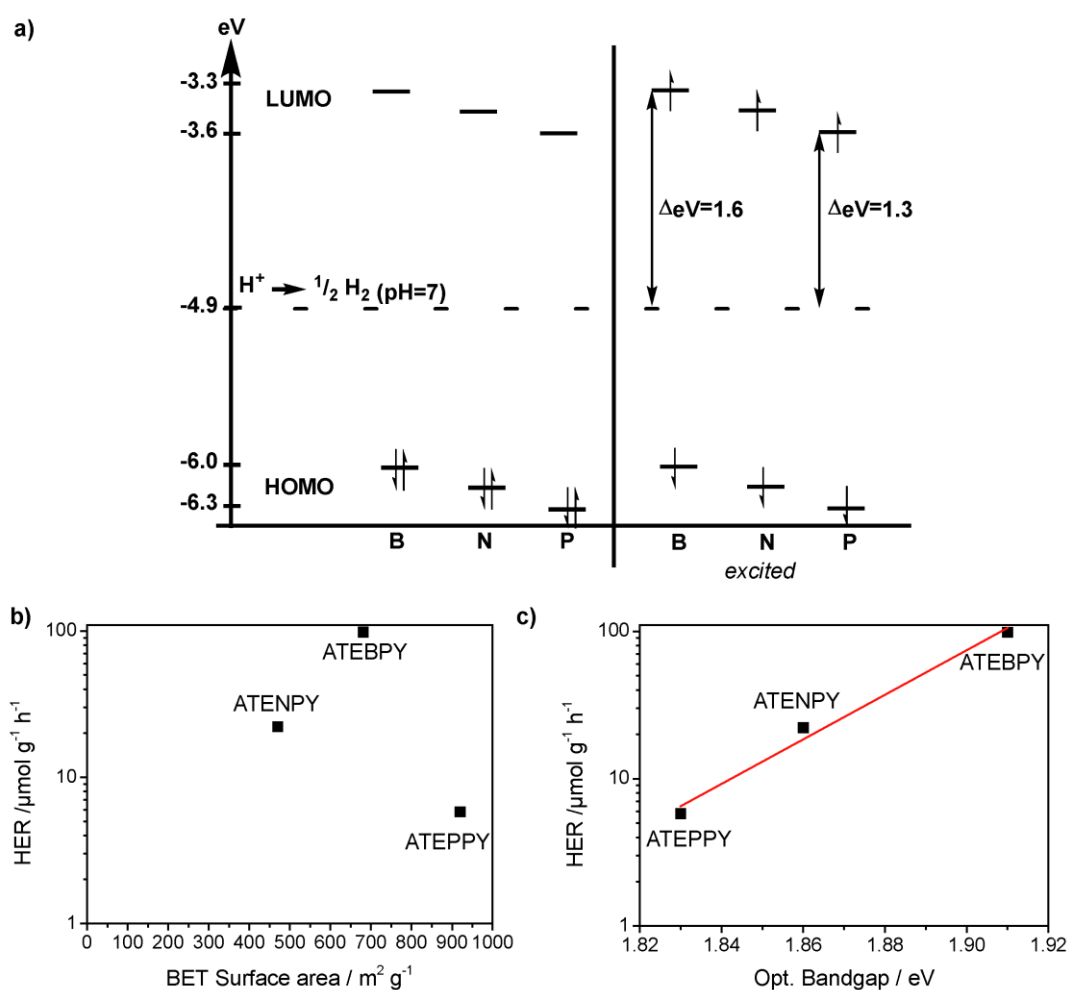


Figure 3.10: Preliminary explanations of HER of A-TEXPY-COF system: a) Energy scheme visualizing the supposed occupation of HOMO and LUMO levels of A-TEBPY, A-TENPY and A-TEPPY-COF in the ground state (left) and in the excited state (right) (adapted from unpublished results of Gökçen Savasci, based on TEXPY monomers, Ochsenfeld-Group). b) Correlation plot of HER against BET surface area, c) correlation plot of HER against opt. bandgap. HER in logarithmic scale.

It is well known that pyrene units show self-trapping of excitons with a corresponding red-shift of the PL emission, once they are stacked.³¹ As discussed above, the bulk material A-TEBPY-COF is stacked with an AA'-type stacking sequence and we therefore ascribe the broad B band PL emission at 711 nm to emission from the stacked pyrene units in the COF. We speculate that the 425 nm A band is due to non-stacked pyrene units which are present in aqueous suspension as a result of an exfoliation process leading to delamination and partial single layer formation.^{19,31} This would also explain the appearance of the A band in the PL spectra of the A-TEBPY-COF suspension in contrast to its absence in the powder PL spectra. These single layers can still transfer their emission energy to the bulk COF, either by reabsorption/emission or by energy transfer into the stacked pyrene units of the COF as seen in Figure 3.9. The postulated monolayer formation requires further experimental validation such as PL measurements of a centrifuged suspension of the COF and AFM characterization of the nanosheets. Furthermore, PL measurements of the

monomer solutions might reveal a similar PL emission at 425 nm. Importantly, the connection between energy transfer and hydrogen evolution still needs to be established, as PL measurements only probe the radiative decay channels in the system, which however may not directly correlate with non-radiative processes such as charge transfer. Determining the total and emissive lifetimes to extract the non-radiative lifetimes may furnish this information.

The absolute hydrogen evolution performance of A-TEBPY-COF and A-TENPY-COF are moderate, ranging between those observed for the phenyltriazine oligomers PTO-300-1 ($60 \mu\text{mol h}^{-1} \text{g}^{-1}$) and PTO-300-2.5 ($170 \mu\text{mol h}^{-1} \text{g}^{-1}$), which were analyzed in a recent study.³²

An important finding of the present study however is the fact that hydrogen evolution is feasible despite the presence of alkyne bonds.

3.3.3 Conclusion

In conclusion, IR and NMR spectroscopy along with PXRD, UV/Vis and sorption data clearly confirm the successful formation of an extended, azine-linked porous network by the condensation reaction of the three novel aldehyde linkers TEBPY, TENPY and TEPPY with hydrazine. Furthermore, photocatalysis experiments show significant hydrogen evolution rates for these rather electron rich systems consisting of aromatic pyrene cores and alkyne bridges. Preliminary results indicate, that a higher lying HOMO of A-TEBPY-COF provides the increased thermodynamic driving force for hydrogen evolution in comparison to A-TENPY-COF and A-TEPPY-COF, which contradicts previous findings for Nx-COF systems.¹⁰ PL studies do not provide so far any explanation for photocatalytic activity, but give indication for a water-induced exfoliation and photon/energy transfer from the resulting nanosheets to the bulk COF. Further studies, on the way in our lab, will concentrate on time-resolved PL and help to understand this transfer, in combination with spectral and morphological characterization of the nanosheets.

3.3.4 Bibliography

Author contributions

Linus Stegbauer wrote the manuscript, edited the figures, designed the synthesis, carried out the sorption measurements and simulated the COF structure and PXRDs. Linus Stegbauer and Sebastian Zech did the synthesis of the starting materials, COFs and did the spectral characterization. Katharina Schwinghammer did the photocatalysis experiments. Florian Ehrat conducted PL measurements did data evaluation and interpreted the results. Gökçen Savasci conducted theoretical calculations of starting materials and COF structures. Jochen Feldmann and Bettina Lotsch discussed the results.

Acknowledgements

We thank K. Gottschling for PXRDs and C. Minke for ssNMR measurements. Financial support by the Fonds der Chemischen Industrie (scholarship for L.S.), the cluster of excellence “Nanosystems Initiative Munich” (NIM, and the Center for NanoScience (CeNS) is gratefully acknowledged.

1. A. P. Côté, A. I. Benin, N. W. Ockwig, M. O’Keeffe, A. J. Matzger and O. M. Yaghi, *Science*, 2005, **310**, 1166–1170.
2. S. Jin, M. Supur, M. Addicoat, K. Furukawa, L. Chen, T. Nakamura, S. Fukuzumi, S. Irle and D. Jiang, *J. Am. Chem. Soc.*, 2015, **137**, 7817–7827.
3. M. Calik, F. Auras, L. M. Salonen, K. Bader, I. Grill, M. Handloser, D. D. Medina, M. Dogru, F. Löbermann, D. Trauner, A. Hartschuh and T. Bein, *J. Am. Chem. Soc.*, 2014, **136**, 17802–17807.
4. S. Jin, X. Ding, X. Feng, M. Supur, K. Furukawa, S. Takahashi, M. Addicoat, M. E. El-Khouly, T. Nakamura, S. Irle, S. Fukuzumi, A. Nagai and D. Jiang, *Angew. Chem.*, 2013, **125**, 2071–2075.
5. X. Feng, L. Chen, Y. Honsho, O. Saengsawang, L. Liu, L. Wang, A. Saeki, S. Irle, S. Seki, Y. Dong and D. Jiang, *Adv. Mater. (Weinheim, Ger.)*, 2012, **24**, 3026–3031.
6. S. Wan, F. Gándara, A. Asano, H. Furukawa, A. Saeki, S. K. Dey, L. Liao, M. W. Ambrogio, Y. Y. Botros, X. Duan, S. Seki, J. F. Stoddart and O. M. Yaghi, *Chem. Mater.*, 2011, **23**, 4094–4097.
7. J. Guo, Y. Xu, S. Jin, L. Chen, T. Kaji, Y. Honsho, M. A. Addicoat, J. Kim, A. Saeki, H. Ihee, S. Seki, S. Irle, M. Hiramoto, J. Gao and D. Jiang, *Nat. Commun.*, 2013, **4**, Art. No. 2736.
8. M. Dogru, M. Handloser, F. Auras, T. Kunz, D. Medina, A. Hartschuh, P. Knochel and T. Bein, *Angew. Chem., Int. Ed.*, 2013, **52**, 2920–2924.
9. J. Thote, H. B. Aiyappa, A. Deshpande, D. Díaz Díaz, S. Kurungot and R. Banerjee, *Chem. - Eur. J.*, 2014, **20**, 15961–15965.
10. V. S. Vyas, F. Haase, L. Stegbauer, G. Savasci, F. Podjaski, C. Ochsenfeld and B. V. Lotsch, *Nat. Commun.*, 2015, **6**, Art. No. 8508.
11. L. Stegbauer, K. Schwinghammer and B. V. Lotsch, *Chem. Sci.*, 2014, **5**, 2789.
12. S. Wan, J. Guo, J. Kim, H. Ihee and D. Jiang, *Angew. Chem., Int. Ed.*, 2008, **47**, 8826–8830.
13. S. Dalapati, S. Jin, J. Gao, Y. Xu, A. Nagai and D. Jiang, *J. Am. Chem. Soc.*, 2013, **135**, 17310–17313.
14. O. F. Mohammed, J. Dreyer, B.-Z. Magnes, E. Pines and Nibbering, Erik T. J., *Chem-PhysChem*, 2005, **6**, 625–636.

15. M. G. Rabbani, A. K. Sekizkardes, Z. Kahveci, T. E. Reich, R. Ding and H. M. El-Kaderi, *Chem.--Eur. J.*, 2013, **19**, 3324–3328.
16. X. Chen, N. Huang, J. Gao, H. Xu, F. Xu and D. Jiang, *Chem. Commun.*, 2014, 6161–6163.
17. H. Vollmann, H. Becker, M. Corell and H. Streeck, *Justus Liebigs Ann. Chem.*, 1937, **531**, 1–159.
18. S. Bernhardt, M. Kastler, V. Enkelmann, M. Baumgarten and K. Müllen, *Chem. - Eur. J.*, 2006, **12**, 6117–6128.
19. G. Venkataramana and S. Sankararaman, *Eur. J. Org. Chem.*, 2005, **2005**, 4162–4166.
20. Z. Li, X. Feng, Y. Zou, Y. Zhang, H. Xia, X. Liu and Y. Mu, *Chem. Commun.*, 2014, **50**, 13825–13828.
21. L. D. Frederickson, *Anal. Chem.*, 1964, **36**, 1349–1355.
22. O. V. Gutov, W. Bury, D. A. Gomez-Gualdrón, V. Krungleviciute, D. Fairen-Jimenez, J. E. Mondloch, A. A. Sarjeant, S. S. Al-Juaid, R. Q. Snurr, J. T. Hupp, T. Yildirim and O. K. Farha, *Chem. - Eur. J.*, 2014, **20**, 12389–12393.
23. B. T. Koo, W. R. Dichtel and P. Clancy, *J. Mater. Chem.*, 2012, **22**, 17460–17469.
24. B. Lukose, A. Kuc and T. Heine, *Chem.--Eur. J.*, 2011, **17**, 2388–2392.
25. T. C. Wang, W. Bury, D. A. Gómez-Gualdrón, N. A. Vermeulen, J. E. Mondloch, P. Deria, K. Zhang, P. Z. Moghadam, A. A. Sarjeant, R. Q. Snurr, J. F. Stoddart, J. T. Hupp and O. K. Farha, *J. Am. Chem. Soc.*, 2015, **137**, 3585–3591.
26. S. Lowell, J. E. Shields, M. A. Thomas and M. Thommes, *Characterization of porous solids and powders: surface area, pore size and density*, Springer Science & Business Media, Dordrecht, Netherlands, 2012.
27. S. Yang, Y. Gong, J. Zhang, L. Zhan, L. Ma, Z. Fang, R. Vajtai, X. Wang and P. M. Ajayan, *Adv. Mater. (Weinheim, Ger.)*, 2013, **25**, 2452–2456.
28. D. J. Martin, K. Qiu, S. A. Shevlin, A. D. Handoko, X. Chen, Z. Guo and J. Tang, *Angew. Chem., Int. Ed.*, 2014, **53**, 9240–9245.
29. H. Kisch, *Angew. Chem., Int. Ed.*, 2013, **52**, 812–847.
30. A. Kudo and Y. Miseki, *Chem. Soc. Rev.*, 2009, **38**, 253–278.
31. M. Fu, F. Ehrat, Y. Wang, K. Z. Milowska, C. Reckmeier, A. L. Rogach, J. K. Stolarczyk, A. S. Urban and J. Feldmann, *Nano Lett.*, 2015, **15**, 6030–6035.
32. K. Schwinghammer, S. Hug, Mesch, M. B., J. Senker and Lotsch, B. V., *Energy Environ. Sci.*, 2015, **8**, 3345–3353.

3.3.5 Supporting Information

The solvents dichloromethane, chloroform, *n*-hexane and ethyl acetate were purified by distillation on a rotary evaporator prior to use. Ethanol was dried according using activated molecular sieve (3 Å, SIGMA ALDRICH). All other commercially available chemicals and solvents used in this work are listed in Table 3.S3, including their sources of supply and purity grade.

Moisture- and air-sensitive reactions were conducted under dry argon (MESSER, purity grade 4.8) in standard SCHLENK glassware or BIOTAGE microwave vials capped with common NS14 rubber septa. Standard syringe techniques were applied to transfer the reagents. Vacuum ($>10^{-3}$ mbar) was provided by a VACUUBRAND RZ6 rotary vane pump. Unless otherwise stated, solvents and solutions were degassed by purging with dry argon under vigorous stirring for at least 15 min.

Analytical **thin-layer chromatography** was performed on MERCK silica gel 60 aluminum sheets containing manganese-activated zinc silicate. Substances were identified by irradiation of UV-light (254 nm) after separation. **Preparative column chromatography** was carried out using MERCK silica gel 60 with a particle size distribution of 15–40 μm . Before elution of products, the columns were pre-treated with a mixture of 0.5 % triethylamine in *n*-hexane during the packing procedure.

EI-Mass spectrometry was performed on a JOEL JMS-700 MStation equipped with a double-focusing sector field detector. Samples were deposited on a platinum filament and heated from 20°C to 1600°C at a rate of 120°/min. **ESI-Mass analysis** was achieved on a THERMO Finnigan LTQ FT Ultra using a THERMO Ion Max ion source with a spray-capillary voltage of 4 kV. **MALDI** analysis was obtained on a BRUKER Daltonics Autoflex II TOF mass spectrometer. Samples were co-crystallized with either sinapinic acid or anthracene and ionized by a nitrogen laser operating at 337 nm. All listed mass values refer to the most abundant isotopic species.

Table 3.S3 Overview of chemicals used in this work.

Compound	Purity	Supplier
4-Bromobenzaldehyde	98 %	ACROS ORGANICS
6-Bromonicotinaldehyde	95 %	SIGMA ALDRICH
Bromine	≥ 99 %	RIEDEL DE HAËN
Celite powder (particle size <0.1 mm)	p. a.	MERCK
Copper iodide	98 %	SIGMA ALDRICH
Dimethylacetamide (anhydrous)	99.5 %	ACROS ORGANICS
Dimethylformamide	99 %	ALFA AESAR

Dioxane (anhydrous)	99.5 %	ACROS ORGANICS
Diphenyl ether	99 %	ACROS ORGANICS
Hydrazine hydrate	≥ 99 %	MERCK
Mesitylene	99 %	ACROS ORGANICS
Pyrene	98 %	MERCK
Sodium sulfate	99 %	GRÜSSING
Tetrahydrofuran (anhydrous, inhibitor-free)	≥ 99.9 %	SIGMA ALDRICH
Tetrakis(triphenylphosphine)palladium(0)	99 %	SIGMA ALDRICH
Tetra- <i>n</i> -butylammonium fluoride	98 %	SIGMA ALDRICH
Triethylamine	≥ 99 %	SIGMA ALDRICH
Trimethylsilylacetylene	98 %	SIGMA ALDRICH

NMR spectra in solution were recorded on BRUKER Avance and JOEL Eclipse devices operating at 270 MHz or 400 MHz in deuterated solvents at room temperature, unless otherwise stated. The chemical shifts (δ) for ^1H - and ^{13}C nuclei refer to tetramethylsilane as an internal standard. Splitting patterns are indicated as *s* (singlet), *d* (doublet), *t* (triplet), *q* (quartet), *m* (multiplet) and *br* (broad).

Solid-state MAS NMR spectra were recorded at ambient temperature on a BRUKER Avance 500 solid-state NMR spectrometer, operating at LARMOR frequencies of 500.2 MHz, 125.8 MHz and 50.7 MHz for ^1H -, ^{13}C - and ^{15}N -nuclei, respectively. The sample was contained in a 4 mm zirconium(IV) oxide rotor (BRUKER), which was mounted in a standard double resonance probe at a MAS frequency of 10 kHz. The ^1H and ^{13}C chemical shifts were referenced relative to tetramethylsilane. The ^1H - ^{13}C cross-polarization (CP) MAS spectra were recorded at a spinning speed of 10 kHz using a ramped-amplitude (RAMP) CP pulse on ^1H , centered on the $n = +1$ Hartmann-Hahn condition, with a nutation frequency ν_{nut} of 55 kHz (^{15}N) and 40 kHz (^{13}C). During a contact time of 7 ms the ^1H radio frequency field was linearly varied about 20%.

UV/Vis data was collected on a JASCO V650 double-beam spectrophotometer equipped with a photomultiplier tube detector. Solid samples were loaded into a special designed holder and pressed against a quartz disc at the edge of the integrating sphere. Data was processed with JASCO's proprietary software Spectra Manager II.

IR-spectra were recorded on a JASCO FT/IR-4100 spectrometer equipped with a diamond ATR unit in a range of 600 cm^{-1} – 4000 cm^{-1} . Data was background corrected and processed with JASCO's proprietary software Spectra Manager II.

Argon sorption measurements were performed at 87 K with a QUANTACHROME Autosorb iQ instrument. Samples of 20 mg were preheated in vacuum at $120\text{ }^{\circ}\text{C}$ for 12 h. For BET calculations pressure ranges were chosen according to the implemented micropore BET assistant. For BET calculations pressure ranges of the Ar isotherms were chosen with the help of the BET Assistant in the ASiQwin software. In accordance with the ISO recommendations multipoint BET tags equal to or below the maximum in $V(1 - P/P_0)$ were chosen. Pore-size distributions were determined using the calculation model for Ar at 87 K on carbon (cylindrical pores, QSDFT/NLDFT equilibrium model) of the ASiQwin software (v3.01) from Quantachrome.

The **pore size distribution** was calculated from argon adsorption isotherms by non-local density functional theory (NLDFT) using the “*Ar-carbon cylindrical pores at 87 K*” kernel (applicable pore diameters 3.5 \AA – 1000 \AA) for argon data as implemented in the AUTOSORB data reduction software.

Microwave reactions were conducted in a BIOTAGE Initiator Classic instrument in sealed pressure vials under magnetic stirring. Reaction mixtures were rapidly cooled after completed heating *via* nitrogen gas flow.

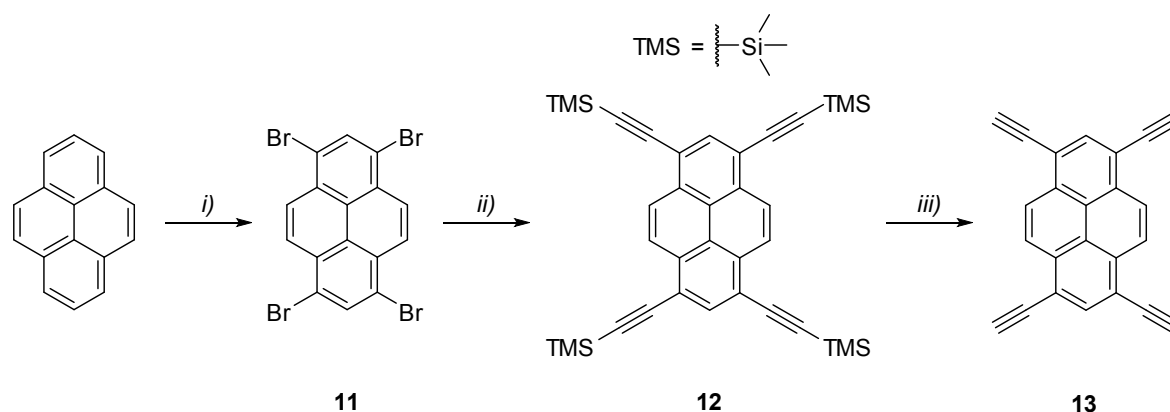
Photocatalytic hydrogen evolution experiments were performed in a double-walled glass reactor kept at a constant temperature ($25\text{ }^{\circ}\text{C}$) by water cooling. The samples (10 mg) were suspended in water (9 mL) and dispersed in an ultrasonic bath for 30 min. The sacrificial electron donor triethanolamine (1 mL, ALFA AESAR) and aqueous hydrogen hexachloroplatinate(IV) solution (6 μL of 8 wt% in H_2O , SIGMA ALDRICH, $\approx 2.2\text{ wt\% Pt}$) as precursor for the *in situ* formation of the platinum co-catalyst was added. The flask was evacuated and purged with argon to remove any dissolved gases. The suspension was top-irradiated through a quartz window with a xenon lamp (NEWPORT, 300 W) equipped with an AM 1.5 filter (AM 1.5, 100 mw cm^{-1}). In the course of the experiment, the headspace of the reactor was periodically sampled and the components were quantified by a THERMO SCIENTIFIC TRACE Ultra gas chromatograph equipped with a thermal conductivity detector, using argon as the carrier gas.

Powder x-ray diffraction experiments were carried out on a STOE Stadi P transmission diffractometer in DEBYE-SCHERRER geometry using $\text{Cu-K}\alpha_1$ -radiation ($\lambda = 1.54051\text{ \AA}$) and a Ge(111) monochromator. The samples were grinded in a mortar and loaded into a glass capillary.

DTA/TG data was collected on a SETARAM TG/DTA 92-24 device at a heating rate of 5 K/min under argon atmosphere.

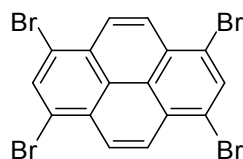
Compound names are those generated by the “*convert structure to name*” algorithm implemented in the PERKIN ELMER ChemBioDraw Ultra 13.0 software.

Synthetic Procedures

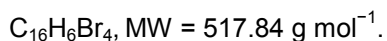


Scheme 3.S7. Three-step synthesis of the starting material 1,3,6,8-tetraethynylpyrene (**13**). Reagents and conditions: *i*) Br_2 , PhNO_2 , $120\text{ }^\circ\text{C}$, 4 h; *ii*) TMS-acetylene, $\text{Pd}(\text{PPh}_3)_4$, CuI , NEt_3 /toluene, $80\text{ }^\circ\text{C}$, 20 h; *iii*) K_2CO_3 , MeOH, rt, 24 h.

1,3,6,8-Tetrabromopyrene



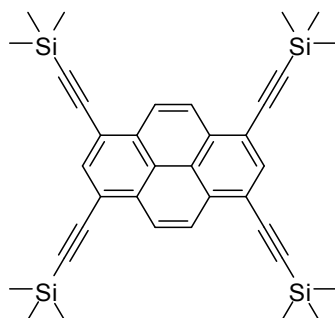
1,3,6,8-Tetrabromopyrene.



According to ref S1: To a solution of pyrene (2.02 g, 10.0 mmol, 1 eq) in nitrobenzene (20 mL) was slowly added bromine (2.26 mL, 44.0 mmol, 4.4 eq) over a period of 1 h with the aid of a syringe pump. The resulting slurry was kept at $120\text{ }^\circ\text{C}$ for 4 h and then allowed to cool to room temperature. The precipitate was collected, washed with copious amounts of ethanol and dried in a desiccator to yield the desired compound (4.83 g, 9.32 mmol, 93.2 %) as an off-white solid.

MS (DEI+, LR): Calculated for $\text{C}_{16}\text{H}_6\text{Br}_4$: 517.7 m/z found: 517.5 m/z $[\text{M}]^+$

1,3,6,8-Tetrakis[(trimethylsilyl)ethynyl]pyrene

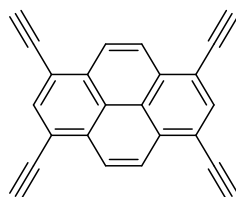


1,3,6,8-Tetrakis[(trimethylsilyl)ethynyl]pyrene.
 $C_{36}H_{42}Si_4$, MW = 587.07 g mol⁻¹.

According to ref S2,3. A degassed suspension of 1,3,6,8-tetrabromopyrene (518 mg, 1.00 mmol, 1 eq) in a mixture of toluene (4 mL) and triethylamine (12 mL) was charged with tetrakis(triphenylphosphine)-palladium(0) (173 mg, 150 μ mol, 0.15 eq) and copper(I)iodide (57.1 mg, 300 μ mol, 0.3 eq) and was heated to 50 °C. Subsequently, (trimethylsilyl)acetylene (793 μ L, 5.50 mmol, 5.5 eq) was added dropwise through a rubber septum and the yellow reaction mixture was kept at 80 °C overnight under inert atmosphere. After dilution with dichloromethane (48 mL), the dark orange suspension was filtrated through celite powder, washed with saturated ammonium chloride solution, 0.1M hydrochloric acid as well as brine (50 mL, respectively) and was evaporated to dryness. Purification of the orange-red residue by flash column chromatography (cyclohexane/toluene, 20:1) provided the desired compound (481 mg, 0.819 mmol, 81.9 %) as a bright orange solid.

¹H-NMR (CDCl₃, 270 MHz): δ = 8.59 (s, 4H), 8.30 (s, 2H), 0.37 (s, 36H) ppm. **¹³C{¹H}-NMR** (CDCl₃, 68 MHz): δ = 134.6, 132.1, 127.1, 122.8, 118.7, 102.9, 102.0, 0.2 ppm. **MS** (DEI+, LR): Calculated for C₃₆H₄₂Si₄: 586.2 *m/z* found: 586.3 *m/z* [M]⁺

1,3,6,8-Tetraethynylpyrene



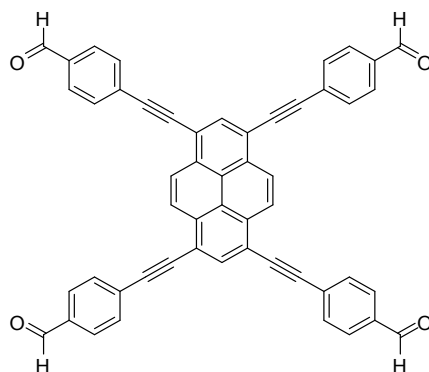
1,3,6,8-Tetraethynylpyrene.

 $C_{24}H_{10}$, MW = 298.34 g mol⁻¹.

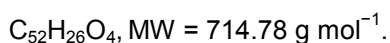
Potassium carbonate (1.11 g, 8.00 mmol, 8 eq) was added to a suspension of 1,3,6,8-tetrakis[(trimethylsilyl)ethynyl]pyrene (587 mg, 1.00 mmol, 1 eq) in methanol (58 mL). The mixture was vigorously stirred at room temperature for 24 h, then poured into water (290 mL) and deep-frozen overnight. After thawing at room temperature, the fine precipitate was collected by filtration and rinsed until neutral with water. The residual filter cake was washed with a small amount of ice-cold methanol and dried in a desiccator to afford the desired compound (293 mg, 0.982 mmol, 98.2 %) as a yellow solid.

¹H-NMR (THF-d₈, 400 MHz, 50 °C): δ = 8.68 (s, 4H), 8.35 (s, 2H), 4.27 (s, 4H) ppm. **¹³C{¹H}-NMR** (THF-d₈, 101 MHz, 50 °C): δ = 135.3, 133.0, 127.5, 124.2, 118.9, 86.1, 81.5 ppm. **MS** (DEI+, LR): Calculated for C₂₄H₁₀: 298.1 *m/z* found: 298.2 *m/z* [M]⁺

1,3,6,8-Tetrakis(4-ethynylbenzaldehyde)pyrene

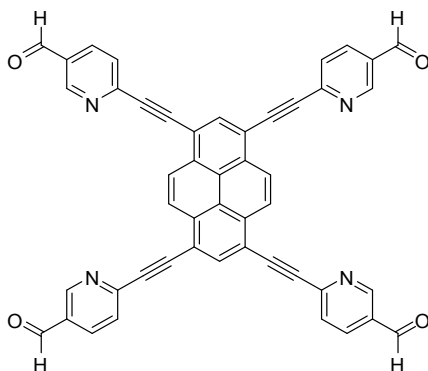


1,3,6,8-Tetrakis(4-ethynylbenzaldehyde)pyrene. (TEBPY)

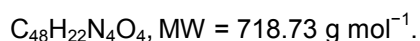


A degassed solution of 4-bromobenzaldehyde (793 mg, 4.20 mmol, 6 eq) in a mixture of tetrahydrofuran (14 mL) and triethylamine (14 mL) was charged with tetrakis(triphenylphosphine)palladium(0) (8.1 mg, 7.0 μmol , 0.01 eq) and copper(I) iodide (2.7 mg, 14 μmol , 0.02 eq) and stirred at room temperature until all solids dissolved. 1,3,6,8-tetraethynylpyrene (209 mg, 0.700 mmol, 1 eq) was added and the resulting orange suspension was kept at 70 °C for 24 h under inert atmosphere. After addition of pyridine (2 mL) and stirring for 5 min at room temperature, the red fine precipitate was collected *via* filtration and successively washed with pyridine, tetrahydrofuran, acetone as well as dichloromethane to give TEBPY (428 mg, 0.599 mmol, 85.5 %) as a fine red powder.

MS (DEI+, HR): Calculated for $\text{C}_{52}\text{H}_{26}\text{O}_4$: 714.1831 m/z found: 714.1860 m/z $[\text{M}]^+$ **IR** (FT, ATR): $\tilde{\nu}$ = 2820 (νCHO), 2725 (νCHO), 2198 ($\nu\text{C}\equiv\text{C}$), 1700 ($\nu\text{C}=\text{O}$), 1598 ($\nu\text{C}=\text{C}$, ar), 1559, 1507, 1470, 1413, 1382, 1302, 1285, 1208, 1163, 1101, 1012, 888, 820 (δCH , oop), 777, 713 cm^{-1}

1,3,6,8-Tetrakis(6-ethynynicotinaldehyde)pyrene

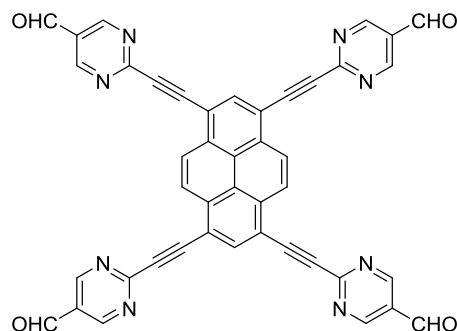
1,3,6,8-Tetrakis(6-ethynynicotinaldehyde)pyrene (TENPY).



A degassed solution of 6-bromo-3-pyridinecarboxaldehyde (822 mg, 4.20 mmol, 6 eq) in a mixture of tetrahydrofuran (14 mL) and triethylamine (14 mL) was charged with tetrakis(triphenylphosphine)palladium(0) (8.1 mg, 7.0 μmol , 0.01 eq) and copper(I) iodide (2.7 mg, 14 μmol , 0.02 eq) and stirred at room temperature until all solids dissolved. 1,3,6,8-tetraethynylpyrene (209 mg, 0.700 mmol, 1 eq) was added and the resulting orange suspension was kept at 70 °C for 24 h under inert atmosphere. After addition of pyridine (2 mL) and stirring for 5 min at room temperature, the red fine precipitate was collected *via* filtration and successively washed with pyridine, tetrahydrofuran, acetone as well as dichloromethane to give TENPY (336 mg, 0.467 mmol, 66.8 %) as a fine red powder.

MS (DEI+, HR): Calculated for $\text{C}_{48}\text{H}_{22}\text{N}_4\text{O}_4$: 718.1641 m/z found: 718.1642 m/z $[\text{M}]^+$ **IR** (FT, ATR): $\tilde{\nu}$ = 2831 (νCHO), 2728 (νCHO), 2200 ($\nu\text{C}\equiv\text{C}$), 1696 ($\nu\text{C}=\text{O}$), 1583 ($\nu\text{C}=\text{C}$, ar), 1552, 1496, 1476, 1403, 1355, 1282, 1247, 1190, 1159, 1118, 1018, 900, 831 (δCH , oop), 782, 751, 713 cm^{-1} .

1,3,6,8-Tetrakis(2-ethynylpyrimidine-5-carbaldehyde)pyrene

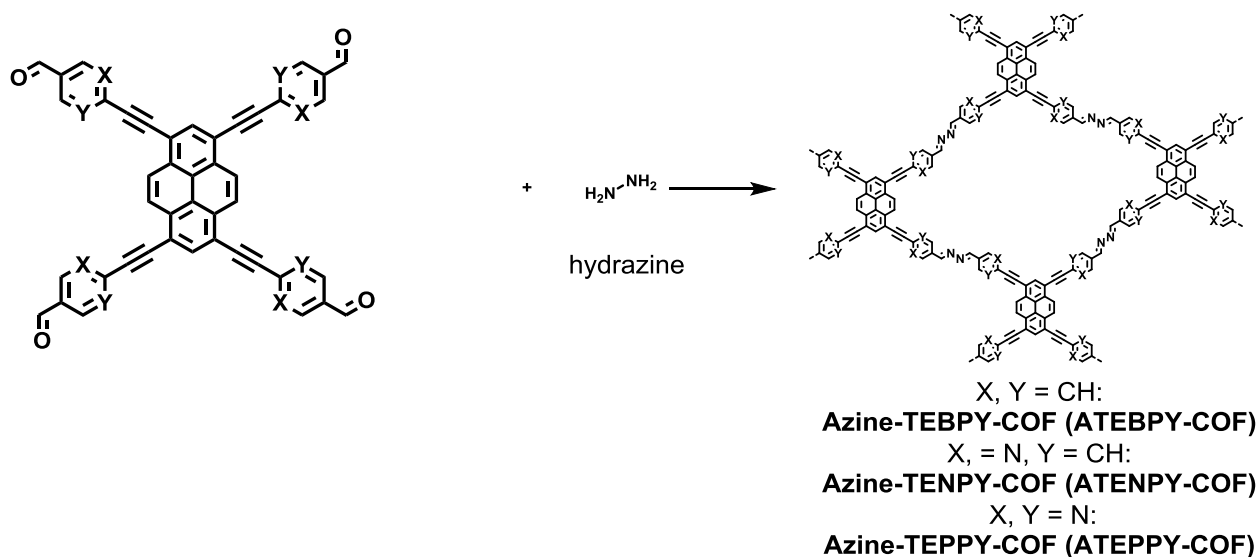


1,3,6,8-Tetrakis(2-ethynylpyrimidine-5-carbaldehyde)pyrene (TEPPY).



A degassed solution of 2-chloropyrimidine-5-carboxaldehyde (220 mg, 1.38 mmol, 5.5 eq) in a mixture of tetrahydrofuran (5 mL) and triethylamine (5 mL) was charged with tetrakis(triphenylphosphine)-palladium(0) (5.8 mg, 5.0 μmol , 0.02 eq) and copper(I) iodide (1.9 mg, 10 μmol , 0.04 eq) and stirred at room temperature until all solids were dissolved. 1,3,6,8-tetraethynylpyrene (75 mg, 0.25 mmol, 1 eq) was added and the resulting orange suspension was kept at 70 °C for 24 h under inert atmosphere. After addition of pyridine (0.2 mL) and stirring for 5 min at room temperature, the red fine precipitate was collected *via* filtration and successively washed with pyridine, CH_2Cl_2 , THF, Isopropanol, water, 1M HCl, water, dilute NaHCO_3 , water, isopropanol and diethylether to give TEPPY (110 mg, 0.152 mmol, 60.9 %) as a fine brown powder.

MS (MALDI-TOF, Anthracene in acetone, LR): Calculated for $\text{C}_{44}\text{H}_{18}\text{N}_8\text{O}_4$: 722.14 m/z found: 721.1 m/z $[\text{M}-\text{H}]^-$ **IR** (FT, ATR): $\tilde{\nu} = 2845$ (νCHO), 2726 (νCHO), 2201 ($\nu\text{C}\equiv\text{C}$), 1657 ($\nu\text{C}=\text{O}$), 1592 ($\nu\text{C}=\text{C}$, ar), 1526, 1426, 1359, 1210, 1171, 1023, 902, 835 (δCH , out-of-plane) cm^{-1} .



Scheme 3.S8. Synthesis of ATEXPY-COFs by acid catalyzed azine formation.

AATEXPY COFs

A 2 mL BIOTAGE® microwave vial was charged with the respective starting material (TEBPY, TENPY or TEPPY, 17.2 mg, 24.0 μmol , 1 eq), capped with a common NS14 rubber septum and flooded with argon by three pump/purge cycles. After addition of the solvent mixture (*o*-dichlorobenzene/dioxane 1:1 v/v: 0.50/0.50 mL for TEBPY, *o*-dichlorobenzene/dimethylacetamide 1:2 v/v: 0.33/0.66 mL for TENPY, *o*-dichlorobenzene/dimethylacetamide 1:1 v/v: 0.50/0.50 mL for TEPPY), the resulting suspension was degassed by four pump/purge cycles under vigorous stirring. 6M aqueous acetic acid (0.1 mL, 0.6 mmol, 25 eq for TEBPY / 0.2 mL, 1.2 mmol, 50 eq. in case of TENPY and 0.3 mL, 1.5 mmol, 75 eq in cas of TEPPY) was then added all at once, directly followed by addition of hydrazine hydrate (3.53 μL , 72.0 μmol , 3 eq). The vial was sealed and heated to 130 °C for 40 min under microwave irradiation. After cooling to room temperature, the vial was transferred to a muffle furnace, where it was slowly heated to 120 °C over a period of 2 h and maintained at this temperature for 72 h. After slow cooling, the fluffy red to brown precipitate was collected *via* suction filtration and thoroughly washed with dimethylformamide (3 \times 2.5 mL), tetrahydrofuran (3 \times 2.5 mL) and dichloromethane (3 \times 2.5 mL). Subsequent drying *in vacuo* furnished A-TEBPY-COF, A-TENPY-COF or A-TEPPY-COF as fluffy red to brown powders.

Analytical data for A-TEBPY-COF:

$^{13}\text{C}\{^1\text{H}\}$ -NMR (MAS, 10 kHz): δ = 159.8, 130.8, 125.8, 117.3, 95.4, 90.9 ppm.
IR (FT, ATR): $\tilde{\nu}$ = 2193 ($\nu\text{C}\equiv\text{C}$), 1620 ($\nu\text{C}=\text{N}$), 1603 ($\nu\text{C}=\text{C}$, ar), 1509, 1407, 1300, 1209, 1171, 1104, 1015, 940, 892, 827 (δCH , oop), 716 cm^{-1} .

Analytical data for A-TENPY-COF:

$^{13}\text{C}\{^1\text{H}\}$ -NMR (MAS, 10 kHz): δ = 159.6, 143.8, 127.4, 116.2, 94.8, 90.7 ppm.

IR (FT, ATR): $\tilde{\nu}$ = 2200 ($\nu\text{C}\equiv\text{C}$), 1622 ($\nu\text{C}=\text{N}$), 1585 ($\nu\text{C}=\text{C}$, ar), 1551, 1496, 1471, 1373, 1314, 1278, 1250, 1125, 1021, 957, 893, 834 (δCH , oop), 754, 718 cm^{-1} .

Analytical data for A-TEPPY-COF:

$^{13}\text{C}\{^1\text{H}\}$ -NMR (MAS, 10 kHz): δ = 159.7, 142.6, 128.5, 117.3, 82.8, 81.8 ppm.

IR (FT, ATR): $\tilde{\nu}$ = 2192 ($\nu\text{C}\equiv\text{C}$), 1658 ($\nu\text{C}=\text{N}$), 1594 ($\nu\text{C}=\text{C}$, ar), 1538, 1496, 1427, 1360, 1220, 1155, 890, 828 (δCH , oop) cm^{-1} .

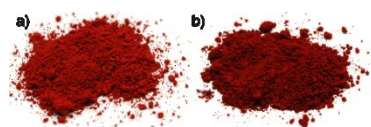


Figure 3.S24. Photographs of COFs obtained from TEBPY (a) and TENPY (b). Photographs were taken with identical exposure parameters.

Solvent Screening of A-TEPPY-COFs

Table 3.S4: Solvent screening results. BET surface of products obtained from the condensation reaction[†] between **TEBPY**, **TENPY** and **TEPPY** and hydrazine hydrate.

Solvent mixture [‡]	BET surface areas [$\text{m}^2 \text{g}^{-1}$]		
	TEBPY	TENPY	TEPPY
anisole	470	—	—
dioxane	565	212*	—
dioxane/mesitylene 1:1	412	—	—
dioxane/mesitylene 1:2	313	—	—
diphenyl ether	566	201*	—
<i>o</i> -DCB	553	—	—
<i>o</i> -DCB/anisole 1:1	565	212	—
<i>o</i> -DCB/ <i>n</i> -BuOH 19:1	405	—	—
<i>o</i> -DCB/DMA 1:2	668/556 [#]	410/470*	625*/720 [§]
<i>o</i> -DCB/DMA 1:1	589	397	921 [§]
<i>o</i> -DCB/DMA 2:1	515	—	—
<i>o</i> -DCB/dioxane 1:1	681	400*	—
<i>o</i> -DCB/ <i>n</i> -BuOH 1:1	—	—	815 [§]

-
- † general conditions: Monomer (1 eq), 6M AcOH (25 eq), N₂H₄·H₂O (3 eq),
1 mL total solvent volume, 40 min at 130 °C (microwave), 72 h at 120 °C
- ‡ stated ratios refer to parts per volume
- * 50 eq AcOH instead of 25 eq were used
- § 75 eq AcOH instead of 25 eq were used
- # conventional oil bath synthesis

Powder X-ray Diffraction and Simulation

Molecular modeling of the COF was carried out using the *Materials Studio* (6.0) suite of programs by *Accelrys*.

The unit cell was defined by one TEBPY (A-TEBPY-COF) molecule bonded via four azine linkages to hydrazine. The initial structure was geometry optimized using the MS Forcite molecular dynamics module (Universal force fields, Ewald summations), and the resulting distance between opposite formyl carbon atoms in the structure was used as the *a* and *c* lattice parameters (initially 16 and 18 Å) of the pseudo square-planar unit cell with *P21/m* symmetry (*c* centered), taking into account the non-C₄ geometry of TEBPY and the shifted AA' stacking of L₄H.^{S4} The crystal structure was geometry optimized using Forcite (resulting in *a* = 25.1 Å, *b* = 25.2 Å and *c* = 6.7 Å for ATEBPY-COF). With similar unit cell dimensions, the AA structure with *P2/m* symmetry and AB structure (*P21/m*) were simulated.

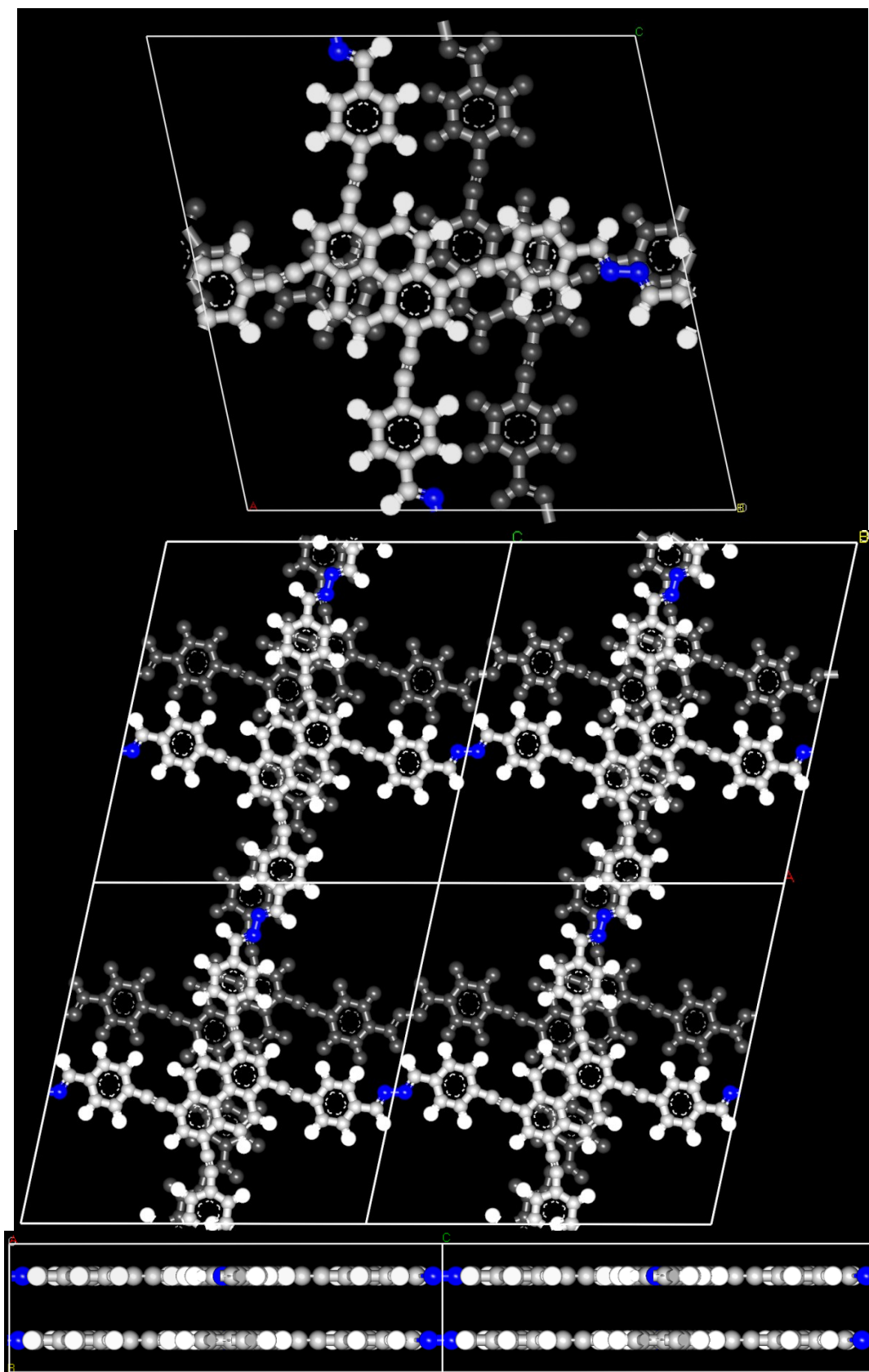


Figure 3.S25. ATEBPY-COF: Simulation of the unit cell content calculated based on a shifted AA' arrangement: View onto the *ab*-plane (top), view onto the *ab*-plane with four unit cells (middle) and view perpendicular to the *c*-axis (bottom).

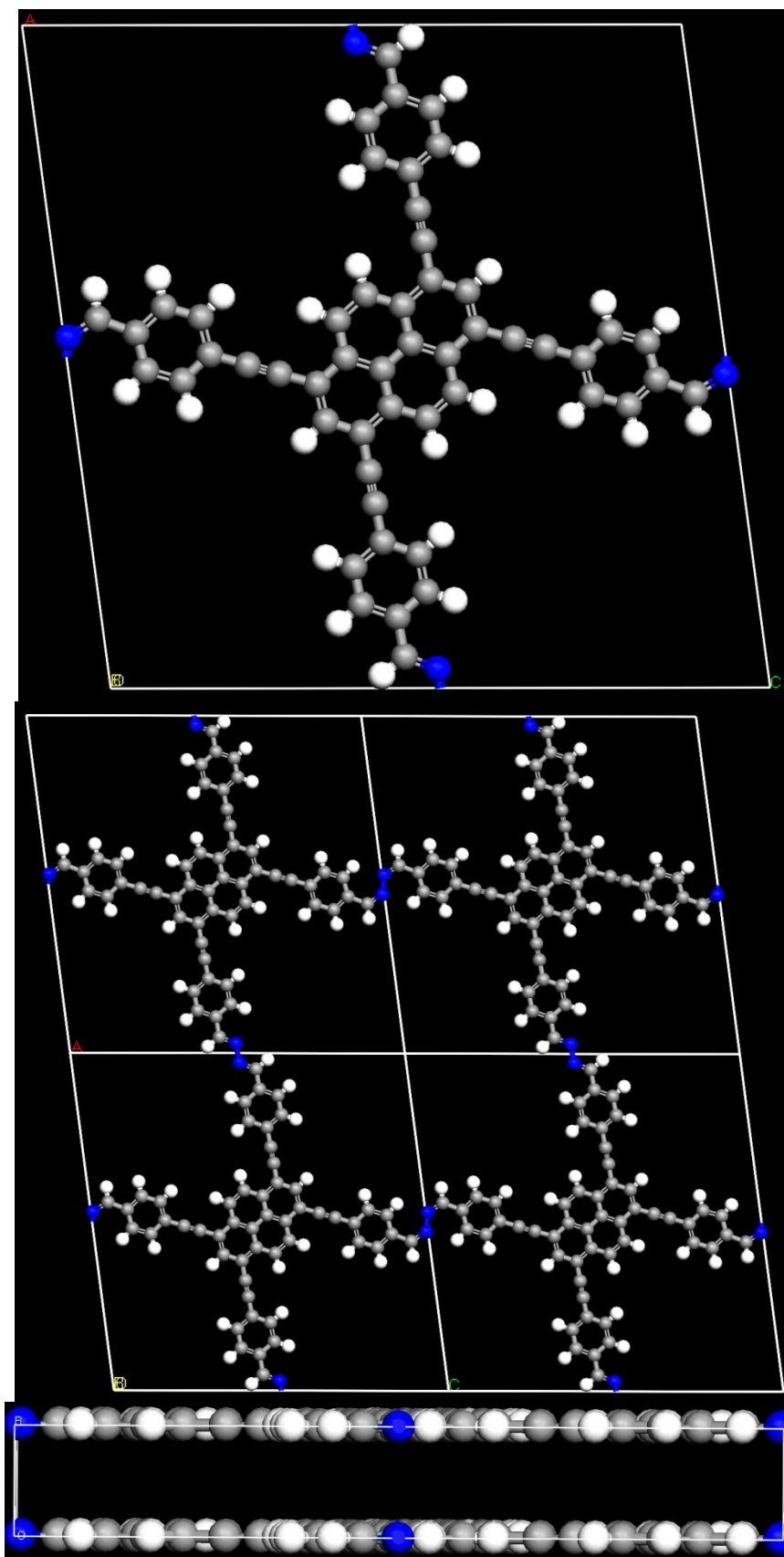


Figure 3.S26. ATEBPY-COF: Simulation of the unit cell content calculated for an AA arrangement: View onto the *ab*-plane (top), view onto the *ab*-plane with four unit cells (middle) and view perpendicular to the *c*-axis (bottom).

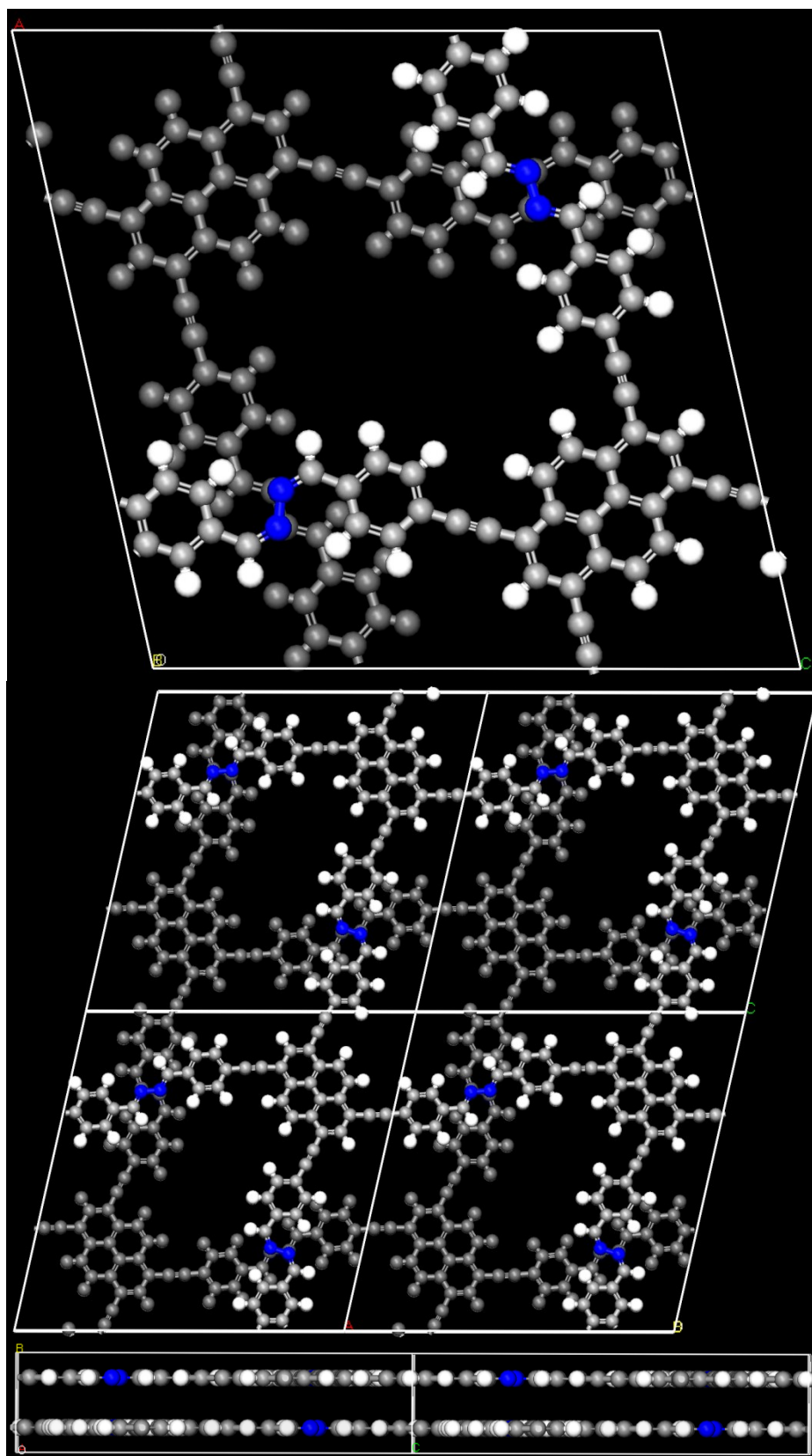


Figure 3.S27. ATEBPY-COF: Simulation of the unit cell content calculated in an AB arrangement: View onto the *ab*-plane (top), view onto the *ab*-plane with four unit cells (middle) and view perpendicular to the *c*-axis (bottom).

FT-IR Spectra

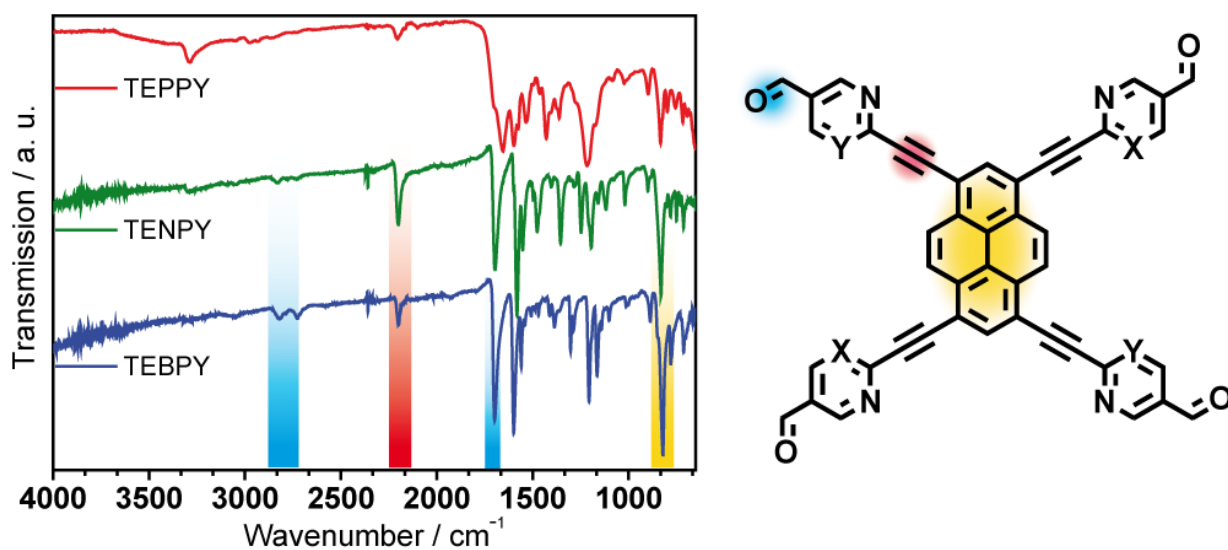


Figure 3.S28. Stack plot showing the FT-IR spectra of TEXPY molecules. The band highlighted in yellow at 821 cm^{-1} corresponds to C-H out of plane stretching of pyrene.^{S5} The band highlighted in blue at 2700 cm^{-1} corresponds to the Fermi double resonance of CHO.

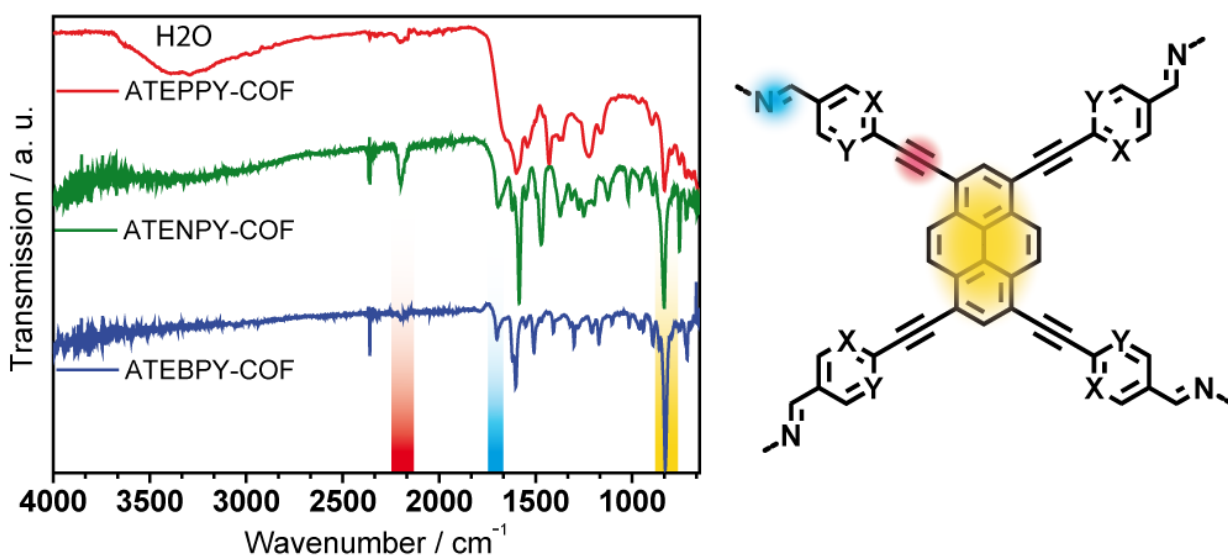


Figure 3.S29. Stack plot showing the FT-IR spectra of ATEXPY-COFs. The band highlighted in yellow at 821 cm^{-1} corresponds to the C-H out of plane stretching of pyrene.^{S5}

CP-MAS NMR Measurements

In all ^{13}C CP-MAS NMR spectra, asterisks indicate spinning side bands.

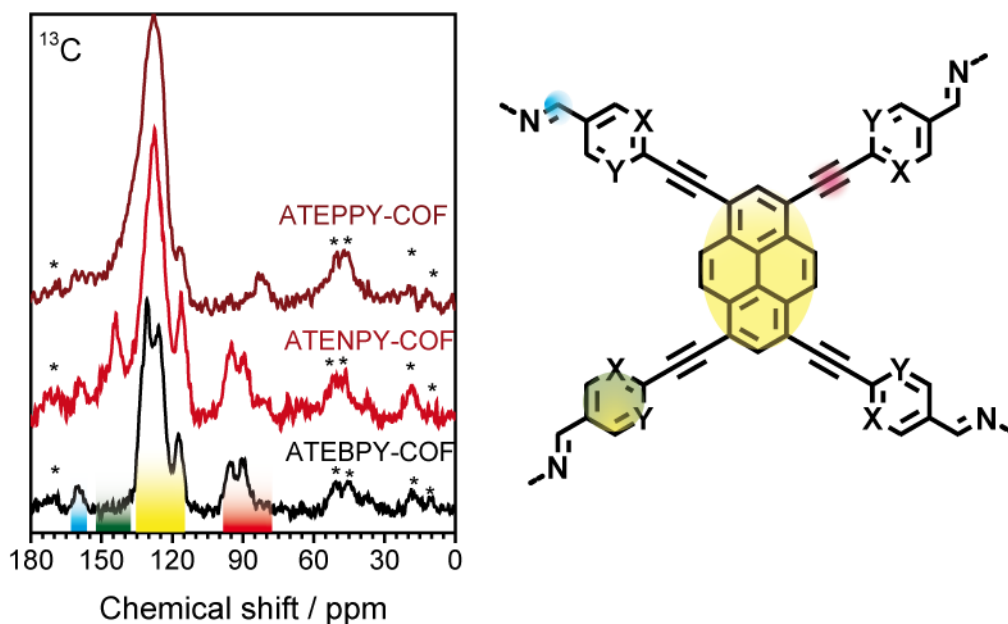


Figure 3.S30. ssNMR characterization of ATEXPY-COFs by ^{13}C CP-MAS NMR spectroscopy and assignment of spectral data. The change of the peripheral aromatic units from phenyl to pyridyl and pyrimidyl is accompanied by the appearance of new downshifted signals (region is marked by green color).

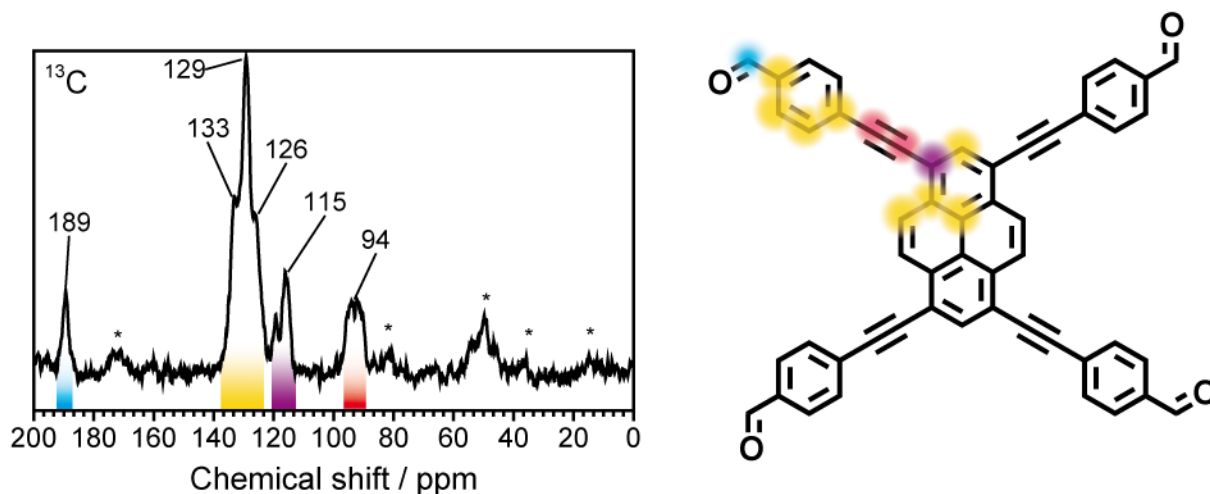


Figure 3.S31. ^{13}C ssNMR of TEBPY linker. The peak at 133 ppm corresponds to the aromatic carbon atom adjacent to the aldehyde and at 126 ppm to the bay pyrene carbons.

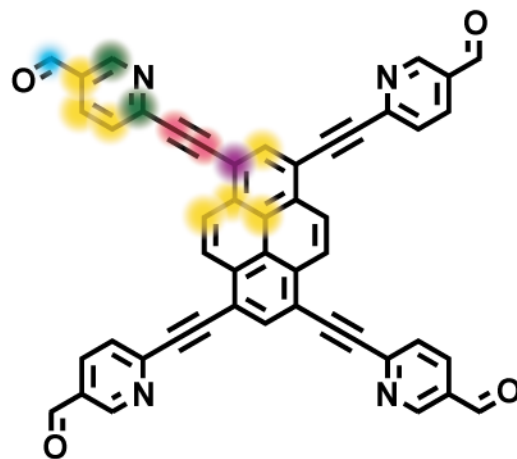
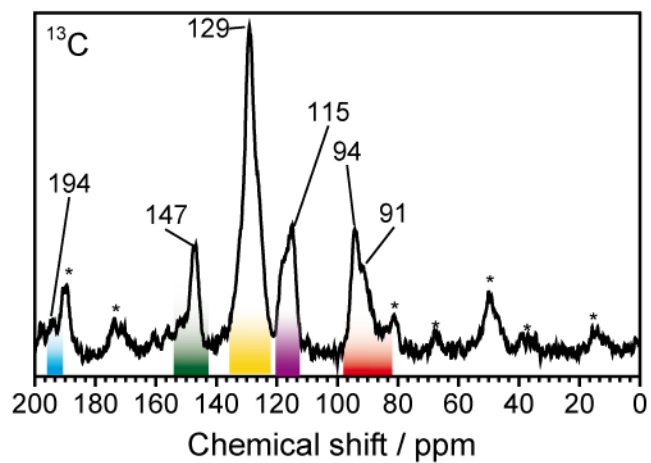


Figure 3.S32. ^{13}C ssNMR of TENPY linker.

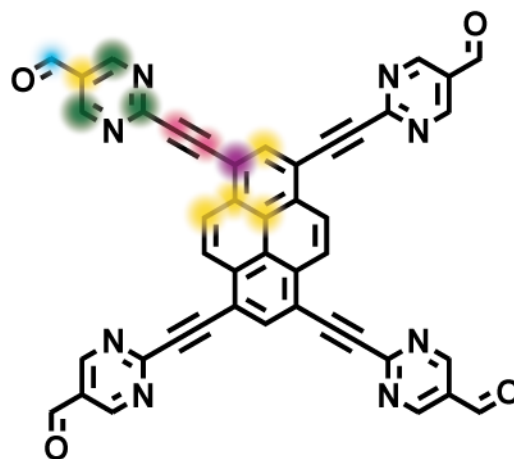
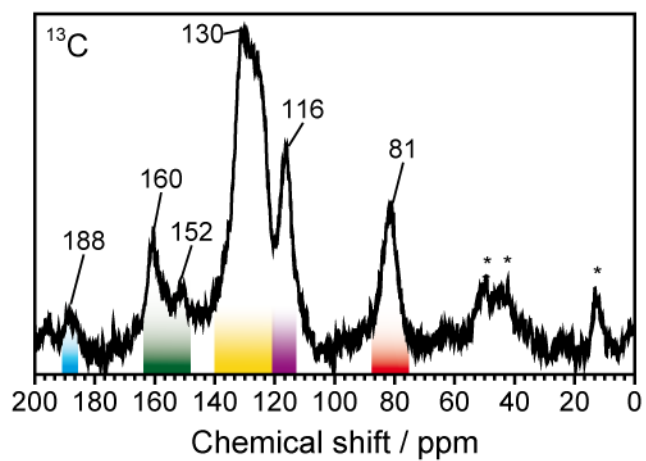


Figure 3.S33. ^{13}C ssNMR of TEPPY linker.

^1H solid-state NMR MAS spectroscopy of ATEXPY-COFs shows the presence of aromatic protons through signals at 7.0 – 7.5 ppm. With increasing nitrogen content the peak of this signal shifts further downfield. The signal around 3.7 ppm corresponds to residual water in the pores, which increases in intensity, in line with increasing nitrogen content and the accordingly increasing polarity of the COF.

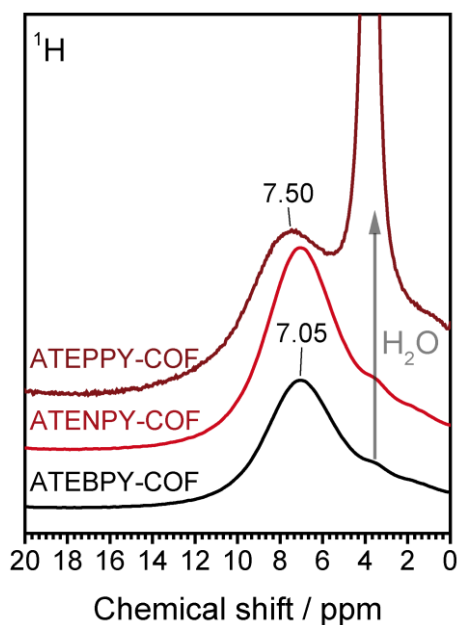


Figure 3.S34. ssNMR characterization of ATEXPY-COFs by ^1H MAS NMR spectroscopy. The change of the peripheral aromatic units from phenyl to pyridyl and pyrimidyl is accompanied by a small downfield shift of the maximum at 7.05 ppm (ATEBPY) to 7.50 ppm (ATEPPY) and an increase of the residual water content in the pores (3.53 ppm).

Ar Sorption Measurements and Pore Size Distribution

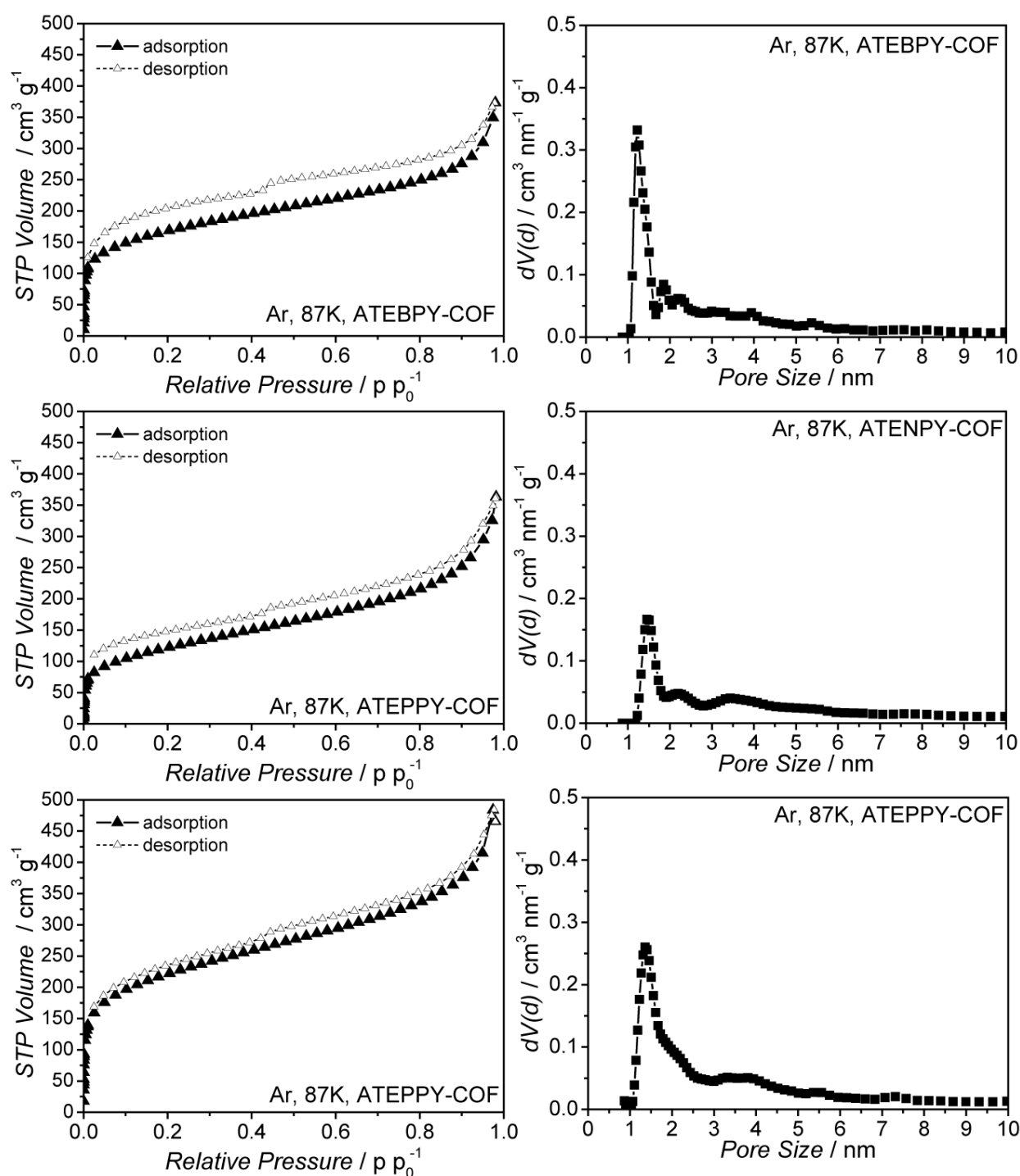


Figure 3.S35. Argon isotherms at 87 K of ATEXPY-COFs. The type I isotherm (adsorption: black triangles, desorption: white triangles) gives BET surface areas of $681 \text{ m}^2 \text{ g}^{-1}$ for ATEBPY-COF, $470 \text{ m}^2 \text{ g}^{-1}$ for ATENPY-COF and $920 \text{ m}^2 \text{ g}^{-1}$ for ATEPPY-COF, respectively. QSDFT (carbon, cylindrical pores) derived pore size distributions showing the formation of micropores in ATEXPY-COFs with maxima between 1.2-1.4 nm consistent with the predicted pore size based on the AA' stacking structure model.

DTA/TG of TENPY

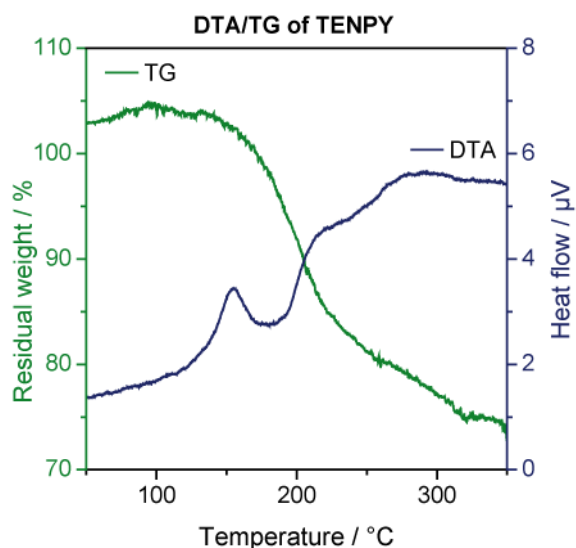


Figure 3.S36. DTA/TG in argon of TENPY monomer revealing its decomposition around 150°C.

Simulation of Ar Sorption and Pore Size Distribution.

Theoretical sorption calculations. Adsorption isotherm simulations were performed with the 'Sorption' module of *Materials Studio*. The Metropolis Monte Carlo method was utilized for calculation of the argon adsorption in the framework in 40 fugacity steps in a logarithmic scale (10^{-5} to 100 kPa), the Universal force field was selected for the energy calculation. All simulations included random insertion/deletion, translation, and rotation moves of molecules with equal probabilities. Atoms in COFs were fixed at their crystallographic positions. An LJ cutoff distance of 13 Å was used. The Ewald & Groups technique was used to compute the electrostatic interactions. All GCMC simulations included a 1,000,000-cycle equilibration period followed by a 10,000,000-cycle production run. The $2 \times 2 \times 2$ unit cell of ATEBPY-COF was used for simulations of the Ar adsorption isotherms at 87 K. BET surface areas were determined from the calculated isotherms by the same method used for treating experimental data at the low relative pressure range of 0.005 to 0.05. The calculated isotherms were imported to Quantachrome Versawin(R) sorption software. Pore size distributions were then calculated by application of the QSDFT (carbon, cylindrical pores) kernel.

Comparison of the calculated PSD with the experimental PSD clearly shows, that ATEBPY-COF is predominantly stacked in a AA'-type fashion.

Kubelka-Munk Plots

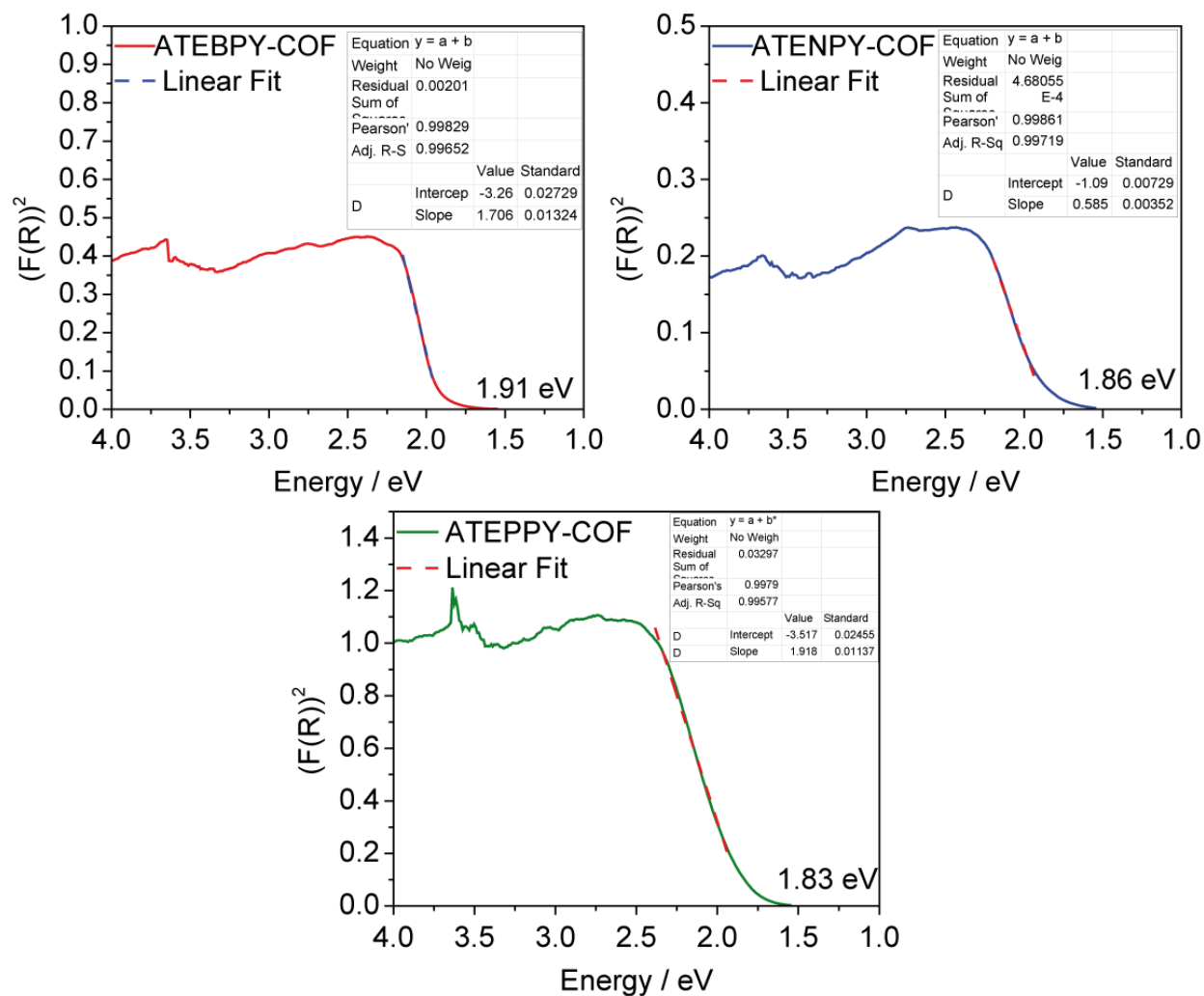


Figure 3.S37. Kubelka-Munk plots of ATEPY-COFs showing a decreasing bandgap with increasing nitrogen content.

Photoluminescence Spectra

Measurements were conducted by Florian Ehrat on a Horiba Fluorolog3. All samples were stirred during the measurement. Spikes in the PL spectra are artifacts of the stir bar hitting the glass wall of the cuvette.

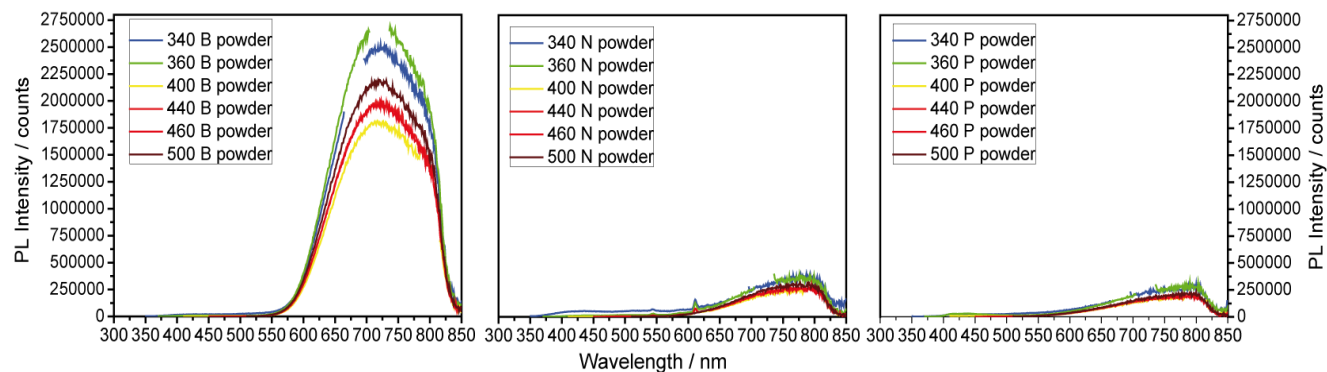


Figure 3.S38. PL emission plot of ATEBPY-COF, ATENPY-COF and ATEPPY-COF in powder form, showing the increasing PL intensity with decreasing nitrogen content.

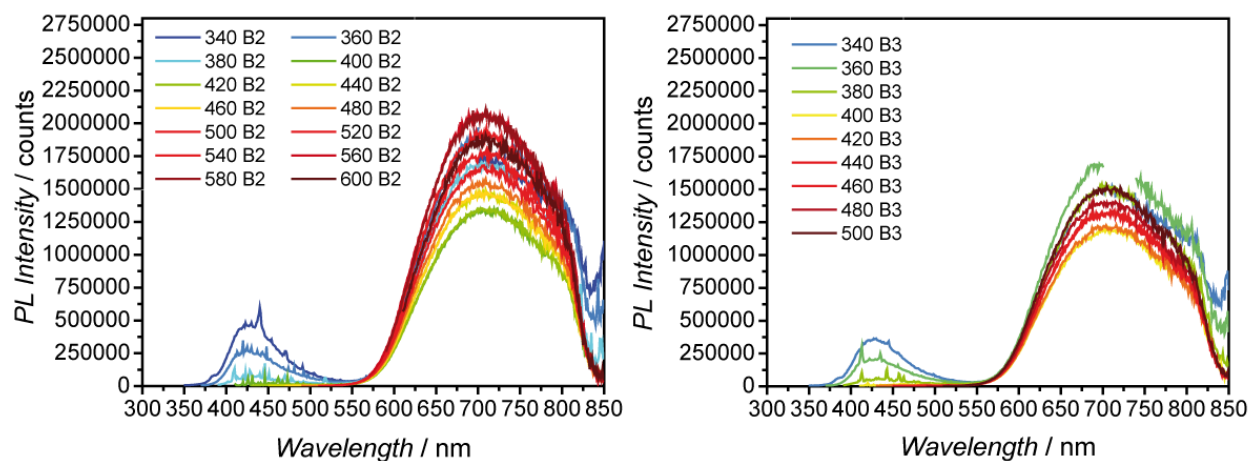


Figure 3.S39. PL emission spectra of ATEBPY-COF as a suspension in PBS buffer + TEOA (**B2**, left), in PBS buffer + TEOA + Pt (**B3**, right), showing the decrease in intensity (PL quench) after addition of i) TEOA and ii) TEOA + Pt to the suspension.

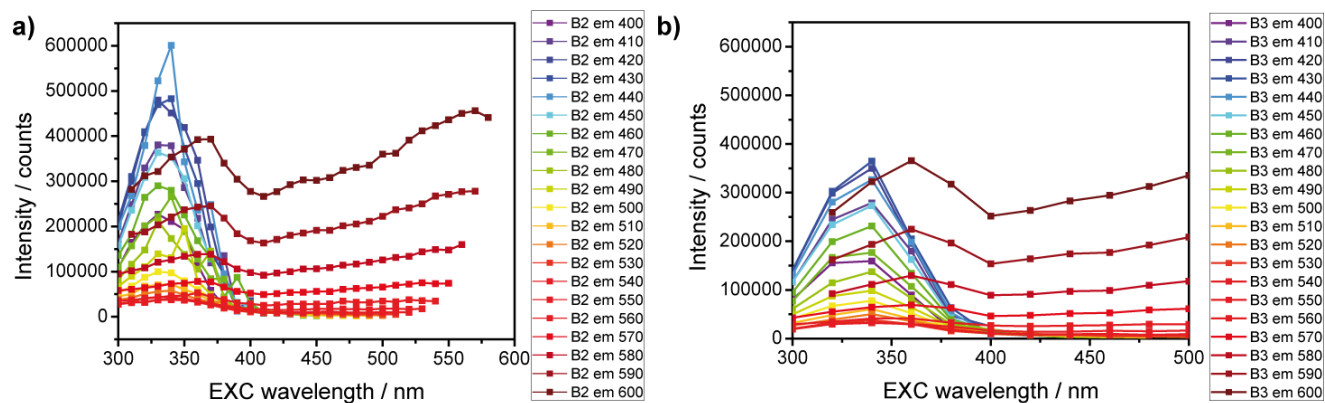


Figure 3.S40. Excitation spectra of ATEBPY-COF in PBS buffer + TEOA (**B2**, a), in PBS buffer + TEOA + Pt (**B3**, b), showing the decrease in intensity (PL quench) after addition of Pt to the suspension and the energy transfer.

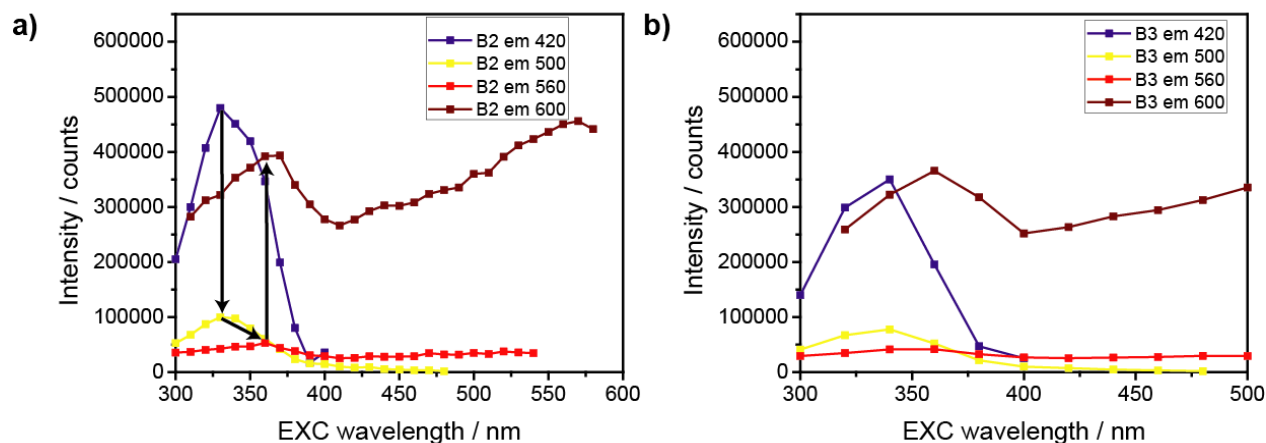


Figure 3.S41. Excitation spectra of ATEBPY-COF in PBS buffer + TEOA (**B2**, a), in PBS buffer + TEOA + Pt (**B3**, b), showing the decrease in intensity (PL quench) after addition of Pt to the suspension and the energy transfer.

References

- S1. H. Vollmann, H. Becker, M. Corell and H. Streeck, *Justus Liebigs Ann. Chem.*, 1937, **531**, 1–159.
- S2. S. Bernhardt, M. Kastler, V. Enkelmann, M. Baumgarten and K. Müllen, *Chem. - Eur. J.*, 2006, **12**, 6117–6128.
- S3. G. Venkataramana and S. Sankararaman, *Eur. J. Org. Chem.*, 2005, **2005**, 4162–4166.
- S4. O. V. Gutov, W. Bury, D. A. Gomez-Gualdrón, V. Krungleviciute, D. Fairen-Jimenez, J. E. Mondloch, A. A. Sarjeant, S. S. Al-Juaid, R. Q. Snurr, J. T. Hupp, T. Yildirim and O. K. Farha, *Chem. - Eur. J.*, 2014, **20**, 12389–12393.
- S5. S. Califano and G. Abbondanza, *The Journal of Chemical Physics*, 1963, **39**, 1016–1023.

4 COVALENT ORGANIC FRAMEWORKS AS SORBENTS FOR WATER VAPOR AND CARBON DIOXIDE SORPTION

4.1 Tunable Water and CO₂ Sorption Properties in Isostructural Azine-based Covalent Organic Frameworks through Polarity Engineering

Linus Stegbauer, Maximilian Werner Hahn, Andreas Jentys, Gökçen Savasci, Christian Ochsenfeld, Johannes A. Lercher and Bettina V. Lotsch

published in *Chem. Mater.* **2015**, 27, 7874–7881.

DOI: 10.1021/acs.chemmater.5b02151

<http://pubs.acs.org/doi/abs/10.1021/acs.chemmater.5b02151>

Formatting and numbering of figures were changed.

Adapted with permission from American Chemical Society.

Abstract

The use of covalent organic frameworks (COFs) in environmental settings such as atmospheric water capture or CO₂ separation under realistic pre- and post-combustion conditions is largely unexplored to date. Herein, we present two isostructural azine-linked COFs based on 1,3,5-triformyl benzene (AB-COF) and 1,3,5-triformylphloroglucinol (ATFG-COF) and hydrazine building units, respectively, whose sorption characteristics are precisely tunable by the rational design of the chemical nature of the pore walls. This effect is particularly pronounced for atmospheric water harvesting, which is explored for the first time using COFs as adsorbents. We demonstrate that the less polar AB-COF acts as a reversible water capture and release reservoir, featuring among the highest water vapor uptake capacity at low pressures reported to date (28 wt% at $<0.3 p p_0^{-1}$). Furthermore, we show tailored CO₂ sorption characteristics of the COFs through polarity engineering, demonstrating high CO₂ uptake at low pressures (< 1 bar) under equilibrium (sorption isotherm) and kinetic conditions (flow TGA, breakthrough) for the more polar ATFG-COF, and very high CO₂ over N₂ (IAST: 88) selectivity for the apolar AB-COF. In addition, the pore walls of both COFs were modified by doping with metal salts (lithium and zinc acetate), revealing an extremely high CO₂ uptake of 4.68 mmol g⁻¹ at 273 K for the zinc-doped AB-COF.

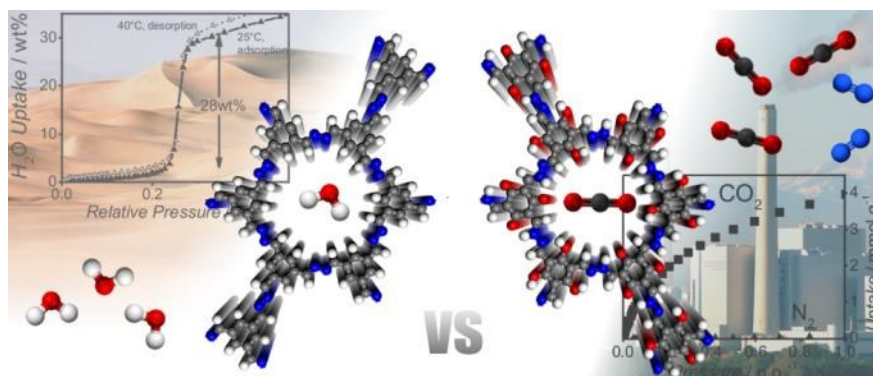


Table of Content

4.1.1 Introduction

Porous materials are key components in many environmental applications such as carbon capture and storage (CCS), atmospheric water capture (AWC) and adsorption chillers/heat pumps. CCS, which involves long-term storage of carbon dioxide underground, currently undergo rapid development as exemplified by test pilot CO₂ capture plants on the megawatt-scale in Germany and Norway. In the light of ongoing anthropogenic emission of CO₂ and its contribution to global warming,¹ new classes of CO₂-selective solid sorbents for carbon capture in power plants are highly desired to slow down the greenhouse effect and to overcome inherent difficulties (e.g. waste, corrosion, stability, efficiency) of established technologies such as amine scrubbing. Depending on the process parameters of CO₂ capture in fossil fuel-fired power plants, a high selectivity towards CO₂ over H₂ at high pressures (>10 atm) (pre-combustion capture) or over N₂ at low pressures (post-combustion capture) is desirable.^{2,3} While the implementation of inherently safe CCS technology is still a grand technical and societal challenge,⁴ the success of this scheme is contingent upon the availability of low-cost, high-capacity CO₂ sorbents with tailor-made sorption properties. Porous polymers, such as Covalent Organic Frameworks (COFs)⁵ or Covalent Triazine Frameworks (CTFs),^{6,7} are unique in the sense that not only their CO₂ uptake behavior can be easily tuned, but they constitute a versatile platform for the selective uptake and release of environmentally relevant gases and vapors in general, such as water.

Space and water heating accounts for more than 70% of the EU households' energy consumption,⁸ and fresh water generation is an ongoing problem in countries with arid climates, as it requires large amounts of energy. Water sorption-based thermally driven heat pumps can significantly help to minimize primary energy consumption generated by industrial or domestic heating and cooling applications. During the last years the development of water sorption technologies has progressed due to utilization of low-grade thermal (waste heat) or solarthermal energy. Currently, silica gel and zeolites are widely applied commercially,⁹ but these sorbents must be heated to 150°C for desorption, so they are far from ideal for the rather low temperatures generated by solar irradiation or waste heat. Furthermore, sorbents which possess high uptakes at low relative humidity (RH) around 30% (the global average vapor content in the atmosphere is 1 vol%, which

corresponds to 32% RH at 25°C)¹⁰ are most relevant for atmospheric water capture. In recent years, metal-organic frameworks and porous carbons came into focus as potential water sorbents.^{11–15} Besides initial experiments by Banerjee and co-workers,^{16–18} COFs have not been investigated as potential water sorbents in detail so far. COFs have garnered significant attention owing to their tunable pore sizes and high porosity combined with their long-range ordered crystalline structure. Yet until very recently, COFs have been largely absent as porous materials in environmental applications such as carbon capture and storage (CCS) or atmospheric water capture (AWC), due to a notable lack of ultramicroporous COFs with appropriate framework polarity and their generally poor hydrolytic stability. However, while most published COFs rely on the formation of water-labile boronate ester linkages, a few other COFs based on hydrolytically-stable connections such as azine¹⁹ and enamine^{20,21} have emerged.

Furthermore, the introduction of Lewis acidic sites into COFs, such as metal ions, has been proposed as a strategy to dramatically enhance their gas sorption capabilities. However, metal ions were never successfully integrated in COFs postsynthetically.^{22–26} It has been shown that doping with metal salts in MOFs can have a significant impact on gas uptakes, especially for CO₂ and H₂ sorption.^{27–30}

Here, we present two isostructural microporous COFs – an azine-benzene-COF (AB-COF) and azine-triformylphloroglucinol-COF (ATFG-COF) based on a water-stable azine linkage (see Figure 4.1) – and develop a versatile COF platform combining the key features for both CO₂ capture and water sorption, namely (i) high CO₂ uptake capacity, (ii) tunable polarity, and (iii) gated water-uptake at low relative humidity. We reveal that these two COFs, though featuring identical pore dimensions, show orthogonal CO₂ uptake behavior under low and high pressures, distinct interaction with CO₂, CO₂ selectivity and water vapor uptake, which can be traced back to differences in the polarity of the two frameworks.

While for AB-COF and ATFG-COF porosity, CO₂ uptake and Henry selectivity towards N₂ have already been investigated by Liu *et al.*,^{31,32} our work reports on the performance of both pristine and metal-doped species as water vapor sorbents for the first time. Furthermore, we comprehensively explore the kinetic CO₂ sorption performance and high-pressure CO₂ uptake of the doped and pristine COFs through flow-TGA and breakthrough measurements to obtain atomistic insights into the host-guest interactions at play.

Furthermore, we show the co-existence of two tautomeric forms in ATFG-COF by a detailed structural analysis, which has important implications for the sorption characteristics and stability of COFs based on the widely used TFG building block.

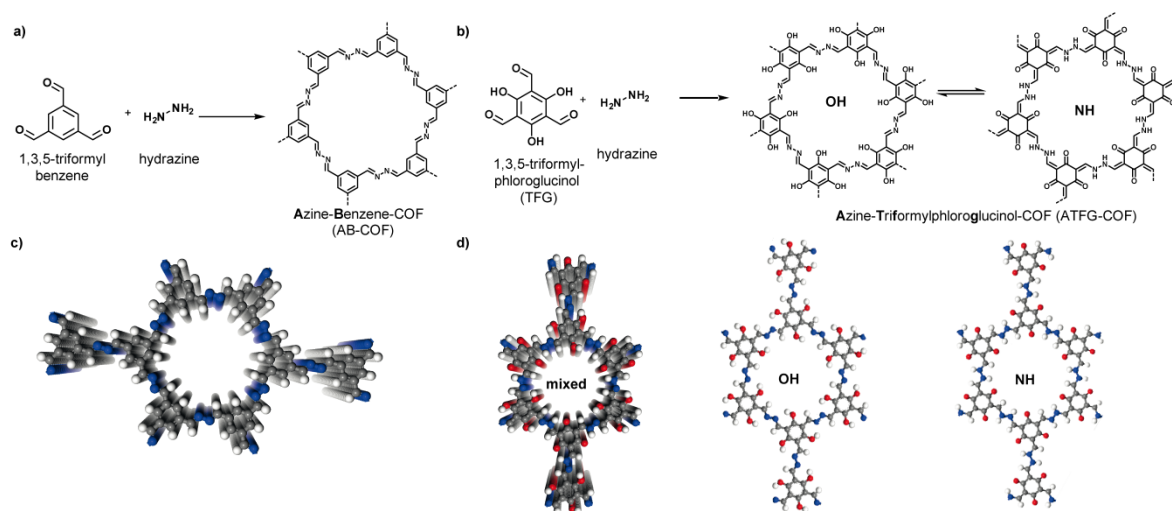


Figure 4.1: Acetic acid catalyzed azine formation furnishes two microporous honeycomb frameworks. (a) Scheme shows the condensation of hydrazine and 1,3,5-triformylbenzene to AB-COF. (b) The condensation of the two monomers to ATFG-COF results in two different tautomers: **OH** (left) and **NH** (right). (c) Structure representation of AB-COF with quasi-eclipsed layer stacking; (d) a mixture of both **OH** and **NH** tautomers within ATFG-COF with quasi-eclipsed layer stacking, and structure of the **OH** and **NH** tautomers (red: oxygen, blue: nitrogen, black: carbon, white: hydrogen.)

4.1.2 Results and Discussion

Synthesis and Structural Characterization of AB-COF and ATFG-COF

The direct comparison and impact of framework polarity on the sorption characteristics of COFs is only meaningful in systems with similar or identical pore dimensions. To this end, the less polar azine-benzene-COF (AB-COF, see Figure 4.1 a and b) and the more polar azine-triformylphloroglucinol-COF (ATFG-COF, see Figure 4.1 c and d) were selected as model systems for comparing the channel wall polarity in the microporous region.

While AB-COF has been published as A-COF1,³¹ ATFG-COF has been published as COF-JLU2 during the revision process.³² AB-COF and ATFG-COF were synthesized by the acetic acid catalyzed reversible condensation of the aldehyde and hydrazine building blocks at 120°C in sealed pressure vials under argon atmosphere for 72 hours (see Figure 4.1) (ESI for details). The products were obtained as fluffy nanocrystalline solids. To remove any starting material or solvent contained in the pores, both COFs were washed several times with methanol, DMF and THF, soaked in DCM for several hours, and subsequently heated to 120°C in high dynamic vacuum (10^{-7} mbar) for 12 h.

Powder x-ray diffraction measurements for both frameworks confirm the formation of crystalline polymers with the unit cell dimensions being consistent with the structure model shown in Figure 4.1 (see ESI for details of the cell metrics). Although ATFG-COF provides a lower crystallinity

than AB-COF (ESI, Figure 4.S1 and 4.S2), both frameworks can be described as hexagonal structures with an idealized $P6/m$ symmetry for the typical (close-to) eclipsed AA layer stacking (ESI, Figure 4.S3 and 4.S4). Note that COF-JLU2 shows a more pronounced crystallinity, probably due to improved synthesis conditions.³² A more detailed discussion of the stacking of ATFG-COF can be found in the sorption section. TEM analysis and selected area electron diffraction (SAED) for AB-COF shows distances of 13 Å (in plane) and 3.3 Å (out of plane) and for ATFG-COF 12 Å and 3.2 Å (ESI, Figure 4.S10). Importantly, both COFs do not show any sign of degradation when immersed in liquid water for hours as seen by PXRD and sorption (ESI, Figures 4.S11-12, Table 4.S1).

¹³C solid-state NMR MAS spectroscopy of AB-COF clearly supports the formation of an azine linkage with the adjacent double-bonded carbon-atom corresponding to the signal at 162 ppm (ESI, Figure 4.S13). The other two signals in the aromatic region (124 and 134 ppm) were also unambiguously assigned to corresponding carbon atoms. The ¹⁵N CP-MAS spectrum shows a single signal at -16 ppm, displaying the formation of the azine linkage (ESI, Figure 4.S13, including ¹H data).

Theoretically, ATFG-COF can exist in two tautomeric forms: A non-aromatic keto-enhydrazine tautomer (heteroradialene, **NH** form) and an aromatic enol-hydrazone (**OH** form) tautomer (see Figure 4.1 c, left and right). The metrics and scattering power of the two tautomers differ minimally, so that differentiation by PXRD is not possible. To get an indepth-view of the local structure of ATFG-COF, we performed a comprehensive solid-state NMR analysis and compared our data to the ¹⁵N shifts obtained from theoretical calculations.

¹⁵N CP-MAS solid-state NMR (Figure 4.2b) clearly indicates that both tautomeric forms, **OH** and **NH**, exist in ATFG-COF. Thus, the presence of the enamine C=C-N (**NH** form) was established by a resonance signal at -202 ppm (N₅), which corresponds well to typical enamines (**NH** form) formed by condensation of TFG with several amines.^{33,34} The more downfield shifted resonance at -92 ppm can be assigned to the imine nitrogen N₄ (**OH** form), which is involved in rather strong cyclic hydrogen bonding to the enol.³⁴ Calculated ¹⁵N chemical shifts for a mixed **OH-NH** form (see Figure 4.2d) using the FermiONs++ program package^{35,36} of a model hexagon (see ESI Figure 4.S19) correspond very well to the ¹⁵N signals observed for ATFG-COF (-197 ppm and -95.5 ppm, ESI, Figure 4.S20, Table 4.S2, see Figure 4.2b). Note that the relative weights of the two forms may be influenced by the presence of water in the pores (see ESI, Figure 4.S14).

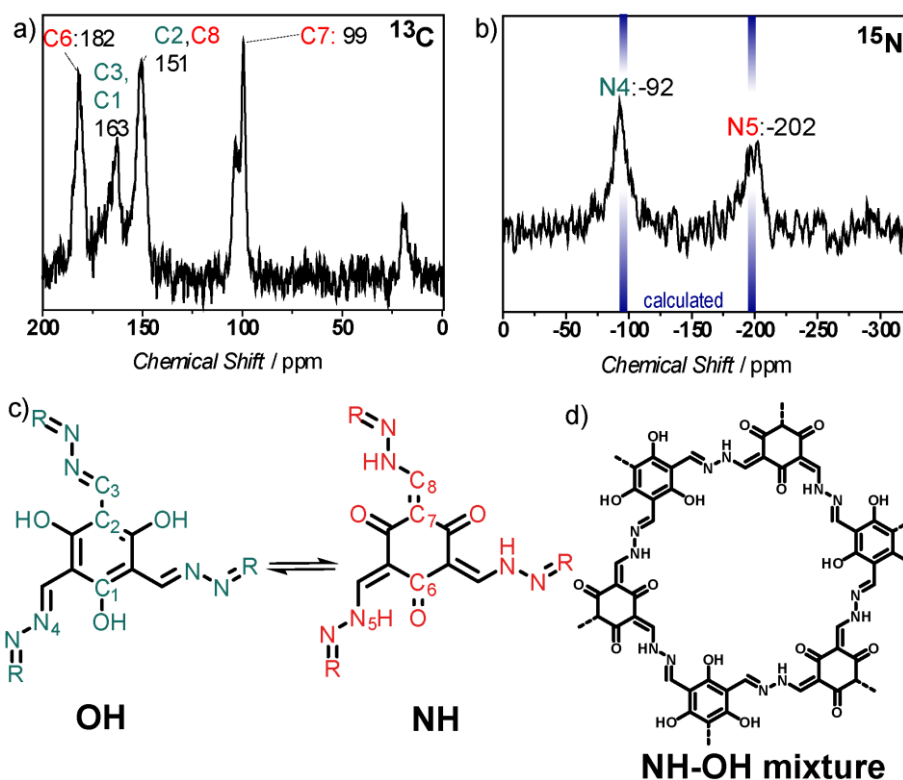


Figure 4.2: ssNMR spectra of ATFG-COF. (a) ^{13}C CP-MAS NMR spectrum, (b) ^{15}N CP-MAS NMR spectrum, blue lines show calculated NMR shifts for a hexagon exhibiting a local tautomeric mixture, (c) assignment of the signals to the **OH** and **NH** tautomeric forms of ATFG-COF. (d) idealized structure of a 50%-50% **NH-OH** local mixture.

^{13}C CP-MAS ssNMR analysis further confirmed the co-existence of two tautomeric structures of ATFG-COF. Two of the four resonances were clearly assigned to the **NH** form: The keto-carbon C_6 (see Figure 4.2a) was observed at 182 ppm and the sp^2 hybridized olefinic carbon C_7 at 99 ppm, which is consistent with the calculated ^{13}C chemical shifts (ESI, Table 4.S3) for the model hexagon (ESI, Figure 4.S20). The resonance at 163 ppm is assigned to both the imine carbon C_3 and the enol carbon C_1 of the **OH** form,³³ while the resonance signal at 151 ppm corresponds to both C_8 and C_2 (see Figure 4.2c for assignments, ESI, Figure 4.S14 for ^1H). We assume that the co-existence of both tautomers, consistent with a high degree of local order, may also be responsible for a lower degree of long-range order (i.e., crystallinity) as observed for ATFG-COF compared to AB-COF.

ATR-IR spectroscopy of AB-COF displays stretching modes in the range $1620\text{--}1630\text{ cm}^{-1}$, which are characteristic of $\text{C}=\text{N}$ moieties in azines.¹⁹ A broad band above 3000 cm^{-1} indicates water within the pores, which has also been detected by means of ^1H ssNMR (ESI, Figures 4.S14, 4.S21-22). The lack of the aldehyde Fermi double resonance at 2872 and 2747 cm^{-1} suggests the absence of the starting material 1,3,5-triformylbenzene. Compared to AB-COF, ATFG-COF shows a rather broad stretching mode between 1530 and 1630 cm^{-1} with a maximum at 1584 cm^{-1} , assignable to $\text{C}=\text{N}$ moieties. The less well-defined bands are an indication of the less ordered structure of ATFG-COF, which is again consistent with the presence of two tautomers.³⁷

Sorption Properties

Argon sorption measurements at 87 K clearly show the formation of micropores in both COFs as indicated by a typical type I adsorption isotherm (ESI, Figure 4.S25, Table 4.S4 for surface area comparison). The isotherm of ATFG-COF has additional type IV characteristics as seen by the small hysteresis extending across the entire relative pressure range. The Brunauer-Emmett-Teller (BET) surface area was calculated to be $1,125 \text{ m}^2 \text{ g}^{-1}$ (total pore volume: $0.47 \text{ cm}^3 \text{ g}^{-1}$, ESI, Figure 4.S25) for AB-COF and $520 \text{ m}^2 \text{ g}^{-1}$ (total pore volume: $0.50 \text{ cm}^3 \text{ g}^{-1}$, see ESI for details, Table 4.S4) for ATFG-COF. Although ATFG-COF, while surpassing COF-JLU2 ($410 \text{ m}^2 \text{ g}^{-1}$),³² shows a smaller BET surface area as compared to AB-COF, it is well in the range of other COFs having 1,3,5-triformylphloroglucinol as a building block ($180\text{-}740 \text{ m}^2 \text{ g}^{-1}$).^{18,21,20} A reason for this may be the decreased reversibility of the enamine bond-forming reaction compared to imine or azine linkage. The pore size distributions (PSD) were evaluated with DFT methods (NLDFT & QSDFT). The experimental PSD exhibits a maximum at 1.3 nm for AB-COF, thereby verifying the theoretical pore diameter of 1.3 nm derived from the structure model (ESI, Figure 4.S25), while the PSD of ATFG-COF shows a maximum around 0.6 nm, but also pores at 1.3 nm. Considering these data, the presence of ATFG-COF domains showing AB-type layer stacking has to be taken into account, as this stacking would result in 0.6 nm wide pores (see ESI Figure 4.S8 for a graphical illustration). While the XRD data are consistent with partial AB-type stacking, they suggest that a significant fraction of ATFG-COF adopts the close-to-eclipsed AA-stacking. Therefore, AB-COF and ATFG-COF represent excellent test systems for the effect of surface chemistry on the sorption of analytes.

Volumetric water vapor isotherms were conducted both at 288 K and 298 K (see Figure 4.3). While AB-COF adsorbs up to 41 wt% at $0.90 p p_0^{-1}$ (22.9 mmol g^{-1}), featuring a S-shape adsorption (IUPAC Type V) isotherm with a steep increase between 0.22 and $0.26 p p_0^{-1}$ (increase from 2.6 wt% (0.5 mmol g^{-1}) to 28 wt% (15.2 mmol g^{-1})) at 288 K (see Figure 4.3a), ATFG-COF with its more polar nitrogen and oxygen sites protruding into the pores adsorbs water vapor starting already at low pressures up to a total amount of 25 wt% at $0.90 p p_0^{-1}$ (13.6 mmol g^{-1}) (see Figure 4.3c), which is indicative of the more pronounced hydrophilicity of ATFG-COF.

Desorption measurements reveal residual water in AB-COF at $0.03 p p_0^{-1}$ (1.1 wt%), while for ATFG-COF a larger amount remains in the pores (2.9 wt%), thus testifying again to its more hydrophilic nature.

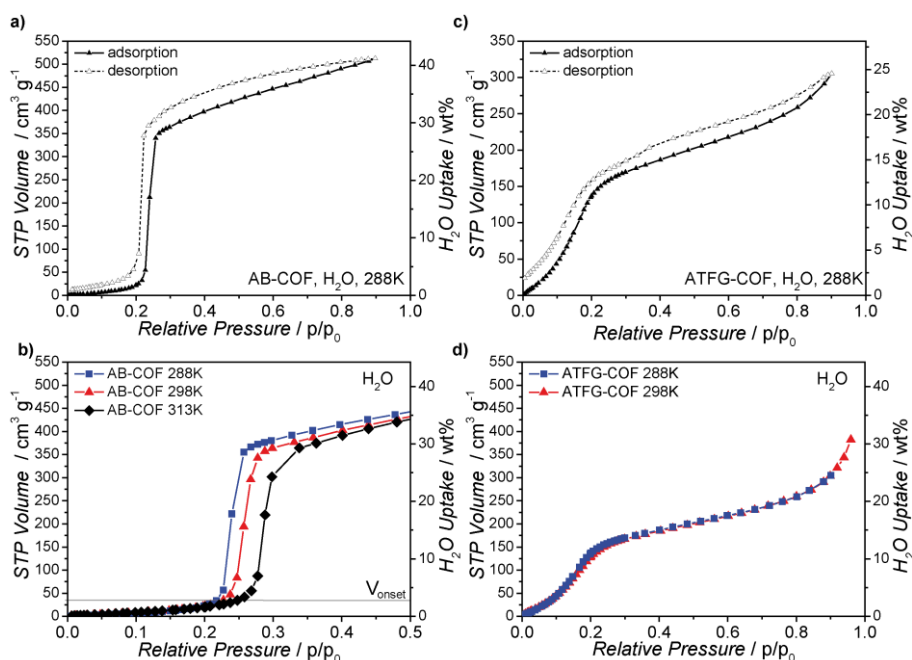


Figure 4.3: Water vapor sorption isotherms at 288 K of (a) AB-COF and (c) ATFG-COF. Comparison of the H₂O isotherms at different temperatures of (b) AB-COF and (d) ATFG-COF, showing two different vapor adsorption mechanisms.

Although both networks have nearly the same pore volume, ATFG-COF shows smaller overall water uptake than AB-COF, which likely is a result of ultra-micropores not accessible to the water sorptive. Overall, while the water vapor uptake behavior of ATFG-COF is similar to hydrophilic charcoals with a moderate uptake at low pressures, AB-COF exceeds most carbon-based water sorbents with an ultra-high uptake of 15.2 mmol g^{-1} at $p/p_0 = 0.26$.³⁸ The hydrophilicity of each network can easily be compared by analyzing the heats of adsorption Q_{st} which were calculated with the help of the Clausius–Clapeyron equation.

While at low coverage (lower than the onset volume, V_{onset} , Figure 4.3b) AB-COF shows a rather small Q_{st} (at zero coverage: 24 kJ mol^{-1}), which increases to an average of 49.4 kJ mol^{-1} between 4 and 30 wt%. This clearly points out that condensation in the confined space of the defined pores is an energetically favored process compared to the latent condensation energy of water (40.7 kJ mol^{-1}). Because the obtained Q_{st} values are higher than the condensation energy of water, AB-COF is an interesting candidate for heat/cooling pump applications. In stark contrast to this behavior, ATFG-COF exhibits very high Q_{st} at low coverages due to the high surface polarity, which steadily decreases to 50.7 kJ mol^{-1} at intermediate coverage (ESI, Figure 4.S26). Heats of adsorption have additionally been calculated by Dubinin-Radushkevich (DR) analysis for comparison, which yields similar Q_{st} values of $\approx 50 \text{ kJ mol}^{-1}$ (ESI, Figures 4.S27–28, Table 4.S5).^{39,40}

Interestingly, by increasing the temperature, AB-COF exhibits a pronounced shift of the knee of the S-shape isotherm towards higher relative pressures (see Figure 4.3b). This behavior can be rationalized by the temperature dependence of the capillary condensation pressure, which is in line with the Kelvin equation (ESI, Figure 4.S29).⁴¹ Capillary condensation has only been shown

to rarely occur in microporous materials and at such low relative pressures ($< 0.3 p/p_0^{-1}$).^{42,43} The rather hydrophobic pore wall of AB-COF weakens vapor-wall interactions such that water vapor uptake first proceeds through complete wetting of the pore walls until a critical film thickness is reached, followed by capillary condensation. Thus, for increasing temperatures higher relative pressures are necessary to achieve this critical thickness.⁴⁴ We note that a similar phenomenon has been observed for activated charcoals and the MOF CAU-10-H,^{45,46,42} yet not for such low relative pressures. In contrast, ATFG-COF has a different water sorption mechanism: We find a gradual consecutive filling of the pores as a result of the higher pore wall polarity (see Figure 4.3c). Therefore, we do not find a notable shift of the isotherm to higher relative pressure with increasing temperature (see Figure 4.3d), which is reminiscent of water vapor isotherms of zeolites.⁴²

AB-COF shows a steep tenfold increase in water uptake within an absolute humidity window as small as 4% at pressures lower than $0.3 p/p_0^{-1}$. This unique feature, together with the unprecedentedly high water uptake capacity at low pressures, distinguishes AB-COF from most other water vapor adsorbents such as MOFs,^{39,42,46-49} and COFs, for which only preliminary water adsorption studies exist.¹⁶⁻¹⁸ Therefore, it renders AB-COF an interesting candidate for atmospheric water capture sorbents for hot desert regions where ground water supply is scarce. These arid areas usually show the highest temperature contrasts between day and night (diurnal temperatures) accompanied by a stark change in humidity. In these regions the typical temperature approaches 45 °C at day with relative humidities lower than 20%. At night there is a huge drop in temperature to around 25°C and an increase in relative humidity to values higher than 50% (equals to $p/p_0^{-1} = 0.5$). This climate enables systems such as AB-COF to act as a water capture and release reservoir, being recharged at night and delivering humidity at day with a capacity as high as 28 wt% (ESI, Figure 4.S30) for water supply or for cooling applications by desorption. Both ATFG-COF and AB-COF show steady and fully reversible water vapor sorption over 4 ad-/desorption cycles with no apparent decline in capacity (ESI, Figure 4.S32).

Modification with Metal Salts

Microporous materials are particularly interesting candidates for carbon dioxide capture in pre- or post-combustion applications which require appropriately adjusted selectivities for CO₂ over other constituents of the gas/vapor mixture under well-defined temperature and pressure conditions. To this end, we investigated the CO₂ sorption capabilities of the two COFs as a function of their channel wall polarity (see Figure 4.4). In addition, we chemically modified the channels by means of metal-doping, which had been predicted earlier to enhance gas sorption capacities and selectivities.²²⁻²⁵ Therefore, AB-COF and ATFG-COF were loaded with either lithium or zinc acetate (LiOAc \times 2 H₂O and Zn(OAc)₂ \times 2 H₂O) by dissolving the salts in methanol and then adding the COF (see ESI for details).

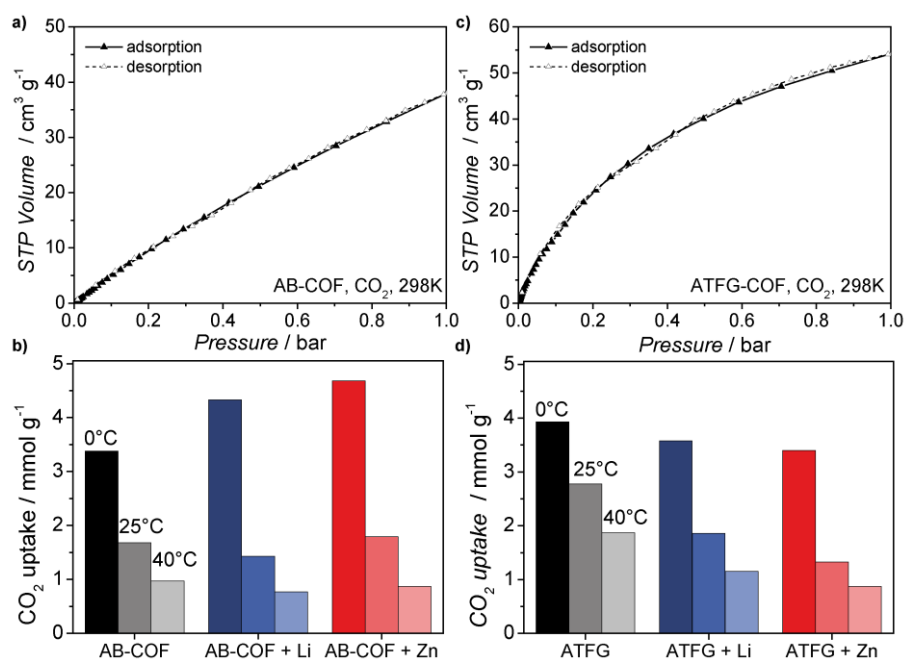


Figure 4.4: CO₂ isotherms at 298 K of (a) AB-COF and (c) ATFG-COF. Comparison of the CO₂ uptakes of metal-doped (b) AB-COF and (d) ATFG-COF with the pristine COFs at different temperatures.

After soaking and washing, Li@AB-COF/Li@ATFG-COF and Zn@AB-COF/Zn@ATFG-COF were obtained, which showed metal loadings of 8% (with respect to all available coordination sites, see ESI for details) for Zn@ATFG-COF, 1% for Li@ATFG-COF, 0.6% for Zn@AB-COF, and 0.8% for Li@AB-COF.

FTIR analysis ascertained that all COFs retained their local structure, and Ar sorption revealed their porous nature (ESI, Table S9), although the accessible BET surface area was lower in all cases (by <10% for AB-COF derivatives, >50% for ATFG-COF derivatives). Higher metal loading in ATFG-COF is expected due to its higher pore polarity, which offers more Lewis-basic sites. To get insights into the local order of the metal-doped COFs, ssNMR spectroscopy was performed, which largely coincides with the spectra of the pristine bulk materials (ESI, Figures 4.S34-S35). Remarkably, ¹⁵N CP MAS NMR of metal@ATFG-COF reveals a new signal at -69 ppm near the imine resonance, which suggests that the metal coordinates preferably to the imine nitrogen of ATFG-COF (see Figure 4.S34).

CO₂ Sorption and Selectivity

Pristine AB-COF shows a CO₂ uptake of 3.38 mmol g⁻¹ at 273 K. The metal-doped forms of AB-COF exhibit enhanced carbon dioxide uptake of 4.68 mmol g⁻¹ (Zn@AB-COF) and 4.33 mmol g⁻¹ (Li@AB-COF), which is an increase by 38% and 28%, respectively, compared to the undoped AB-COF. The doped COF thus outperforms most porous polymers such as BILP-10 (4.02 mmol g⁻¹),⁵⁰ PPN-6-SO₃Li (4.26 mmol g⁻¹)⁵¹ and CTF-6PM (4.20 mmol g⁻¹)⁵², PCTF-1 (3.24 mmol g⁻¹)⁶, PCTF-5 (2.58 mmol g⁻¹)⁷ and, to the best of our knowledge, surpasses all 2D

and 3D COFs reported to date, such as TpPa-1 (3.57 mmol g^{-1}),²⁰ COF-6 (3.84 mmol g^{-1})⁵ or 3D COF-103 (1.73 mmol g^{-1}).⁵ With increasing temperature (298 K and 313 K, ESI, Figure 4.4b and d) the advantage of doping becomes gradually less apparent. In contrast, while metal-doped ATFG-COF does not show any enhanced carbon dioxide uptake at any temperature as compared to the undoped material, the uptake capacity of the pristine ATFG-COF is already as high as 3.93 mmol g^{-1} at 273 K, 2.40 mmol g^{-1} at 298 K and 1.87 mmol g^{-1} at 313 K (see ESI Table 4.S9 for the uptakes of metal-doped ATFG-COF, see Figure 4.S38 for isotherms). Heats of adsorption Q_{st} were shown to be generally higher for ATFG-COF materials ($33.3\text{-}42.6 \text{ kJ mol}^{-1}$) than for AB-COF materials ($29.7\text{-}32.2 \text{ kJ mol}^{-1}$, ESI, Figure 4.S39), which is again in line with the increased polarity of ATFG-COF.

While the doping of AB-COF by metal ions significantly enhances the CO_2 uptake, ATFG-COF, which offers hemi-chelating coordination sites (see ESI Figure 4.S33), does not show any improvement. Whereas the exposed metal-sites⁵³ in doped AB-COF may lead to stronger CO_2 affinity than that provided by the azine-moieties in the undoped COF, the inherently stronger sorption sites of pristine ATFG-COF may be blocked by the metal ions and, hence, the CO_2 affinity of the doped ATFG-COF is lower than that of the parent material.

Notably, both ATFG-COF and AB-COF retain their excellent carbon dioxide uptake performance after being exposed to liquid water (ESI, Figures 4.S11-S12). Also, both COF materials do not show a notable decline in BET surface area after this treatment (ESI Table S1).

In the next step, we studied the suitability of both COFs as potential flue gas sorbents by calculating the CO_2 over N_2 selectivity at 298 K based on the ideal adsorbed solution theory (IAST) (85 vol% N_2 / 15 vol% CO_2) and Henry selectivity (see ESI for details, ESI, Figures 4.S40-S41). According to the more realistic IAST, the material with the highest selectivity is AB-COF (Henry: 102, IAST: 88), followed by Zn@ATFG-COF (Henry: 98, IAST: 84). Apart from Li@AB-COF (13/16) and Zn@AB-COF (48/55) all other samples still have higher selectivities (>65) compared to other porous polymers such as CTFs (IAST between 20-41).^{37,54} AB-COF with the highest selectivity even outperforms the recently published $[\text{HO}_2\text{C}]_{100\%}\text{-H}_2\text{P-COF}$ (77).⁵⁵ The best overall performing material with respect to both uptake and selectivity is pristine ATFG-COF (Henry: 151, IAST: 65), for which IAST and Henry selectivities have also been measured at 313 K (69/68).

We have further addressed the performance of our materials under pre-combustion (high pressure CO_2 adsorption) and post-combustion conditions (thermogravimetric analysis under flow conditions, breakthrough experiments) by simulation of different pressure and temperature scenarios as well as gas mixtures. To this end, the syntheses of four of the above materials were scaled up to obtain 1 g of each COF.

Kinetic CO_2 Performance.

First, the adsorption of CO₂ under flow conditions at atmospheric pressure (10 vol% CO₂ in N₂) as relevant in post-combustion capture was studied by means of thermogravimetric analysis. Indeed, a higher uptake of ATFG-COF at 30 °C (0.3 mmol g⁻¹) and 50 °C (0.15 mmol g⁻¹) was observed, which is a result of its higher channel wall polarity and the resulting Langmuir-type CO₂ adsorption behavior as compared to AB-COF and its metal-doped derivatives (ESI, Figure 4.S42).

To further investigate post-combustion performance the most promising material ATFG-COF was used in breakthrough experiments. It is the first time that breakthrough experiments have been applied to COFs.

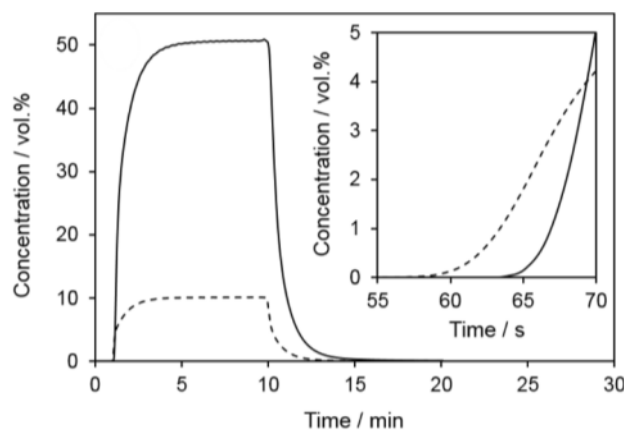


Figure 4.5: Breakthrough curves of ATFG-COF. CO₂ (solid line) and Ar (dotted line). Time before CO₂ breakthrough of ATFG-COF (162 mg) is 6 s.

The breakthrough curve of ATFG-COF in a gas flow (50 vol% CO₂, 40 vol% N₂, 10 vol% Ar as tracer, 50 °C) was well-defined with an uptake of CO₂ before breakthrough of 1.2 mmol g⁻¹ for ATFG-COF. (Figure 4.5, see ESI for details). This uptake is comparable to the single gas CO₂ isotherm measured at 313 K ($p/p_0 = 0.5$, 1.23 mmol g⁻¹). The adsorption process was fully reversible in pure N₂ already at the adsorption temperature of 50 °C, and no further CO₂ was detected by an increase of the desorption temperature to 100 °C. This is in agreement with the relatively weak interaction of the sorbent with CO₂ (physisorption) as expected from heats of adsorption of 29-33 kJ mol⁻¹.

H₂/CO₂ High Pressure Performance.

Next, the materials were further investigated by high pressure CO₂/H₂ adsorption. Under pre-combustion separation conditions, CO₂ has to be selectively adsorbed over H₂ at maximum pressures up to 30 bar at 35 °C.^{56,57} The most applied method for pre-combustion CO₂ capture at elevated pressures is a separation of CO₂/H₂ by a reduction of the pressure during the desorption step (pressure swing adsorption, PSA).

The adsorption isotherms at 35 °C as a function of pressure up to 30 bar are illustrated in Figure 4.6. The trend of the H₂ isotherms is comparable for all sorbents with a maximum of approximately 4 mmol g⁻¹ at 30 bar (Figure 4.6, see ESI for details). Notably, the CO₂ sorption capacity of

ATFG-COF is significantly lower under these conditions as compared to AB-COF, which is most noticeable at higher pressures (Figure 4.6). While the hydrophilic ATFG-COF adsorbs far more CO₂ at pressures <1 bar due to its Langmuir-type sorption behavior (see Figure 4.4), the doubled BET area of AB-COF plays a crucial role in high pressure capacity. The molar amount of adsorbed CO₂ on ATFG-COF was lower compared to H₂ when the partial pressure was higher than 5 bar (Figure 4.6a).

The adsorption capacities of the pristine and doped AB-COFs are in a similar range as that of silica-based physisorptive materials commonly studied for high pressure CO₂ capture and storage.⁵⁷ In comparison to zeolite 13 X, a benchmark adsorbent for CO₂ separation, the isotherms are more applicable for pressure swing applications, i.e., desorption at lower partial pressures.

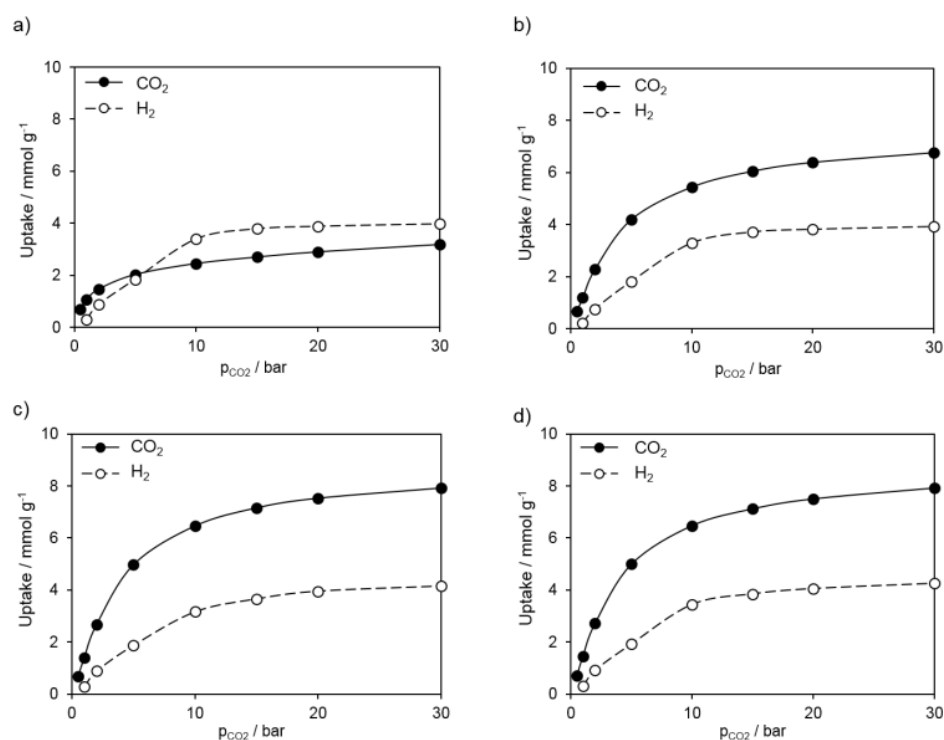


Figure 4.6: High-pressure adsorption isotherms of (a) ATFG-COF, (b) AB-COF, (c) Li@AB-COF and (d) Zn@AB-COF. CO₂ (filled circles) and H₂ (empty circles).

In contrast, the adsorption isotherms of CO₂ for both undoped and metal-doped AB-COF samples were significantly steeper as compared to H₂ and therefore an efficient separation of CO₂/H₂ is possible over the total pressure range up to 30 bar.

The maximum CO₂ uptake at 30 bar increased by 25% when Li (35 wt%) and Zn (35 wt%) were incorporated as compared to pristine AB-COF (28 wt%) (Figure 4.6b, c and d). A similar trend after metal-doping has been observed for Li@HKUST-1 for high pressure CO₂ adsorption as well.³⁰ This increase in the maximum adsorption capacity in combination with the largely unchanged H₂ uptake allows a higher CO₂ separation capacity and therefore renders Zn@AB-COF and Li@AB-COF most applicable for high pressure CO₂ capture.

4.1.3 Conclusion

In conclusion, we have developed a versatile COF platform comprising two isostructural crystalline azine-based COFs, AB-COF and ATFG-COF, featuring identical pore topologies but widely different framework polarities. The more polar ATFG-COF forms two tautomeric structures at room temperature, which have been identified and shown to co-exist for the first time in covalent organic frameworks. The COFs were doped with metal salts and the pore channel polarity was determined by a systematic study of their carbon dioxide and water sorption characteristics, which were identified as suitable descriptors for the framework polarities and gas/vapor loading capacities. ATFG-COF exhibits high CO₂ uptake at low pressures and good selectivity, along with good uptakes under atmospheric flow conditions (TGA and breakthrough experiments), which makes this polar COF a promising candidate for post-combustion CO₂ capture. Furthermore, we show that modification of AB-COF with Zn yields the highest CO₂ uptake observed for COFs to date, boding well for the potential of metal-doping to enhance and tailor the gas and vapor sorption characteristics of COFs. We further find that AB-COF with its distinct S-shape adsorption profile exhibits extremely high water uptake capacities already at low pressures, which is, to our knowledge, among the highest at pressures $< 0.3 p p_0^{-1}$ for all carbon-based porous materials.³⁸ This renders AB-COF an intriguing candidate for atmospheric water capture and release in arid climates, e.g. in deserts. In addition, AB-COF shows a 23% increase in the heat of adsorption compared to the condensation energy of water, which is a desired feature for application as a desiccant in heat pumps.

4.1.4 Bibliography

Author Contributions

Linus Stegbauer wrote the manuscript, edited the figures, designed and did the synthesis of all COFs, did sorption measurements, simulated the COF structure and PXRDs, and did the spectral characterization. Maximilian Hahn did flow the TGA and breakthrough experiments, including their evaluation and wrote a part of the manuscript. Gökçen Savasci did the theoretical calculation of ssNMR ¹³C and ¹⁵N chemical shifts and wrote a part of the manuscript.

Acknowledgment

Financial support by the Max Planck Society, Deutsche Forschungsgemeinschaft (SPP 1362), Fonds der Chemischen Industrie, FCI (scholarship for L. S.), the cluster of excellence "Nanosystems Initiative Munich" (NIM) and the Center for NanoScience (CeNS) is gratefully acknowledged. We thank Prof. T. Bein and Prof. W. Schnick for granting access to the XRD and NMR facility, and V. Duppel, C. Minke, S Hug for their assistance with the material analysis. C.O. acknowledges SFB749 for financial support.

References

1. T. Stocker, L. Alexander and M. Allen, *Climate change 2013: The physical science basis ; Working Group I contribution to the fifth assessment report of the Intergovernmental Panel on Climate Change*, WMO IPCC, Geneva, 2014.
2. M. E. Boot-Handford, J. C. Abanades, E. J. Anthony, M. J. Blunt, S. Brandani, N. Mac Dowell, J. R. Fernandez, M.-C. Ferrari, R. Gross, J. P. Hallett, Haszeldine, R. Stuart, P. Heptonstall, A. Lyngfelt, Z. Makuch, E. Mangano, Porter, Richard T. J., M. Pourkashanian, G. T. Rochelle, N. Shah, J. G. Yao and P. S. Fennell, *Energy Environ. Sci.*, 2014, **7**, 130–189.
3. D. M. D'Alessandro, B. Smit and J. R. Long, *Angew. Chem., Int. Ed.*, 2010, **49**, 6058–6082.
4. International Energy Agency, *Carbon Capture and Storage: Legal and Regulatory Review*, http://www.iea.org/publications/insights/insightpublications/CCSReview_4thEd_FINAL.pdf (last accessed April 2015).
5. H. Furukawa and O. M. Yaghi, *J. Am. Chem. Soc.*, 2009, **131**, 8875–8883.
6. A. Bhunia, V. Vasylyeva and C. Janiak, *Chem. Commun. (Cambridge, U. K.)*, 2013, **49**, 3961–3963.
7. A. Bhunia, I. Boldog, A. Moller and C. Janiak, *J. Mater. Chem. A*, 2013, **1**, 14990–14999.
8. European Environment Agency, *Household energy consumption by end-use in the EU-27*, <http://www.eea.europa.eu/data-and-maps/figures/households-energy-consumption-by-end-uses-4> (last accessed April 2015).
9. E.-P. Ng and S. Mintova, *Microporous Mesoporous Mater.*, 2008, **114**, 1–26.
10. NASA, *Earth Fact Sheet*, <http://nssdc.gsfc.nasa.gov/planetary/factsheet/earthfact.html> (last accessed April 2015).
11. F. Jeremias, V. Lozan, S. K. Henninger and C. Janiak, *Dalton Trans.*, 2013, **42**, 15967–15973.
12. P. Küsgens, M. Rose, I. Senkovska, H. Fröde, A. Henschel, S. Siegle and S. Kaskel, *Microporous Mesoporous Mater.*, 2009, **120**, 325–330.
13. K. László, O. Czakkel, G. Dobos, P. Lodewyckx, C. Rochas and E. Geissler, *Carbon*, 2010, **48**, 1038–1048.
14. J. K. Brennan, T. J. Bandosz, K. T. Thomson and K. E. Gubbins, *Colloids Surf., A*, 2001, **187–188**, 539–568.

15. N. C. Burtch, H. Jasuja and K. S. Walton, *Chem. Rev. (Washington, DC, U. S.)*, 2014, **114**, 10575–10612.
16. B. P. Biswal, S. Chandra, S. Kandambeth, B. Lukose, T. Heine and R. Banerjee, *J. Am. Chem. Soc.*, 2013, 5328–5331.
17. D. B. Shinde, S. Kandambeth, P. Pachfule, R. R. Kumar and R. Banerjee, *Chem. Commun. (Cambridge, U. K.)*, 2015, **51**, 310–313.
18. S. Kandambeth, V. Venkatesh, D. B. Shinde, S. Kumari, A. Halder, S. Verma and R. Banerjee, *Nat. Commun.*, 2015, **6**, Article No. 6786.
19. S. Dalapati, S. Jin, J. Gao, Y. Xu, A. Nagai and D. Jiang, *J. Am. Chem. Soc.*, 2013, **135**, 17310–17313.
20. S. Chandra, S. Kandambeth, B. P. Biswal, B. Lukose, S. M. Kunjir, M. Chaudhary, R. Barbarao, T. Heine and R. Banerjee, *J. Am. Chem. Soc.*, 2013, **135**, 17853–17861.
21. S. Kandambeth, A. Mallick, B. Lukose, M. V. Mane, T. Heine and R. Banerjee, *J. Am. Chem. Soc.*, 2012, **134**, 19524–19527.
22. F. Gao, Z. Ding and S. Meng, *Sci. Rep.*, 2013, **3**, 1882.
23. J.-H. Guo, H. Zhang, M. Gong and X.-L. Cheng, *Struct. Chem.*, 2013, **24**, 691-703.
24. J.-H. Guo, H. Zhang and Y. Miyamoto, *Phys. Chem. Chem. Phys.*, 2013, **15**, 8199–8207.
25. J.-H. Guo, H. Zhang, Z.-P. Liu and X.-L. Cheng, *J. Phys. Chem. C*, 2012, **116**, 15908–15917.
26. X. Feng, L. Liu, Y. Honsho, A. Saeki, S. Seki, S. Irle, Y. Dong, A. Nagai and D. Jiang, *Angew. Chem., Int. Ed.*, 2012, **51**, 2618–2622.
27. Y.-S. Bae, B. G. Hauser, O. K. Farha, J. T. Hupp and R. Q. Snurr, *Microporous Mesoporous Mater.*, 2011, **141**, 231–235.
28. M. Bosch, M. Zhang, D. Feng, S. Yuan, X. Wang, Y.-P. Chen and H.-C. Zhou, *APL Mater.*, 2014, **2**, 124103.
29. M. Kubo, A. Shimojima and T. Okubo, *J. Phys. Chem. C*, 2012, **116**, 10260–10265.
30. Z. Xiang, Z. Hu, D. Cao, W. Yang, J. Lu, B. Han and W. Wang, *Angew. Chem., Int. Ed.*, 2011, **50**, 491–494.
31. Z. Li, X. Feng, Y. Zou, Y. Zhang, H. Xia, X. Liu and Y. Mu, *Chem. Commun. (Cambridge, U. K.)*, 2014, **50**, 13825–13828.
32. Z. Li, Y. Zhi, X. Feng, X. Ding, Y. Zou, X. Liu and Y. Mu, *Chem. - Eur. J.*, 2015, **21**, 12079–12084.

33. A. Makal, W. Schilf, B. Kamieński, A. Szady-Chelmieńska, E. Grech and K. Woźniak, *Dalton Trans.*, 2011, **40**, 421–430.
34. B. Feldscher, A. Stammeler, H. Bögge and T. Glaser, *Chem. - Asian J.*, 2014, **9**, 2205–2218.
35. J. Kussmann and C. Ochsenfeld, *J. Chem. Phys.*, 2013, **138**, 134114.
36. J. Kussmann and C. Ochsenfeld, *J. Chem. Theory Comput.*, 2015, **11**, 918–922.
37. S. Hug, M. B. Mesch, H. Oh, N. Popp, M. Hirscher, J. Senker and B. V. Lotsch, *J. Mater. Chem. A*, 2014, **2**, 5928–5936.
38. G.-P. Hao, G. Mondin, Z. Zheng, T. Biemelt, S. Klosz, R. Schubel, A. Eychemüller and S. Kaskel, *Angew. Chem., Int. Ed.*, 2015, **54**, 1941–1945.
39. G. Akiyama, R. Matsuda and S. Kitagawa, *Chem. Lett.*, 2010, **39**, 360–361.
40. Dubinin, M. M., *Chem. Rev. (Washington, DC, U. S.)*, 1960, **60**, 235–241.
41. M. Thommes, J. Morell, K. A. Cychoz and M. Fröba, *Langmuir*, 2013, **29**, 14893–14902.
42. H. Furukawa, F. Gándara, Y.-B. Zhang, J. Jiang, W. L. Queen, M. R. Hudson and O. M. Yaghi, *J. Am. Chem. Soc.*, 2014, **136**, 4369–4381.
43. Y.-K. Seo, J. W. Yoon, J. S. Lee, Y. K. Hwang, C.-H. Jun, J.-S. Chang, S. Wuttke, P. Bazin, A. Vimont, M. Daturi, S. Bourrelly, P. L. Llewellyn, P. Horcajada, C. Serre and G. Férey, *Adv. Mater. (Weinheim, Ger.)*, 2012, **24**, 806–810.
44. G. Q. Lu and X. S. Zhao, *Nanoporous materials: Science and engineering*, Imperial College Press, London, 2004.
45. D. Xu, P. Xiao, J. Zhang, G. Li, G. Xiao, P. A. Webley and Y. Zhai, *Chem. Eng. J. (Amsterdam, Neth.)*, 2013, **230**, 64–72.
46. D. Frohlich, S. K. Henninger and C. Janiak, *Dalton Trans.*, 2014, **43**, 15300–15304.
47. F. Jeremias, A. Khutia, S. K. Henninger and C. Janiak, *J. Mater. Chem.*, 2012, **22**, 10148–10151.
48. S. K. Henninger, F. Jeremias, H. Kummer and C. Janiak, *Eur. J. Inorg. Chem.*, 2012, 2625–2634.
49. A. Khutia, H. U. Rammelberg, T. Schmidt, S. Henninger and C. Janiak, *Chem. Mater.*, 2013, **25**, 790–798.
50. M. G. Rabbani, A. K. Sekizkardes, O. M. El-Kadri, B. R. Kaafarani and H. M. El-Kaderi, *J. Mater. Chem.*, 2012, **22**, 25409–25417.
51. W. Lu, D. Yuan, J. Sculley, D. Zhao, R. Krishna and H.-C. Zhou, *J. Am. Chem. Soc.*, 2011, **133**, 18126–18129.

52. S. Ren, M. J. Bojdys, R. Dawson, A. Laybourn, Y. Z. Khimyak, D. J. Adams and A. I. Cooper, *Adv. Mater. (Weinheim, Ger.)*, 2012, **24**, 2357–2361.
53. J. Lan, D. Cao, W. Wang and B. Smit, *ACS Nano*, 2010, **4**, 4225–4237.
54. Y. Zhao, K. X. Yao, B. Teng, T. Zhang and Y. Han, *Energy Environ. Sci.*, 2013, **6**, 3684–3692.
55. N. Huang, X. Chen, R. Krishna and D. Jiang, *Angew. Chem., Int. Ed.*, 2015, **54**, 2986–2990.
56. M. Kanniche, R. Gros-Bonnivard, P. Jaud, J. Valle-Marcos, J.-M. Amann and C. Bouallou, *Appl. Therm. Eng.*, 2010, **30**, 53–62.
57. M. W. Hahn, M. Steib, A. Jentys and J. A. Lercher, *J. Mater. Chem. A*, 2014, **2**, 13624–13634.

4.1.5 Supporting Information

Materials and Methods

All reagents were purchased from commercial sources and used without further purification. The starter 1,3,5-triformylphloroglucinol^{S1} was prepared according to ref.^{S1} and the NMR data are consistent with those given in the literature.

Infrared spectra were recorded on a Perkin Elmer Spektrum BX II FT-IR equipped with an ATR unit (Smith Detection Dura-Sample IIR diamond). The spectra were background-corrected.

The ¹³C and ¹⁵N **MAS NMR spectra** were recorded at ambient temperature on a Bruker Avance 500 solid-state NMR spectrometer, operating at frequencies of 500.1 MHz, 125.7 MHz and 50.7 MHz for ¹H, ¹³C and ¹⁵N, respectively. The sample was contained in a 4 mm ZrO₂ rotor (Bruker) which was mounted in a standard double resonance MAS probe. The ¹³C and ¹⁵N chemical shifts were referenced relative to TMS and nitromethane, respectively.

The ¹H-¹⁵N and ¹H-¹³C cross-polarization (CP) MAS spectra were recorded at a spinning speed of 10 kHz using a ramped-amplitude (RAMP) CP pulse on ¹H, centered on the $n = +1$ Hartmann-Hahn condition, with a nutation frequency ν_{nut} of 55 kHz (¹⁵N) and 40 kHz (¹³C). During a contact time of 7 ms the ¹H radio frequency field was linearly varied about 20%.

Powder x-ray diffraction data were collected using a Bruker D8-advance diffractometer in reflectance Bragg-Brentano geometry employing Cu filtered CuK α -monochromator focused radiation (1.54059 Å) at 1600 W (40 kV, 40 mA) power and equipped with a Lynx Eye detector (fitted at 0.2 mm radiation entrance slit). Samples were mounted on Ge (111) sample holders after dispersing the powders with ethanol and letting the slurry dry to form a conformal film on the holder. The samples were measured with a 2θ -scan from 2° to 30° as a continuous scan with 3046 steps and 5 s/step (acquisition time 4 h 47 min 45 s).

Transmission electron microscopy data were obtained with a Philips CM30/ST microscope with LaB₆ cathode, at an acceleration voltage of 300 kV. The powder was dispersed in *n*-butanol. One drop of the suspension was placed on a holey carbon/copper grid.

Argon, carbon dioxide, nitrogen and water vapor sorption measurements were performed at 87, 273, 288, 298 and 313 K with a Quantachrome Instruments Autosorb iQ MP with vapor option. Samples of 20 mg were preheated *in vacuo* (10⁻⁷ mbar) at 120 °C for 12 h. For BET calculations pressure ranges were chosen according to the implemented micropore BET assistant. For BET calculations pressure ranges of the Ar isotherms were chosen with the help of the BET Assistant in the ASiQwin software. In accordance with the ISO recommendations multipoint BET tags equal to or below the maximum in $V(1 - P/P_0)$ were chosen.

Pore-size distributions were determined using the calculation model for Ar at 87 K on carbon (cylindrical pores, QSDFT/NLDFT equilibrium model) of the ASiQwin software (v3.01) from Quantachrome.

The isosteric heats of adsorption were calculated from the CO₂ adsorption isotherms using the Quantachrome software ASiQwin (v3.01) based on the Clausius – Clapeyron equation.

The used water for vapor sorption was in Millipore® quality, and degassed for five minutes *in vacuo* before use. Different temperatures were controlled by a thermostat using water as coolant. At temperatures >288 K a homebuilt heating cable was used to heat the glass tube above the thermostat-heated sample to 50-60 °C, so that no condensation of water can occur.

Inductively coupled plasma atomic emission spectroscopy (ICP-AES) was done on a VARIAN VISTA RL simultaneous spectrometer (Agilent Technologies, Santa Clara, California, USA) with a CCD-detector.

Flow TGA experiments: The CO₂ uptake was determined via a Setaram Sensys Evo thermogravimetric analyser (TGA) under atmospheric flow conditions (10 vol.% CO₂ in N₂ and 100 vol.% CO₂) at 50 °C and a total flow rate of 16 mL min⁻¹. Roughly 20 mg of the sample was dried in a platinum crucible under a flow of pure N₂ (16 mL min⁻¹) at 100 °C for 4 h prior to adsorption. The adsorption time to obtain quasi equilibrium adsorption isotherms was set to 2 h.

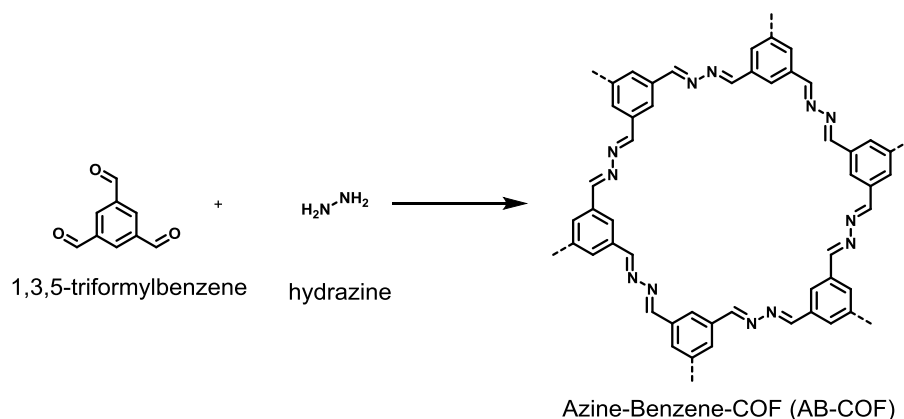
Breakthrough curves were obtained in a tubular reactor (4 mm diameter) operated at 50 °C (adsorption temperature) and a constant total flow of 100 mL min⁻¹ in an automated adsorption set-up.^{S2} The sorbents were dried in a flow of pure N₂ at 100 °C for 1 h prior to adsorption. The gas mixture for the adsorption step contained 50 vol.% CO₂, 40 vol.% N₂ and 10 vol.% Ar tracer. Desorption of the adsorbents was performed in pure N₂ at 50 °C and 100 °C. The concentrations of all gases were determined with a Pfeiffer OmniStar GSD 320 mass spectrometer. The catalyst bed comprised approximately 150 mg of the adsorbent mixed with 1 g of SiC (d_{SiC} ~ 80 μm). The adsorbents were not further processed and fractionated after the synthesis. The particle size of the sorbent was below 80 μm. The gas hourly space velocity (GHSV) in the reactor was 1200 h⁻¹.

H₂ and CO₂ high pressure isotherms were measured at 35 °C and pressures between 0.5 – 30 bar by a Rubotherm magnetic suspension balance as previously reported.^{S3} Approximately 50 mg of the sorbent was placed in a steel crucible and dried at 100 °C for 6 h under vacuum prior to adsorption. In order to correct for the buoyancy of the sample in H₂ and CO₂ at different temperatures and pressures, blank adsorption isotherms of non-adsorbing glass spheres were determined and subtracted from the isotherms.

Calculations. Structures for all three tautomeric forms of the ATFG-COF were optimized at the PBE0-D3/Def2-TZVP level of theory. Using these structures, NMR chemical shifts were computed at the B97-2/pcS-1 level of theory, that has been found to be a reliable compromise between

accuracy and computational cost.^{S4a} All calculations were performed using the FermiONs++ program package.^{S4b-c}

Synthetic Procedures

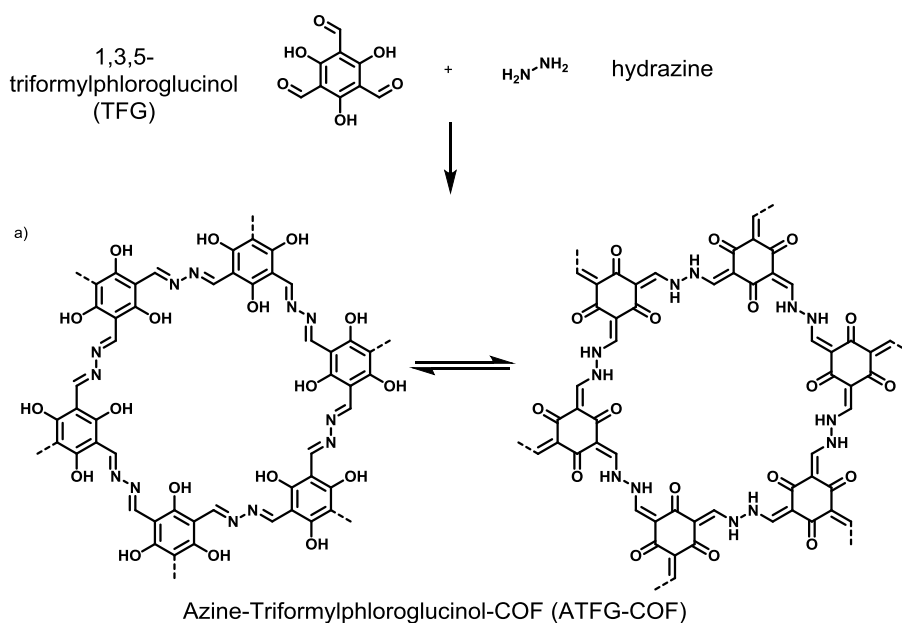


Scheme 4.S1. Synthesis of AB-COF by acid catalyzed hydrazone formation.

AB-COF

To a Biotage® 20 mL microwave vial 250 mg (1.5 mmol, 2.0 eq.) of 1,3,5-triformylbenzene and a stir bar was added. The vial was temporarily sealed with a rubber septum. Subsequently, the vial was flushed three times in argon/vacuum cycles. 9.5 mL of *o*-dichlorobenzene and 0.5 mL of *n*-butanol were added and the vial was again degassed three times in argon/vacuum cycles. In one shot 110 μL hydrazine hydrate (2.25 mmol, 3 eq.) was added under stirring. Then 3.4 mL of aqueous 6M acetic acid (20.5 mmol, 27.4 eq.) was added, the vial was sealed and heated in a muffle furnace at 120 °C for 72 h. The vial was opened and the slurry suspension was transferred by a polyethylene pipette to a Büchner funnel and filtered. The filter cake was scratched off and transferred to an Erlenmeyer flask, washed with DMF (1 x 10 mL) and THF (2 x 10 mL) and again filtered off.

For the 3-gramm-synthesis (1g each for metal soaking) this experiment has been parallelized for 12 times on this scale.



Scheme 4.S2. Synthesis of AB-COF by acid catalyzed hydrazone formation.

ATFG-COF

To a Biotage® 20 mL microwave vial 180 mg (0.88 mmol, 2.0 eq.) of 1,3,5-triformylphloroglucinol(QUELLE) and a stir bar was added. The vial was temporarily sealed with a rubber septum. Subsequently, the vial was flushed three times in argon/vacuum cycles. It was added 6.0 mL of dioxane and 0.5 mL of mesitylene and the vial was again degassed three times in argon/vacuum cycles. In one shot 64 μL hydrazine hydrate (1.32 mmol, 3 eq.) was added under stirring. Then 2.0 mL of aqueous 6M acetic acid (20.5 mmol, 27.4 eq.) was added, the vial was sealed and heated in a muffle furnace at 120 °C for 72 h. The vial was opened and the slurry suspension was transferred by a polyethylene pipette to a Büchner funnel and filtered. The filter cake was scratched off and transferred to an Erlenmeyer flask, washed with DMF (1 x 10 mL) and THF (2 x 10 mL) and again filtered off.

For the 1-gramm-synthesis this experiment has been parallelized for 6 times on this scale.

Powder X-ray Diffraction and Simulation

Molecular modeling of the COF was carried out using the *Materials Studio* (5.5) suite of programs by *Accelrys*.

The unit cell was defined by two 1,3,5-triformylbenzene (AB-COF) /1,3,5-triformylphloroglucinol (ATFG-COF) molecules bonded via six azine linkages to hydrazine. The initial structure was geometry optimized using the MS Forcite molecular dynamics module (Universal force fields, Ewald summations), and the resultant distance between opposite formyl carbon atoms in the structure was used as the *a* and *b* lattice parameters (initially 15 Å) of the hexagonal unit cell with *P6/m* symmetry (*bnn* net). The interlayer spacing *c* was chosen as 3.44 Å (AB-COF) 3.3 Å (ATFG-COF), according to the 001 stacking reflection of the powder at $2\theta = 26.4^\circ$ (AB-COF) and 27.2° (ATFG-COF), respectively, and the crystal structure was geometry optimized using Forcite (resulting in $a = b = 15.24$ Å for AB-COF and $a = b = 15.87$ Å for ATFG-COF (NH form), 15.61 Å for ATFG-COF (OH form), 15.13 Å for ATFG-COF (mixed form)).

As Ar sorption indicates a pore size of 0.6 nm for ATFG-COF, further simulation on the stacking order (only for NH form) was carried out:

- AB stacking in *P3* symmetry (*gra* net) with $a = b = 15.48$ Å and $c = 6.88$ Å. This structure results in ≈ 0.6 nm pores (see Fig.4S8).
- ABC stacking (*R3* symmetry) with $a = b = 15.39$ Å and $c = 7.03$ Å.

The MS Reflex Plus module was then used to calculate the PXRD pattern, which matched the experimentally observed pattern closely in both the positions and intensity of the reflections:

- AB-COF: *P6/m* (AA stacking)
- ATFG-COF: both *P6/m* (AA stacking) and *P3* (AB stacking). This finding is supported by the pore size distribution obtained by Ar sorption (see Fig. 4S25).

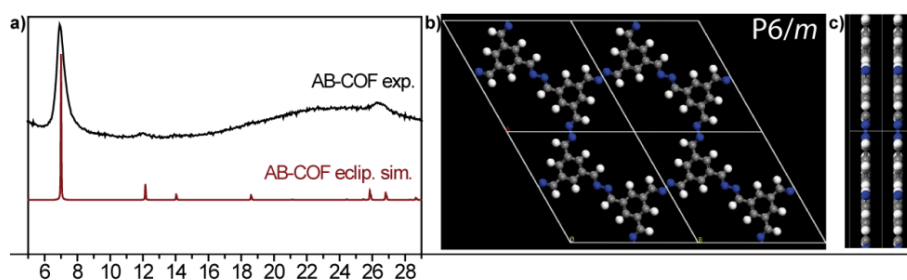


Figure 4.S1. Characterization of AB-COF by PXRD. (a) PXRD suggests a (close to) eclipsed layer stacking for AB-COF. (b) View along the *c*-axis of four unit cells of AB-COF. (c) Interlayer stacking distance is 3.4 Å.

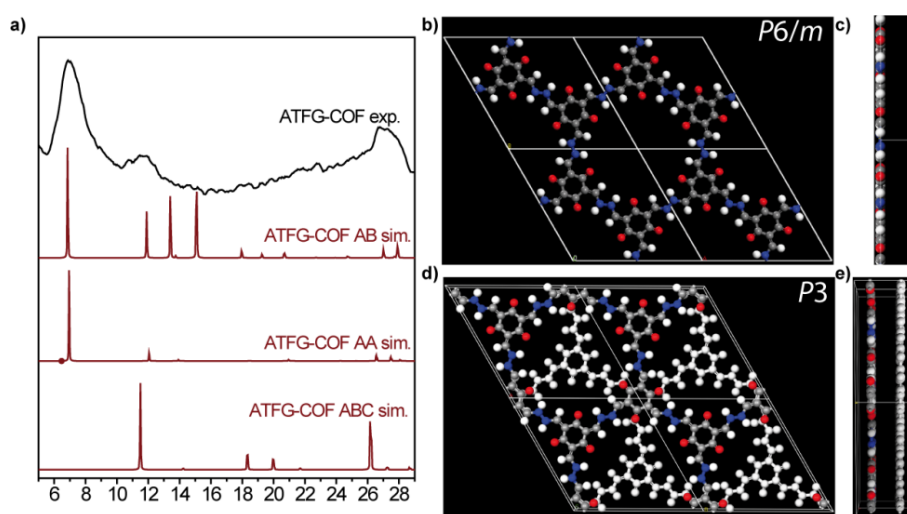


Figure 4.S2. Characterization of ATFG-COF by PXRD. (a) PXRD suggests a mixture of eclipsed (AA) and staggered AB layer stacking for ATFG-COF. (b) and (d) View along the *c*-axis of four unit cells for both stacking modes. (c) and (e) The interlayer stacking distance is between 3.3 Å. The structure model for the ABC staggered layer stacking is shown in Fig. S9.

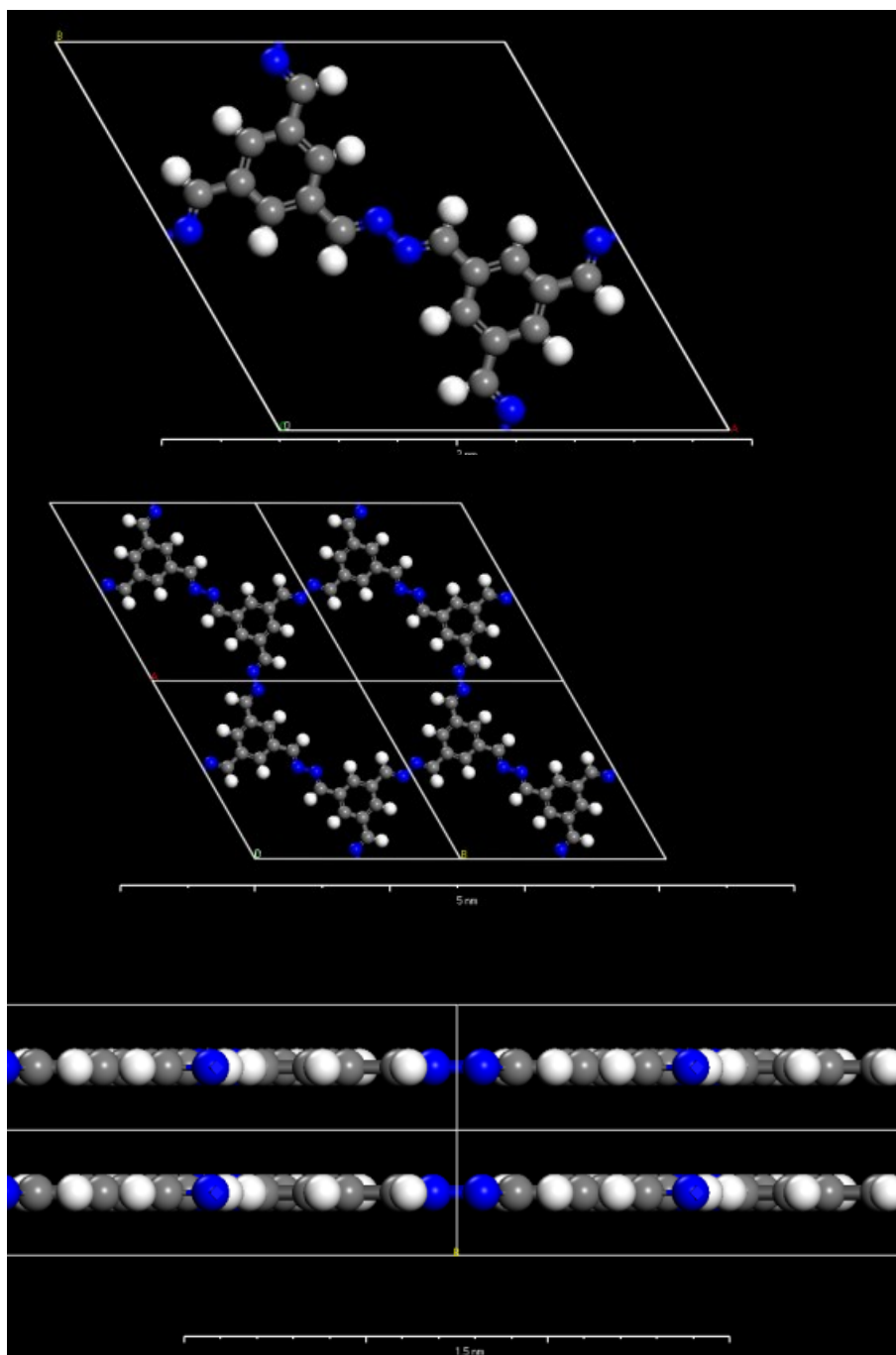


Figure 4.S3. AB-COF: Simulation of the unit cell content calculated in an eclipsed arrangement: View onto the *ab*-plane (top), view onto the *ab*-plane with four unit cells (middle) and view perpendicular to the *c*-axis (bottom).

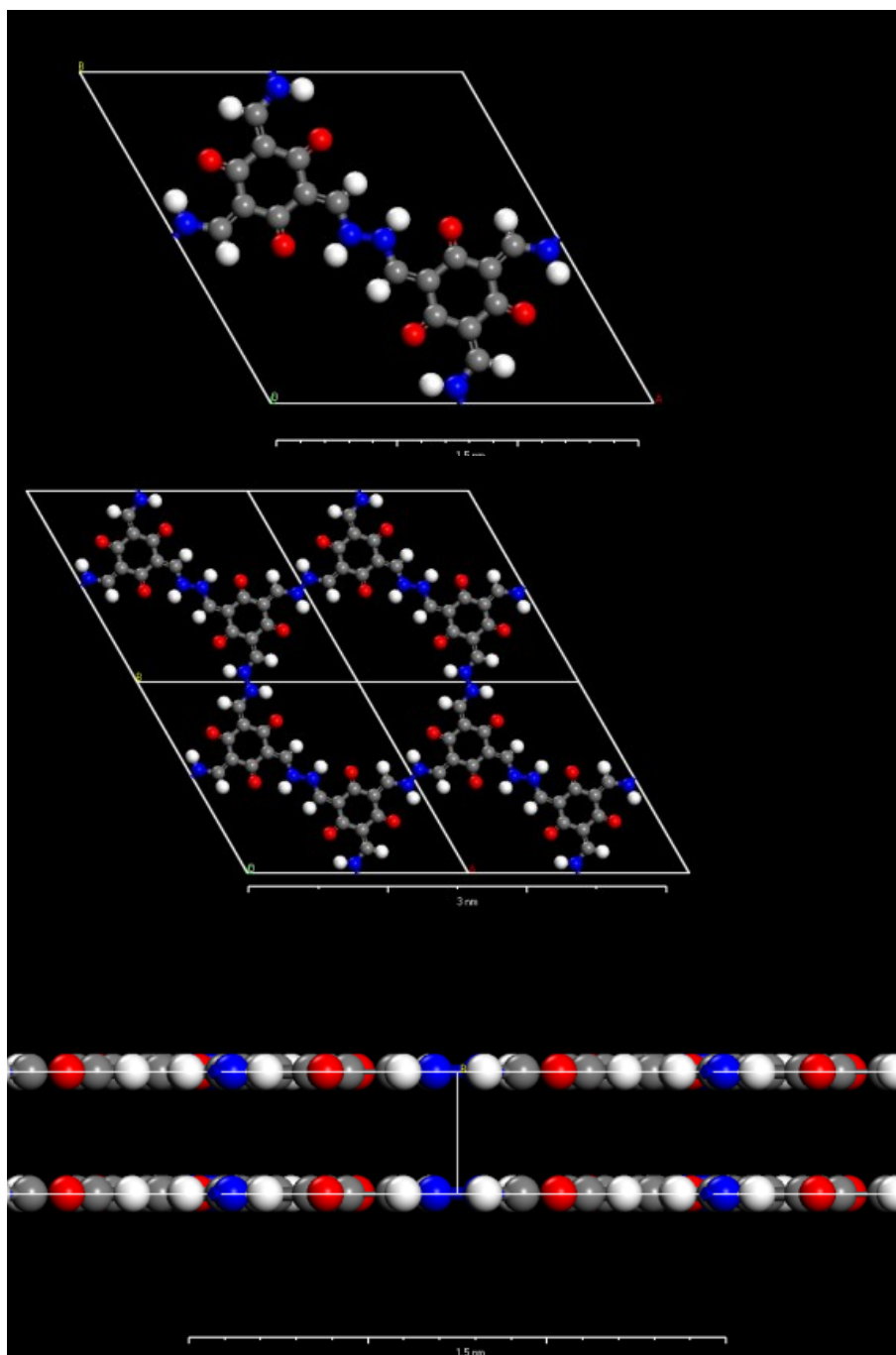


Figure 4.S4. ATFG-COF: Simulation of the unit cell content (NH form) calculated in an eclipsed arrangement: View onto the ab -plane (top), view onto the ab -plane with four unit cells (middle) and view perpendicular to the c -axis (bottom).

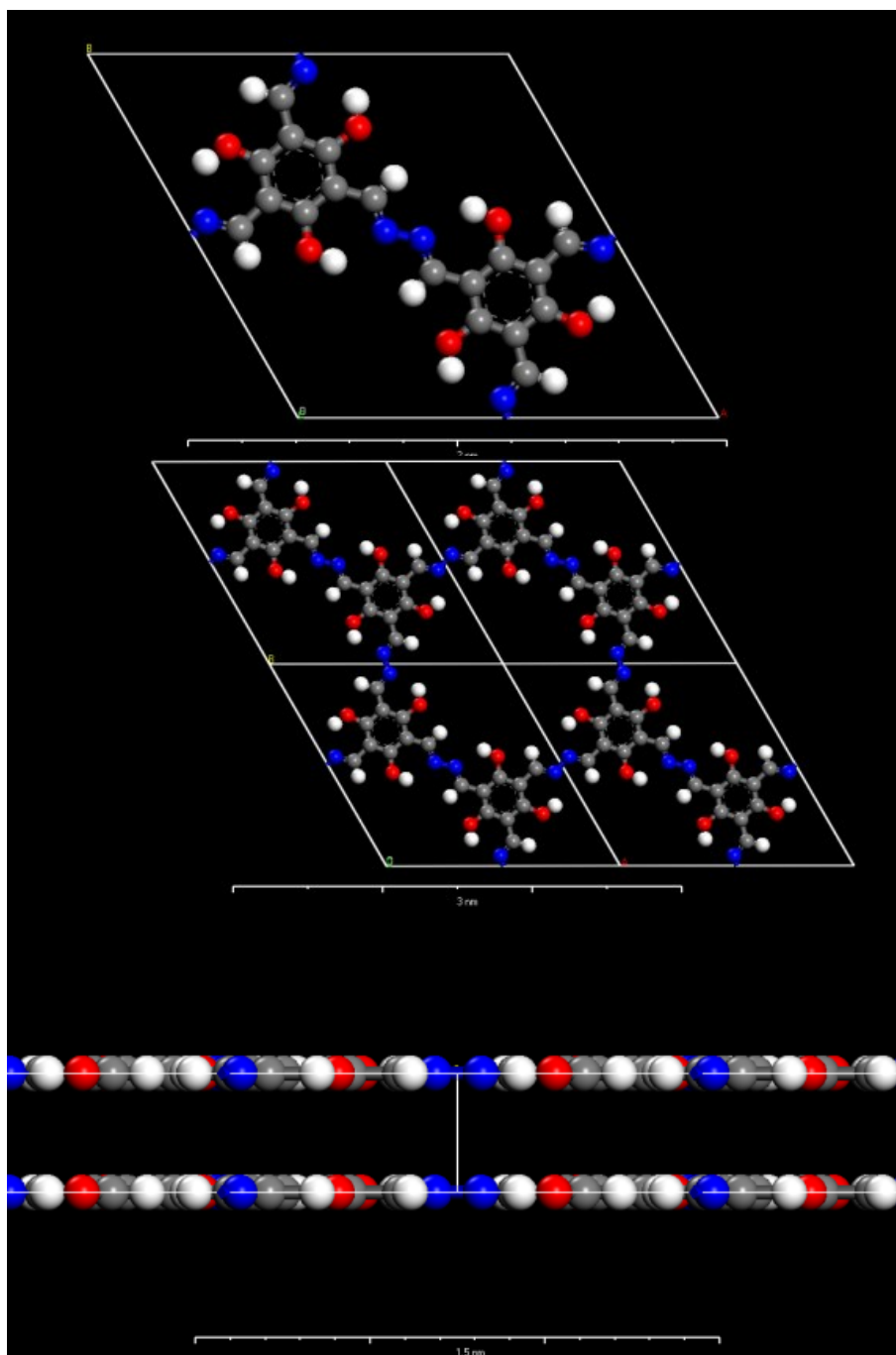


Figure 4.S5. ATFG-COF: Simulation of the unit cell content (OH form) calculated in an eclipsed arrangement: View onto the ab -plane (top), view onto the ab -plane with four unit cells (middle) and view perpendicular to the c -axis (bottom).

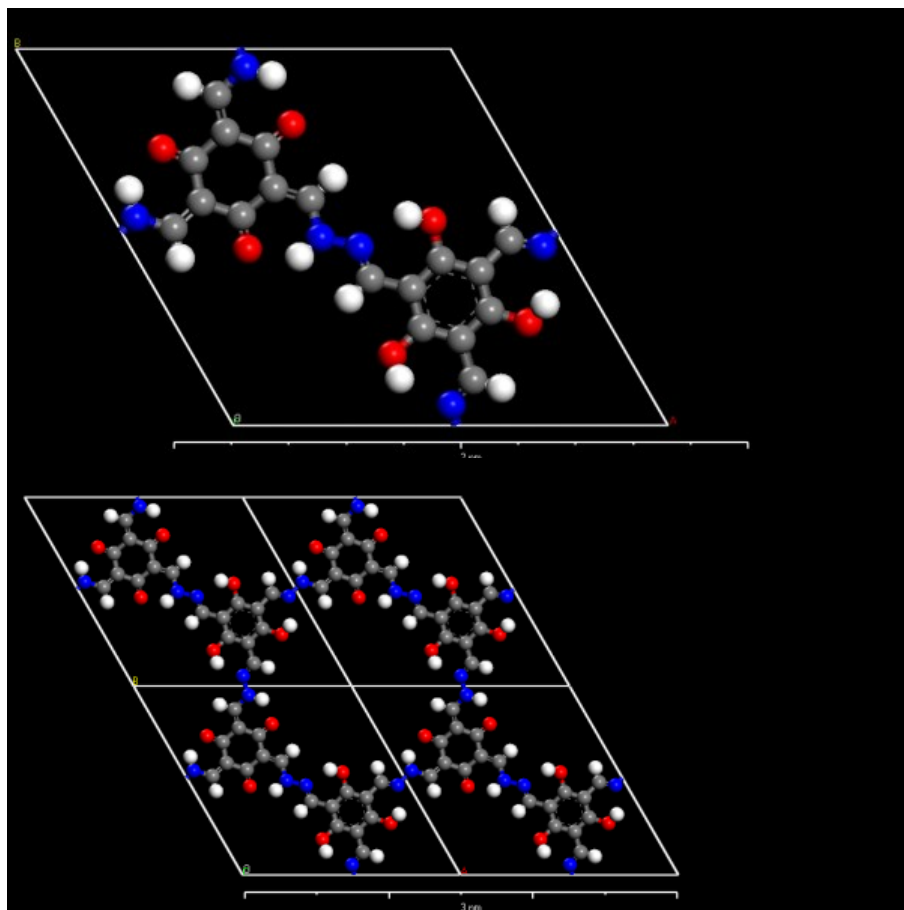


Figure 4.S6. ATFG-COF: Simulation of the unit cell content (OH-NH mixed form) calculated in an eclipsed arrangement: View onto the ab -plane (top), view onto the ab -plane with four unit cells (bottom).

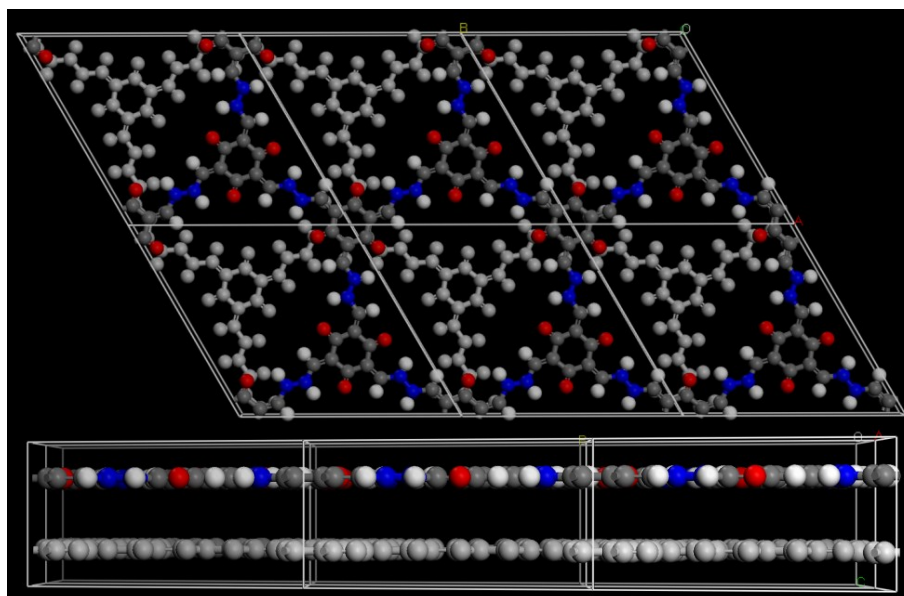


Figure 4.S7. ATFG-COF: Simulation of the unit cell content (NH form) calculated in a staggered AB arrangement: View onto the ab -plane of six unit cells (top), view perpendicular to the c -axis (bottom). The second layer is coloured in light grey for clarity.

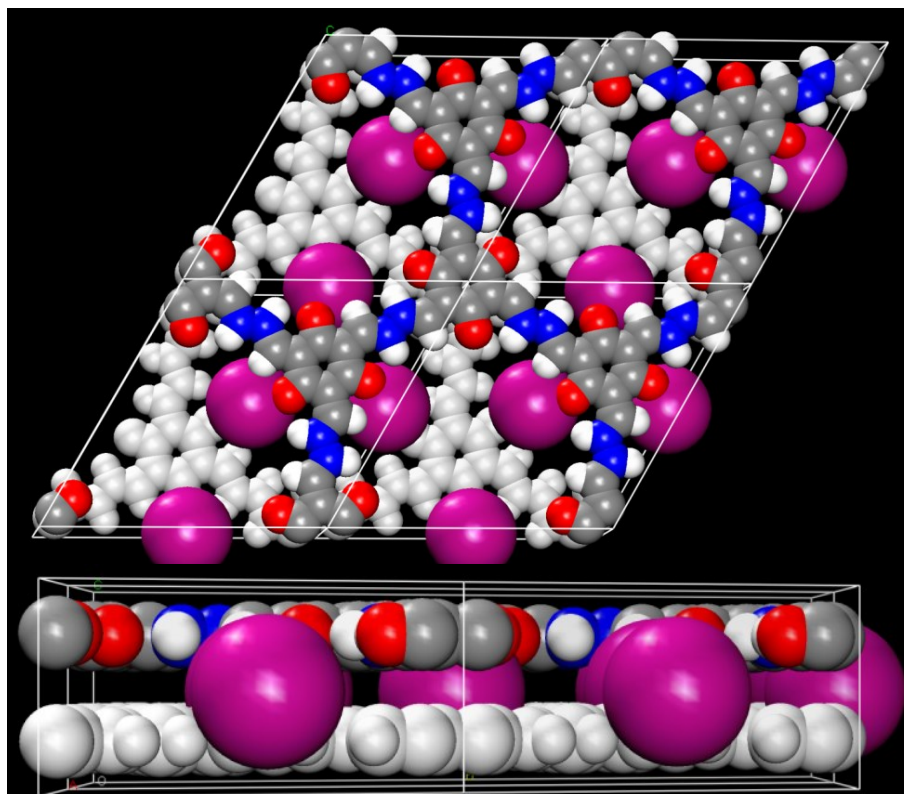


Figure 4.S8. Pore size of ATFG-COF (AB stacking): Simulation of the unit cell content (NH form) calculated in a staggered AB arrangement: View onto the *ab*-plane of four unit cells (top), view perpendicular to the *c*-axis (bottom), CPK model, violet sphere has a diameter of 0.6 nm to illustrate the pores (pore size derived from sorption data). Second layer is coloured in light grey for clarity.

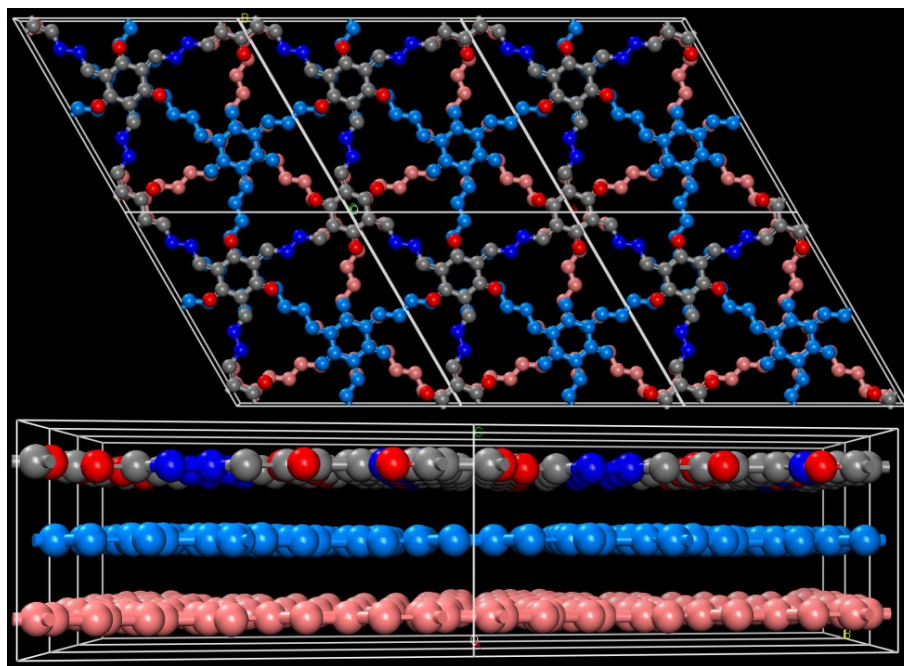


Figure 4.S9. ATFG-COF: Simulation of the unit cell content (NH form) calculated in a staggered ABC arrangement: View onto the ab -plane of six unit cells (top), view perpendicular to the c -axis (bottom). The second layer is coloured in light blue, the third layer is coloured in light red for clarity. H atoms are omitted.

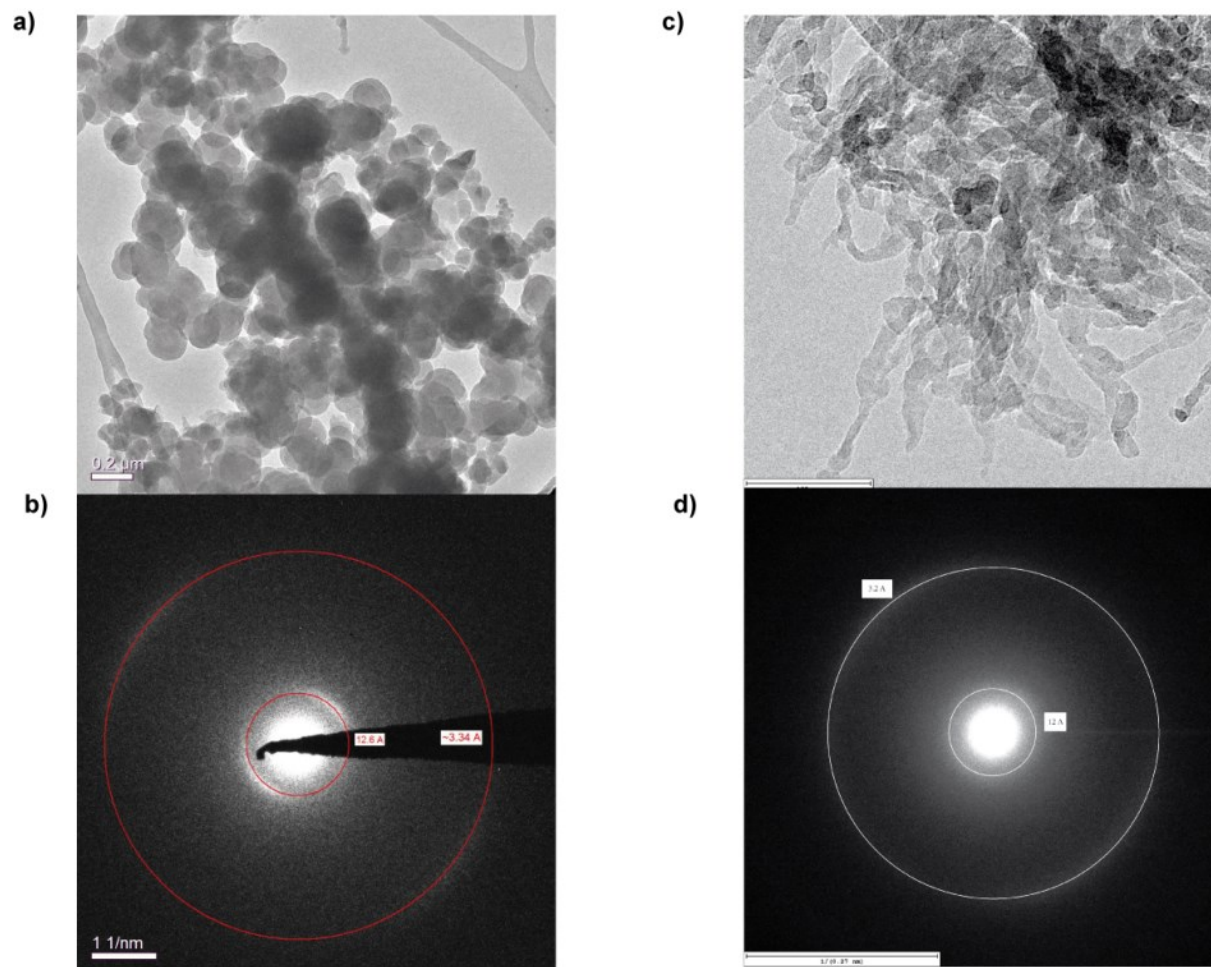
Transmission electron microscopy

Figure 4.S10. TEM images of (a) AB-COF and (c) ATFG-COF, selected-area electron diffraction (SAED) of (b) AB-COF and (d) ATFG-COF.

Stability of AB-COF and ATFG-COF in Water

Stability in water has been tested by soaking the corresponding COF (20 mg) in water for 3 h at room temperature. PXRD was recorded after filtration and drying in vacuum overnight.

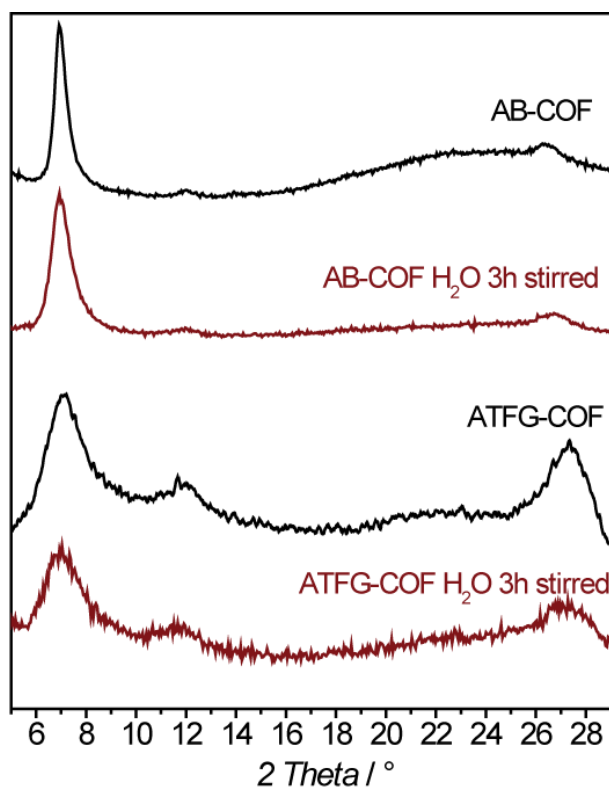


Figure 4.S11. PXRD measurements showing the retention of the (low) crystallinity after treatment with water (3h, stirred).

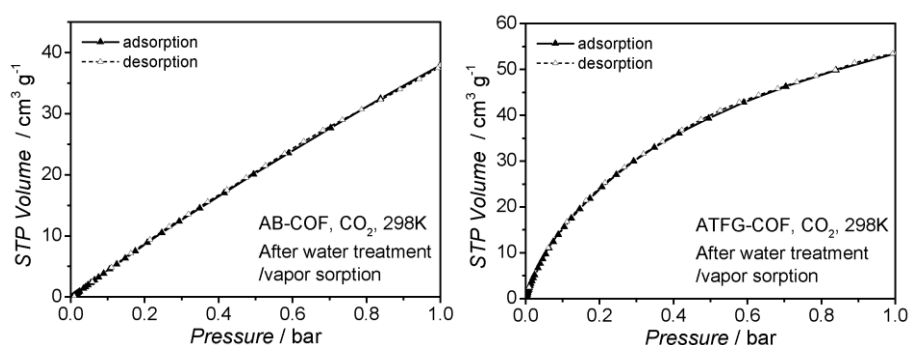


Figure 4.S12. CO₂ adsorption after water treatment of AB-COF and ATFG-COF. Maximum uptake corresponds to 1.68 mmol g⁻¹ (AB-COF) and 2.37 mmol g⁻¹ (ATFG-COF).

Table 4.S1. Comparison of Ar BET surface area and CO₂ uptakes before and after water treatment (3h, stirring)*.

COF	AB-COF	AB-COF after water	ATFG-COF	ATFG-COF after water
BET / m ² g ⁻¹	1120	1080	520	506
CO ₂ uptake 298 K / mmol g ⁻¹	1.68	1.68/1.68**	2.40	2.37/2.38**

* all samples were activated (outgassed) at 120°C for 12 h in UHV.

**samples after water vapor sorption measurements.

CP-MAS NMR Measurements

^1H solid-state NMR MAS spectroscopy of AB-COF shows the presence of aromatic protons through signals at 7.85 ppm. Further shifted to downfield a shoulder signal at 8.46 ppm corresponds to the proton adjacent to the sp^2 -carbon of the aldehyde-derived azine. The signal around 4.5 ppm corresponds to residue of water in the pores.

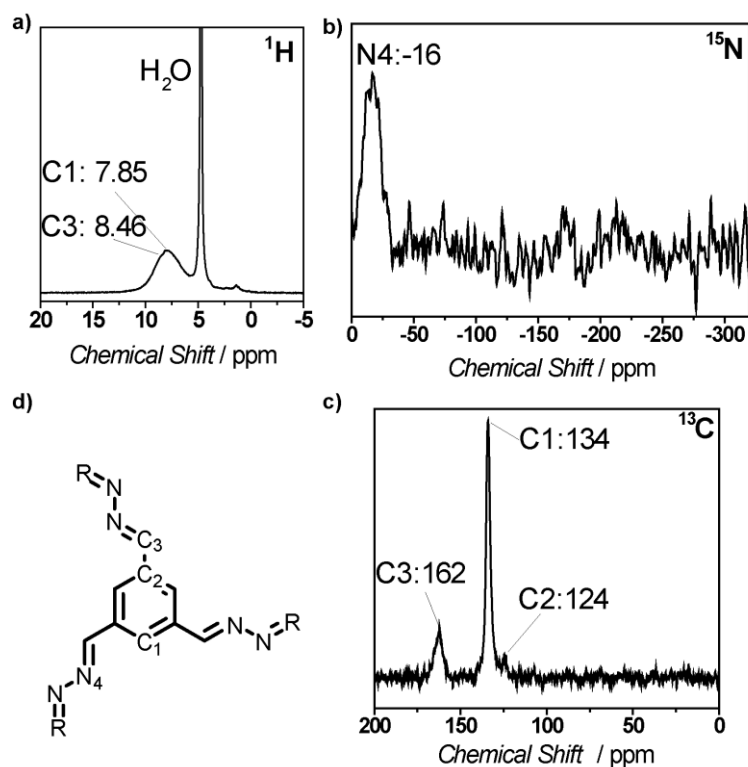


Figure 4.S13. ssNMR characterization of AB-COF by (a) ^1H MAS NMR spectroscopy, (b) ^{15}N CP-MAS NMR spectroscopy (c) ^{13}C CP-MAS NMR spectroscopy. (d) Assignment of spectral data.

^1H ssNMR MAS spectroscopy shows the presence of downfield shifted protons adjacent to the sp^2 carbons through signals at 7.85 ppm. The more downfield shifted signal at 12.62 ppm corresponds to the phenolic proton of the **OH** tautomer and the enhydrazin N-H of the **NH** tautomer. The signal around 4.5 ppm corresponds to residual water in the pores.

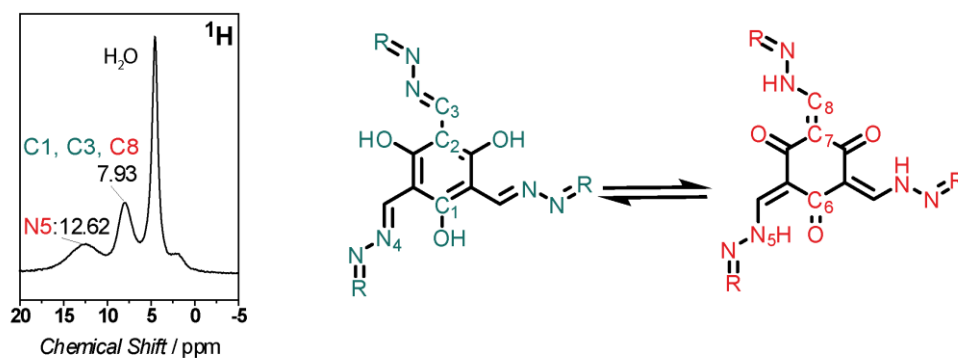


Figure 4.S14. ^1H MAS ssNMR characterization of ATFG-COF and assignment to OH and NH tautomeric forms of ATFG COF.

Theoretical NMR shift calculations

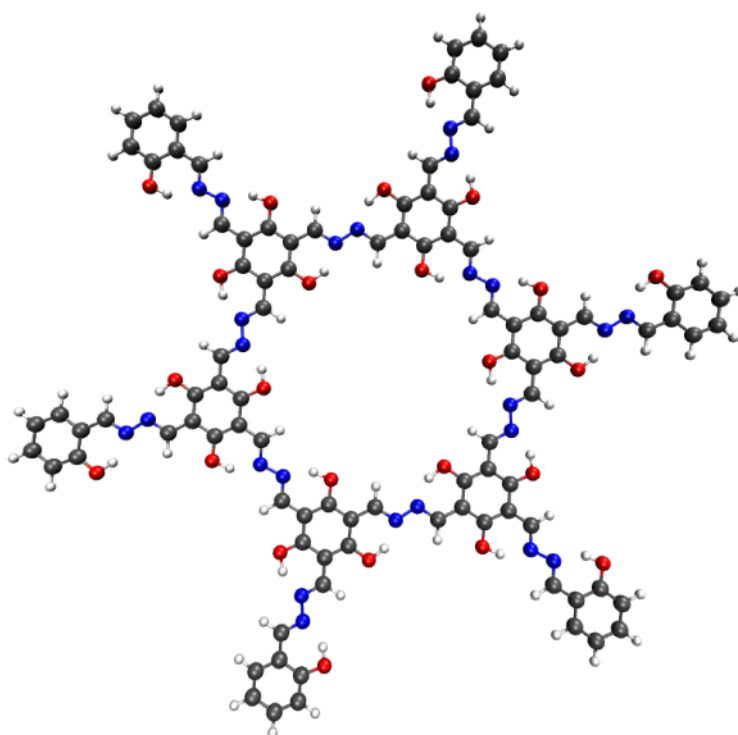


Figure 4.S15. Optimized geometry for the OH form of ATFG-hexagon, obtained at the PBE0-D3/def2-TZVP level of theory.

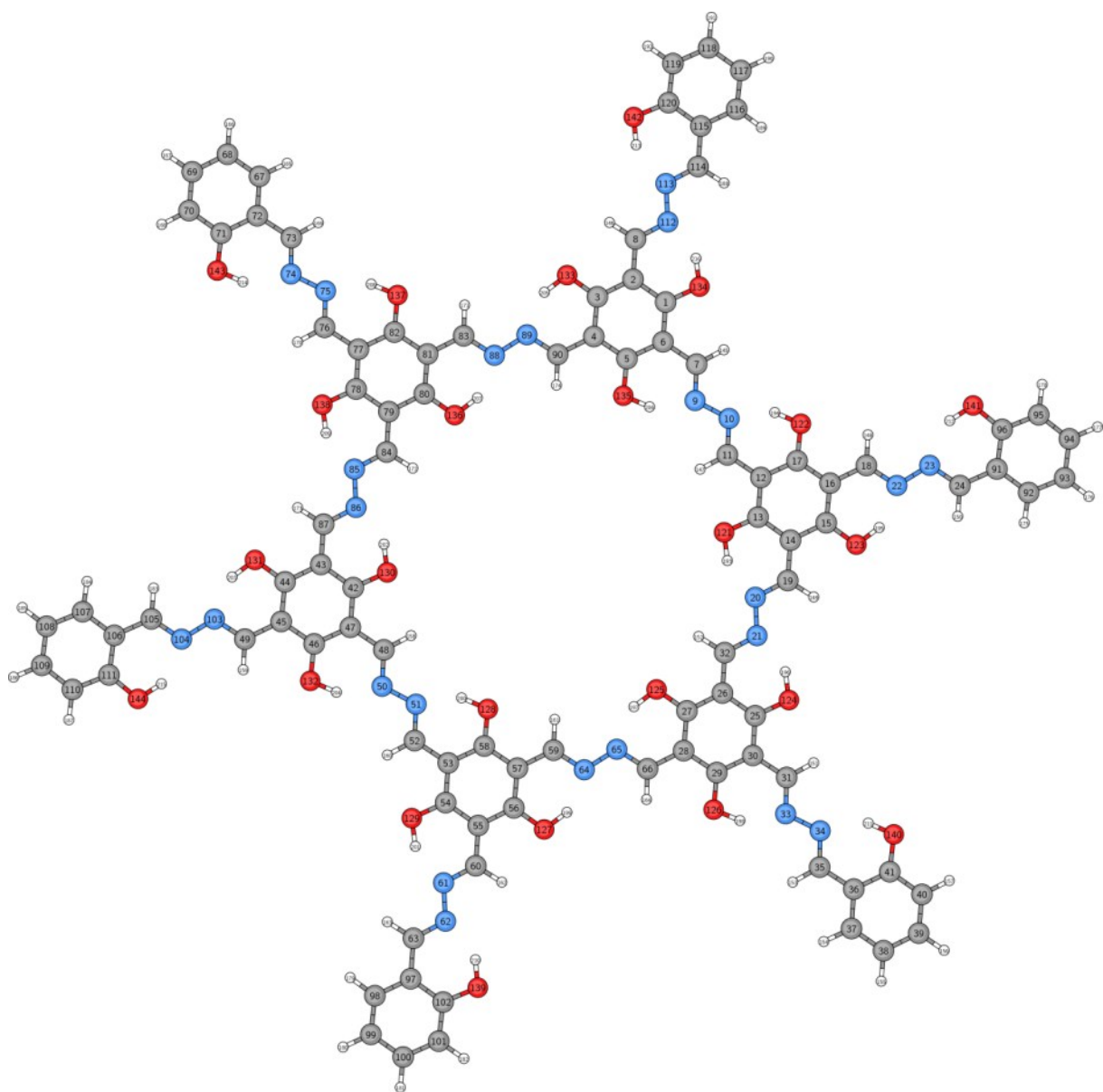


Figure 4.S16. Atom labels for the OH form of ATFG-hexagon.

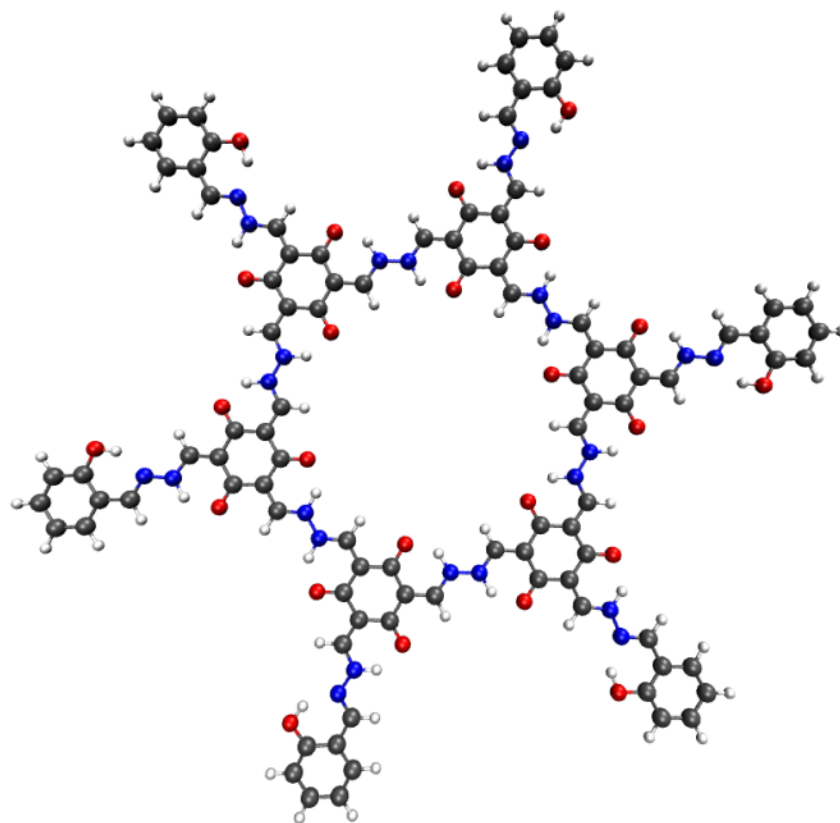


Figure 4.S17. Optimized geometry for the **NH** form of an ATFG-hexagon, obtained at the PBE0-D3/def2-TZVP level of theory.

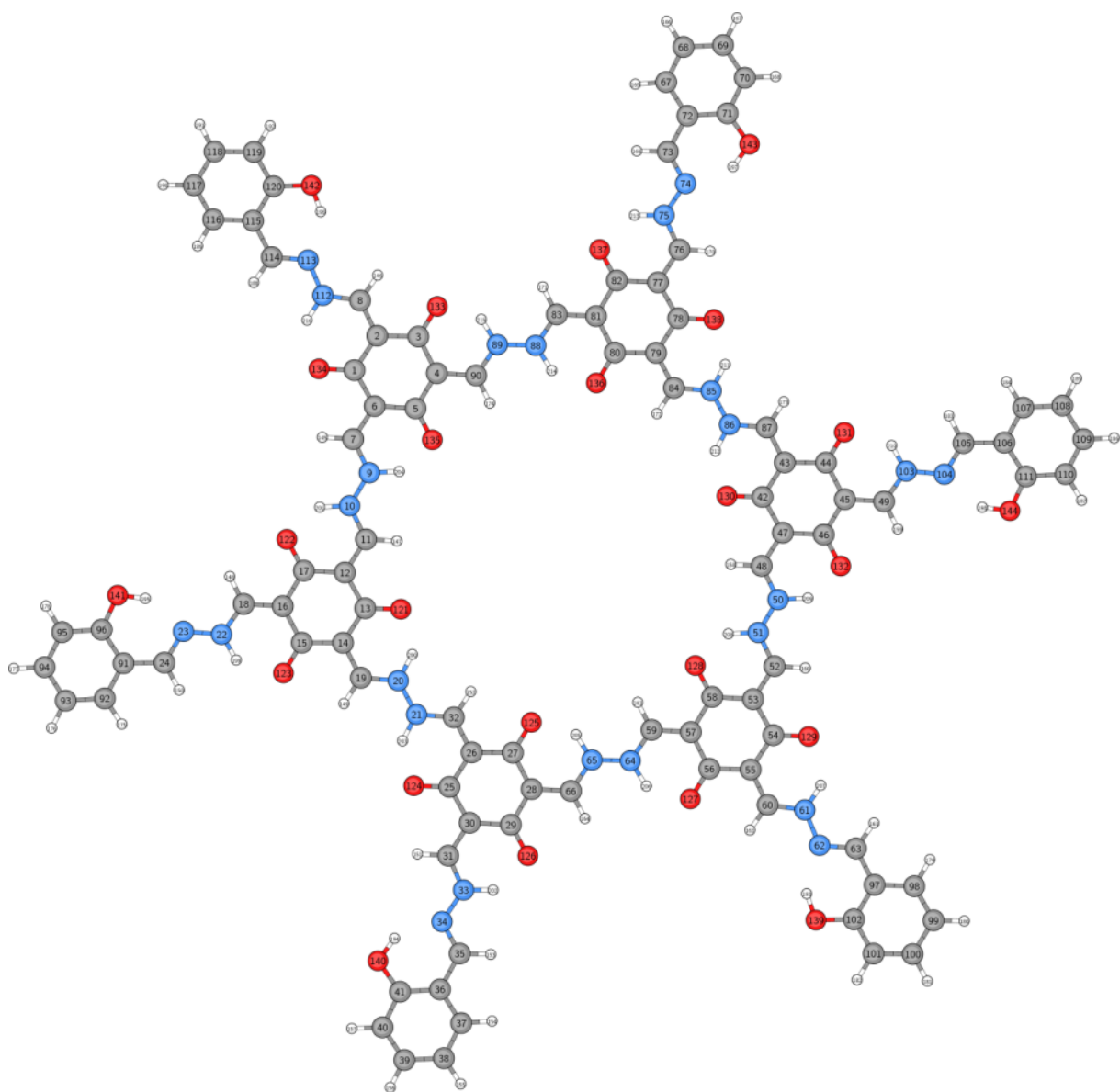


Figure 4.S18. Atom labels for the NH form of an ATFG-hexagon.

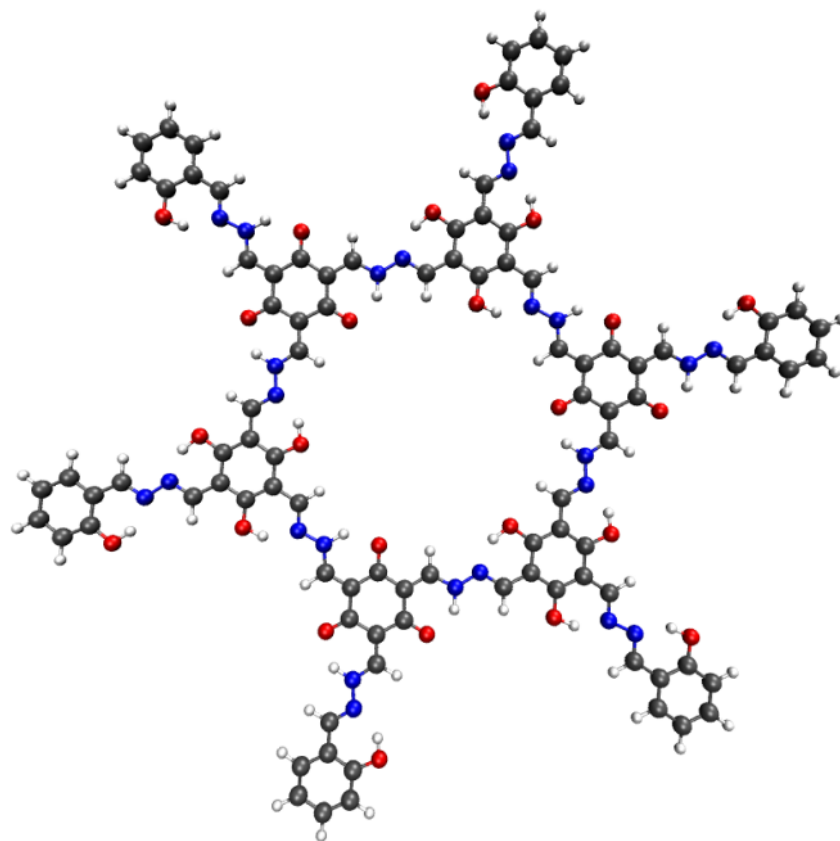


Figure 4.S19. Optimized geometry for the mixed **OH-NH** form of an ATFG-hexagon, obtained at the PBE0-D3/def2-TZVP level of theory.

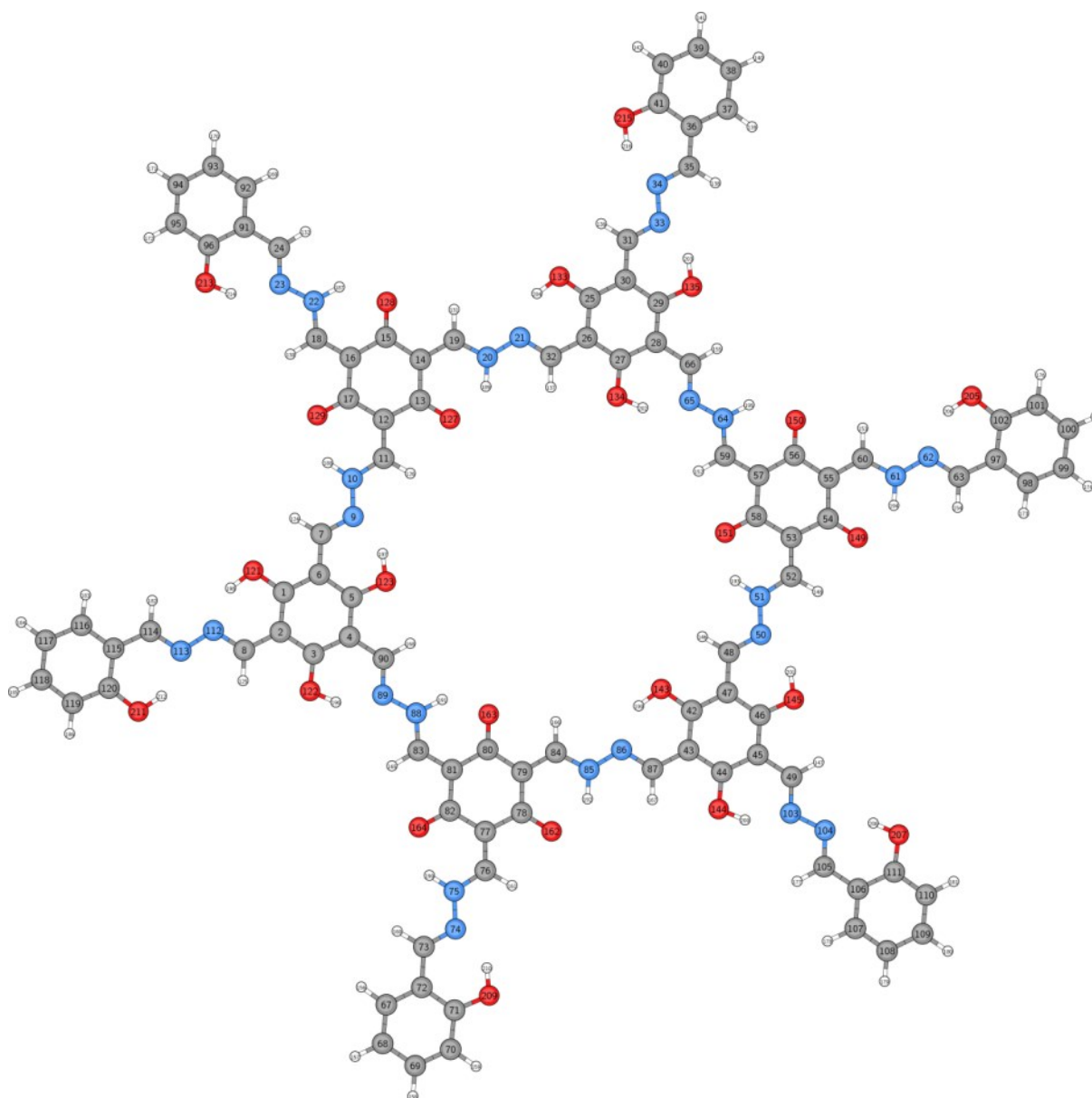


Figure 4.S20. Atom labels for the mixed **OH-NH** form of an ATFG-hexagon.

Table 4.S2. Calculated ^{15}N -NMR chemical shifts for all three tautomeric forms of an AFG-hexagon on the B97-2/pcS-1//PBE0-D3/Def2-TYVP level of theory. Due to the lack of symmetrical treatment within the used program package, symmetry equivalent chemical shifts were averaged afterwards.

Atom Number	NMR Chemical Shift [ppm]			
	OH form	NH form	OH/NH mixed form	
9	-69.04	-218.23	-95.50	-
10	-69.03	-218.63	-	-196.53
20	-68.98	-219.58	-	-197.01
21	-68.79	-218.98	-95.76	-
65	-69.63	-218.86	-95.49	-
64	-69.64	-217.70	-	-197.44
51	-69.11	-218.20	-	-197.12
50	-69.15	-218.49	-95.04	-
86	-68.97	-219.61	-95.83	-
85	-68.72	-219.14	-	-197.00
88	-69.67	-218.97	-	-196.92
89	-69.68	-217.76	-95.29	-
Averaged Chemical Shift	-69.20	-218.68	-95.49	-197.00

Table 4.S3. Calculated ^{13}C -NMR chemical shifts for the OH-NH mixed form of an ATFG-hexagon on the B97-2/pcS-1//PBE0-D3/Def2-TYVP level of theory. Due to the lack of symmetrical treatment within the used program package, symmetry equivalent chemical shifts were averaged afterwards.

^{13}C -NMR Chemical Shift, OH-NH mixed tautomer [ppm]					
Atom Type	Atom Number	Calculated	Averaged	Experimental	Deviation
C-OH	1	169.08			
	3	168.00			
	5	167.61			
	25	168.27			
	27	167.72	168.24	163	-5.24
	29	168.99			
	42	167.64			
	44	168.90			
	46	168.00			
Arom., OH form	4	97.70			
	6	97.92			
	26	97.72			
	28	97.80	97.80	99	1.20
	43	97.90			
	47	97.76			
C=N, OH form	7	148.13			
	32	147.74			
	48	147.63			
	66	147.79	147.80	151	3.20
	87	147.76			
	90	147.75			
C=O	13	184.91			
	15	184.92	184.97	182	-2.97

	17	184.89			
	54	185.09			
	56	184.88			
	58	184.83			
	78	185.17			
	80	185.04			
	82	184.96			
C=N, NH form	11	152.47			
	19	152.36			
	52	152.60	152.48	151	-1.48
	59	152.49			
	83	152.47			
	84	152.50			
Arom., NH form	12	104.76			
	14	105.04			
	53	104.85	104.90	99	-5.90
	57	104.99			
	79	104.91			
	81	104.87			

FT-IR Spectra

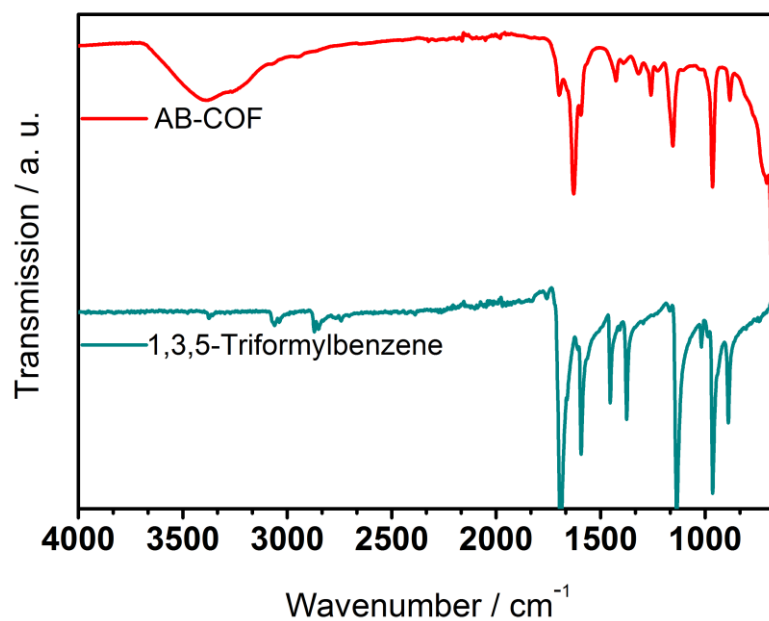


Figure 4.S21. Stack plot showing the FT-IR spectra of AB-COF and the starting material 1,3,5-triformylbenzene.

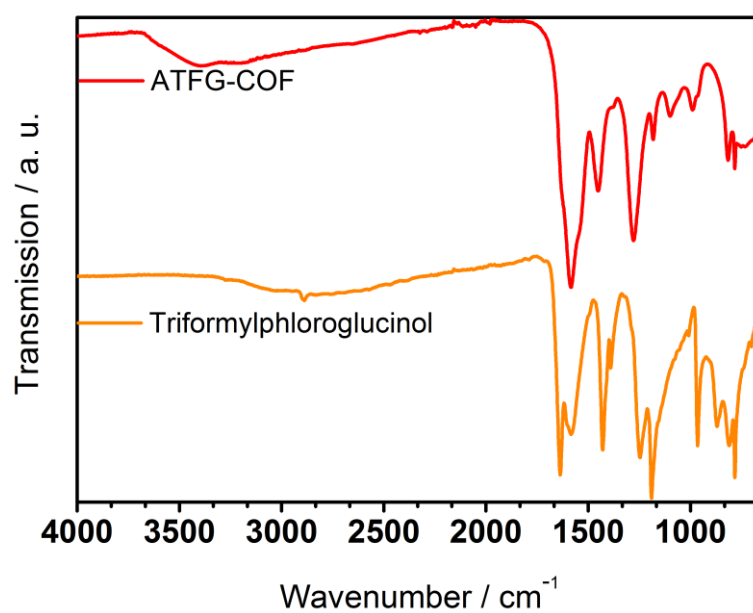


Figure 4.S22. Stack plot showing the FT-IR spectra of ATFG-COF and the starting material tri-formylphloroglucinol.

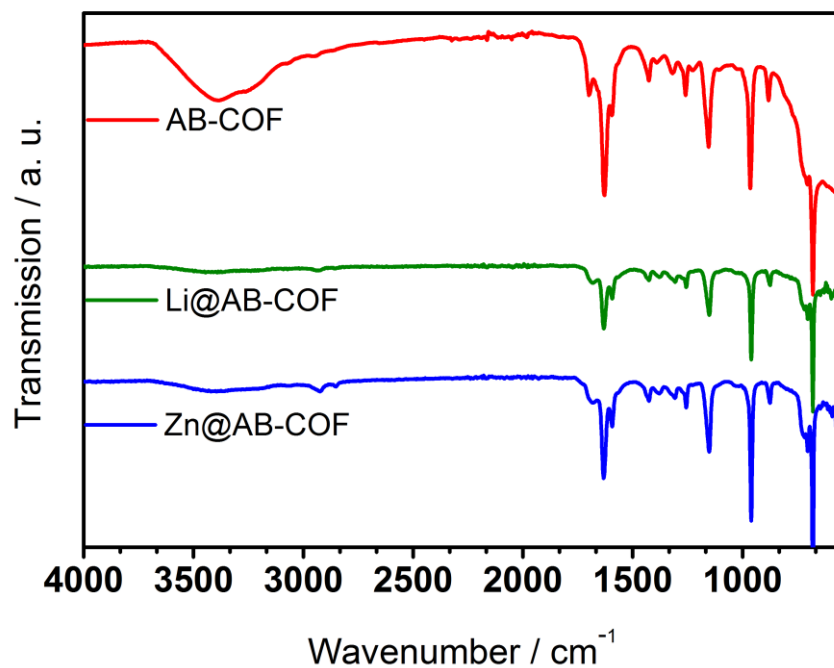


Figure 4.S23. Stack plot showing the FT-IR spectra of AB-COF and its metal-doped derivatives.

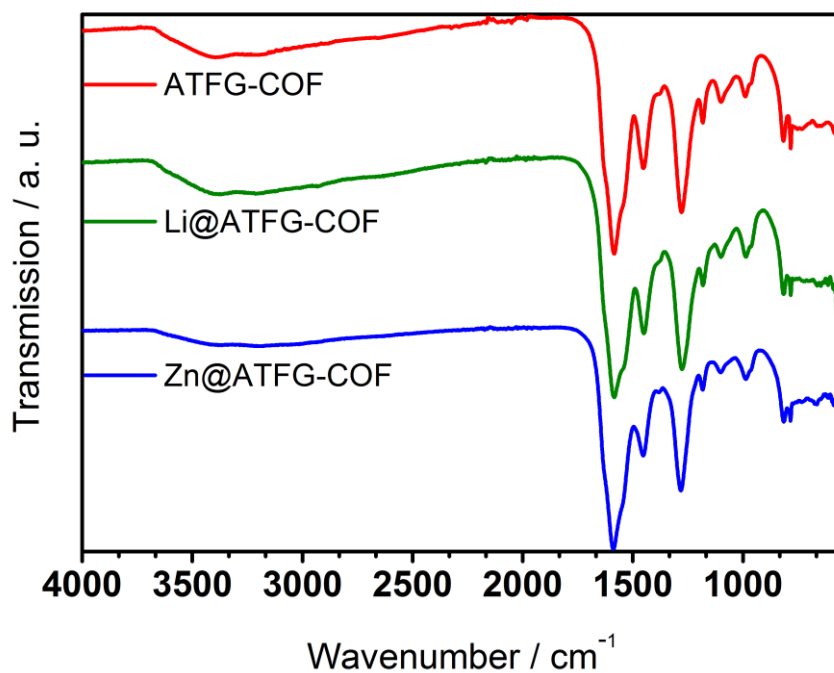


Figure 4.S24. Stack plot showing the FT-IR spectra of ATFG-COF and its metal-doped derivatives.

Ar Sorption Measurements and Pore Size Distribution

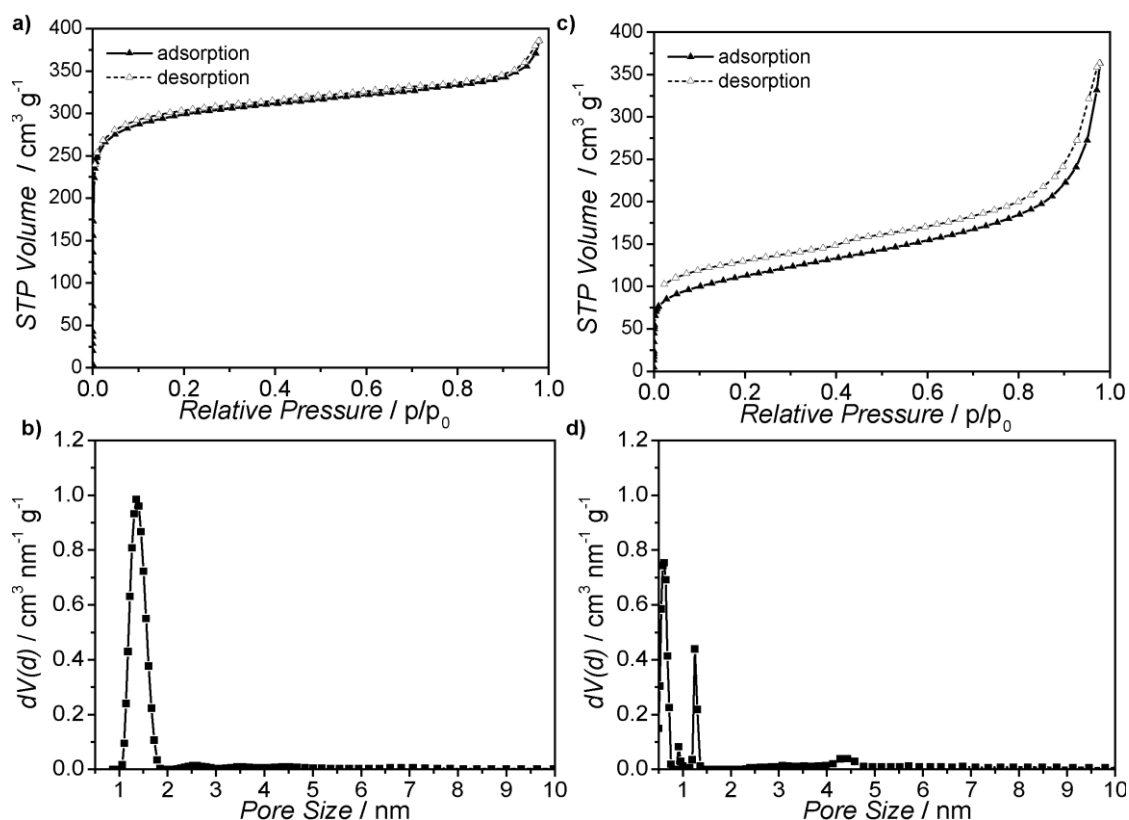


Figure 4.S25. Argon isotherms at 87 K of (a) AB-COF and (c) ATFG-COF. The type I isotherm (adsorption: black triangles, desorption: white triangles) gives a BET surface area of $1,125 \text{ m}^2 \text{ g}^{-1}$ for AB-COF and the type I/IV isotherm with H3 hysteresis of ATFG-COF gives a BET surface area of $520 \text{ m}^2 \text{ g}^{-1}$, respectively. QSDFT (AB-COF)/NLDFT (ATFG-COF) derived pore size distributions showing the formation of micropores in (b) AB-COF and (c) ATFG-COF, consistent with the predicted size based on the structure model.

Pore-size distributions were determined using the calculation model for Ar at 87 K/ N_2 at 77 K on carbon (cylindrical pores, QSDFT (AB-COF)/NLDFT(ATFG-COF) equilibrium model) of the ASiQwin software (v3.01) from Quantachrome.

Table 4.S4. Comparison of BET and DFT-derived surface areas with different sorptives.

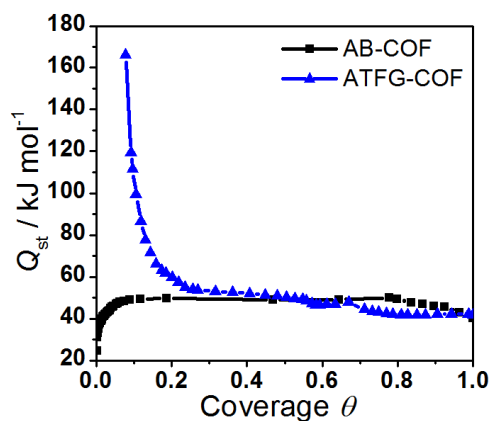
COF	AB-COF		ATFG-COF	
	Ar	N ₂	Ar	N ₂
DFT SA	1139*	1132*	1101**	NA***
BET SA	1125	1042	520	492

* QSDFT derived surface area (carbon, cylindrical pores)

** NLDFT derived surface area (carbon, cylindrical pores)

*** N₂ isotherm has not been completed due to ultra-long equilibration times (stopped after 70 h; only 4 of 97 points))

Water vapor sorption

**Figure 4.S26.** Isosteric heats of adsorption of AB-COF and ATFG-COF.

A Dubinin-Radushkevich analysis has been performed according to refs S5 and S6, as shown in Fig. 4.S27-28.

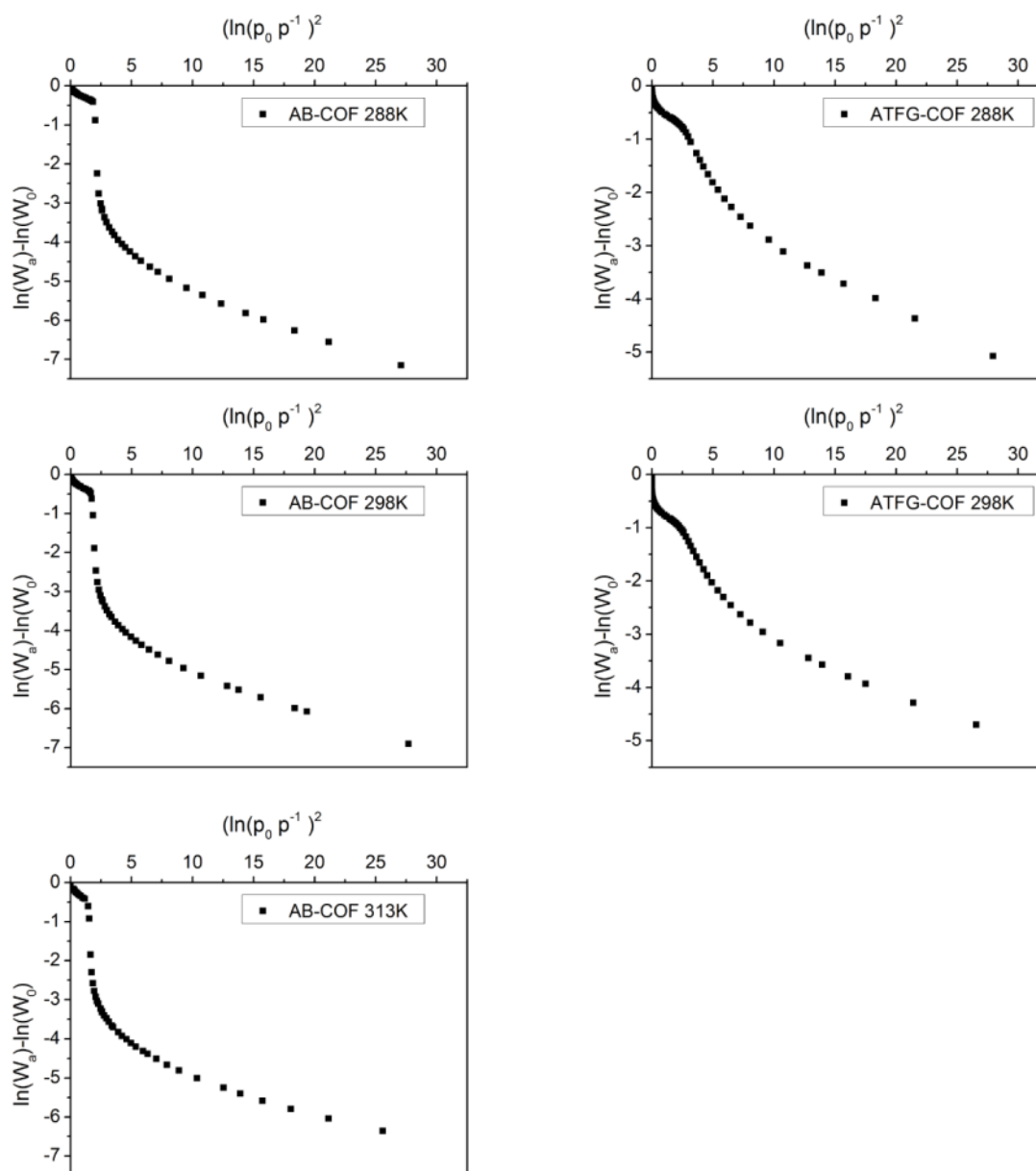


Figure 4.S27. Dubinin-Radushkevich (DR) plots.

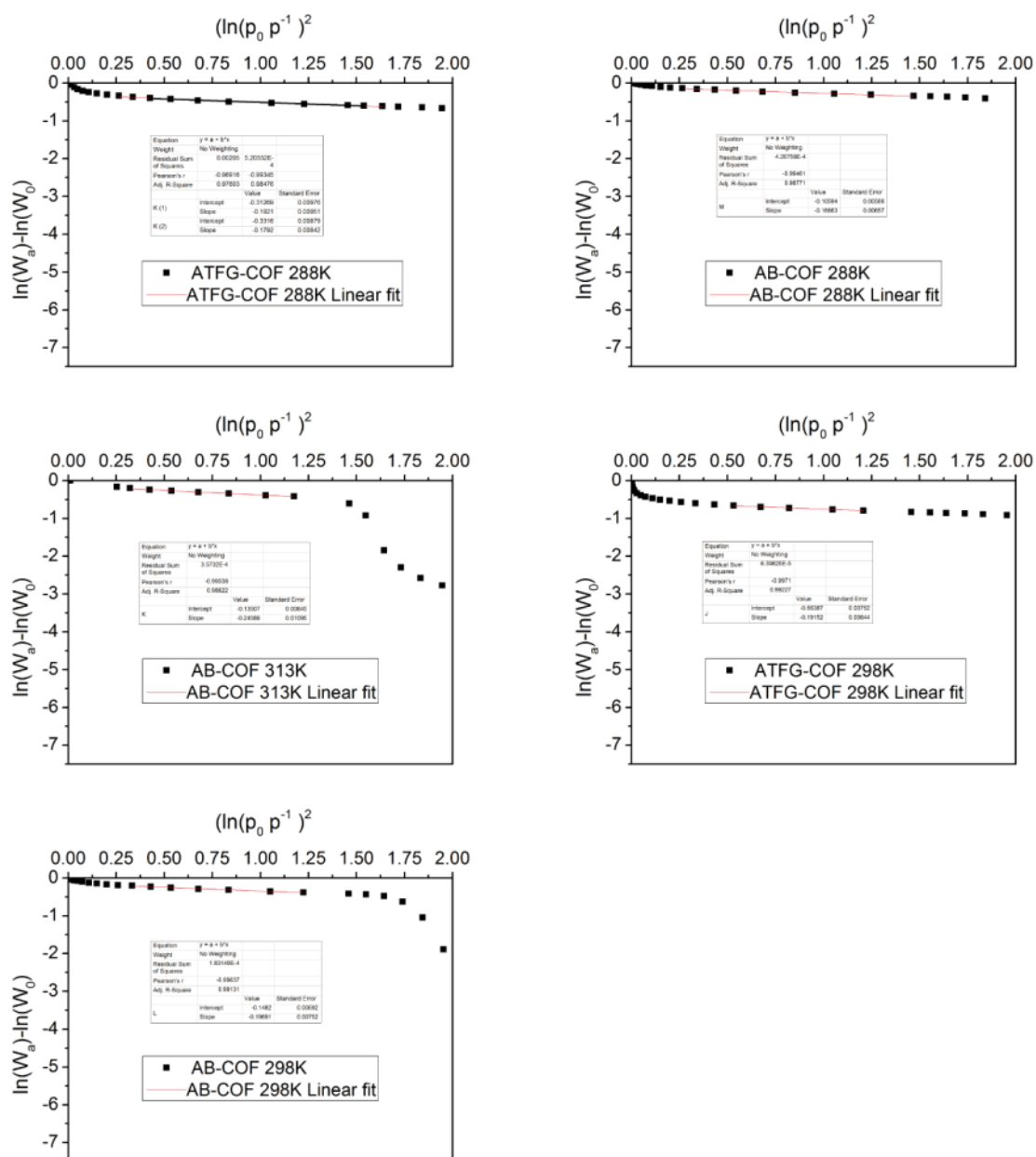


Figure 4.S28. Linear fits for the Dubinin-Radushkevich (DR) plots shown in Fig. 4.S27.

Table 4.S5. Heats of adsorption of water vapor for the two COFs.

COF	AB-COF			ATFG-COF	
Temp.	288	298	313	288	298
Used range in P/P ₀	0.30-0.60	0.33- 0.56	0.34-0.56	0.22-0.52	0.33-0.48
Q _{st} /kJ mol ⁻¹	50.4	49.6	48.6	50.2	49.7
Q _{st} [*] /kJ mol ⁻¹	49.4			50.7	

The asterisk indicates heats of adsorption calculated by the Clausius–Clapeyron equation as average of the single Q_{st} at a coverage range of 0.25-0.72.

For the water adsorption isotherms (288 K, 298 K, 313 K) of AB-COF the condensation pressure (the pressure where the steep increase in uptake starts) has been chosen for the Kelvin equation:

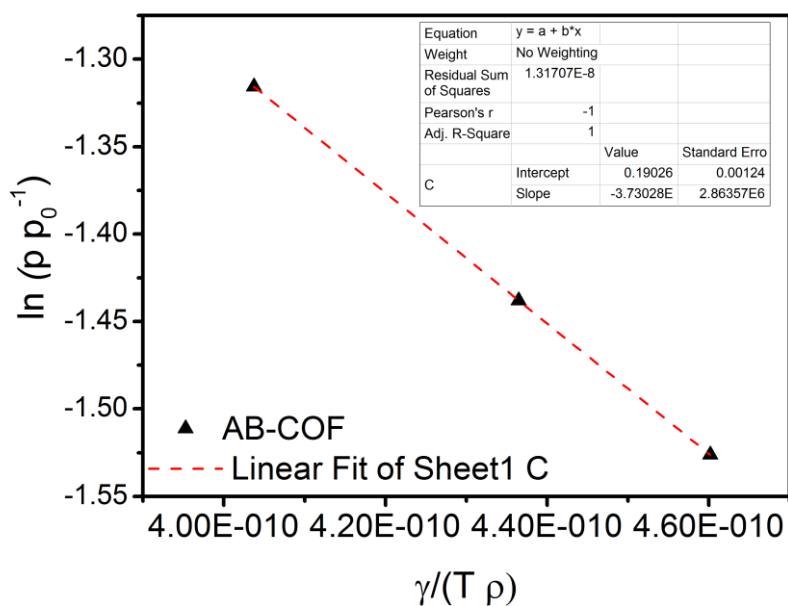
$$\ln\left(\frac{P}{P_0}\right) = \frac{-2\gamma}{rRT\rho} \cos \theta$$

Where r is the pore radius, R is the universal gas constant, γ is the surface tension, ρ is the molar liquid density, T is the temperature, and θ is the effective contact angle of the adsorbate on the pore surface.

Both the molar liquid density^{S7} and the surface tension^{S8} of water are temperature-dependent and the corresponding values for 288 K, 298 K and 313 K have been used for calculation, resulting in the following plot:

Table 4.S6. Data used for the Kelvin plot.^{S7, S8}

Temp. [K]	Condensation pressure [p/p_0^{-1}]	surface tension [N m^{-1}]	molar bulk density [mol m^{-3}]
313	0.26826	0.00696	55075
298	0.23738	0.0072	55344
288	0.21734	0.00735	55458

**Figure 4.S29.** Plot of Kelvin equation of AB-COF.

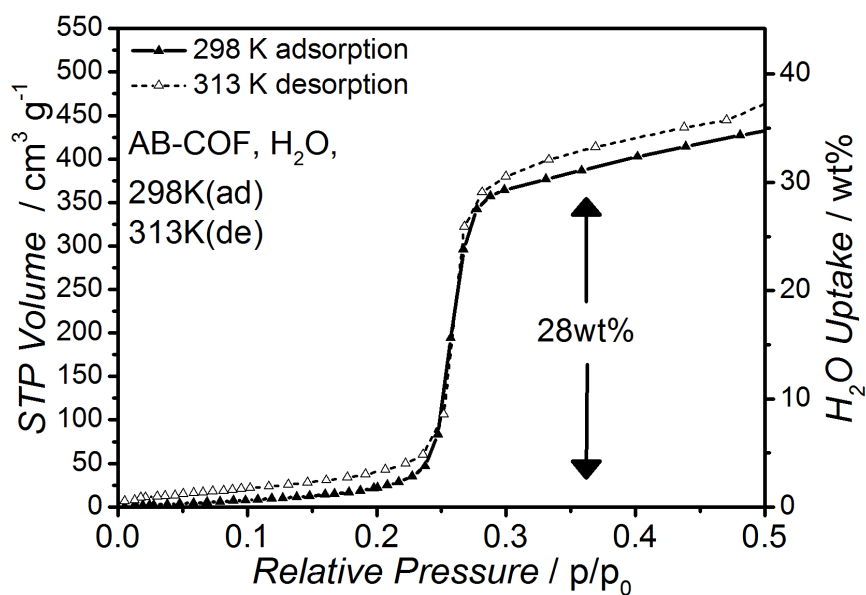


Figure 4.S30. Working capacity of AB-COF for atmospheric water capture in arid climates.

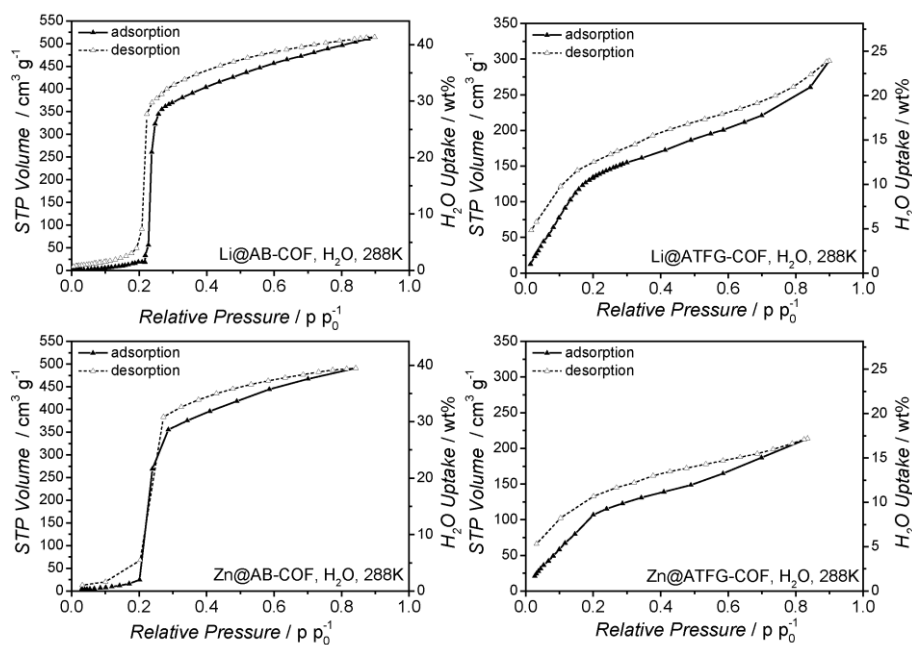


Figure 4.S31. Water sorption on metal-modified COF samples.

The cycle measurements were performed with the following settings:

AB-COF Adsorption pressure: 0.27 p/p₀

AB-COF Desorption pressure: 0.10 p/p₀

ATFG-COF Adsorption pressure: 0.31 p/p₀

ATFG-COF Desorption pressure: 0.015 p/p₀

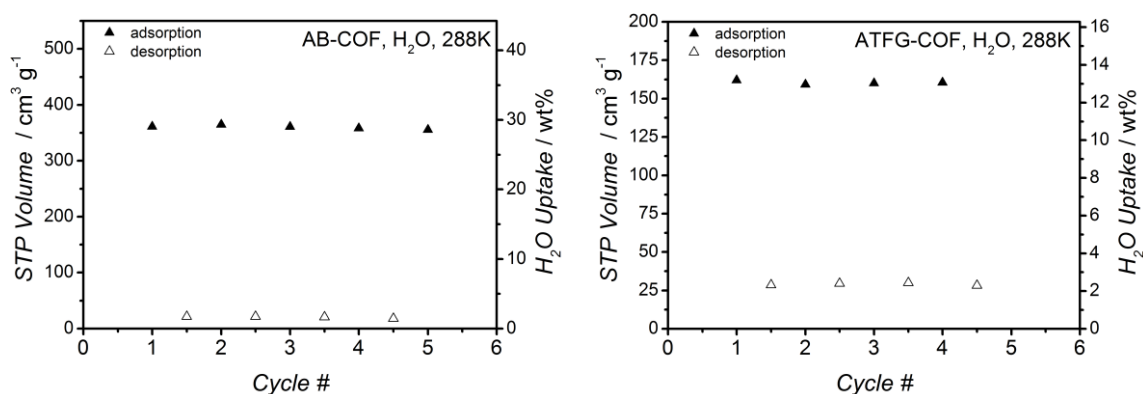


Figure 4.S32. Cycle measurements of water vapor sorption on AB-COF and ATFG-COF at 288 K.

Modification (“doping”) of COFs with metal salts

Li@AB-COF

In a 250 mL-flask with a stir bar 1959 mg of lithium acetate dihydrate (19.2 mmol, 6 eq.) were added to 100 mL of methanol. To the resulting clear solution, 1000 mg (3.2 mmol, 1.0 eq.) of AB-COF were added and the suspension was stirred for 24 h. The slurry suspension was transferred by a polyethylene pipette to a Büchner funnel and filtered. The filter cake was scratched off and transferred to an Erlenmeyer flask, washed with methanol (3 x 100 mL) and THF (2 x 100 mL), again filtered off, and dried under vacuum.

Zn@AB-COF

In a 250 mL-flask with a stir bar 4214 mg of zinc acetate dihydrate (19.2 mmol, 6 eq.) were added to 100 mL of methanol. To the resulting clear solution, 1000 mg (3.2 mmol, 1.0 eq.) of AB-COF were added and the suspension was stirred for 24 h. The slurry suspension was transferred by a polyethylene pipette to a Büchner funnel and filtered. The filter cake was scratched off and transferred to an Erlenmeyer flask, washed with methanol (3 x 100 mL) and THF (2 x 100 mL), again filtered off, and dried under vacuum.

Li@ATFG-COF

In a 50 mL-flask with a stir bar 60 mg of lithium acetate dihydrate (0.6 mmol, 6 eq.) were added to 4 mL of methanol. To the resulting clear solution, 40 mg (0.1 mmol, 1.0 eq.) of ATFG-COF were

added and the suspension was stirred for 24 h. The slurry suspension was transferred by a polyethylene pipette to a Büchner funnel and filtered. The filter cake was scratched off and transferred to an Erlenmeyer flask, washed with methanol (3 x 4 mL) and THF (2 x 4 mL), again filtered off, and dried under vacuum.

Zn@ATFG-COF

In a 50 mL-flask with a stir bar 129 mg of zinc acetate dihydrate (0.6 mmol, 6 eq.) were added to 4 mL of methanol. To the resulting clear solution, 40 mg (0.1 mmol, 1.0 eq.) of ATFG-COF were added and the suspension was stirred for 24 h. The slurry suspension was transferred by a polyethylene pipette to a Büchner funnel and filtered. The filter cake was scratched off and transferred to an Erlenmeyer flask, washed with methanol (3 x 4 mL) and THF (2 x 4 mL), again filtered off, and dried under vacuum.

The metal content has been determined by ICP-AES spectroscopy; see Table 4.S7.

A unit cell of AB-COF/ATFG-COF provides one coordination site for each nitrogen atom. The number of nitrogen atoms is six in both COFs. The molecular weight of the unit cell of AB-COF is $312.34 \text{ g mol}^{-1}$, and $408.33 \text{ g mol}^{-1}$ for ATFG-COF, respectively. With these data in our hands the number of occupied coordination sites was calculated.

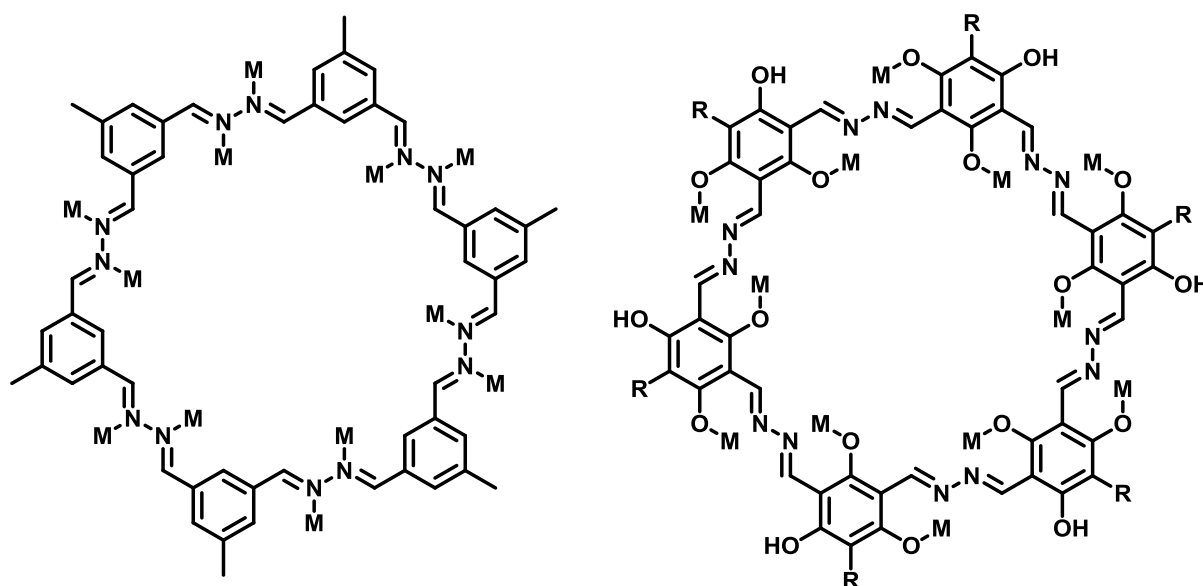


Figure 4.S33. AB- and ATFG-COF; all available coordination sites throughout the network are indicated by coordination of "M".

Table 4.S7. Calculation of occupied coordination sites of the network.

Sample	Molecular weight of COF [mg mmol ⁻¹]	Metal content by ICP [mg g ⁻¹]	Metal content [mmol g ⁻¹]	Number of	Percentage of
				coordination sites in empty COF [mmol g ⁻¹]	occupied coordination sites [%]
Li@AB-COF	312.34	1.1	0.16	19.2	0.8
Zn@AB-COF	312.34	7.72	0.12	19.2	0.6
Li@ATFG-COF	408.33	0.97	0.14	14.7	1
Zn@ATFG-COF	408.33	77.22	1.18	14.7	8

Solid-state NMR spectroscopy of Metal@COF compounds

For IR data please refer to the IR section G (Figures 4.S23-S26). Note that in the ¹³C NMR spectra, acetate residues of the metal salts can be observed (Fig. 4.S34), which is expected due to charge compensation of the metal cations.

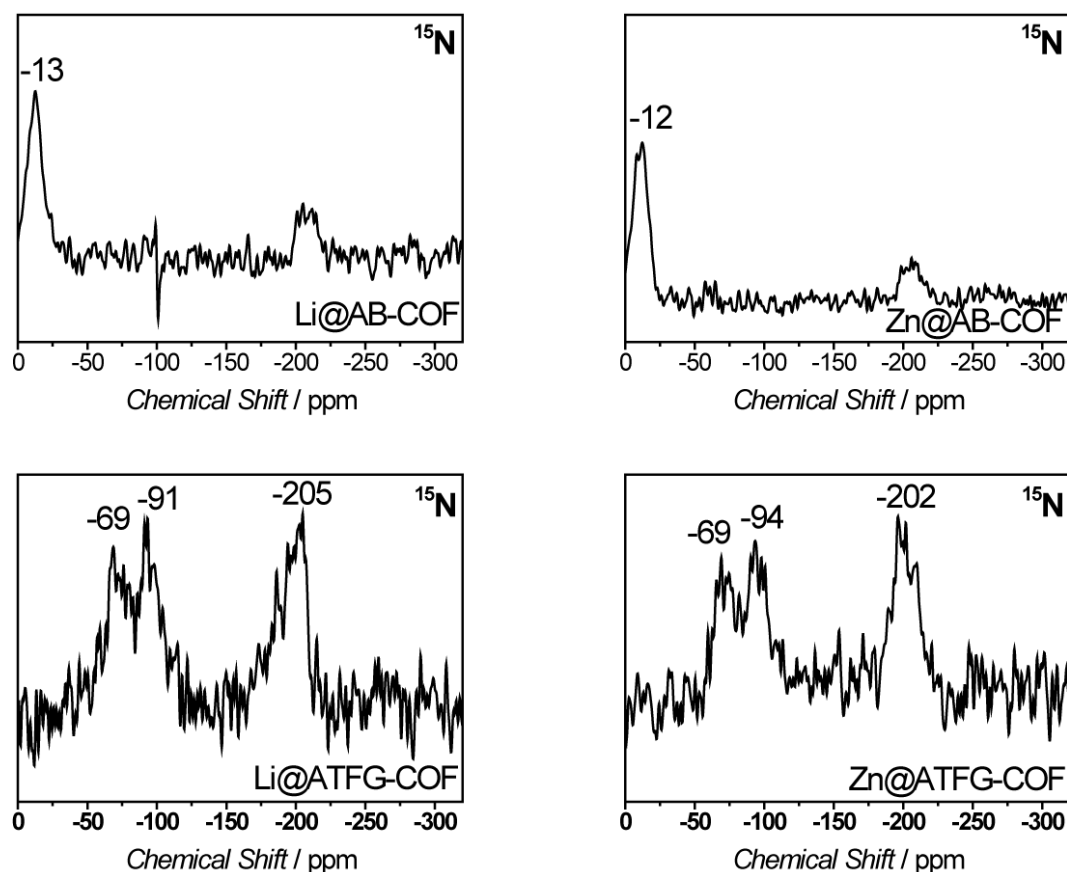


Figure 4.S34. ¹⁵N MAS NMR data of metal containing COF derivatives.

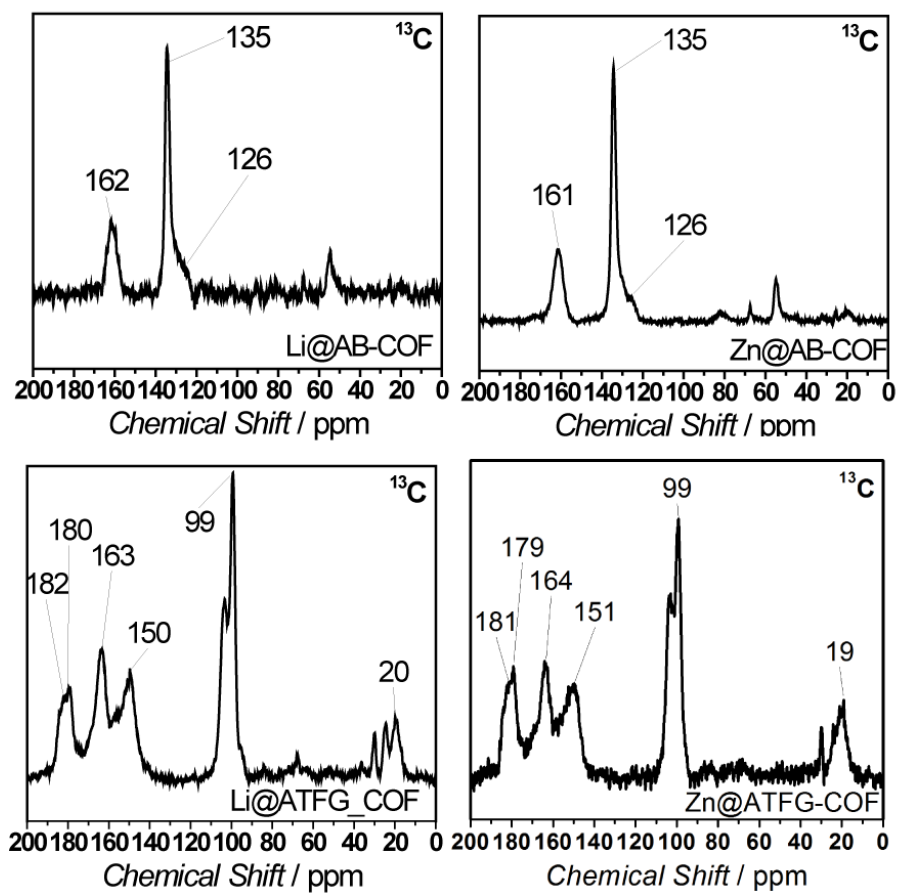


Figure 4.S35. ^{13}C MAS NMR data of metal containing COF derivatives.

Carbon dioxide and nitrogen sorption

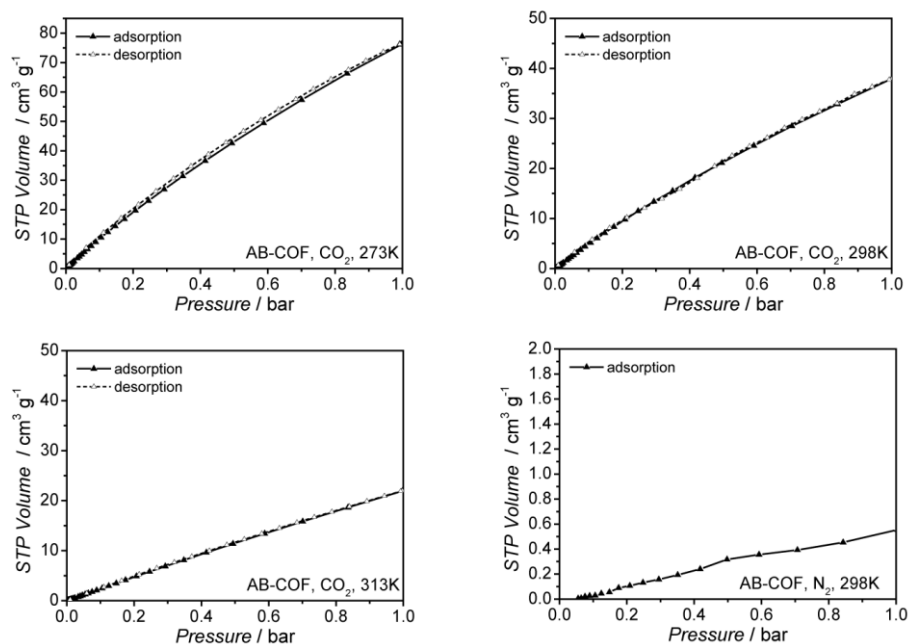


Figure 4.S36. AB-COF, CO₂ isotherms at 273, 298 and 313 K, N₂ at 298 K. Experimental conditions are given above.

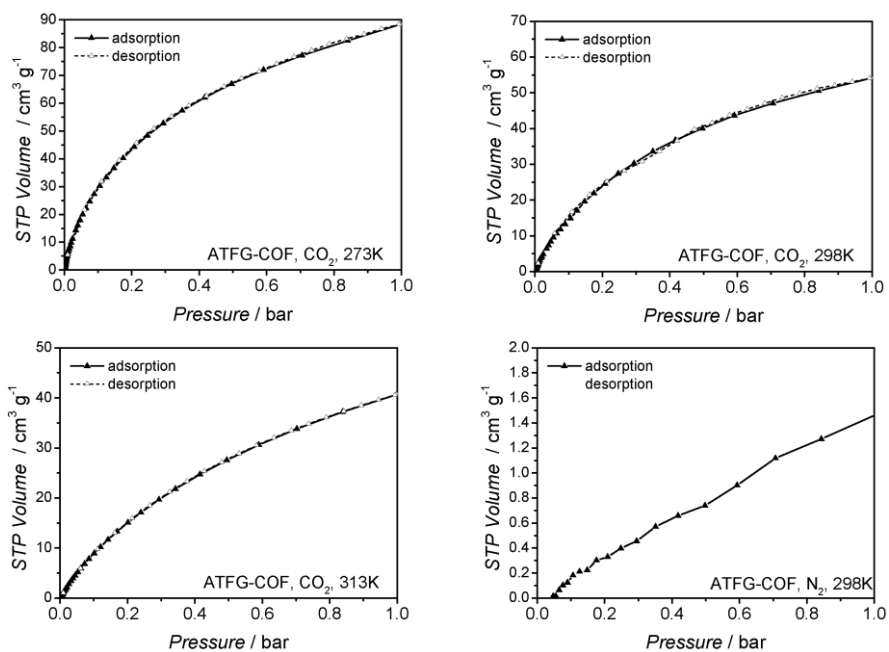


Figure 4.S37. ATFG-COF, CO₂ isotherms at 273, 298 and 313 K, N₂ at 298 K.

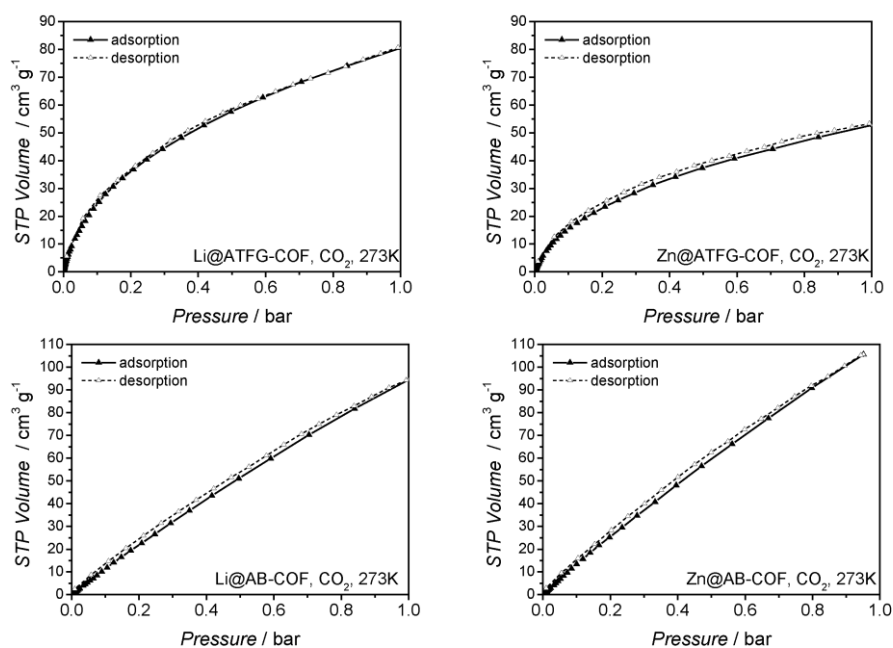


Figure 4.S38. Metal-modified COF samples, CO₂ isotherms at 273 K.

Table 4.S8. Comparison of the residual volumes (in cc g⁻¹) of CO₂ after desorption at 273 K.

COF	AB-COF			ATFG-COF		
	Li	Zn	-	Li	Zn	-
Adsorption*	0.87	1.05	1.08	4.77	2.86	5.83
Desorption*	2.53	2.87	1.24	5.61	3.75	5.50
Residual Volume*	1.66	1.82	0.16	0.84	0.92	0.33
$V_{\text{residue}}/V_{\text{total}}$ [%]**	1.8	1.7	0.2	1.0	1.8	0.4

* At 0.01 bar.

** V_{total} at 1 bar.

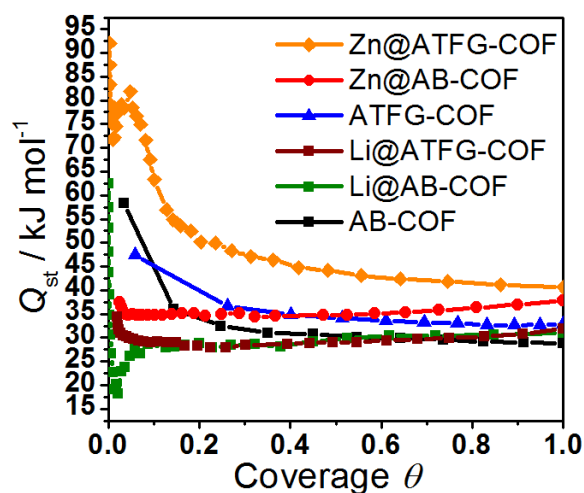


Figure 4.S39. CO₂ heats of adsorption plotted against coverage for different COFs.

Henry selectivity has been measured by the ratio of the initial slopes of the CO₂ and N₂ isotherms up to 0.1 p/p_0 (0.35 in rare cases for N₂).

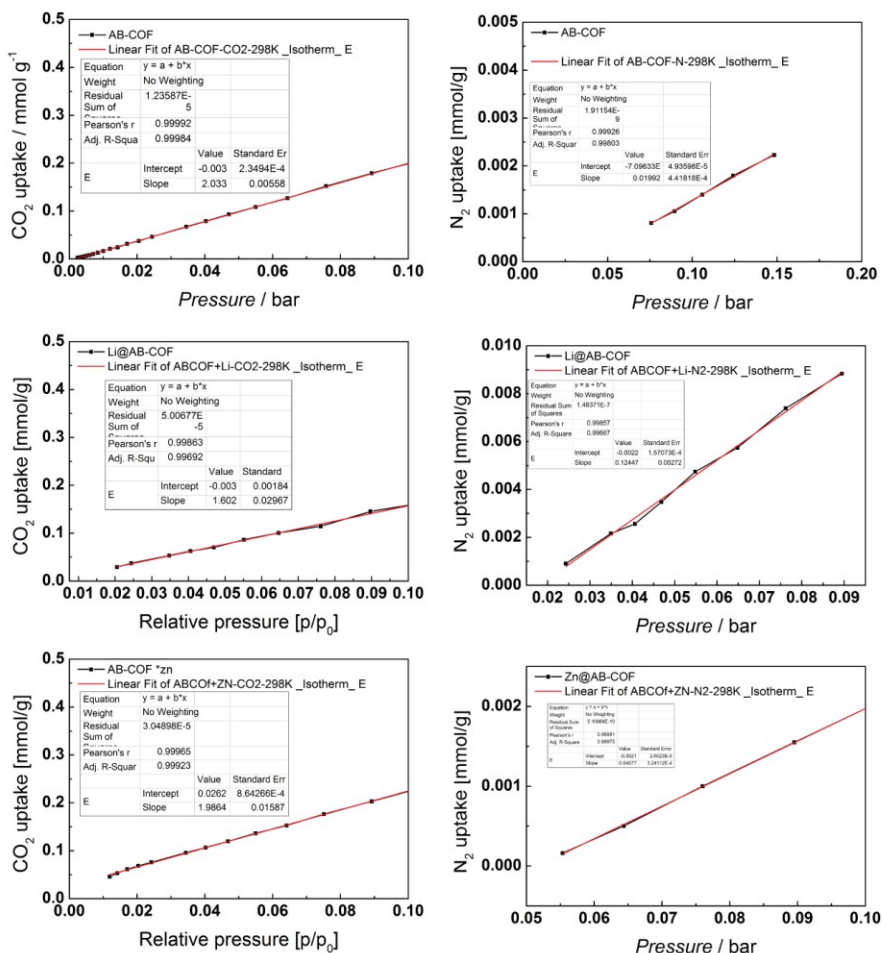


Figure 4.S40. Henry Plots and linear fits of AB-COF and its metal-derivatives at 298K.

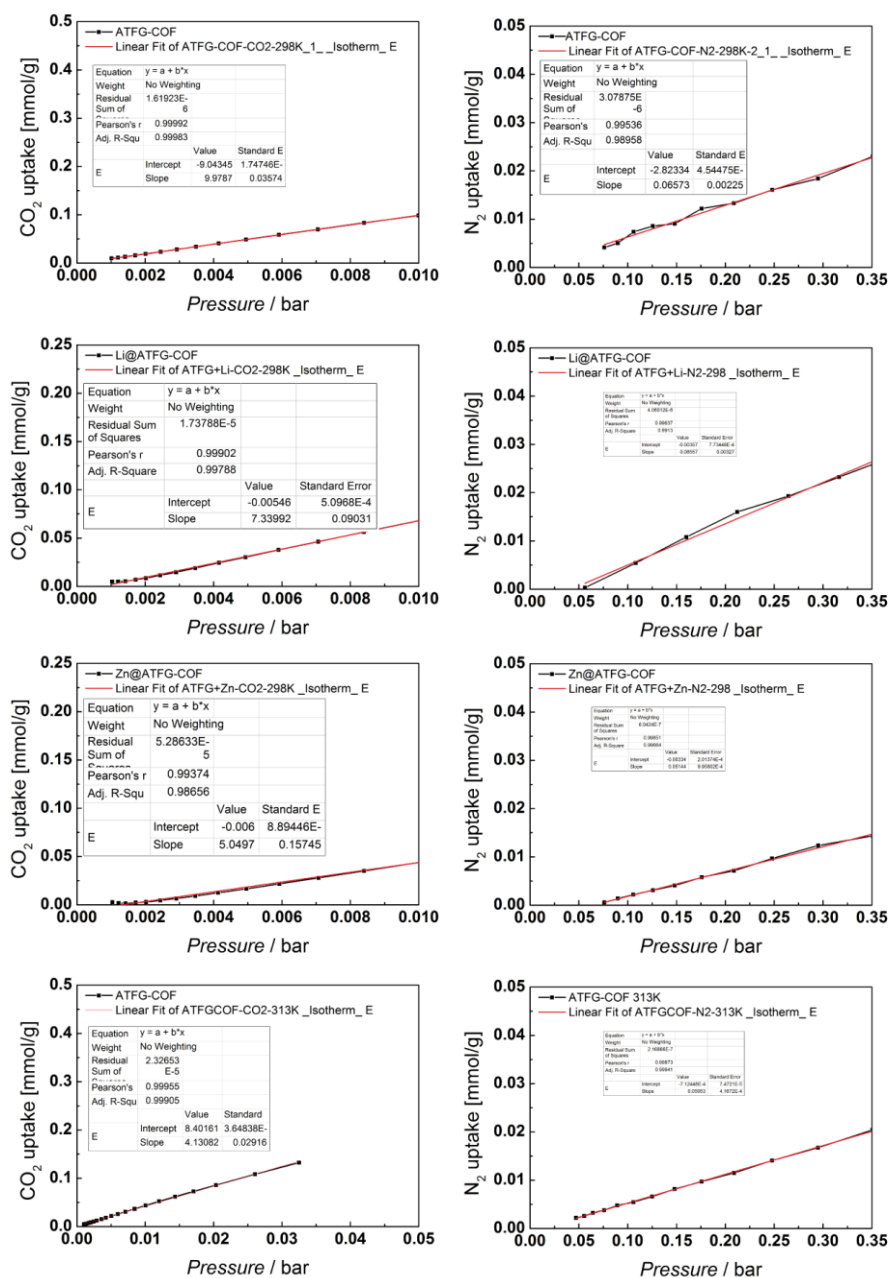


Figure 4.S41. Henry Plots of ATFG-COF and its metal-derivatives at 298K, and ATFG-COF at 313K.

Table 4.S9. BET surface areas, CO₂ and N₂ uptakes, heats of adsorption and CO₂/N₂ selectivities of various COFs.

Sample	BET SA [m ² g ⁻¹]	CO ₂ uptake [mmol g ⁻¹] ^a			N ₂ uptake ^b [mmol g ⁻¹]	Q _{st} [kJ mol ⁻¹]	Selectivity ^c	
		273 K	298 K	313 K			Henry	IAST
AB-COF	1125	3.38	1.68	0.97	0.02	29.7	102	88
Li@AB-COF	988	4.33	1.43	0.77	0.10	32.2	13	16
Zn@AB-COF	1120	4.68	1.79	0.87	0.06	31.8	48	55
ATFG-COF	520	3.93	2.40	1.87	0.06	33.3	151	65
Li@ATFG-COF	242	3.58	1.86	1.16	0.08	34.9	86	72
Zn@ATFG-COF	162	3.40	1.33	0.87	0.06	42.6	98	84
ATFG-COF							68*	69*

^aAt 1 bar. ^bAt 1 bar and 298 K. ^cAt 298 K. *At 313 K.

Flow TGA for pre-combustion

Experimental details can be found in the “Materials and Methods” section. The atmospheric adsorption of CO₂ under flow conditions is illustrated in Figure 4.S42. The adsorption of CO₂ is higher by a factor 1.5 to 2 at 30 °C as compared to 50 °C due to the exothermic nature of adsorption. The uptakes were by a factor of 4 (ATFG-COF) to 10 (Li@AB-COF and Zn@AB-COF) higher at CO₂ partial pressures of 1000 mbar (Figure 4.S42 b) compared to 100 mbar (Figure 4.S42 a), which is in line with the heats of adsorption that were in the range of physisorption (Figs. 4.S39/Table 4.S9). The uptakes of all sorbents were comparable under a non-diluted CO₂ stream, whereas at lower CO₂ partial pressures the adsorption was highest for ATFG-COF (Figure 4.S42).

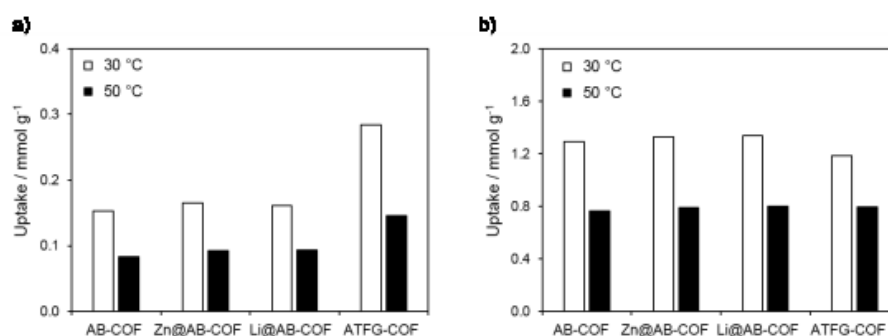


Figure 4.S42. Atmospheric adsorption of (A) 10 vol.% CO₂ in N₂ and (B) 100 vol.% CO₂ under flow conditions determined by TGA.

Breakthrough measurements

Experimental details can be found in “Materials and Methods”. Breakthrough curves were obtained for ATFG-COF as depicted in Figure 4.5 in the main text. The synthesis procedure (stirring for 24 h) of Li@AB-COF, Zn@AB-COF and AB-COF (see section J) lead to a strong decrease in the average particle size. The electrostatically charged adsorbents allowed no sufficient fractioning and, therefore, AB-COF, Li@AB-COF and Zn@AB-COF were excluded from further measurements due to a non-quantifiable pressure drop over the reactor column leading to a higher apparent uptake. These experiments were therefore discarded.

It should be noted that the CO₂ concentration selected for the breakthrough experiments (50 vol.%) was higher compared to the CO₂ content of flue gas concentrations 10-15 vol.%. The reason for this choice is the resulting lower standard deviation. The breakthrough curves of ATFG-COF are depicted in Figure 4.5 in the main text. The breakthrough was well-defined for both adsorbents with an uptake before breakthrough of 1.2 mmol g⁻¹ for ATFG-COF. Adsorption was fully reversible in pure N₂ already at the adsorption temperature of 50 °C. No further CO₂ was detected by an increase of the desorption temperature to 100 °C. This is in agreement with the weak interaction of the sorbents with CO₂ (physisorption) that is expected for heats of adsorption around 30 kJ mol⁻¹.

References

- S1. J. H. Chong, M. Sauer, B. O. Patrick, M. J. MacLachlan, *Org. Lett.* 2003, **5**, 3823–3826.
- S2. M. W. Hahn, M. Steib, A. Jentys, J. A. Lercher, *J. Phys. Chem. C* 2015, **119**, 4126–4135.
- S3. M. W. Hahn, M. Steib, A. Jentys, J. A. Lercher, *J. Mater. Chem. A* 2014, **2**, 13624–13634.
- S4. a) D. Flaig, M. Maurer, M. Hanni, K. Braunger, L. Kick, M. Thubauville, C. Ochsenfeld, *J. Chem. Theory Comput.* 2014, **10**, 572–578. b) J. Kussmann, C. Ochsenfeld, *J. Chem. Phys.* 2013, **138**, 134114. c) J. Kussmann, C. Ochsenfeld, *J. Chem. Theory Comput.* 2015, **11**, 918–922.
- S5. G. Akiyama, R. Matsuda, S. Kitagawa, *Chem. Lett.* 2010, **39**, 360–361.
- S6. M. M. Dubinin, *Chem. Rev.* 1960, **60**, 235–241.
- S7. M. Tanaka, G. Girard, R. Davis, A. Peuto, N. Bignell, *Metrologia* 2001, **38**, 301–309.
- S8. N. B. Vargaftik, B. N. Volkov, L. D. Voljak *J. Phys. Chem. Ref. Data* 1983, **12**, 817.

4.2 Synthesis of Triazine-Based Materials by Functionalization with Alkynes

Nicole E. Braml, Linus Stegbauer, Bettina V. Lotsch, Wolfgang Schnick

published in *Chem.--Eur. J.* **2015**, *21*, 7866-7873.

DOI: 10.1002/chem.201405023

<http://onlinelibrary.wiley.com/doi/10.1002/chem.201405023/abstract>

Abstract

In this contribution, we report on novel functionalized triazines, which represent new precursors for C/N(H) compounds or suitable building blocks for carbon-based functional networks. Our results provide insights into the structural properties of molecular carbon nitride materials and their design principles. Tris(1-propynyl)-1,3,5-triazine ($C_3N_3(C_3H_3)_3$) and tris(1-butynyl)-1,3,5-triazine ($C_3N_3(C_4H_5)_3$) were prepared by substitution reactions of cyanuric chloride ($C_3N_3Cl_3$) with prop-1-yne and but-1-yne. The crystal structure of tris(1-propynyl)-1,3,5-triazine was solved in the orthorhombic space group *Pbcn* ($Z=4$, $a=1500.06$ (14), $b=991.48$ (10), $c=754.42$ (6) pm, $V=1122.03$ (18) $\times 10^6$ pm³), whereas tris(1-butynyl)-1,3,5-triazine crystallized in the triclinic space group *P*-1 ($Z=6$, $a=1068.36$ (12), $b=1208.68$ (12), $c=1599.38$ (16) pm, $\alpha=86.67$ (3), $\beta=86.890$ (4), $\gamma=86.890$ (4) $^\circ$, $V=1997.7$ (4) $\times 10^6$ pm³). For both structures, planar triazine units and layerlike packing of the molecules were observed. Tris(1-propynyl)-1,3,5-triazine is built up from hydrogen-bonded zig-zag strands, whereas tris(1-butynyl)-1,3,5-triazine shows parallel layered arrangements. Both compounds were investigated by NMR spectroscopy, IR spectroscopy, and differential thermal analysis/thermogravimetric analysis, which provided insights into their structural, chemical, and thermal properties. In addition, tris(1-propynyl)-1,3,5-triazine was pyrolyzed and a new polymeric triazine-based compound containing mesitylene units was obtained. Its structural features and properties are discussed in detail.

Author contributions

Nicole Braml and Linus Stegbauer wrote the manuscript, edited the figures, designed and did the synthesis of the molecules and polymer. N.B. did the x-ray crystal structure determination and DTA TG measurements. L.S. did sorption measurements.

4.3 Nitrogen-rich Covalent Triazine Frameworks as High-Performance Platforms for Selective Carbon Capture and Storage.

Stephan Hug, Linus Stegbauer, Hyunchul Oh, Michael Hirscher, Bettina V. Lotsch

published in Chem. Mater. **2015**, 27, 8001–8010

DOI: 10.1021/acs.chemmater.5b03330

<http://pubs.acs.org/doi/abs/10.1021/acs.chemmater.5b03330>

Abstract

The search for new efficient physisorbents for gas capture and storage is the objective of numerous ongoing researches in the realm of functional framework materials. Here we present the CO₂ and H₂ uptake capacities of nitrogen rich covalent triazine frameworks based on lutidine, pyrimidine, bipyridine and phenyl units, showing superior gas uptakes and extremely high CO₂ selectivities towards N₂. The CO₂ uptake of a bipyridine-CTF synthesized at 600 °C (5.58 mmol g⁻¹, 273 K) is the highest reported for all CTFs so far and the second highest for all porous organic polymers (POPs). Moreover, the CO₂ selectivity towards N₂ of a nitrogen-rich pyrimidine-based CTF synthesized at 500 °C (Henry: 189, IAST: 502) is the highest reported for all POPs, and the H₂ uptake of CTF1 synthesized at 600 °C at 1 bar (2.12 wt%, 77 K) is the highest found for all CTFs to date as well. With the wide range of sorption data at hand, we carve out general trends in the gas uptake behavior within the CTF family and nitrogen-containing porous polymers in general, revealing the dominant role of the micropore volume for maximum CO₂ uptake, while we find that the nitrogen content is a secondary effect weakly enhancing the CO₂ uptake. The latter however was identified as the main contributor to the high CO₂/N₂ selectivities found for the CTFs. Furthermore, ambient water vapor sorption has been tested for CTFs for the first time, confirming the highly hydrophilic nature of CTFs with high nitrogen content.

Author contributions

Stephan Hug, Linus Stegbauer and Hyunchul Oh wrote the manuscript and edited the figures. S.H. designed and did the synthesis of all materials. S.H. did CO₂, Ar and N₂ sorption measurements. L.S. carried out the water vapor sorption measurements. Hyunchul Oh did H₂ sorption measurements.

5 DESIGN PRINCIPLES, FUNCTIONALIZATION AND SCREENING OF COFs - UNPUBLISHED RESULTS

5.1 Doping of Photocatalytically-active TFPT-COF by Perylene Moieties

Linus Stegbauer, Katharina Schwinghammer and Bettina V. Lotsch

To further probe the potential of TFPT-COF as a visible-light photocatalyst, a “doped” derivative was synthesized (see Figure 4.1). Molecule **DPDI** was synthesized via double-bromination of Perylene-3,4,9,10-tetra-carboxylic dianhydride and subsequent aryl ether formation with 3,5-di-*tert*-buty-phenol, followed by a bis-Imide formation with *p*-phenyldiamine.

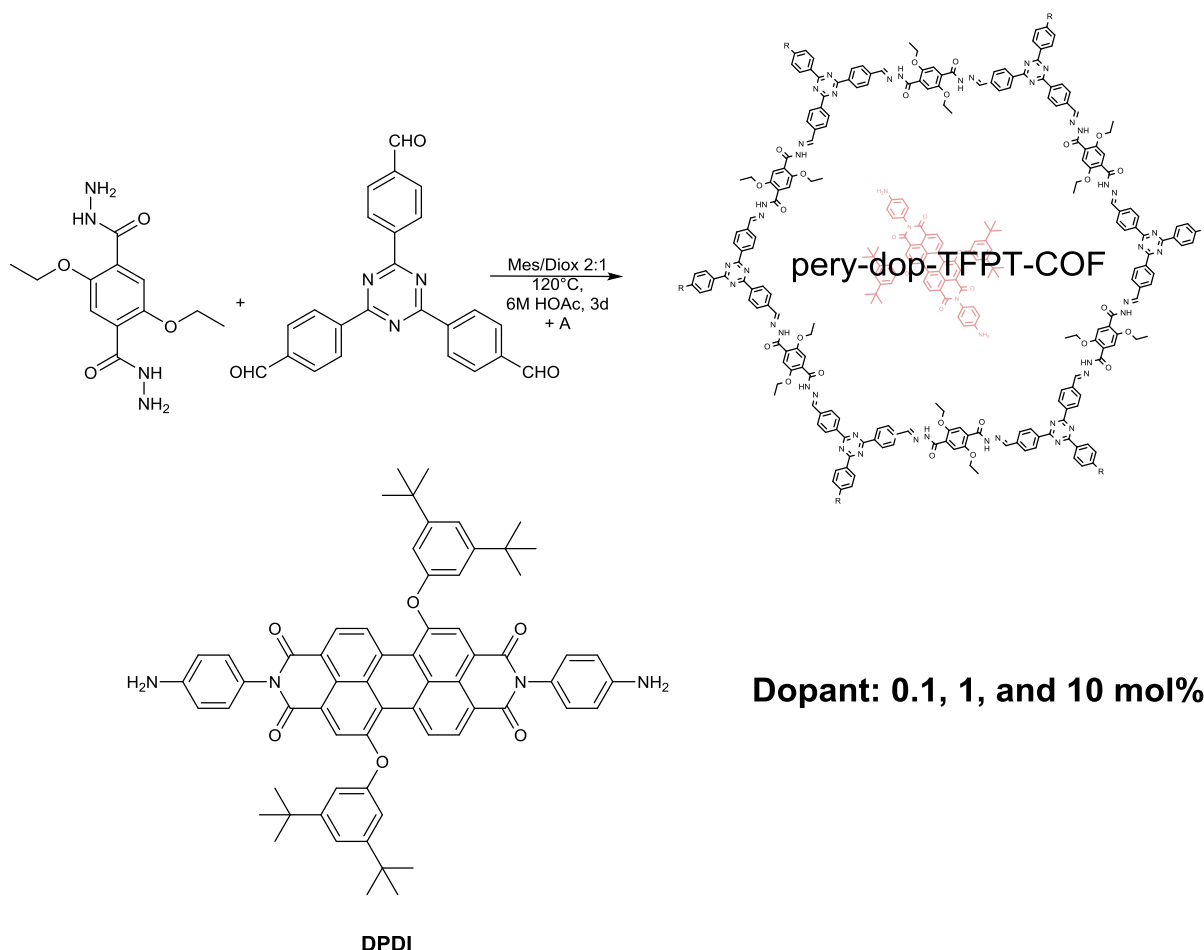


Figure 5.1: Synthesis of doped TFPT-COF (0.1mol%, 1.0mol% and 10mol%) by acid catalyzed hydrazone formation.

Several molar ratios of 0.1 mol%, 1.0 mol% and 10 mol% of diamino perylene diimide (DPDI) was added to the reaction mixture, leading to perylene-doped TFPT-COFs, which are crystalline and structurally related to the TFPT-COF (see Figure 4.4).

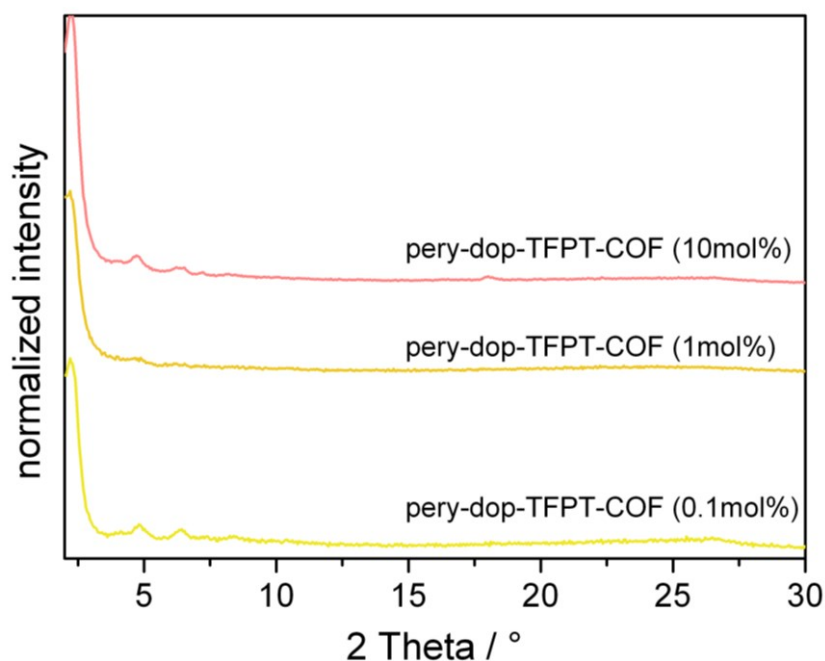


Figure 5.2: PXRDs of doped TFPT-COF with perylene derivative DPDI.

UV/VIS reflectance measurements confirm increased absorption around 550 nm, associated with the perylene moiety, which is also mirrored by the colours of each sample, which gradually change from yellow (0.1%) via orange (1.0%) to lilac (10%) (see Figure 5.3).

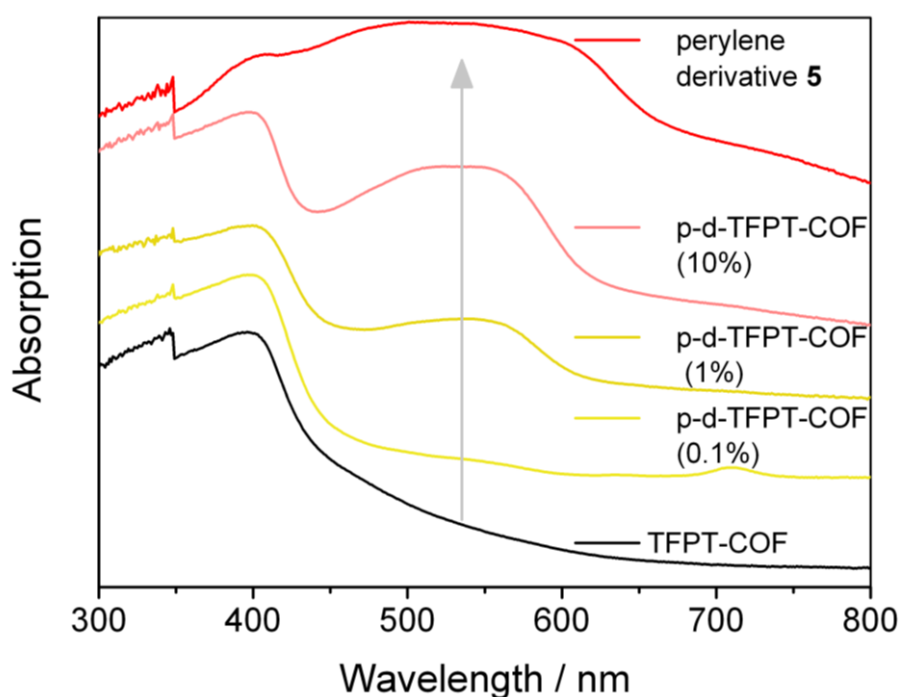


Figure 5.3: UV/VIS diffuse reflectance spectra of TFPT-COF (black) and its doped version by perylene DPDI derivatives (yellow to light red).

Wavelength-dependent photocatalytic hydrogen evolution reveals that the absolute quantum yield is significantly decreased, both at 400 nm and 550 nm (see Figure 5.4).

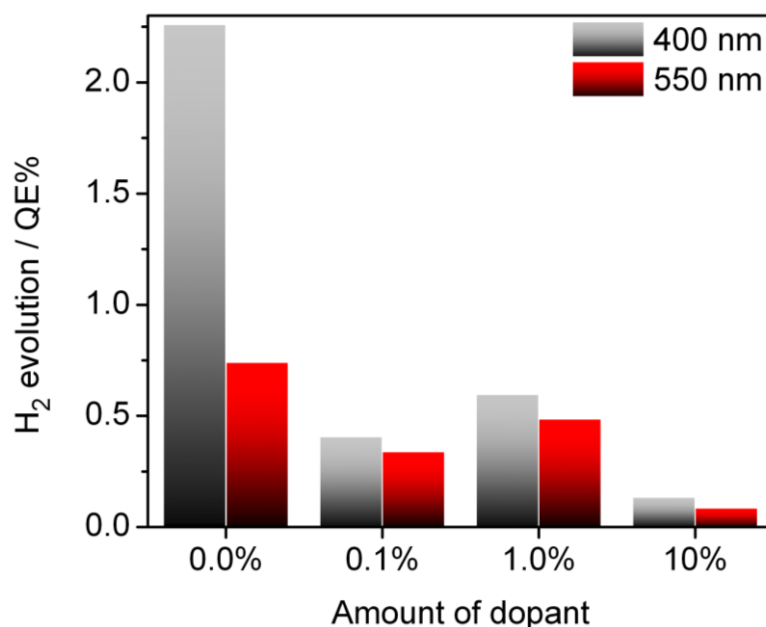


Figure 5.4: Quantum efficiency of doped and non-doped TFPT-COF at 400 nm (black) and 550 nm (red).

While looking at relative quantum yields (QE at 400 nm is set to 1 of the corresponding sample) a significant increase can be observed at 550 nm compared to the non-doped sample. This observation suggests that the perylene dopant significantly enhances the light harvesting capability of the TFPT-COF (see Figure 5.5), while decreasing its overall catalytic performance, perhaps due to loss in crystallinity or accessible pore volume.

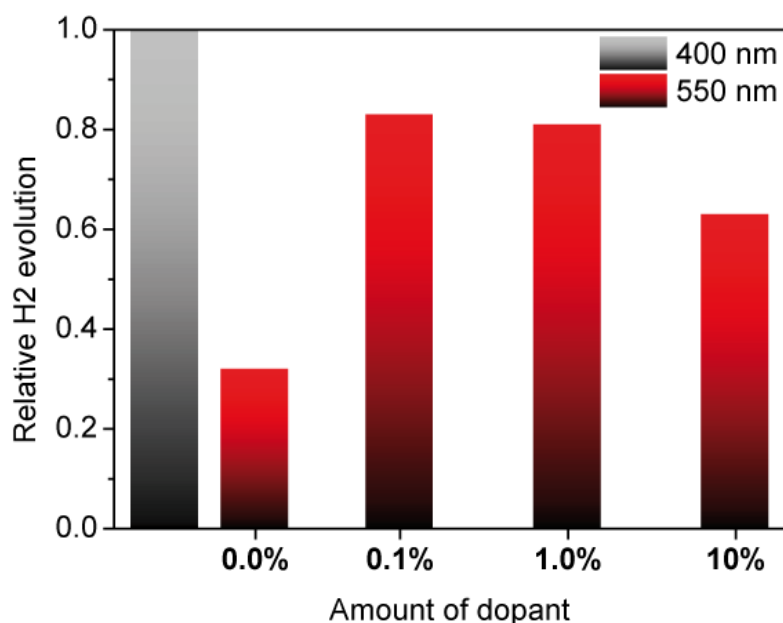


Figure 5.5: Comparison of relative quantum efficiencies (QE(400nm) set to 1 for the corresponding sample, black) of doped and non-doped TFPT-COF at 550 nm (red).

5.2 Crystallite and Particle sizes of TFPT-COF & Exfoliation

Linus Stegbauer, Helga Hoier, Viola Duppel and Bettina V. Lotsch

The x-ray powder diffraction pattern of TFPT-COF shows broadened reflection due to the small crystallite (domain) sizes. A closer look at the integral breadth β^1 derived from full width at half maximum (FWHM) of the stacking reflection 001 at $2\theta = 26.4^\circ$ revealed a coherently scattering domain size in c direction of 13 nm according to the Scherrer equation (form factor K assumed to be 0.9).² The reflections belonging to the a and b directions revealed an average domain size of 45 ± 21 nm.

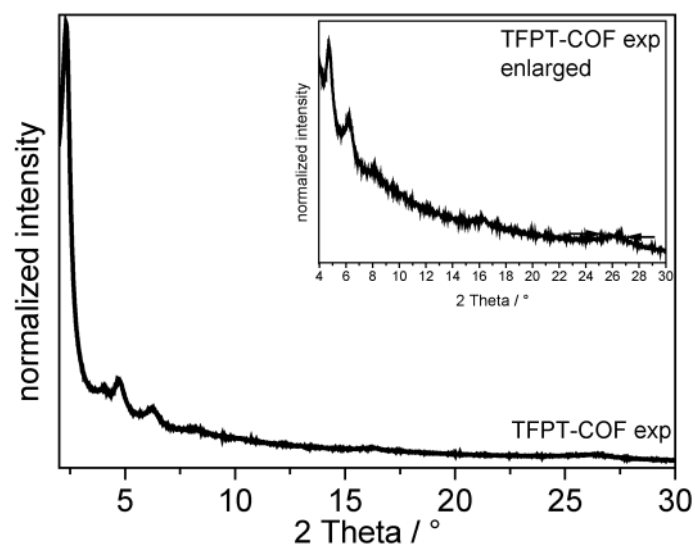


Figure 5.6: PXRD of TFPT-COF used for calculation of crystallite sizes by the Scherrer equation.

This size range is confirmed by TEM, which shows crystallites with similar domain sizes in *a* and *b* direction (see Figure 5.7).

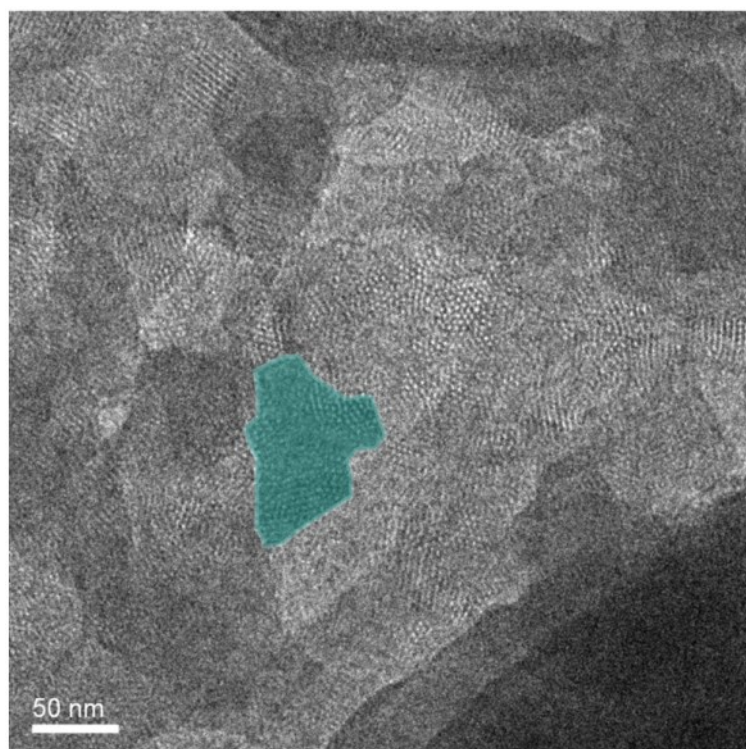


Figure 5.7: TEM image (300 kV) of TFPT-COF on a copper grid, showing the average lateral crystallite size to be < 100 nm.

Therefore, disc-shaped crystallites are assumed for TFPT-COF, which is used as input for the simulations by *Materials Studio* in Figure 5.8.

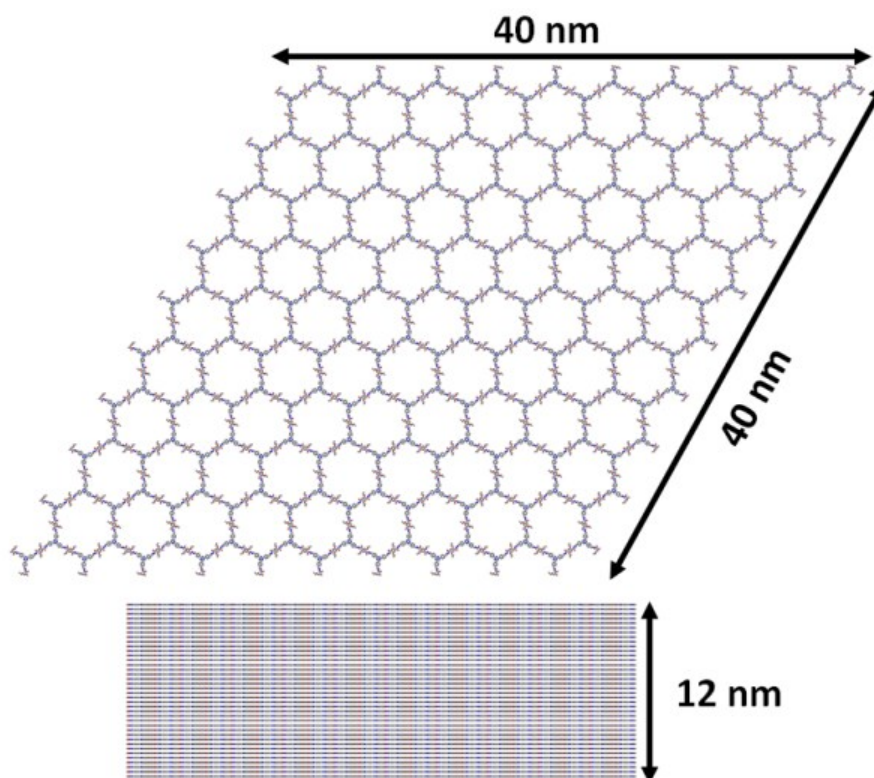


Figure 5.8: Simulation of a $40 \times 40 \times 12 \text{ nm}^3$ crystallite, consisting of 81×48 hexagons.

A particle size distribution based on small angle x-ray scattering (SAXS, measured as powder in reflection), measured by Helga Hoier (Max Planck Institute for Solid State Research, Stuttgart) showed a most frequent particle size of 83 nm, indicating that two crystallites may agglomerate to form one nanoparticle.

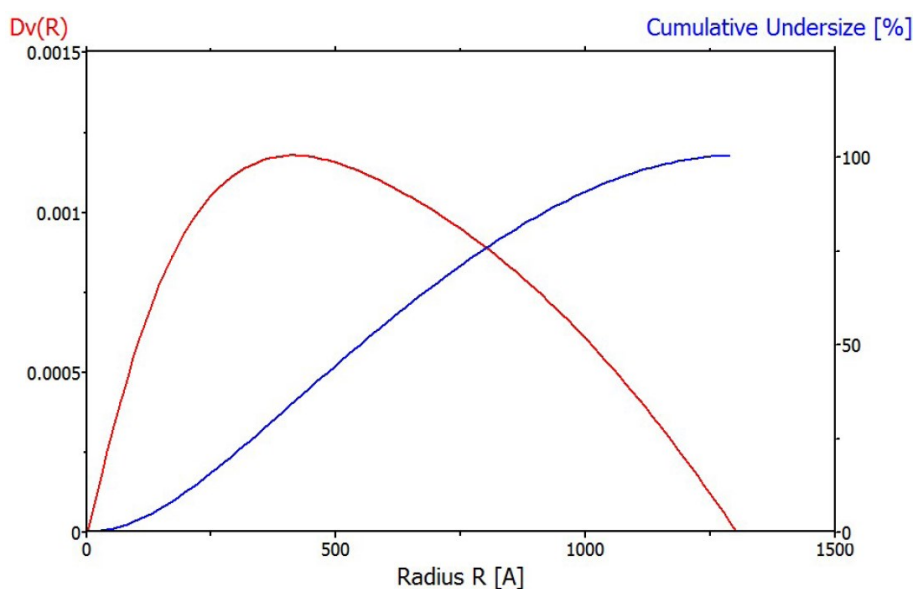


Figure 5.9: Particle radius distribution of TFPT-COF from SAXS experiments. Most frequent radius: 41.6 nm, average radius: 57.1 nm.

Exfoliation of TFPT-COF could be achieved by sonication of TFPT-COF in dichloromethane (DCM) for 30 min. Dropcasting of the colloidal solution on a silicon wafer and subsequent AFM analysis showed tiny disc-shaped particles (see Figure 5.10). Although these very small particles gave the impression of AFM artefacts, AFM data on a plain wafer dropcasted from DCM did not show these small particles. In light of the small crystallite and particle sizes obtained from the bulk material (see above), it is reasonable to assume that the tiny exfoliated particles of indeed exfoliated COF particles.

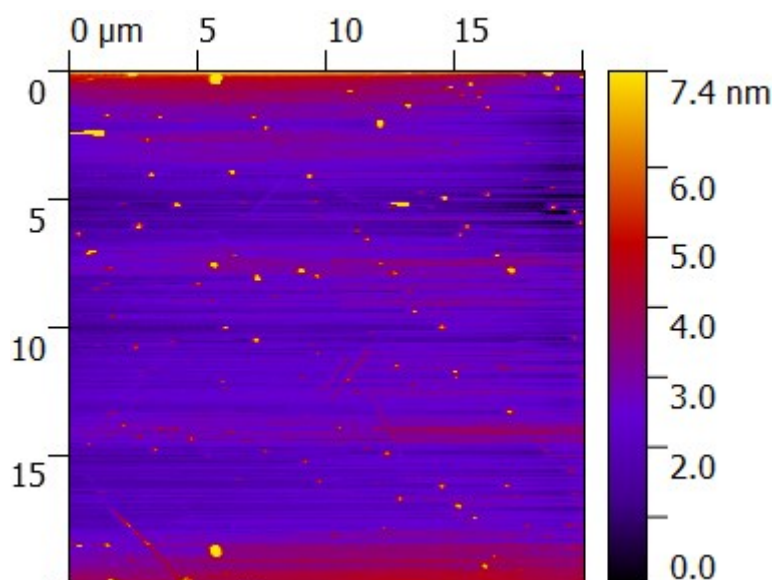


Figure 5.10: AFM picture of TFPT-COF exfoliated in DCM and dropcasted on a Si wafer.

The picture was further evaluated to obtain a height distribution and a particle radius distribution (assumed for a profile of a circular shape).

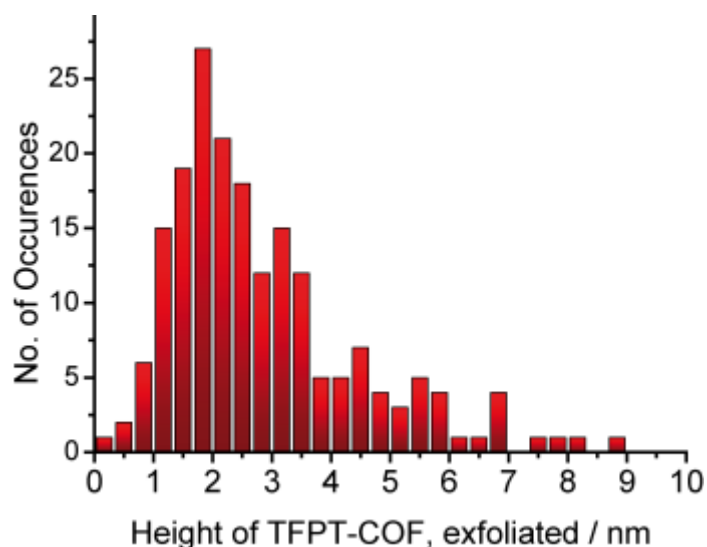


Figure 5.11: Height distribution of TFPT-COF nanosheets.

The mean height of the particles is 2.8 ± 1.7 nm. Compared to the bulk material (12 nm crystallite size in *c* direction), the height has been reduced by a factor of 4 by exfoliation. Single layers with a height of 0.34 nm were hardly observed.

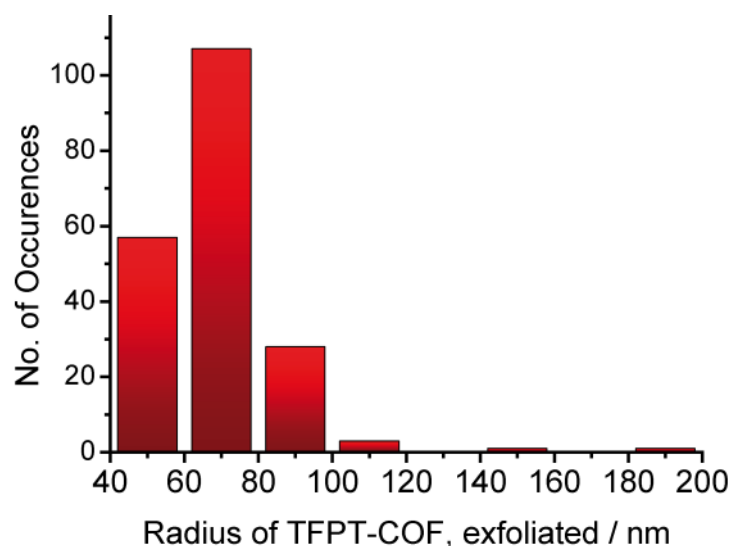


Figure 5.12: Radius distribution of TFPT-COF nanosheets, assuming disc-shaped particles.

The average radius is 65 ± 20 nm. The bulk data (by SAXS measurements, see above) showed a slightly smaller average diameter of 57 nm. This leads to the conclusion that exfoliation only leads to a vertical reduction in particle size and but does not influence the lateral size.

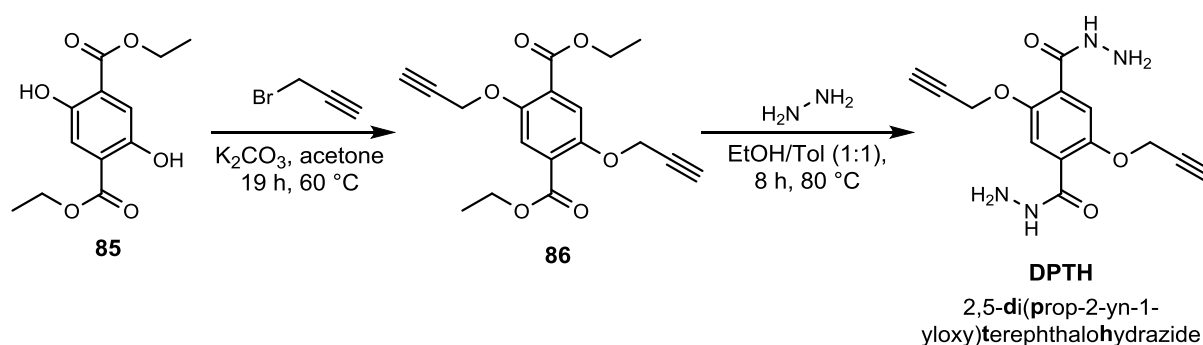
5.3 Preparing Covalent Organic Frameworks for *Click* Reactions

Linus Stegbauer, Li Gao and Bettina V. Lotsch

5.3.1 Modification of DETH with Alkyne and Azide Moieties.

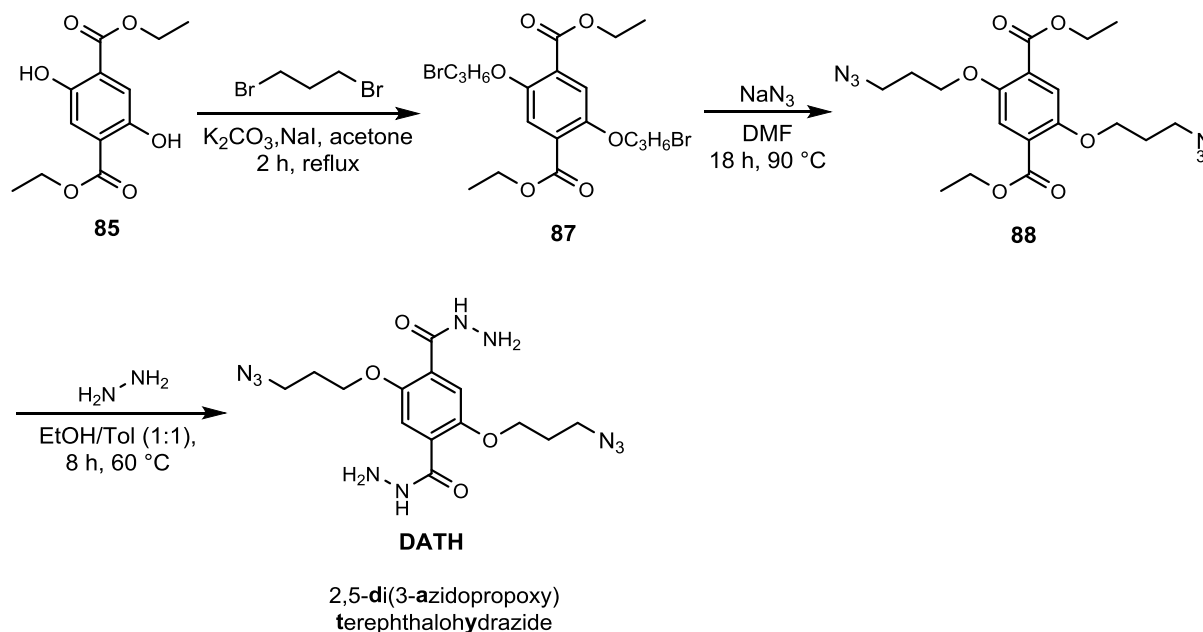
Using conventional Williamson ether synthesis the hydroxyl groups of **85** are etherified by deprotonation via potassium carbonate and subsequent nucleophilic substitution with the respective alkyl halide, carried out at 120 °C for 19 hours in acetonitrile as a one-pot reaction (Scheme 5.1). The target compound precipitates in water and can easily be isolated. Residues of alkyl halides are removed *in vacuo*. The same strategy can be applied for the introduction of the propargyl residue using acetone instead of acetonitrile as a solvent to yield alkyne **86**. The ester group is

transformed into a hydrazide function by adding an excess amount of hydrazine hydrate leading to 2,5-di(prop-2-yn-1-yloxy)terephthalohydrazide (**DPTH**). (Scheme 5.1).



Scheme 5.1. Synthetic route to 2,5-bis(prop-2-yn-1-yloxy)terephthalohydrazide DPTH.

Synthesis of compound 2,5-di(3-azidopropoxy)terephthalohydrazide (**DATH**) is done via a three-step synthesis (Scheme 5.2). Etherification of commercially available diester **85** with 1,3-dibromopropane leads to formation of dibromide **87**. The terminal bromide moiety is then exchanged with an azide group by treatment with sodium azide to give compound **88** in a nucleophilic substitution (S_N2). Introduction of the hydrazide function is done similar to compound **DPTH** by adding an excess amount of hydrazine hydrate.



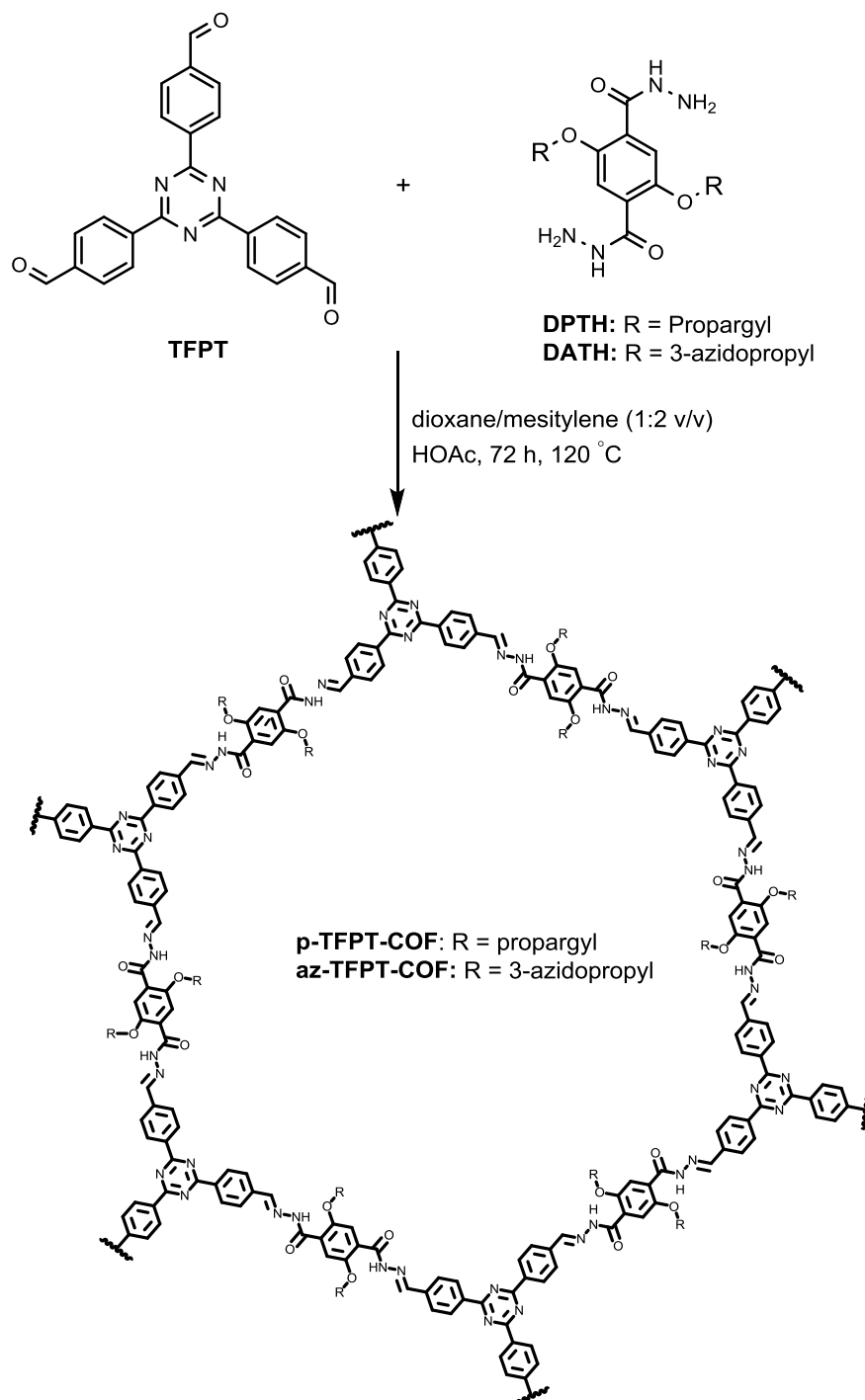
Scheme 5.2. Synthetic route to 2,5-bis(3-azidopropoxy)terephthalohydrazide (DATH).

5.3.2 Synthesis of Modified TFPT-COF Derivatives

The subsequent condensation reaction of TFPT with the terephthalate derivatives **DPTH** or **DATH** is carried out using the common reaction conditions, i.e. acetic acid catalyzed condensation in dioxane/mesitylene (1:2 v/v) at 120 °C in a sealed pressure vial under argon atmosphere

for 72 hours to give the two functionalized propargyl-TFPT-COF (p-TFPT-COF) (Scheme 5.3) or azido-TFPT-COF (az-TFPT-COF), respectively.

Due to the generally lower thermal stability of azide functions, temperature settings for **DATH** were adjusted accordingly.



Scheme 5.3. Synthesis of p-TFPT-COF and az-TFPT-COF.

DPTH and **DATH** derivatives were obtained with reasonable yield and high purity. GC-MS analysis showed that dibromide **87** undergoes base catalyzed elimination of the terminal bromide to

the corresponding allyl moiety at long reaction times. Additionally to shortening the reaction time and decreasing the temperature the crude mixture of **87** was purified by column purification. Subsequent hydrazide formation as well as COF formation with 100 mol% **DPTH** and 100 mol% **DATH**, respectively, was also successful, giving insoluble, yellowish powders. FT-IR-spectra show characteristic bands of the alkyne triple bond and the azide function at 2116 cm^{-1} and 2096 cm^{-1} , respectively. The fact that these bands can clearly be seen in the FT-IR-spectra is a clear proof that the TFPT-COF has been successfully functionalized using the modified building units **DPTH** and **DATH**. Powder diffraction (Figure 5.13) proves that both COFs are crystalline, however their degree of crystallinity is poor compared to TFPT-COF. Especially the introduction of the azide function seems to have a negative influence on the crystallinity, which might be due to the azide functions leading to non-planar moieties and causing a decrease of long-range order.

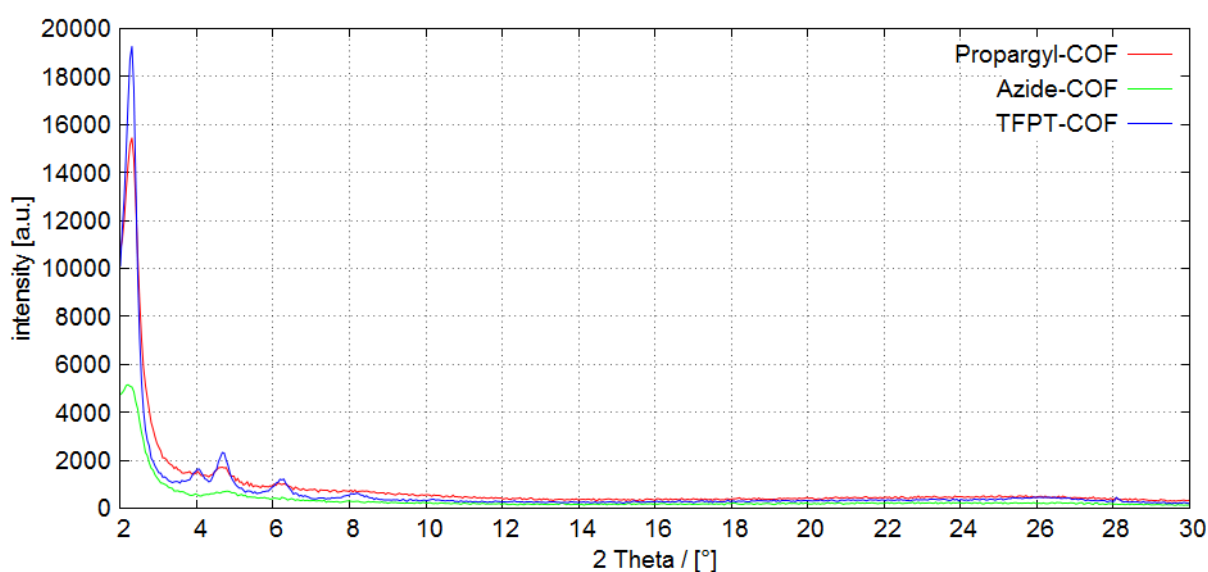


Figure 5.13: Experimental powder pattern of propargyl-COF (p-TFPT-COF), azide-COF (az-TFPT-COF) and TFPT-COF

The newly synthesized COFs display significantly lower BET surface areas than TFPT-COF. The initial assumption that the azide function decreases the structural order is supported by the proposition that crystallinity correlates with the surface area and the lower BET surface area of the az-TFPT-COF compared to the p-TFPT-COF.

Brunauer-Emmet-Teller (BET) surface areas by argon sorption:

Compound	p-TFPT-COF	az-TFPT-COF	TFPT-COF
BET surface area ($\text{m}^2\text{ g}^{-1}$)	179	92	1603

A temperature screening was performed for the p-TFPT-COF synthesis (1 h duration).

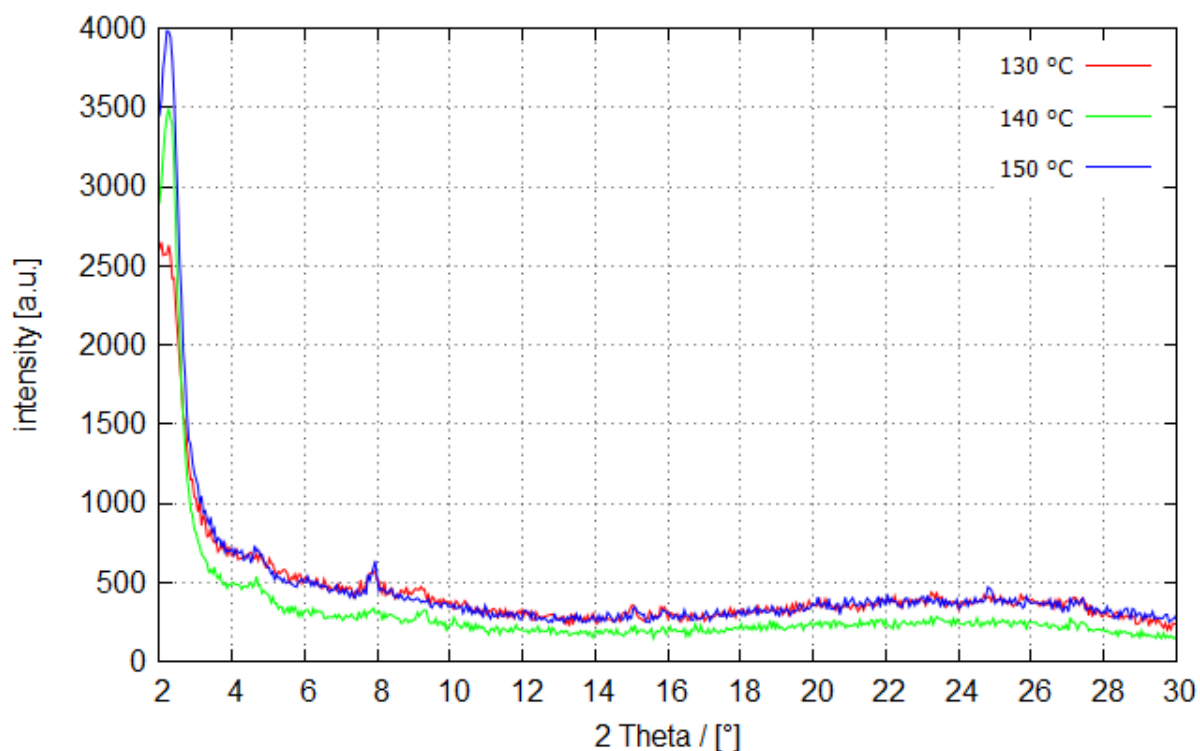


Figure 5.14: Experimental powder pattern of p-TFPT-COF synthesized at 130 °C, 140 °C and 150 °C.

The results indicate that compromises between crystallinity and surface area have to be taken in order to obtain optimal results. Similar to the microwave assisted TFPT-COF synthesis the p-TFPT-COF synthesis yields products of lower quality when compared to the conventional solvothermal procedure.

Calculated BET surface areas for p-TFPT-COF by Ar sorption:

Reaction temperature	130 °C	140 °C	150 °C
BET surface area ($\text{m}^2 \text{g}^{-1}$)	18	46	39

All foregoing results were obtained for solvent combination mes/diox 2:1, which showed best results for conventional TFPT-COF synthesis with the not functionalized linker DETH. Two other solvent ratios were used for determination of solvent influences. For this the temperature was kept at 140°C (1 h).

Calculated BET surface areas for p-TFPT-COF by Ar sorption:

mesitylene:dioxane ratio	3:1	1:1
BET surface area ($\text{m}^2 \text{g}^{-1}$)	23	66

Change of the solvent ratio does not lead to significant improvement of the surface area compared to the standard ratio 2:1 (see above).

5.3.3 Functionalization of TFPT-COF by Reconversion

Another approach has been tried by introduction of the functionalized DPTH *via* reconversion (see Chapter 3.1). A preformed standard TFPT-COF is then subjected to the synthesis conditions (2:1 mes/diox, 6M HOAc, 120°C, 3 d) and DPTH is added to the reaction solution. This approach leads to higher surface areas of the resulting p-TFPT-COFs although at the expense of an incomplete functionalization of the framework.

Calculated BET surface areas for p-TFPT-COF by Ar sorption (via reconversion):

DPTH in relation to DETH* (mol%)	100 mol%	66 mol%
BET surface area ($\text{m}^2 \text{g}^{-1}$)	826	1158

*Amount of DETH initially used for TFPT-COF synthesis.

IR measurements indicated an acetylenic C-H stretch vibration at 2116 cm^{-1} . ^{13}C Solid state NMR of the p-TFPT-COF showed a signal corresponding very well in chemical shift to the alkyne carbon atoms in DPTH (77 ppm, see Figure 5.15; compare to molecular DPTH: 79 ppm, see 5.3.5). Also ^1H solid-state NMR showed acetylenic protons at 3.7 ppm (comp. to molecular DPTH: 3.6 ppm, see Figure 5.15).

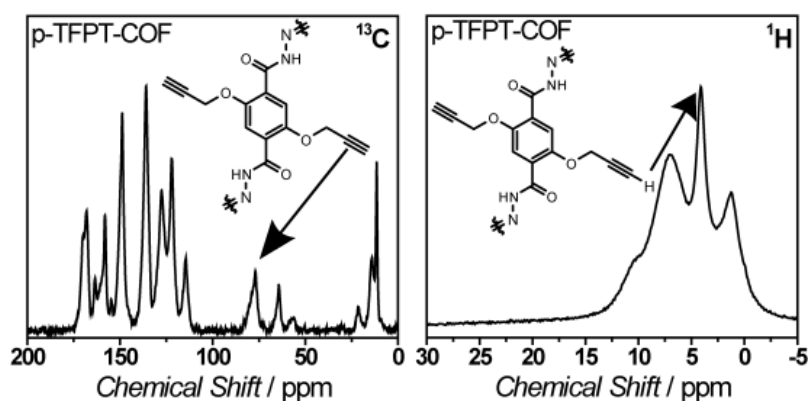


Figure 5.15: Solid state NMR of p-TFPT-COF via reconversion.

5.3.4 Conclusion and Outlook

Conclusion

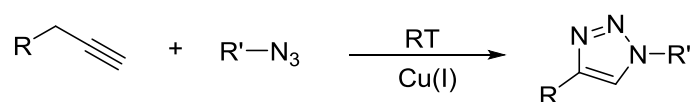
This work shows that it is possible to substitute the DETH ethoxy function with various other residues *via* Williamson etherification, of which the propargyl and azide substituted building blocks were successfully used to synthesize covalent organic frameworks. However the obtained COFs displayed rather poor crystallinity and BET surface areas, if the functionalized building block was solely used. A reconversion strategy turned out as successful and the functionalization is revealed by means of IR and ssNMR.

All in all it has been shown that the TFPT-COF can be modified in various ways using derivatives of DETH; however the structural order is disturbed, thus resulting in lower BET surface areas as well as low crystallinity.

Outlook

The current properties of p-TFPT-COF and az-TFPT-COF, especially the BET surface areas, are not satisfactory. In order to improve this, an extensive screening of reaction parameters, e.g. reaction temperature, acid concentration, dioxane/mesitylen ratio etc., will be needed. Screening all these parameters would take up a considerable amount of time without guarantying to actually solve the issue. Therefore improving the microwave-assisted TFPT-COF synthesis would speed up this time-consuming process and would also offer an attractive possibility for future industrial application to examine reaction parameters of COF-synthesis at a much faster rate.

The long term goal is to utilize the alkyne or the azide function for copper catalyzed click chemistry, which has already been archived for other COF systems.³⁻⁶

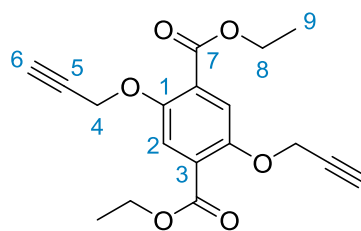


Scheme 5.4: Click reaction of alkynes with azides.

This would allow introducing a vast number of interesting functional groups into the TFPT-COF system, which could tune the properties of the material in various ways. For example, increasing the light harvesting ability of the TFPT-COF material would be very desirable. This could be done by linking the TFPT-COF with a chromophore that causes a bathochromic shift.

5.3.5 Experimental Data

Diethyl 2,5-bis(prop-2-yn-1-yloxy)terephthalate



Chemical Formula: $C_{18}H_{18}O_6$
Molecular Weight: 330.3

86

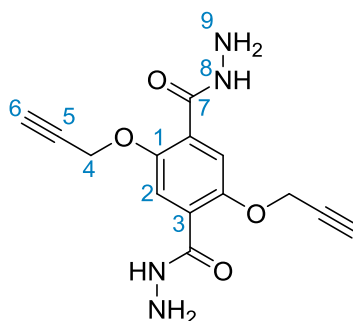
To a degassed suspension of diethyl 2,5-dihydroxyterephthalate **85** (1.05 g, 4.00 mmol, 1 eq) and potassium carbonate (2.21 g, 16.0 mmol, 4 eq) in 20 mL acetone was added dropwise 3-bromo-prop-1-yne (1.78 mL, 2.38 g, 16.0 mmol, 4 eq). The suspension was stirred for 19 h at 60 °C. The reaction mixture was cooled to room temperature and poured into 50 mL ice-cold dest. water. The precipitate was isolated and dried *in vacuo* to give target compound (1.28 g, 3.87 mmol, 97 %) **86** as colourless needles.

^1H NMR (400 MHz, CDCl_3): δ 1.38 (t, $J = 7.1$ Hz, 6H, H-9), 2.53 (s, 4H, H-6), 4.37 (q, $J = 7.3$, 6.6 Hz, 4H, H-8), 4.74 (s, 4H, H-4), 7.55 (s, 2H, H-2) ppm.

^{13}C NMR (100 MHz, CDCl_3): δ 14.2 (C-9), 58.2 (C-4), 61.6 (C-8), 76.3 (C-6), 78.0 (C-5), 118.9 (C-2), 125.8 (C-3), 151.3 (C-1), 165.1 (C-7) ppm.

IR (FT, ATR): 3279 (m, ν ($\text{C}\equiv\text{C-H}$)), 2990 (w, ν ($-\text{CH}_2-$)), 2126 (w, ν ($\text{C}\equiv\text{C}$)), 1698 (s, ν ($\text{C}=\text{O}$)), 1503 (m, ν (Aryl $\text{C}=\text{C}$)), 1419 (s), 1382 (s), 1206 (s), 1009 (s), 882 (w), 783 (m) cm^{-1} .

2,5-bis(prop-2-yn-1-yloxy)terephthalohydrazide



Chemical Formula: $C_{14}H_{14}N_4O_4$
Molecular Weight: 302.3

DPTH

To a degassed solution of **86** (248 mg, 0.75 mmol, 1 eq) in 4 mL EtOH/Tol (1:1) was added hydrazine hydrate (0.365 mL, 375 mg, 7.5 mmol, 10 eq). The solution was stirred for 8 h at 80 °C. Afterwards the reaction mixture was stirred overnight at room temperature. Volatiles were removed *in vacuo*, and compound **DPTH** (152 mg, 50.3 mmol, 67 %) was isolated and dried to give an off-white powder.

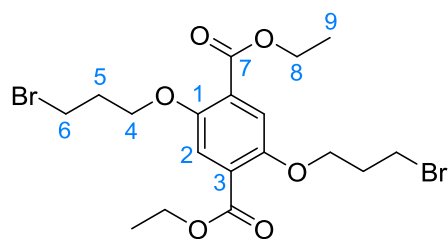
^1H NMR (400 MHz, DMSO- d_6): δ 3.59 (s, 2H, H-6), 4.55 (br, 4H, H-9), 4.87 (s, 4H, H-4), 7.45 (s, 2H, H-2), 9.28 (s, 2H, H-8) ppm.

^{13}C NMR (100 MHz, DMSO- d_6): δ 57.3 (C-4), 79.4 (C-6), 79.5 (C-5), 115.9 (C-2), 126.1 (C-3), 149.3 (C-1), 164.0 (C-7) ppm.

HRMS (EI, positive): calc. for $\text{C}_{14}\text{H}_{14}\text{N}_4\text{O}_4$ (M) $^+$: 302.1015; found: 302.1001.

IR (FT, ATR): 3312 (w, v (-NH $_2$)), 3186 (m, v (C \equiv C-H)), 2933 (w, v (-CH $_2$ -)), 2110 (w, v (C \equiv C)), 1643 (m, δ (-NH $_2$)), 1584 (s, v (C=O)), 1514 (m, v (Aryl C=C)), 1489 (m), 1199 (s), 1026 (s), 976 (s), 901 (m), 749 (s) cm^{-1} .

Diethyl 2,5-bis(3-bromopropoxy)terephthalate



Chemical Formula: $\text{C}_{18}\text{H}_{24}\text{Br}_2\text{O}_6$
Molecular Weight: 496.2

87

A degassed mixture of diethyl-2,5-dihydroxyterephthalate **85** (1.57 g, 6 mmol, 1 eq), 1,3-dibromopropane (9.32 mL, 18.5 g, 90 mmol, 15 eq), potassium carbonate (7.80 g, 56.4 mmol, 9.4 eq) and sodium iodide in 12 mL acetone was stirred for 2 h under reflux conditions. The solvent was evaporated and the crude product was purified by column chromatography (EtOAc:Hex = 3:7).

Fraction 1: 420 mg, 14 %

Fraction 2: 1.22 g, 41 %

Fraction 3: 155 mg, 5 %

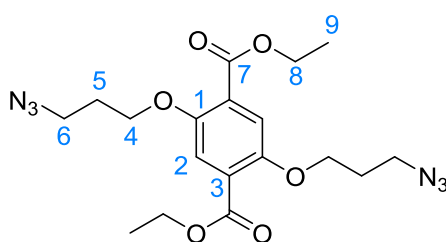
Fraction 4: 57 mg, 2 %

Fractions 2 and 3 contained target compound **87** in form of a colourless powder, whereas fraction 1 and 4 contained target compound **87** as well as small amounts of side product. Spectroscopic data was consistent to literature.

^1H NMR (400 MHz, CDCl_3): δ 1.37 (t, $J = 7.1$ Hz, 6H, H-9), 2.23 – 2.40 (m, 4H, H-5), 3.64 (t, $J = 6.4$ Hz, 4H, H-6), 4.15 (t, $J = 5.7$ Hz, 4H, H-4), 4.36 (q, $J = 7.1$ Hz, 4H, H-8), 7.38 (s, 2H, H-2) ppm.

^{13}C NMR (100 MHz, CDCl_3): δ 14.4 (C-9), 30.0 (C-5), 32.5 (C-6), 61.5 (C-8), 67.2 (C-4), 117.0 (C-2), 124.9 (C-3), 151.7 (C-1), 165.6 (C-7) ppm.

Diethyl 2,5-bis(3-azidopropoxy)terephthalate



Chemical Formula: $\text{C}_{18}\text{H}_{24}\text{N}_6\text{O}_6$
Molecular Weight: 420.4

88

A degassed solution of **87** (229 mg, 0.462 mmol, 1 eq) and sodium azide (750 mg, 11.5 mmol, 25 eq) in 4 mL dry DMF was stirred at 90 °C for 18 h. The reaction was stopped, cooled down to room temperature and the reaction mixture was poured into 40 mL ice-cold dest. water. The colourless precipitate was filtered and dried *in vacuo* to give target compound **88** (190 mg, 0.45 mmol, 98 %).

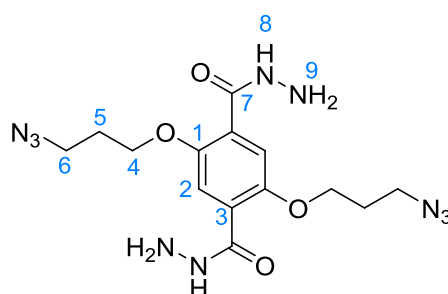
^1H NMR (400 MHz, CDCl_3): δ 1.38 (t, $J = 7.1$ Hz, 6H, H-9), 2.06 (p, $J = 6.3$ Hz, 4H, H-5), 3.56 (t, $J = 6.6$ Hz, 4H, H-6), 4.10 (t, $J = 5.8$ Hz, 4H, H-4), 4.36 (q, $J = 7.1$ Hz, 4H, H-8), 7.36 (s, 2H, H-2) ppm.

^{13}C NMR (100 MHz, CDCl_3): 14.4 (C-9), 28.9 (C-5), 48.1 (C-6), 61.4 (C-8), 66.3 (C-4), 116.9 (C-2), 124.8 (C-3), 151.7 (C-1), 165.5 (C-7) ppm.

^{14}N NMR (29 MHz, CDCl_3): δ -128.54, -167.41, -318.03 ppm.

HRMS (ESI, positive): calc. for $\text{C}_{18}\text{H}_{24}\text{N}_6\text{O}_6$ ($\text{M}+\text{Na}$) $^+$: 443.1655; found: 443.1657.

IR (FT, ATR): 3065 (w, v (Aryl-H)), 2987 (w, v ($-\text{CH}_2-$)), 2092 (s, v ($-\text{N}_3$)), 1684 (s, v ($\text{C}=\text{O}$)), 1504 (m, v (Aryl $\text{C}=\text{C}$)), 1423 (s), 1381 (s), 1302 (m), 1211 (s), 1110 (m), 1046 (s), 967 (s), 933 (m), 860 (m), 782 (m), 747 (m) cm^{-1} .

2,5-bis(3-azidopropoxy)terephthalohydrazide

Chemical Formula: C₁₄H₂₀N₁₀O₄
Molecular Weight: 392.4

DATH

To a degassed solution of **88** (50.5 mg, 0.12 mmol, 1 eq) in 1 mL EtOH/Tol (1:1) was added hydrazine hydrate (0.0583 mL, 60.1 mg, 1.2 mmol, 10 eq). The solution was stirred for 8 h at 60 °C. Afterwards the reaction mixture was stirred overnight at room temperature. Volatiles were removed *in vacuo*, and compound **DATH** (36 mg, 0.092 mmol, 76 %) was isolated and dried to give a white powder.

¹H NMR (270 MHz, DMSO-*d*₆): δ 2.00 (p, J = 6.4 Hz, 4H, H-5), 3.54 (t, J = 6.6 Hz, 4H, H-6), 4.11 (t, J = 6.0 Hz, 4H, H-4), 4.56 (br, 4H, H-9), 7.34 (s, 2H, H-2), 9.29 (br, 2H, H-8) ppm.

¹³C NMR (68 MHz, DMSO-*d*₆): δ 28.61 (C-5), 48.47 (C-6), 67.12 (C-4), 115.21 (C-2), 126.03 (C-3), 150.11 (C-1), 164.39 (C7) ppm.

HRMS (ESI, positive): calc. for C₁₄H₂₁N₁₀O₄ (M+H)⁺: 393.1747; found: 393.1747.

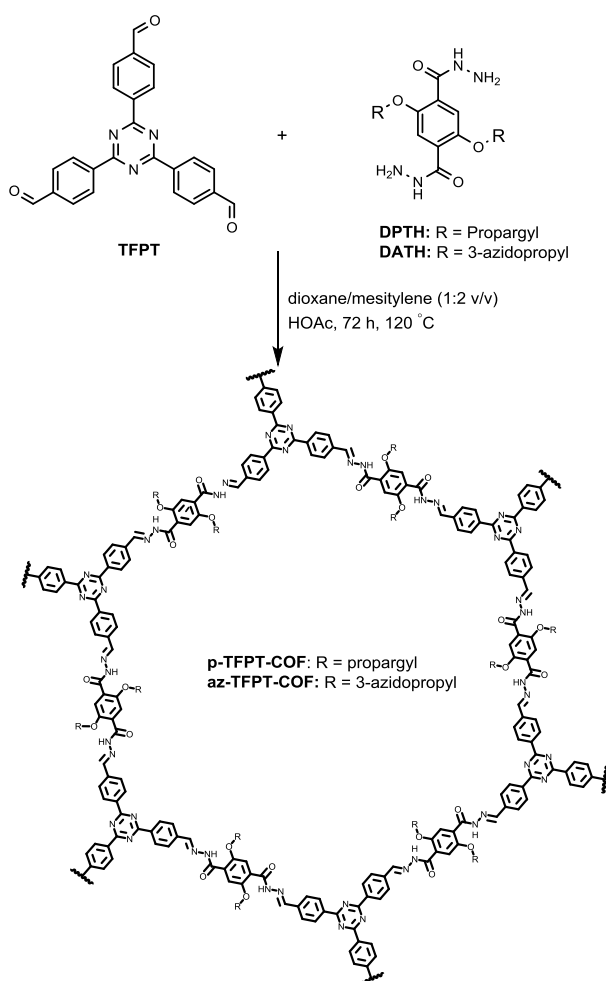
IR (FT, ATR): 3318 (m, v (-NH₂)), 2939 (w, v (-CH₂-)), 2109 (s, v (-N₃)), 1650 (m, δ (-NH₂)), 1600 (s, v (C=O)), 1498 (m, v (Aryl C=C)), 1394 (s), 1275 (m), 1212 (s), 1114 (m), 1038 (s), 952 (m), 887 (s), 811 (s), 768 (m) cm⁻¹.

General Procedure of Azide-/Propargyl-COF Synthesis

To a degassed mixture of TFPT (17.3 mg, 0.044 mmol, 1 eq) and either compound **DPTH** (20 mg, 0.066 mmol, 1.5 eq) or compound **DATH** (25.9 mg, 0.066 mmol, 1.5 eq), 0.66 mL mesitylene and 0.33 mL 1,4-dioxane were added. The reaction mixture was degassed once more, before adding 100 μL aqueous 6M acetic acid. The reaction vessel was sealed and heated at 120 °C for 72 h. After cooling to room temperature the product was filtered and washed with DMF (1 x 7 mL) and THF (2 x 7 mL) to give stoichiometric amounts of x-TFPT-COF.

Microwave Assisted Azide-/Propargyl-COF Synthesis

To a degassed mixture of TFPT (17.3 mg, 0.044 mmol, 1 eq) and either compound **DPTH** (20 mg, 0.066 mmol, 1.5 eq) or compound **DATH** (25.9 mg, 0.066 mmol, 1.5 eq), 0.66 mL mesitylene and 0.33 mL 1,4-dioxane were added. The reaction mixture was degassed once more, before adding 100 μ L aqueous 6M acetic acid. The reaction vessel was sealed and heated at 140 $^{\circ}$ C for 1 h in a synthetic microwave oven. After cooling to room temperature the product was filtered and washed with DMF (1 x 7 mL) and THF (2 x 7 mL) to give x-TFPT-COF.



5.4 Towards Implementing new Chromophoric Moieties in COFs and Polymers

Several approaches were made to build up COFs from chromophores. To give an impression about the different dyes and the efforts made, all the molecules so far achieved are sketched in the following schemes. The molecules, if not otherwise stated, were synthesized and characterized, but never successfully integrated in a (new) COF.

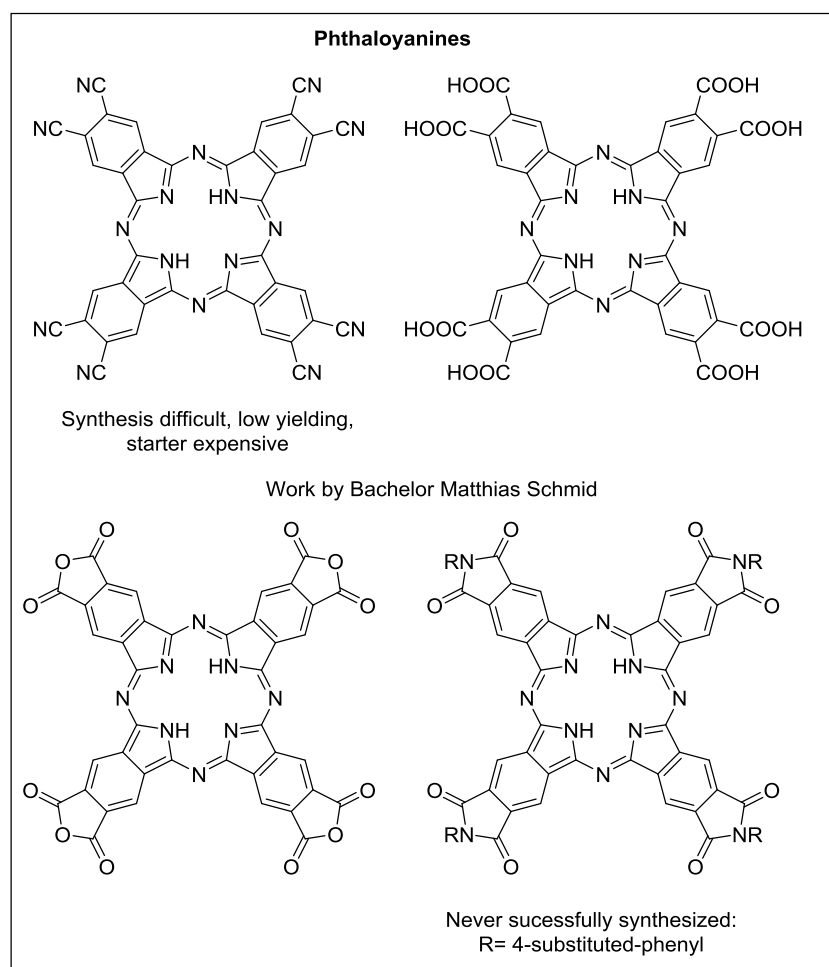
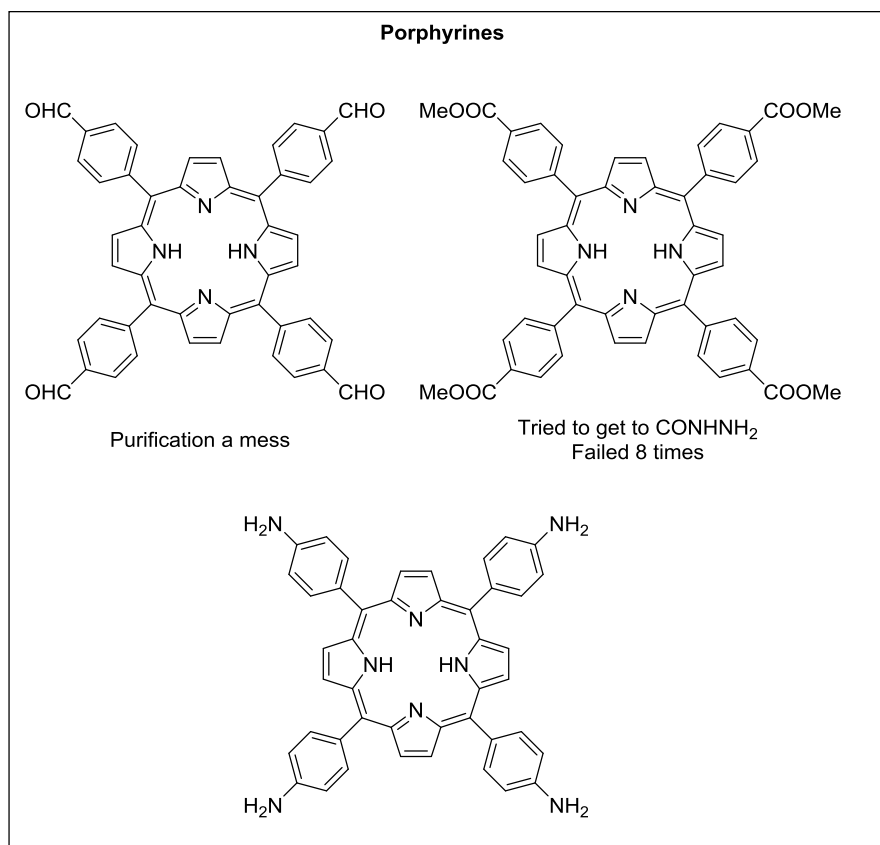
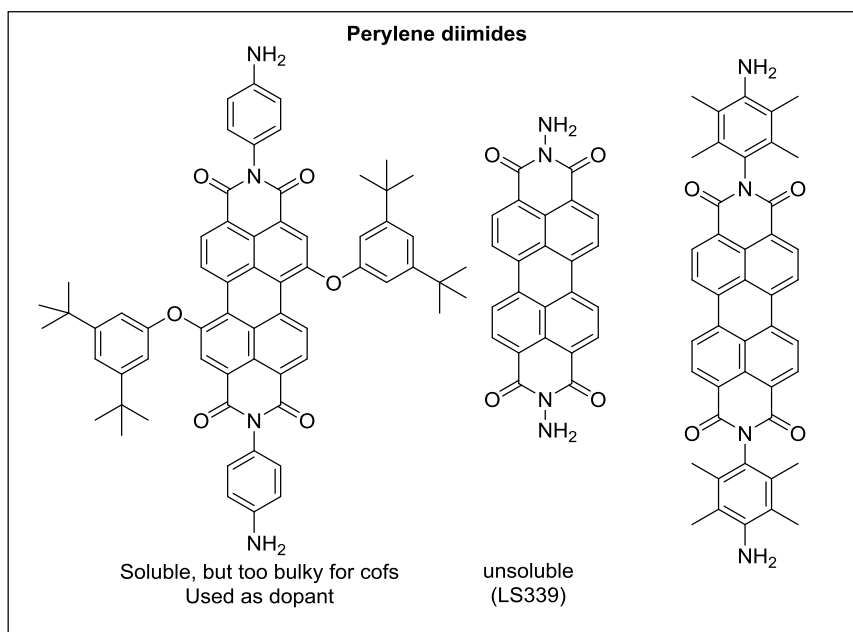


Figure 5.16: Synthetic work on phthalocyanines by Matthias Schmid (bachelor thesis).

**Figure 5.17:** Synthetic work on porphyrines.**Figure 5.18:** Synthetic work on perylenes.

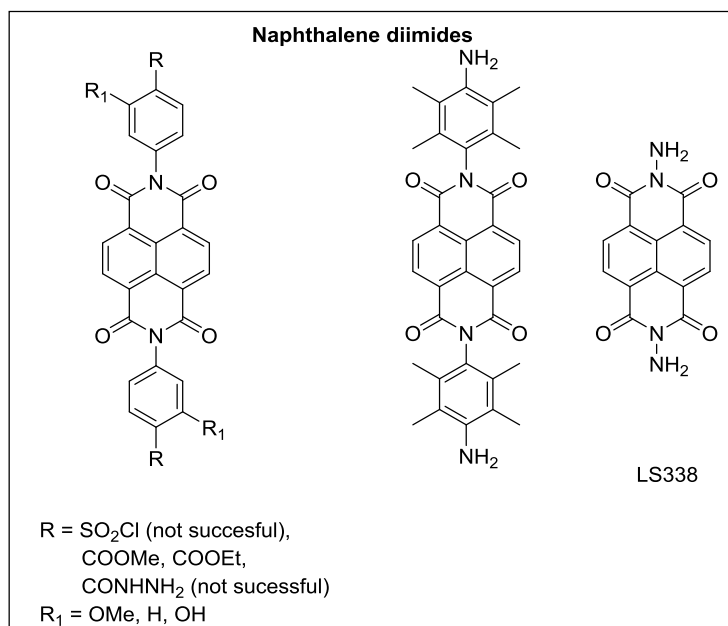


Figure 5.19: Synthetic work on naphthalenes.

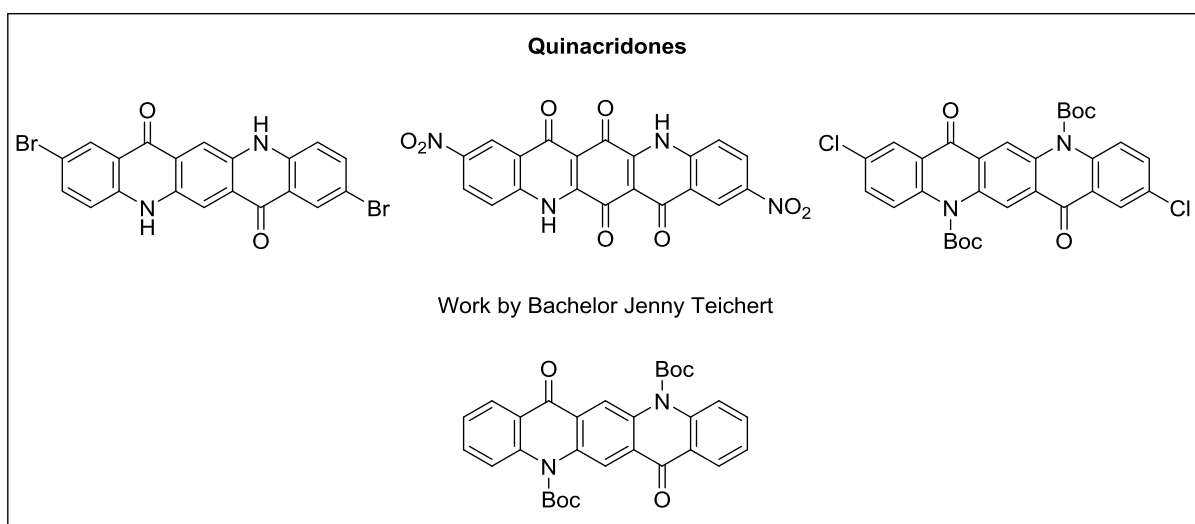


Figure 5.20: Synthetic work on quinacridones.

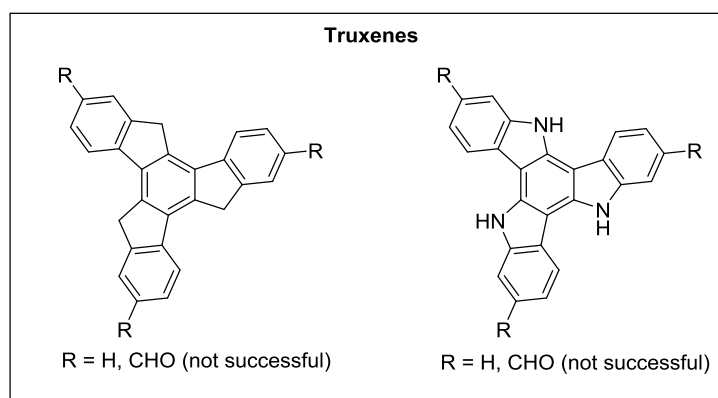


Figure 5.21: Synthetic work on truxenes.

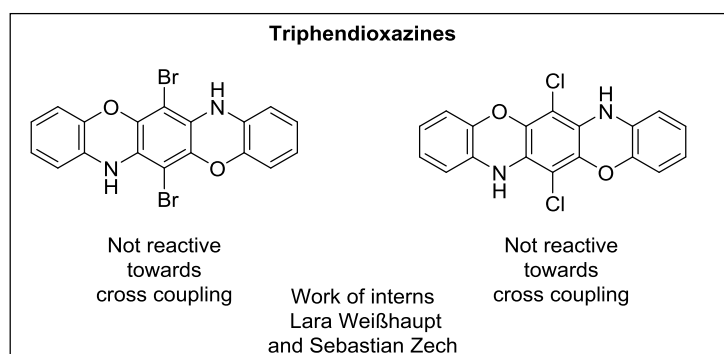


Figure 5.22: Synthetic work on triphendioxazines.

Further C_3 symmetric molecules were synthesized, containing oxadiazole, heptazine and hexaazatrinaphthalene and triphenylamine moieties.

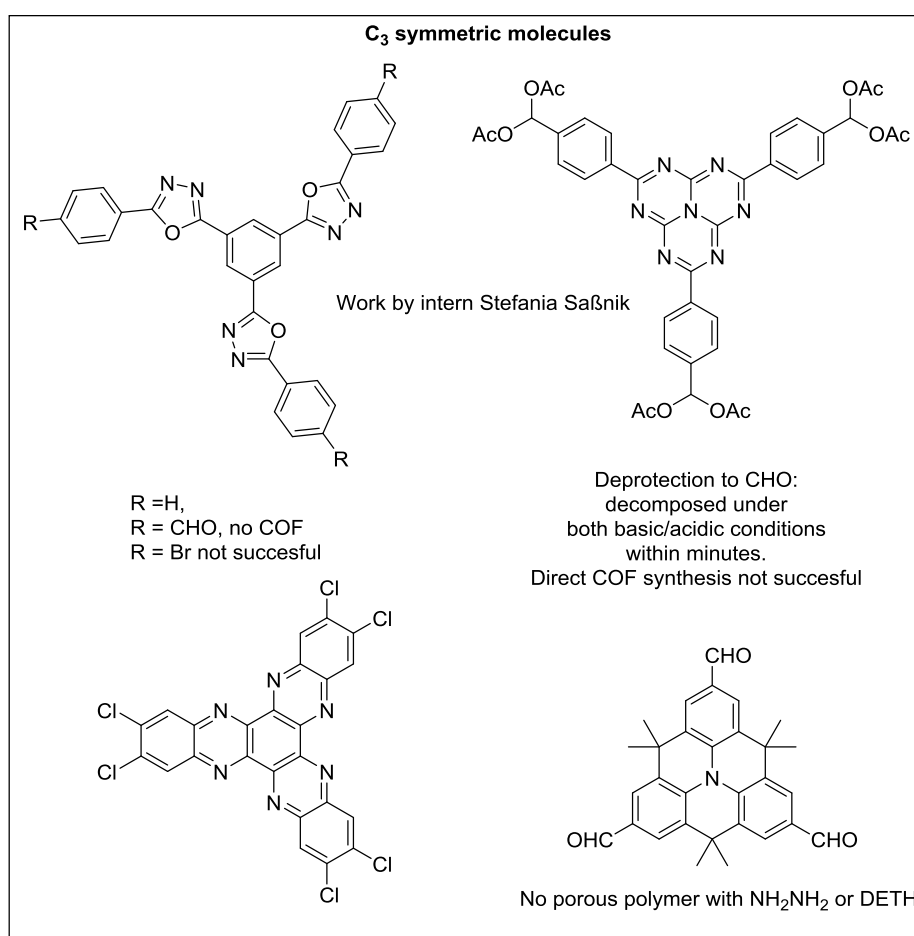


Figure 5.23: Synthetic work on C_3 symmetric molecules.

Tritopic hydrazides were synthesized but never successfully integrated in a porous and/or crystalline COF.

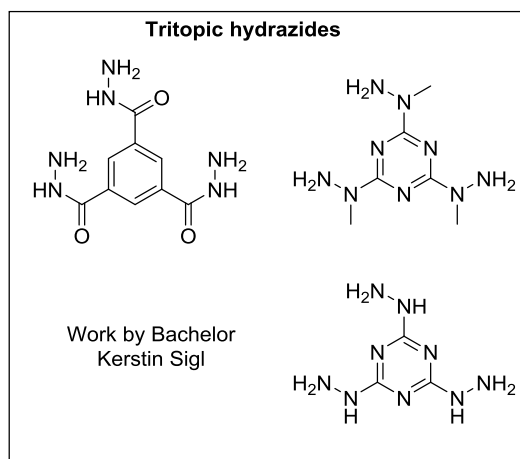


Figure 5.24: Synthetic work on tritopic hydrazides.

Some ditopic linkers decomposed during the last step (hydrazide formation).

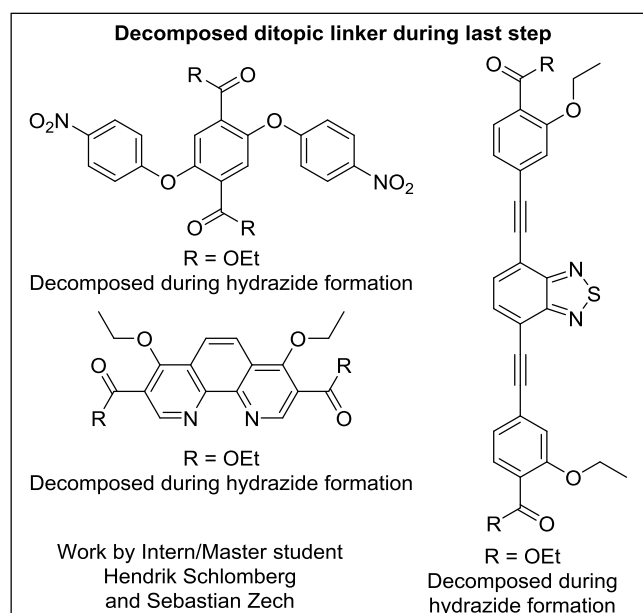


Figure 5.25: Synthetic work on ditopic linkers towards hydrazides.

Several potential COF linkers were synthesized, but never successfully integrated in a COF.

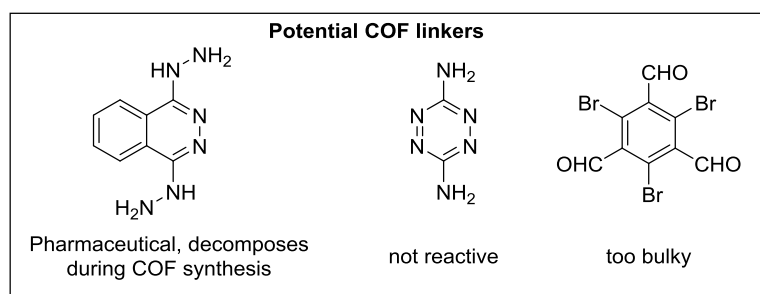


Figure 5.26: Synthetic work on ditopic linkers towards hydrazides.

5.4.1 Conclusions: The Art of Building Block Synthesis

As many organic building blocks, although offering twofold or threefold symmetric amine or aldehyde functionalization for C-N COFs, neither form a COF nor a porous polymer under standard conditions (mes/diox 1:1, 6M HOAc), either a larger amount of building blocks or a change in the design of building blocks is necessary. As synthesis of organic building blocks made up 60% of the total time spent for the practical work of this thesis, concluding remarks shall not be hidden from the reader.

Several general remarks regarding the organic synthesis of COF building blocks shall be made here, which are explained in the following sub chapter. This sub-chapter is to some degree subjective, although it is based upon four years of experience with COFs.

Remarks on Synthetic Plans towards Aldehyde-bearing COF Building Blocks

The number of maximum steps shall be limited to four linear steps for building block synthesis: By a short efficient synthesis, a large amount of building block is accessible, which can be used for screening. Parallel synthesis plans are always preferred to linear serial ones.

It is absolutely crucial to keep the number of new molecules during the synthesis, especially in the first steps, to a minimum. Experience shows that synthesis plans involving many new, literature-unknown molecules most often lead to a dead-end as a result of labile intermediates or unknown reaction conditions. The synthesis planning for covalent organic frameworks is completely different to natural product synthesis.

If two building blocks are synthesized for one COF it doubles the effort in organic synthetic work. It is advisable, for newly synthesized aldehyde linkers to focus first on azine frameworks, where the ditopic linker hydrazine is commercially available. If a tritopic aldehyde bearing linker is synthesized, the first screening shall be concentrated on azine-based COFs. All TEXPY monomers neither give a porous polymer nor a COF if combined with DETH.

For any azine or hydrazone-based COFs, which show the best chemical stability besides imide and triazine based-COFs, the synthesis of C₃ or C₄ symmetric aldehydes is crucial. A smart synthetic plan is absolutely necessary, because C₃ symmetric tritopic aldehydes, known in the literature, are scarce, and mostly rely on low-yielding chromium(VI) based oxidations. The best synthetic approaches for diverse syntheses of new linkers based on a selected core molecule, such as triazine, pyrene etc. is best achieved by cross-coupling reactions. For aldehyde-based systems, several electrophiles with aldehyde functionality are commercially available (see Figure 5.27) and were employed in the synthesis of the A-TEXPY-COF systems (see Chapter 3.3).

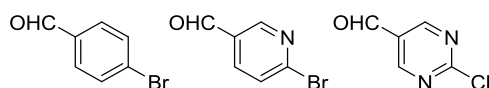


Figure 5.27: Commercially available aldehyde-based electrophiles used for synthesis of TEXPY building blocks.

A closer look into the literature revealed several further para-substituted aldehydes as potential electrophilic building blocks. Note that the aldehydes keep the coplanar geometry if a fluorine atom is introduced in the ortho position (see Figure 5.28).



Figure 5.28: Commercially available aldehyde-based electrophiles as potential building blocks.

These electrophiles offer an easy access to C_3 or C_4 symmetric aldehydes *via* *Sonogashira* or *Suzuki* cross couplings, which are chemically compatible to the aldehyde moiety. The use of *Stille* cross-couplings, although chemically compatible to aldehydes, is not considered here due to toxicity reasons. There is a plethora of C_3 or C_4 substituted appropriate nucleophiles commercially available (Figure 5.29) or easily accessible within 2-3 literature known steps (Figure 5.30).

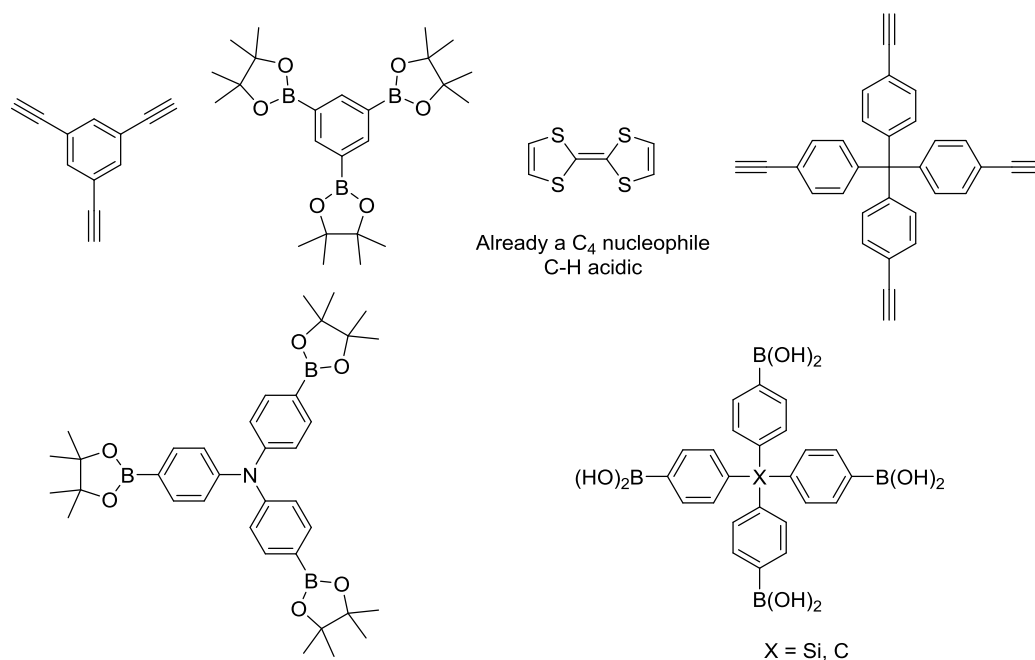


Figure 5.29: Commercially available nucleophiles for cross-couplings.

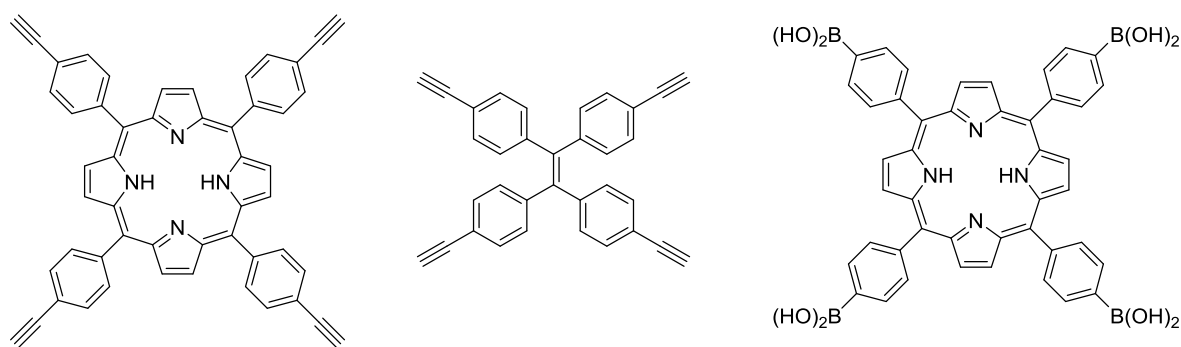


Figure 5.30: Easily accessible nucleophiles for cross-couplings.

Nucleophilic, aldehyde bearing aromatic starting materials are only achievable with temporary acetal protection of the aldehyde. Commercially available *p*-bromobenzaldehyde diethyl acetal offers an easy access to the lithiated species by metal-halogen exchange (Figure 5.31). All the other electrophilic aldehydes (Figure 5.27 and Figure 5.28) can be converted to nucleophilic building blocks by (i) protection and (ii) metal-halogen exchange. For pyrimidine based aldehydes, a lithiated species is probably not stable, so either a magnesium or zinc species may be more suitable. This gives far more variety and modularity in building block synthesis. There are many C_3 or C_4 symmetric tri- or tetrabromides commercially available, which are appropriate for the subsequent *Kumada* or *Negishi* cross-couplings.

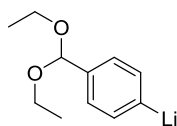


Figure 5.31: Nucleophilic acetal for subsequent cross-coupling reactions.

The nucleophilic protected (stable!) propionaldehyde diethyl acetal is commercially available (Figure 5.32) for multifold *Sonogashira* cross coupling with tri- and tetrabromides.⁷

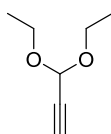


Figure 5.32: Nucleophilic propionaldehyde diethyl acetal for subsequent *Sonogashira* cross-coupling reactions.

5.5 On the Way to Highly Porous COFs

5.5.1 Screening of TFPT-COF

On the way to highly porous and crystalline COFs optimal conditions have to be found. Due to the complex multi-step syntheses of the building blocks DETH and TFPT, a lot of effort has been put into developing straightforward access to screening and at the same time minimizing the amount of starting materials used.

Screening of Solvent Mixtures

Initial publications about covalent organic frameworks used solvent mixtures consisting of an ether (e.g. dioxane) and an aromatic solvent (e.g. mesitylene) in different ratios.^{3,8–15} Only small efforts have been put into publication of screening procedures and effects on the crystallinity of the resulting frameworks,¹⁶ leading to a time-consuming trial-and-error screening after the synthesis of new building blocks. Later publications introduced further binary mixtures of alcohols (e.g. ethanol,¹⁰ *n*-butanol¹⁷), partly chlorinated aromatic solvents (*o*-dichlorobenzene),¹⁸ and polar aprotic solvents (e.g. *N,N*-dimethylacetamide).¹⁸ Especially COFs utilizing hardly soluble building blocks such as phthalocyanines¹⁸ or naphthalenebismides¹⁹ were synthesized in more polar solvent mixtures (e.g. *o*-dichlorobenzene/ *N,N*-dimethylacetamide 1:2, referred to *magic mixture* in lab jargon).²⁰ TFPT-COF has been screened in different ratios of mesitylene/dioxane, showing that the preferred mixture for TFPT-COF is diox/mes 1:2 with a resulting surface area of 1602 m² g⁻¹. Samples with surface areas higher than 500 m² g⁻¹ show crystallinity to a different extent, and a proper correlation between surface area and crystallinity has not been observed for TFPT-COF.¹⁹ BET surface area measurements give an indication of the whole sample quality such as 50 mg, while PXRD measurements only give information about a small amount of the corresponding sample, which is hit by the x-ray beam in the ray path. As a consequence of this the selection of the best conditions was mainly based on the highest BET surface areas achieved in each screening as long as the sample is reasonably crystalline. The duration of conventional solvothermal COF synthesis is usually three days.¹¹ Extension to six days led to a decline in surface area (232 m² g⁻¹) (see Figure 5.33, entry with asterisk).

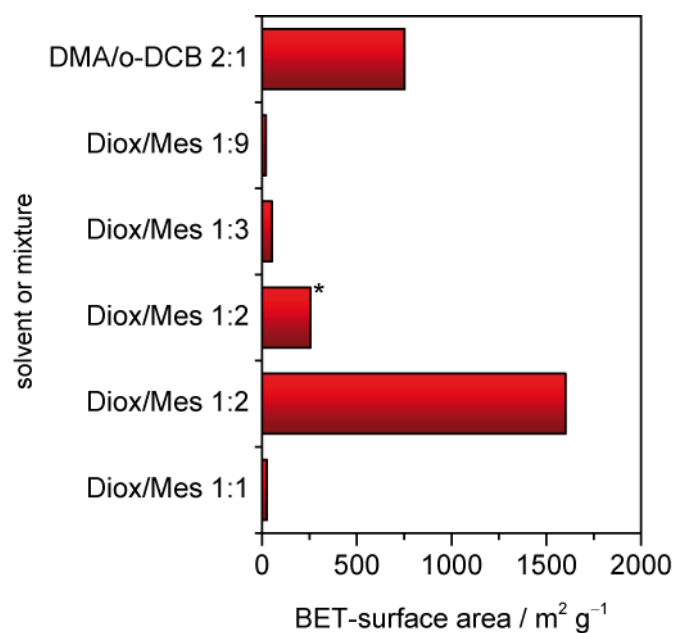


Figure 5.33: Solvent screening of TFPT-COF. Conditions: 1 mL solvent mixture, 0.1 mL 6 M HOAc, 72 h, 120°C (oil bath). Asterisk indicates longer reaction time (144 h).

Screening of Acetic Acid Concentration

Standard 6M HOAc was replaced by different other concentrations. As a conclusion, 6M HOAc (27.4 eq.) gave the highest surface area and is therefore the best choice in this system, which is agreement with the initial publication about hydrazone COFs.¹¹

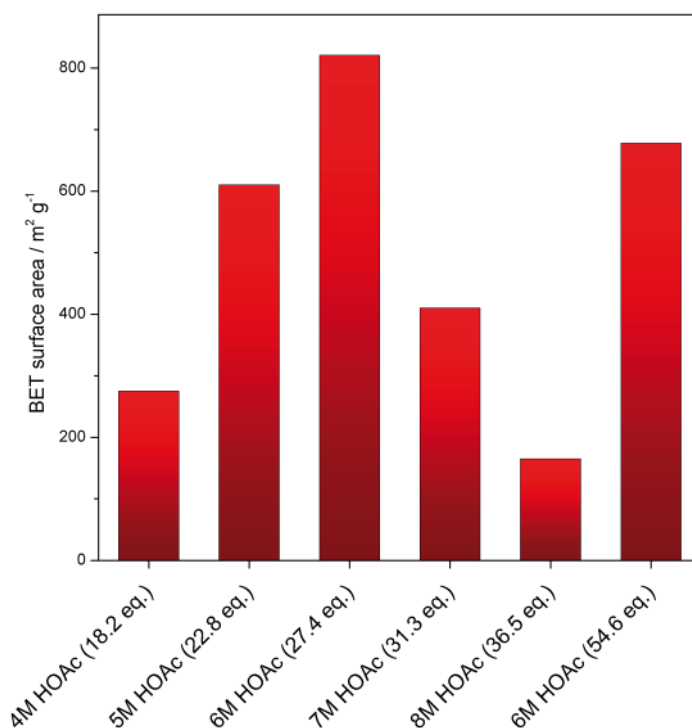


Figure 5.34: HOAc concentration screening of TFPT-COF. Conditions: 1 mL solvent mixture, 0.1 mL HOAc (for 54.6 eq 6M. 0.2 mL) in varying concentrations, 72 h, 120°C.

Screening of Heating Sources

Traditional COF synthesis has been carried out in sealed glass ampoules.¹¹ COF synthesis in the Lotsch lab is usually carried out in a 0.5 – 2 mL microwave vial from Biotage®, optionally under stirring. After sealing the vial is heated in an oil bath, in a microwave or in a muffle furnace. These methods were compared (see Figure 5.35), showing that a combination of microwave for a short duration (<1 h) at 150-160°C and tempering for 3 days at 120 °C in a muffle furnace is the best combination for high surface areas. Tempering in an oil bath may lead to irreproducible results (compare Figure 5.33 and Figure 5.35) because of the inhomogeneous temperature distribution.

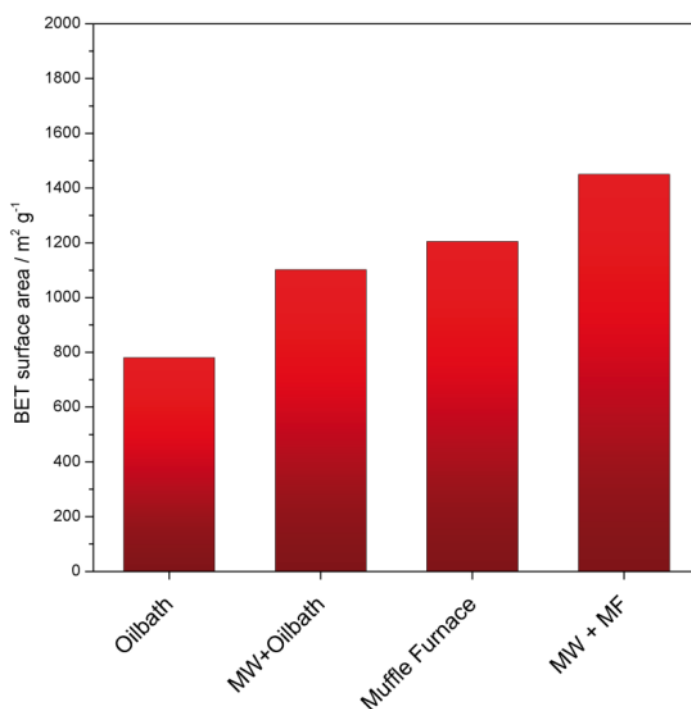


Figure 5.35: Screening of TFPT-COF with regard to the heating conditions. Conditions: 1 mL solvent mixture, 0.1 mL 6 M HOAc, 72 h, 120°C. Microwave samples were preheated for 45 min to 150°C and then tempered for the 72 h.

Screening of Additives

Addition of strong acids (pKa < 1) may have a beneficial influence on COF formation. Therefore, different additives in substoichiometric amounts were added to the reaction mixture and the BET surface area was measured for the resulting TFPT-COF.

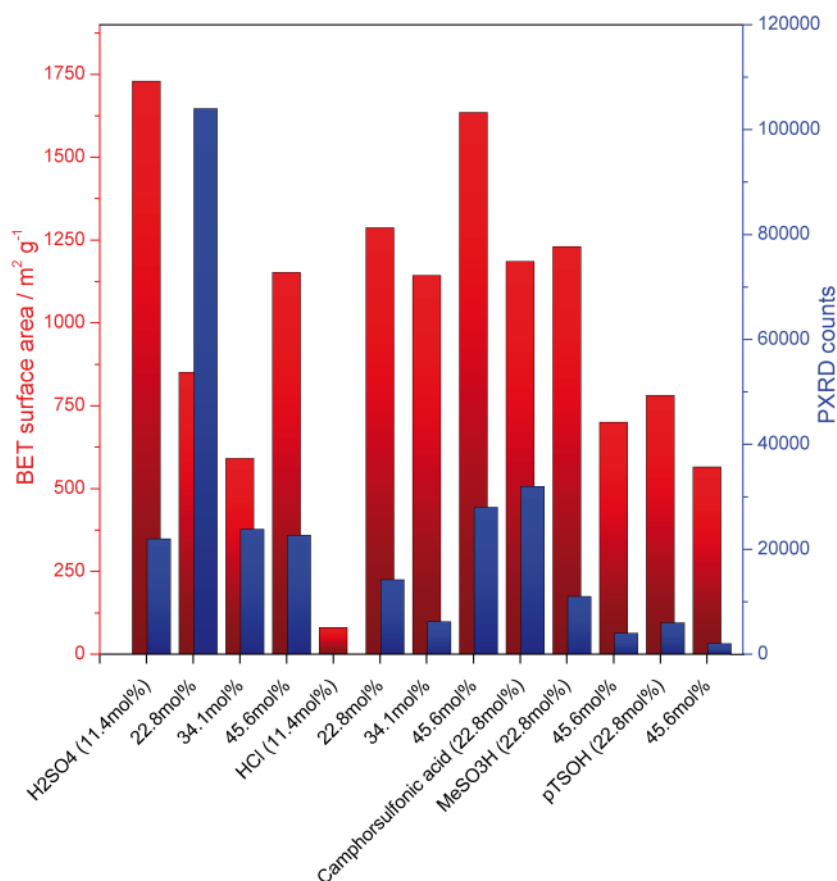


Figure 5.36: Solvent screening of TFPT-COF. Conditions: 1 mL diox/mes 1:2, 0.1 mL 6 M HOAc, 150°C (45 min)/120°C (72 h) (MW/MF). 0.5 M additive in different amounts; asterisk indicates longer reaction time (144 h).

All in all, there is no clear general trend visible. The addition of higher amounts (>11.4 mol%) of sulphur based acids leads to a decrease in surface area, although with 22.8 mol% of sulphuric acid added, the crystallinity could be significantly improved (entry 2, blue bar, Figure 5.36) compared to all other entries. Hydrochloric acid as additive does indeed show a high surface area with 45.6 mol% loading. Both PXRD counts and surface area of this entry are very comparable to entry 1. The additive of choice is 11.4 mol% H₂SO₄.

Screening of Different Acids

Further screening focused on different acids as a replacement for standard 6M acetic acid (Entry 1). Different acids in the pKa range between 5 and 7 were chosen, where special attention was paid to thermic stability, because the COF forming reaction involves high temperatures and long duration.

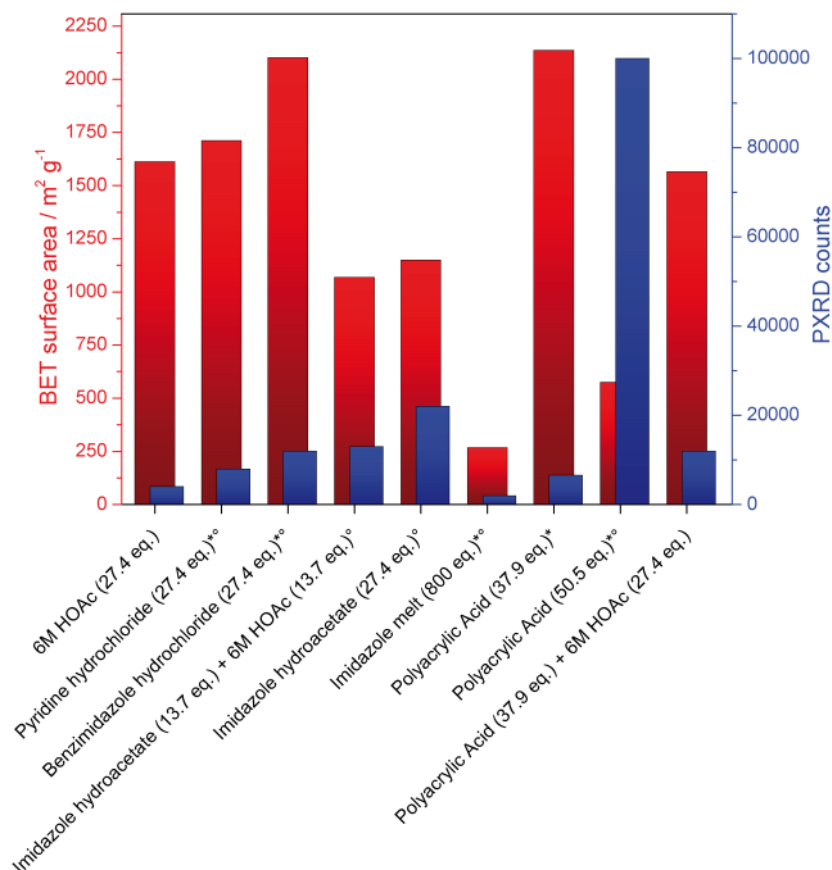


Figure 5.37: Solvent screening of TFPT-COF. Conditions: 1 mL 2:1 mes:diox, 30 min microwave (150°C) + 72 h in muffle furnace (120°C). Asterisk indicate addition of 0.1 mL water; degree indicates addition of 0.114 eq 0.5 M H₂SO₄ as additive.

As a trend, optimal conditions for TFPT-COF synthesis are achieved with acids in the pKa range 5-6 (see Table 5.1), leading to high BET surface areas up to 2200 m² g⁻¹. Looking at the PXRD counts, the trend is not that clear, however. High crystallinity does not necessarily result in a high BET surface area. For some entries a contrary behavior has been observed (e.g. polyacrylic acid entries 7 and 8). Several explanations may be given for this behavior: i) there may be some amorphous oligomeric residues trapped in the crystalline framework, ii) not all pores may be accessible, iii) a highly crystalline oligomeric form of the COF has been formed, consisting of a few connected building blocks. This oligomer may not provide extended honeycomb networks and therefore is much less porous. A comparable case has been found for oligomeric CTFs.²¹

Table 5.1: pKa values of acids used (in water).²²

Acid	pKa
HOAc	4.76
Pyridinium	5.32
Benzimidazolium	5.4
Imidazolium	6.95
Polyacrylic acid	6±0.5 ²³

Reproduction of Selected Samples

Reproduction of the samples with the highest surface area revealed a spread in quality of the synthesized TFPT-COF (Figure 5.38). Further parameters, which were so far not screened, may play a minor, yet appreciable role in COF formation and may thus also influence the BET surface area.

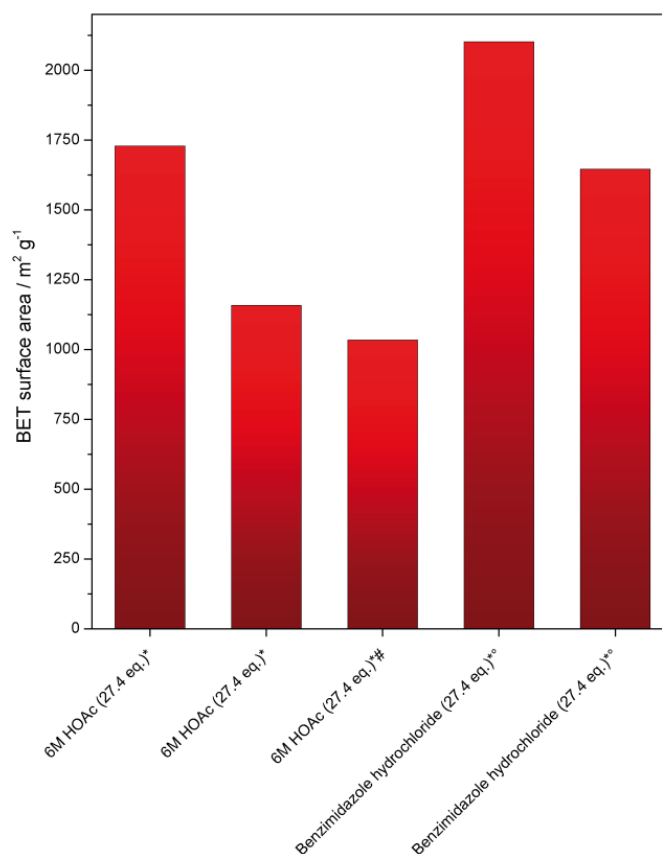


Figure 5.38: Reproduction of selected TFPT-COF samples. Conditions: 1 mL 2:1 mes:diox, 30 min microwave (150°C) + 72 h in muffle furnace (120°C). Asterisks indicate addition of 0.114 eq 0.5 M H₂SO₄ as additive, degree indicates addition of 0.1 mL water; hash indicates large scale.

Long Term Storage of TFPT-COF

Two samples were stored for one year under ambient conditions in a glass screw capped vial with a polyurea cap and aluminium foil as sealant in the cap. The BET surface area was measured before (see Figure 5.39, entries “...(27.4 eq)”) and after (see Figure 5.39, entries one year later”) this period of time. The results indicate partial loss of porosity (see Figure 5.39), apparently to a limit of around $800 \text{ m}^2 \text{ g}^{-1}$. The relative decrease in surface area was higher the higher the surface area initially was.

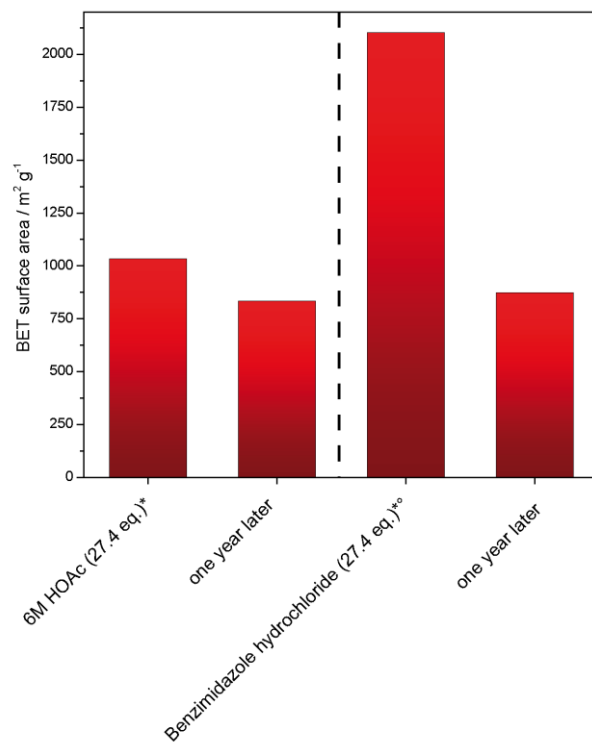


Figure 5.39: Long-term storage of TFPT-COF. Conditions: 1 mL 2:1 mes:diox, 30 min microwave (150°C) + 72 h in muffle furnace (120°C). Asterisk indicates addition 0.114 eq 0.5 M H_2SO_4 as additive; degree indicates addition of 0.1 mL water.

5.5.2 Screening of AB-COF

Solvent Screening

Screening of different solvents revealed high surface areas for a whole range of solvent combinations. Even with high amounts, e.g. as a solvent, of acetic acid or benzoic acid in the solvent mixture, high surface areas can be achieved in AB-COF. Intensities of the *100* reflection in PXRD only correspond to the surface area in a small extent. For future measurements a better measure for crystallinity may be the FWHM in combination with the intensity of *100*.

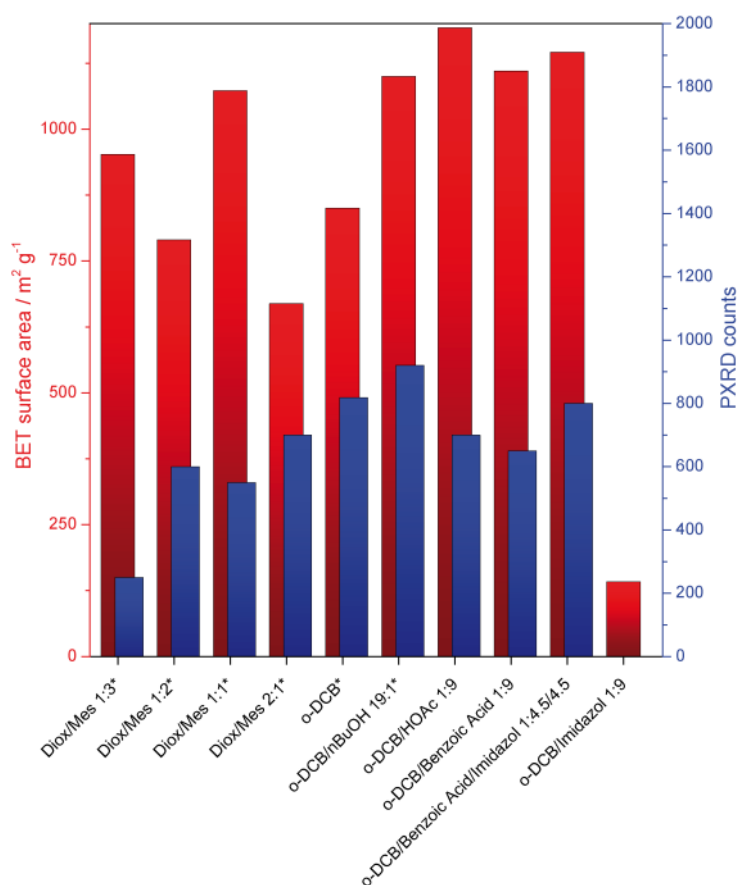


Figure 5.40: Solvent screening of AB-COF. Conditions: 2 mL solvent, 30 min microwave (150°C) + 72 h in muffle furnace (120°C). Asterisk indicates 27.4 eq. 6M HOAc. Additives: 0.114 eq. 0.5 M H₂SO₄.

Screening: Varying the Stoichiometric Amount of Acetic Acid

Varying the amount of acetic acid leads to a decrease in surface area for all solvent mixtures investigated, both with significantly higher and lower amounts of acetic acid compared to the standard of 27.4 eq. Entries 2 and 5 clearly show once again that a high crystallinity did not go in line with a high surface area.

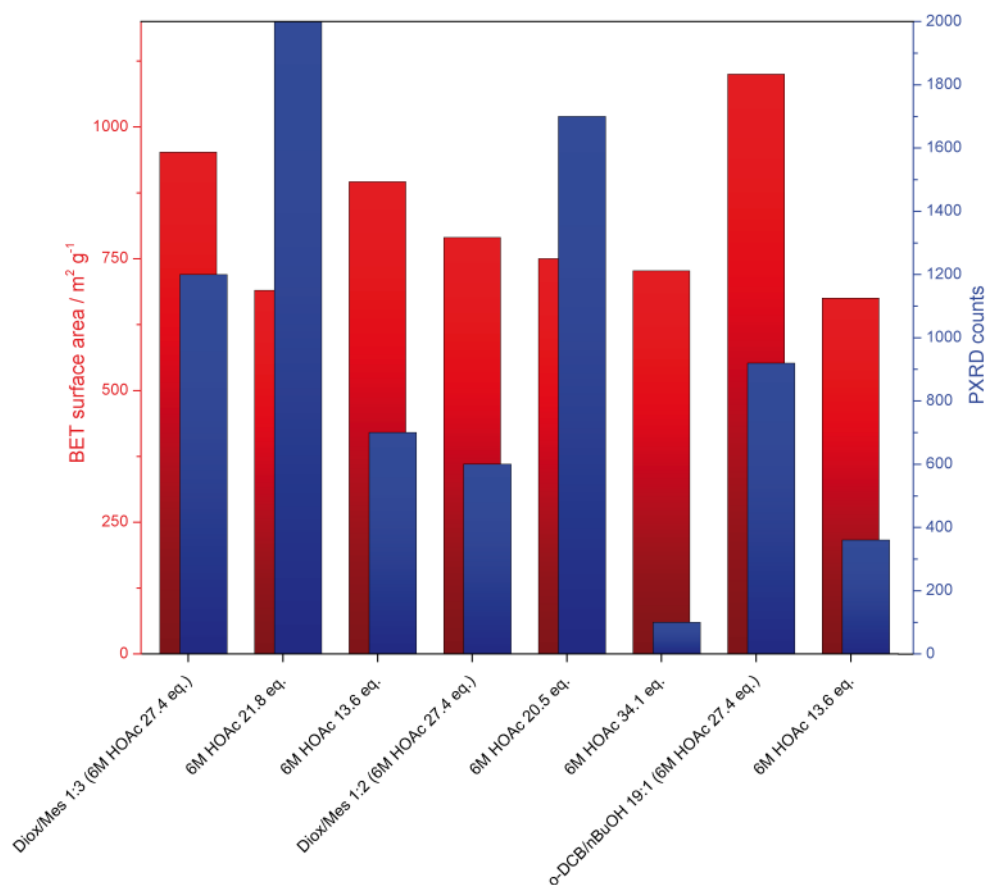


Figure 5.41: Screening of the amount of acetic acid used for AB-COF. Conditions: 2 mL solvent, varying amount of 6M HOAc, 30 min microwave (150°C) + 72 h in muffle furnace (120°C). Additives: 0.114 eq. 0.5 M H₂SO₄.

Screening of Sulfuric Acid as Additive

0.5M 11.4mol% H₂SO₄ as additive improves the surface areas in three solvent systems (diox/mes 1:3 (entry 1&2), *o*-DCB/*n*BuOH 19:1 (Entry 3&4), *o*-DCB (Entry 5&6), see Figure 5.42). For the PXRD intensities, there is no clear trend observable.

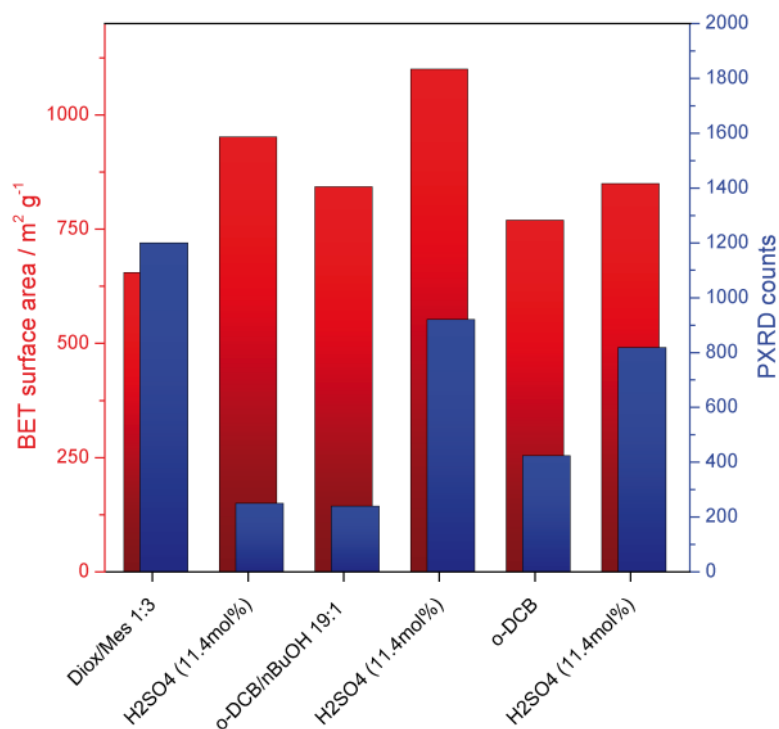


Figure 5.42: Sulfuric acid as additive for AB-COF synthesis. Conditions: 2 mL solvent, 27.4 eq. 6M HOAc, 30 min microwave (150°C) + 72 h in muffle furnace (120°C). Odd entry numbers correspond to additive free solvents. Even entry numbers are solvents with sulfuric acid as additive.

Screening of Different Acids

The synthesis of AB-COF seems to be much less sensitive towards variation of the acid. Even benzoic acid with a lower pK_a than acetic acid gives a high BET surface area, also in combination with imidazole (see Table 5.2 for pK_a values). Solely imidazole as acid cannot provide the required acidity. Also mixtures of pure HOAc with 10% *o*-DCB give very high surface area. Benzimidazole hydrochloride and imidazole hydroacetate with their lower acidity cause a decrease of the surface area of AB-COF.

Table 5.2: pKa values of acids used (in water).²²

Acid	pKa
HOAc	4.76
Benzoic acid	4.19
Benzimidazolium	5.4
Imidazolium	6.95

Nevertheless, as shown in Figure 5.43 the screening of different acids did not lead to a significant increase of the BET surface area when compared to the standard 27.4 eq. 6M HOAc.

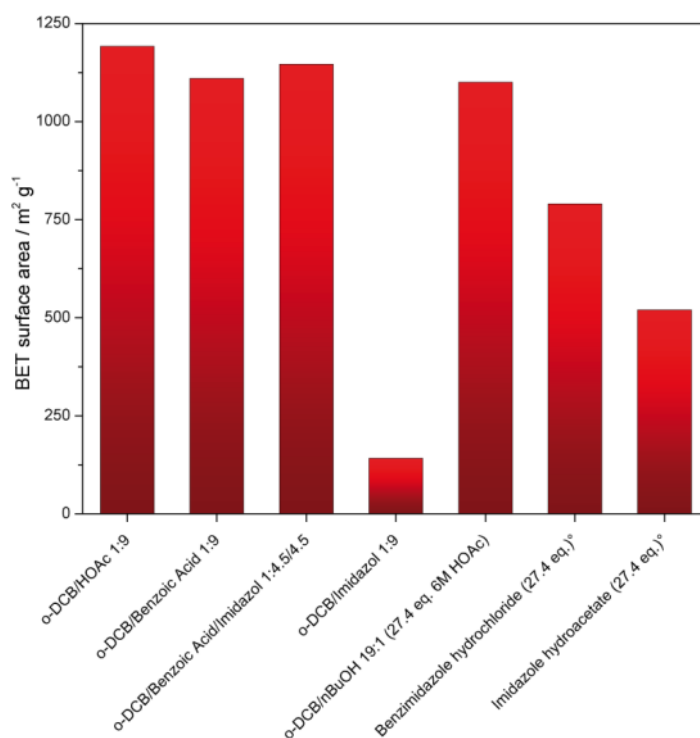


Figure 5.43: Acid screening for AB-COF synthesis. Conditions: 2 mL solvent, 27.4 eq. 6M HOAc, 30 min microwave (150°C) + 72 h in muffle furnace (120°C). Additives: 0.114 eq. 0.5 M H₂SO₄.

Screening of Starting Material Concentration and Reproducibility

AB-COF synthesis in *o*-DCB/*n*-BuOH 19:1 (solvent mixture A) turns out to be very reproducible. In six experiments the as-synthesized COF gave an average BET surface area of 1091 ± 51 m² g⁻¹. A higher 1,3,5-triformylbenzene concentration in solvent mixture A does not lead to a decrease in surface area, therefore an upscale is achievable. In other solvent systems reproduction is also feasible, although the spread of the surface area is wider.

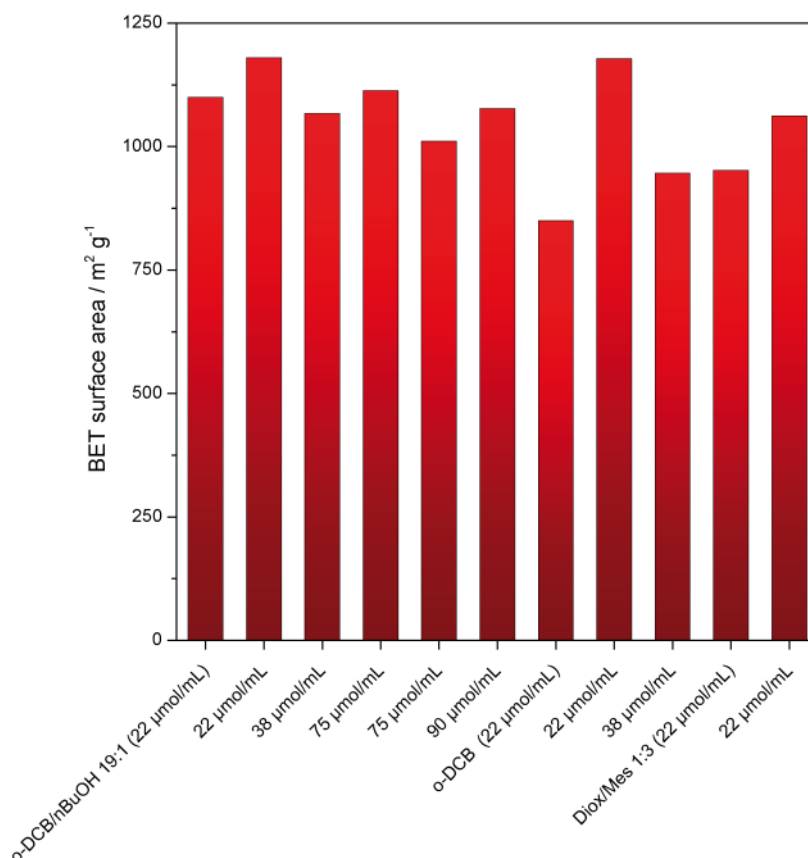


Figure 5.44: Concentration screening and reproducibility for AB-COF synthesis. The label shows the concentration of TFB in the solvent mixture. Conditions: 2 mL solvent, 27.4 eq. 6M HOAc, 30 min microwave (150°C) + 72 h in muffle furnace (120°C). Additives: 0.114 eq. 0.5 M H₂SO₄.

5.5.3 Conclusions of Conventional Screening

In conclusion, the screening of different additives in TFPT-COF revealed no conclusive trend. Furthermore, the reproduced samples showed a smaller BET surface area compared to the initial experiments. Nevertheless, TFPT-COF with 2177 m² g⁻¹ could be synthesized and characterized (see Figure 5.45 for sorption isotherm), which is an improvement of 35% compared to the initial BET of 1603 m² g⁻¹. This clearly demonstrates, that a high surface area can be achieved by sufficient screening, which is very close to the theoretical Connolly surface area of the simulated crystal structure as derived by *Materials Studio* (2250 m² g⁻¹). Results so far indicate, that this high surface area comes at the cost of a certain lability of the framework: If stored for one year, the surface area declined significantly to one third. The loss of surface area may be related to a humidity induced partly exfoliation of TFPT-COF during storage (see chapter 5.2).

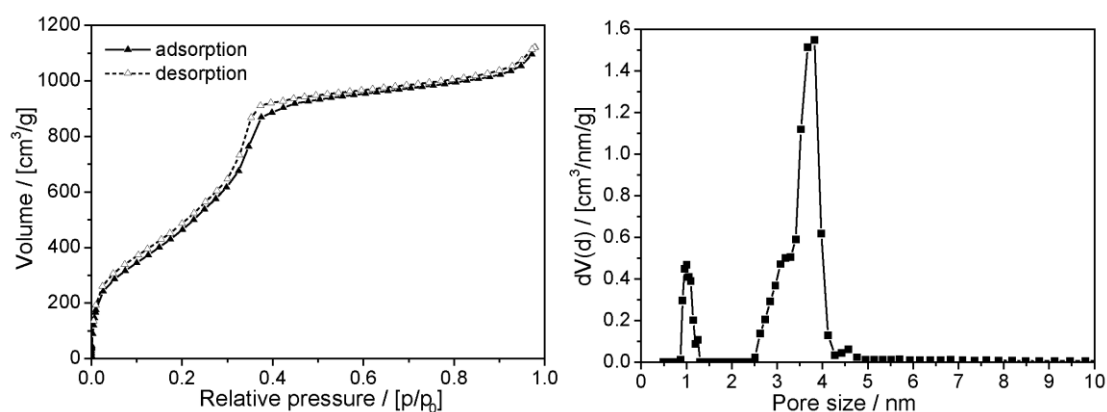


Figure 5.45: Sorption isotherm (left) and NLDFT-derived PSD (right) of optimized TFPT-COF with a BET surface area of $2177 \text{ m}^2 \text{ g}^{-1}$ and a pore volume of $1.38 \text{ cm}^3 \text{ g}^{-1}$.

Screening of AB-COF revealed high surface areas ($>1000 \text{ m}^2 \text{ g}^{-1}$) over a rather broad solvent and acid range, although with generally lower crystallinity, when directly compared to TFPT-COF. Out of these screenings the conclusion can be drawn that the azine linked AB-COF is easier to push to high surface areas compared to hydrazone linked TFPT-COF, in the sense that AB-COF is less sensitive towards synthesis conditions. A reason for this might be the higher amounts of single bonds in DETH ($12\times$) compared to hydrazine ($1\times$). DETH has several conformers, which were compared by conformational analysis.²⁴ Although a coplanar one is energetically favoured, at least three other conformers appear at the typical COF synthesis temperature of 120°C , corresponding to an energy window of 3.2 kJ mol^{-1} with probabilities of appearance higher than 1% .²⁴

5.5.4 Microwave synthesis of TFPT-COF

Screening of Reaction Temperature

Microwave assisted synthesis in organic chemistry has shown to yield more and cleaner products in a much shorter time,²⁵ and has also been transferred to B-O based COF synthesis.^{26–28} Microwave radiation creates a homogenous heat map throughout the vial, thus avoiding the typical overheated and underheated areas caused by laws of convection and conduction. It turned out that the TFPT-COF synthesis can be carried out in a synthetic microwave oven, and by this, the reaction time can be shortened to several minutes. Therefore various reaction parameters were screened with the aim of improving the microwave assisted synthesis of TFPT-COF.

Temperature screening at a fixed duration of 1 h per reaction shows that the level of crystallinity and the BET surface area fluctuate significantly without a clear pattern.

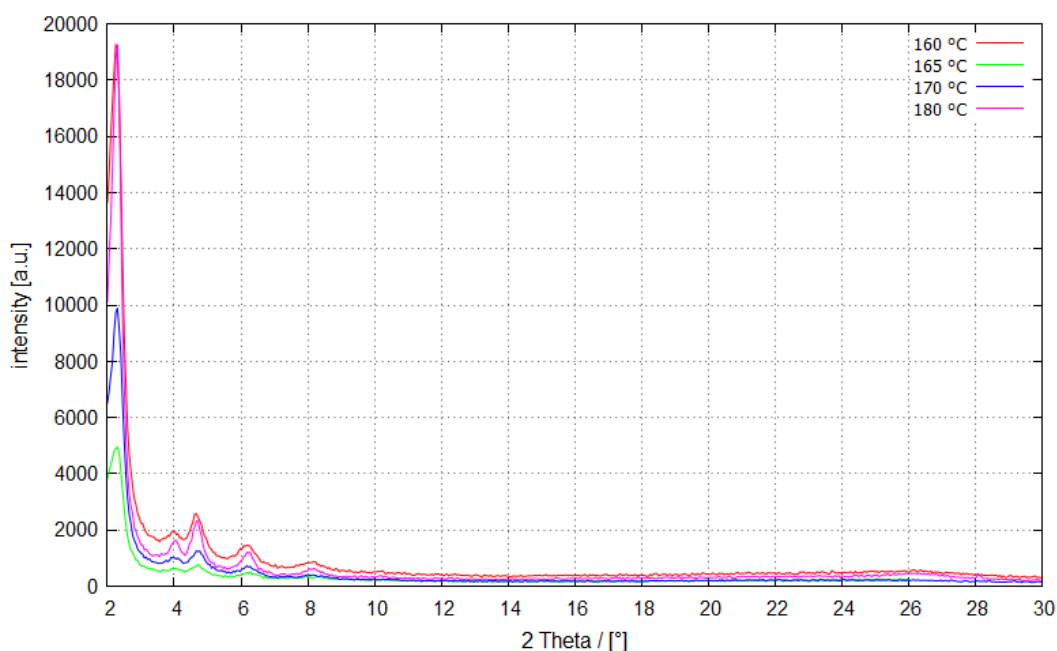


Figure 5.46: Experimental powder pattern of TFPT-COF synthesized at 160 °C, 165 °C, 170 °C and 180 °C.

From this screening, it seems that a higher reaction temperature leads to higher BET surface areas.

Calculated BET surface areas for TFPT-COF by Ar sorption:

Reaction temperatur.	160 °C	165 °C	170 °C	180 °C
BET surface area (m ² g ⁻¹)	429	291	670	655

Screening of Acid Concentration

Further screening studies included the effect of different acetic acid concentrations and longer reaction times on the TFPT-COF system – in particular the crystallinity.

Screening results of various acetic acid concentrations in TFPT-COF synthesis show that the currently used acetic acid concentration of 6 M (addition of 6M HOAc equals to an overall concentration of 0.6 M HOAc in the solvent mixture, see Figure 5.47) is by far the best choice. The use of acetic acid concentrations > 6 M decreases the crystallinity of TFPT-COF to a higher extent if directly compared to lower acid concentrations < 6 M. In general it is not advisable to use higher acid concentrations because strong acids seem to decompose TFPT-COF.

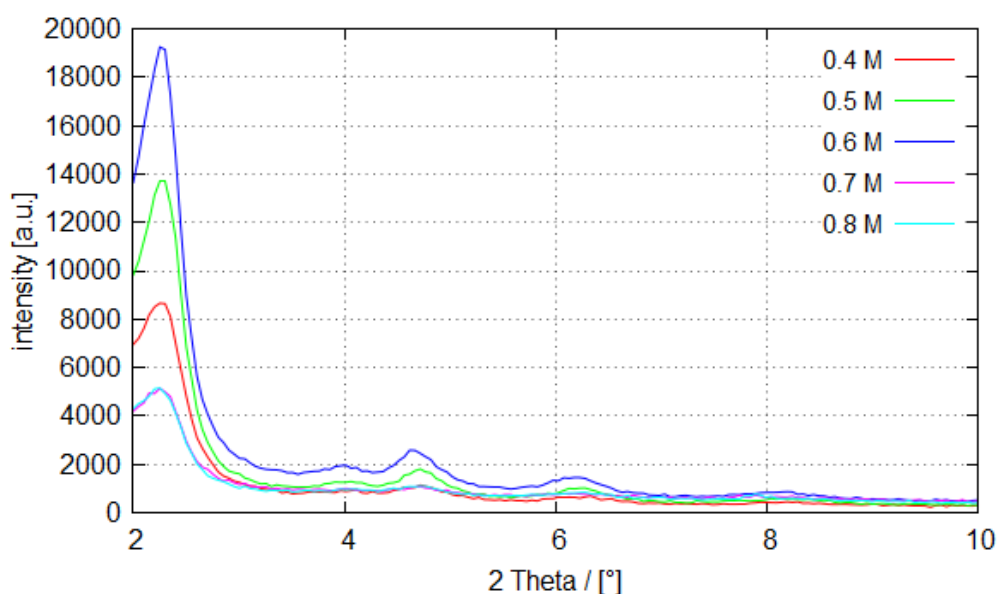


Figure 5.47: Experimental powder pattern of TFPT-COF using various acid concentrations at 150 °C for 1h.

Screening of Reaction Time

Studies on the optimal reaction time for the microwave assisted TFPT-COF synthesis show that a reaction time of two hours yields TFPT-COFs of high crystallinity. Shorter as well as longer reaction times show a significantly lower crystallinity (Figure 5.48).

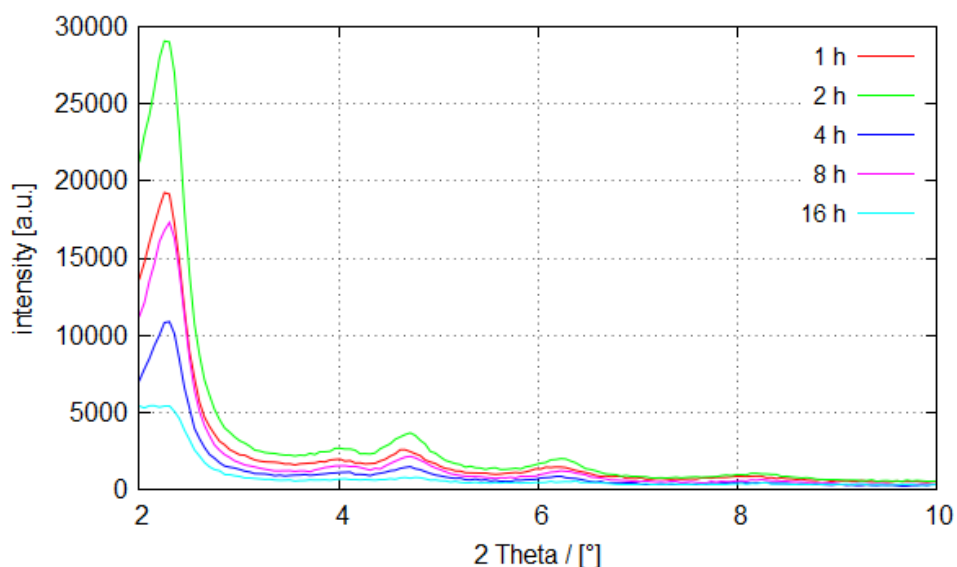


Figure 5.48: Experimental powder patterns of TFPT-COF using various acid concentrations at 150 °C for 1h.

Conclusions from Microwave-assisted Screening

The discovery of microwave assisted TFPT-COF synthesis allows to synthesize up to ten times faster than the conventional synthesis. But the obtained product via microwave radiation turned out to be inferior compared to conventionally synthesized TFPT-COF regarding the surface area.

A subsequent tempering at 120°C in muffle furnace is highly recommended for higher surface areas.

The discovery of microwave-assisted TFPT-COF synthesis allows to synthesize the COF up to ten times faster compared to the conventional synthesis. This has previously been shown for B-O based COFs.^{27,28} However, the product obtained *via* microwave heating turned out to be inferior compared to conventionally synthesized TFPT-COF regarding the surface area. A subsequent tempering at 120°C in a muffle furnace is therefore highly recommended to obtain higher surface areas.

So far, COFs have been regarded as 2D or 3D polymers, although it is known from several 1D polymers such as polyimides and, lately, covalent triazine frameworks,²¹ that depending on the bond-forming reaction, oligomeric units are also formed. For further understanding and investigation of potential oligomeric units in COFs, matrix-assisted laser desorption/ionization (MALDI) – time-of-flight (TOF) would be a suitable technique, which has been successfully used for insoluble polyimides.^{29,30} Oligomers of COFs may play a crucial part in their photocatalytic activity.²¹

5.6 References

1. C. Weidenthaler, *Nanoscale*, 2011, **3**, 792–810.
2. P. Scherrer, *Nachr. Ges. Wiss. Göttingen*, 1918, **26**, 98–100.
3. A. Nagai, Z. Guo, X. Feng, S. Jin, X. Chen, X. Ding and D. Jiang, *Nat. Commun.*, 2011, **2**, Art. No. 536.
4. Q. Fang, S. Gu, J. Zheng, Z. Zhuang, S. Qiu and Y. Yan, *Angew. Chem., Int. Ed.*, 2014, **53**, 2878–2882.
5. N. Huang, X. Chen, R. Krishna and D. Jiang, *Angew. Chem., Int. Ed.*, 2015, **54**, 2986–2990.
6. N. Huang, R. Krishna and D. Jiang, *J. Am. Chem. Soc.*, 2015, **137**, 7079–7082.
7. G. Venkataramana and S. Sankararaman, *Eur. J. Org. Chem.*, 2005, **2005**, 4162–4166.
8. S. Wan, J. Guo, J. Kim, H. Ihee and D. Jiang, *Angew. Chem., Int. Ed.*, 2009, **48**, 5439–5442.
9. S. Wan, J. Guo, J. Kim, H. Ihee and D. Jiang, *Angew. Chem., Int. Ed.*, 2008, **47**, 8826–8830.
10. S. Wan, F. Gándara, A. Asano, H. Furukawa, A. Saeki, S. K. Dey, L. Liao, M. W. Ambrogio, Y. Y. Botros, X. Duan, S. Seki, J. F. Stoddart and O. M. Yaghi, *Chem. Mater.*, 2011, **23**, 4094–4097.

11. F. J. Uribe-Romo, C. J. Doonan, H. Furukawa, K. Oisaki and O. M. Yaghi, *J. Am. Chem. Soc.*, 2011, **133**, 11478–11481.
12. A. P. Côté, H. M. El-Kaderi, H. Furukawa, J. R. Hunt and O. M. Yaghi, *J. Am. Chem. Soc.*, 2007, **129**, 12914–12915.
13. A. P. Côté, A. I. Benin, N. W. Ockwig, M. O’Keeffe, A. J. Matzger and O. M. Yaghi, *Science (Washington, DC, United States)*, 2005, **310**, 1166–1170.
14. F. J. Uribe-Romo, J. R. Hunt, H. Furukawa, C. Klöck, M. O’Keeffe and O. M. Yaghi, *J. Am. Chem. Soc.*, 2009, **131**, 4570–4571.
15. H. M. El-Kaderi, J. R. Hunt, J. L. Mendoza-Cortes, A. P. Cote, R. E. Taylor, M. O’Keeffe and O. M. Yaghi, *Science (Washington, DC, United States)*, 2007, **316**, 268–272.
16. X. Feng, L. Chen, Y. Dong and D. Jiang, *Chem. Commun. (Cambridge, U. K.)*, 2011, **47**.
17. X. Chen, M. Addicoat, S. Irle, A. Nagai and D. Jiang, *J. Am. Chem. Soc.*, 2012, **135**, 546–549.
18. X. Ding, J. Guo, X. Feng, Y. Honsho, J. Guo, S. Seki, P. Maitarad, A. Saeki, S. Nagase and D. Jiang, *Angew. Chem., Int. Ed.*, 2011, **50**, 1289–1293.
19. S. Jin, K. Furukawa, M. Addicoat, L. Chen, S. Takahashi, S. Irle, T. Nakamura and D. Jiang, *Chem. Sci.*, 2013, **4**, 4505–4511.
20. S. Jin, X. Ding, X. Feng, M. Supur, K. Furukawa, S. Takahashi, M. Addicoat, M. E. El-Khouly, T. Nakamura, S. Irle, S. Fukuzumi, A. Nagai and D. Jiang, *Angew. Chem., Int. Ed.*, 2013, **52**, 2017–2021.
21. K. Schwinghammer, S. Hug, Mesch, M. B., J. Senker and Lotsch, B. V., *Energy Environ. Sci.*, 2015, **8**, 3345–3353.
22. W. M. Haynes, *CRC handbook of chemistry and physics: A ready-reference book of chemical and physical data*, 2015.
23. M. Sakurai, T. Imai, F. Yamashita, K. Nakamura, T. Komatsu and I. T. Nakagawa, *Polym J*, 1993, **25**, 1247–1255.
24. Gökçen Savasci, *Quantum-Chemical Investigations on a Hydrazone-Based Photocatalytically Active Covalent Framework*, Master’s thesis, München, 2014.
25. Kappe, C. Oliver, *Angew. Chem., Int. Ed.*, 2004, **43**, 6250–6284.
26. M. Dogru, A. Sonnauer, S. Zimdars, M. Doblinger, P. Knochel and T. Bein, *CrystEngComm*, 2013, **15**, 1500–1502.
27. N. L. Campbell, R. Clowes, L. K. Ritchie and A. I. Cooper, *Chem. Mater.*, 2009, **21**, 204–206.

28. L. K. Ritchie, A. Trewin, A. Reguera-Galan, T. Hasell and A. I. Cooper, *Microporous Mesoporous Mater.*, 2010, **132**, 132–136.
29. H. R. Kricheldorf, S.-c. Fan, L. Vakhtangishvili, G. Schwarz and D. Fritsch, *J. Polym. Sci. A Polym. Chem.*, 2005, **43**, 6272–6281.
30. A. P. Gies, W. K. Nonidez, M. Anthamatten, R. C. Cook and J. W. Mays, *Rapid Commun. Mass Spectrom.*, 2002, **16**, 1903–1910.

6 CONCLUSION AND OUTLOOK

Since the first publication on COFs in 2005 concerted research efforts have been directed at these porous and crystalline materials, targeting their applications in gas capture and storage,^{1,2} catalysis,^{3,4,5} capacitors^{6,7} and solar cells.^{8,9} The tunability of the pore size from 0.6 nm¹⁰ to 5.3 nm¹¹ via the concepts of *Reticular Chemistry* is an important feature of COFs.^{12–14} Functionalization of the pore has been achieved by introduction of functionalized building blocks, providing azide,¹⁵ alkyne¹⁶ and hydroxyl functional groups.¹⁷ This functionality is then further used in post-synthetic modification to attach fullerenes,¹⁸ carboxylic acids,¹⁷ proline derivatives¹⁹ and persistent radicals such as TEMPO⁶ covalently to the framework.

In this thesis, six new COFs based on hydrazone and azine linkage were synthesized, characterized and new applications were found, which previously were not accessible by COFs. Introducing the triazine 1,3,5-*tris*-(4-formyl-phenyl)triazine (TFPT) in a hydrazone based COF, it was demonstrated for the first time that TFPT-COF is able to efficiently act as photocatalyst in visible-light driven hydrogen production with quantum efficiencies higher than 2%.²⁰ This quantum efficiency is on a level with the best light-element photocatalysts known so far and therefore opens the way to a new class of application of COFs. Recently, utilization of TFPT in the azine-based N3-COF in our group and comparison to the pyrimidine (N2)-, pyridine (N1)- and benzene (N0)-centered counterparts revealed first indications of the structural and electronic features relevant for photocatalysis and the mechanism involved in photocatalytic hydrogen production.²¹ If the nitrogen content of the central aromatic unit is increased, the hydrogen evolution rate goes up as well. All of these COFs are yellow solids, which only absorb a small part of the solar irradiation. First steps towards increasing visible light absorption have been taken by doping TFPT-COF with perylene units, shifting the absorption to the red region, although at the cost of a lower hydrogen evolution rate.

A closer look at the crystal properties of TFPT-COF revealed disc-shape crystallites with less than 100 nm in all dimensions. The dimensions in the stacking direction could further be decreased by a factor of four by exfoliation. With this new form of TFPT-COF, new synthetic ways and spectroscopic investigations seem possible.

Functionalization with azide and alkyne groups of TFPT-COF was achieved by a co-condensation and a post-modification/reconversion approach. This functionalized TFPT-COF enables for example the covalent introduction of photosensitizers or water oxidation catalysts.

In the second generation of azine COFs, the pyrene-based ATEXPY-COFs (X=B,N,P) offer absorption maxima well overlapping with the solar spectrum. The building blocks 1,3,6,8-tetrakis(4-ethynylbenzaldehyde)pyrene (TEBPY), 1,3,6,8-tetrakis(6-ethynylnicotin-aldehyde)pyrene (TENPY) and 1,3,6,8-tetrakis(2-ethynylpyrimidine-5-carbaldehyde)pyrene (TEPPY) were synthesized and transformed in an subsequent step into the corresponding ATEXPY-COFs. Owing to the low crystallinity of these COFs, their structures and layer stacking

behavior were investigated with supporting physisorption simulations, revealing a shifted AA' stacking in a zigzag pattern between adjacent layers in the solid state. This method^{22,23} has been applied for the first time to COFs. The ATEXPY-COFs differ in their peripheral aromatic unit in nitrogen content. ATEBPY-COF with peripheral phenyl units showed the highest hydrogen evolution rate when irradiated with solar light. In contrast to the Nx systems investigated before, this time the increase in the nitrogen content is in the peripheral aromatic units. ATENPY-COF with peripheral pyridine units and ATEPPY with peripheral pyrimidine units both show a lower hydrogen evolution rate than ATEBPY-COF with peripheral phenyl units. Therefore the trend was established that increasing nitrogen content leads to a decreasing hydrogen evolution rate for ATEXPY-COFs. This finding was further investigated by optical photoluminescence measurements, showing a reduction in fluorescence intensity with increasing nitrogen content. PL spectra in aqueous suspension with two distinct bands indicate an energy/photon transfer between two species. We suppose this energy transfer happens between exfoliated single sheets and the bulk COF. Further PL life time studies are on their way.

Future steps are aimed at making the water oxidation reaction feasible with COFs as semiconducting backbone. Suitable water oxidation catalysts require significant oxidative power (i.e. a positive valence band / low lying HOMO) embedded within an extremely robust and oxidation resistant overall catalytic system. Because many COFs have an energetically high-lying HOMO, self-oxidation of COFs rather than water oxidation usually occurs. This factor can be addressed by the following approaches: i) The use of very electron-poor building blocks such as triazine or other heteroaromatic building units, which lower the HOMO level; ii) integration of bio-inspired building blocks which are known to be resistant under oxidizing conditions such as flavin; iii) covalent attachment of metal-containing water oxidation catalysts such as Ru,²⁴ Ir or Cu complexes on the COF postsynthetically.^{25,26}

Two further isostructural azine-linked COFs were investigated based on 1,3,5-triformyl benzene (AB-COF) and 1,3,5-triformylphloroglucinol (ATFG-COF) as well as hydrazine building units. The sorption characteristics of these COFs are precisely tunable by the rational design of the chemical nature of the pore walls. This effect is particularly pronounced for atmospheric water harvesting, which is explored for the first time using COFs as water vapor adsorbents with promising results. Both COFs also exhibit high CO₂ uptakes and selectivities towards CO₂ over N₂, which was demonstrated under equilibrium (sorption) and kinetic conditions (flow TGA, breakthrough). This is an important key step towards application of COFs in post-combustion carbon dioxide capture. In addition, the pore walls of both COFs were modified by doping with metal salts (lithium and zinc acetate), which is the first time that CO₂ sorption properties of a metal-modified COF were measured. This study clearly demonstrates that a new key property needs to be considered on the search for optimal sorbents for capture of CO₂ or atmospheric water: Not solely the pore size but also the pore wall polarity determines the uptake behavior and the isotherm of the corresponding materials.

6.1 References

1. H. Furukawa and O. M. Yaghi, *J. Am. Chem. Soc.*, 2009, **131**, 8875–8883.
2. N. Huang, R. Krishna and D. Jiang, *J. Am. Chem. Soc.*, 2015, **137**, 7079–7082.
3. Y. Hou, X. Zhang, J. Sun, S. Lin, D. Qi, R. Hong, D. Li, X. Xiao and J. Jiang, *Microporous Mesoporous Mater.*, 2015, **214**, 108–114.
4. S. Lin, C. S. Diercks, Y.-B. Zhang, N. Kornienko, E. M. Nichols, Y. Zhao, A. R. Paris, D. Kim, P. Yang, O. M. Yaghi and C. J. Chang, *Science (Washington, DC, United States)*, 2015, **349**, 1208–1213.
5. S.-Y. Ding, J. Gao, Q. Wang, Y. Zhang, W.-G. Song, C.-Y. Su and W. Wang, *J. Am. Chem. Soc.*, 2011, **133**, 19816–19822.
6. F. Xu, H. Xu, X. Chen, D. Wu, Y. Wu, H. Liu, C. Gu, R. Fu and D. Jiang, *Angew. Chem., Int. Ed.*, 2015, **54**, 6814–6818.
7. C. R. DeBlase, K. Hernández-Burgos, K. E. Silberstein, G. G. Rodríguez-Calero, R. P. Bisbey, H. D. Abruña and W. R. Dichtel, *ACS Nano*, 2015, **9**, 3178–3183.
8. J. Guo, Y. Xu, S. Jin, L. Chen, T. Kaji, Y. Honsho, M. A. Addicoat, J. Kim, A. Saeki, H. Ihee, S. Seki, S. Irle, M. Hiramoto, J. Gao and D. Jiang, *Nat. Commun.*, 2013, **4**, Art. No. 2736.
9. M. Dogru, M. Handloser, F. Auras, T. Kunz, D. Medina, A. Hartschuh, P. Knochel and T. Bein, *Angew. Chem., Int. Ed.*, 2013, **52**, 2920–2924.
10. H. Ma, H. Ren, S. Meng, Z. Yan, H. Zhao, F. Sun and G. Zhu, *Chem. Commun. (Cambridge, U. K.)*, 2013, **49**, 9773–9775.
11. S. Jin, K. Furukawa, M. Addicoat, L. Chen, S. Takahashi, S. Irle, T. Nakamura and D. Jiang, *Chem. Sci.*, 2013, **4**, 4505–4511.
12. J. R. Hunt, C. J. Doonan, J. D. LeVangie, A. P. Côté and O. M. Yaghi, *J. Am. Chem. Soc.*, 2008, **130**, 11872–11873.
13. H. M. El-Kaderi, J. R. Hunt, J. L. Mendoza-Cortes, A. P. Cote, R. E. Taylor, M. O'Keeffe and O. M. Yaghi, *Science (Washington, DC, United States)*, 2007, **316**, 268–272.
14. A. P. Côté, H. M. El-Kaderi, H. Furukawa, J. R. Hunt and O. M. Yaghi, *J. Am. Chem. Soc.*, 2007, **129**, 12914–12915.
15. A. Nagai, Z. Guo, X. Feng, S. Jin, X. Chen, X. Ding and D. Jiang, *Nat. Commun.*, 2011, **2**, Art. No. 536.
16. D. Jiang, H. Xu, X. Chen, J. Gao, J. Lin, M. Addicoat and S. Irle, *Chem. Commun. (Cambridge, U. K.)*, 2013.

17. N. Huang, X. Chen, R. Krishna and D. Jiang, *Angew. Chem., Int. Ed.*, 2015, **54**, 2986–2990.
18. L. Chen, K. Furukawa, J. Gao, A. Nagai, T. Nakamura, Y. Dong and D. Jiang, *J. Am. Chem. Soc.*, 2014, **136**, 9806–9809.
19. H. Xu, J. Gao and D. Jiang, *Nat. Chem.*, 2015, **7**, 905–912.
20. L. Stegbauer, K. Schwinghammer and B. V. Lotsch, *Chem. Sci.*, 2014, **5**, 2789.
21. V. S. Vyas, F. Haase, L. Stegbauer, G. Savasci, F. Podjaski, C. Ochsenfeld and B. V. Lotsch, *Nat. Commun.*, 2015, **6**, Art. No. 8508.
22. T. C. Wang, W. Bury, D. A. Gómez-Gualdrón, N. A. Vermeulen, J. E. Mondloch, P. Deria, K. Zhang, P. Z. Moghadam, A. A. Sarjeant, R. Q. Snurr, J. F. Stoddart, J. T. Hupp and O. K. Farha, *J. Am. Chem. Soc.*, 2015, **137**, 3585–3591.
23. O. V. Gutov, W. Bury, D. A. Gomez-Gualdrón, V. Krungleviciute, D. Fairen-Jimenez, J. E. Mondloch, A. A. Sarjeant, S. S. Al-Juaid, R. Q. Snurr, J. T. Hupp, T. Yildirim and O. K. Farha, *Chem. - Eur. J.*, 2014, **20**, 12389–12393.
24. J. J. Concepcion, J. W. Jurss, Brennaman, M. Kyle, P. G. Hoertz, Patrocinio, Antonio Otávio T., Murakami Iha, Neyde Yukie, J. L. Templeton and T. J. Meyer, *Acc. Chem. Res.*, 2009, **42**, 1954–1965.
25. X. Sala, I. Romero, M. Rodríguez, L. Escriche and A. Llobet, *Angew. Chem., Int. Ed.*, 2009, **48**, 2842–2852.
26. A. Sartorel, M. Bonchio, S. Campagna and F. Scandola, *Chem. Soc. Rev.*, 2013, **42**, 2262–2280.

7 APPENDIX

7.1 Table of Abbreviations

Å	Ångstrom
Ac	acetyl
ATEBPY	azine(1,3,6,8-tetrakis(4-ethynylbenzaldehyde)pyrene)
ATENPY	azine(1,3,6,8-tetrakis(6-ethynylnicotinaldehyde)pyrene)
ATEPPY	azine(1,3,6,8-tetrakis(2-ethynylpyrimidin-5-carbaldehyde)pyrene)
ATEXPY	sum of ATEBPY, ATENPY, ATEPPY
ATR	attenuated total reflectance
Bn	benzyl
COF	covalent organic framework
conc.	concentrated
COSY	Correlated spectroscopy
DATH	2,5-di(3-azidopropoxy)terephthalohydrazide
DCM	dichloromethane
DCVC	dry-column vacuum chromatography
DEI	direct electron ionization
DETH	2,5-diethoxy-terephthalohydrazide
diox	1,4-dioxane
DMA	<i>N,N</i> -dimethylacetamide
DMSO	dimethylsulfoxide
DPDI	2,9-bis(4-aminophenyl)-5,12-bis(3,5-di- <i>tert</i> -butylphenoxy)anthra[2,1,9-def:6,5,10-d'e'f']diisoquinoline-1,3,8,10(2H,9H)-tetraone
DPTH	2,5-di(prop-2-yn-1-yloxy)terephthalohydrazide
EDX	energy-dispersive x-ray spectroscopy

eq.	equivalent(s)
Et	ethyl
FCC	flash column chromatography
FT	Fourier transform
HOMO	highest occupied molecular orbital
HRMS	high resolution mass spectrometry
IPA	isopropyl alcohol
<i>i</i> -Pr	<i>iso</i> -propyl
IR	infrared spectroscopy
LRMS	low resolution mass spectrometry
LUMO	lowest unoccupied molecular orbital
MALDI	matrix-assisted laser desorption/ionization
MAS	magic angle spinning
Me	methyl
mes	mesitylene
MOF	metal-organic framework
MW	molecular weight
<i>n</i> -Bu	<i>n</i> -butyl
NHE	normal hydrogen electrode (pH = 0)
NMR	nuclear magnetic resonance
<i>o</i> -DCB	<i>ortho</i> -dichlorobenzene
oop	out-of-plane
Ph	phenyl
ppm	parts per million
PXRD	power x-ray diffraction

R _f	retention factor (TLC)
rt	room temperature
sat.	saturated
SEM	scanning electron microscopy
solv.	solvent
t-Bu	tert-butyl
TEBPY	1,3,6,8-tetrakis(4-ethynylbenzaldehyde)pyrene
TENPY	1,3,6,8-tetrakis(6-ethynynicotinaldehyde)pyrene
TEPPY	1,3,6,8-tetrakis(2-ethynylpyrimidin-5-carbaldehyde)pyrene
TEXPY	sum of TEBPY, TENPY, TEPPY
TEM	transmission electron microscopy
TFA	trifluoro acetic acid
TFB	1,3,5-benzenetricarbaldehyde
TFG	1,3,5-triformylphloroglucinol
TFPT	tri(4-formylphenyl)triazine
THF	Tetrahydrofuran
TLC	thin layer chromatography
TMS	trimethylsilyls
UV	ultraviolet
VIS	visible
wt	Weight

7.2 List of publications

Published as part of this thesis

- 1. A hydrazone-based covalent organic framework for photocatalytic hydrogen production,**

Linus Stegbauer, Katharina Schwinghammer, Bettina V. Lotsch, *Chem. Sci.* **2014**, *5*, 2789.

2. Tunable Water and CO₂ Sorption Properties in Isostructural Azine-based Covalent Organic Frameworks through Polarity Engineering,

Linus Stegbauer, Maximilian W. Hahn, Andreas Jentys, Gökçen Savasci, Christian Ochsenfeld, Johannes A. Lercher, Bettina V. Lotsch
Chem. Mater. **2015**, *27*, 7874-7881.

Not part of this thesis

1. Nitrogen-rich covalent triazine frameworks as high-performance plat-forms for selective carbon capture and storage.

Stephan Hug, Linus Stegbauer, Hyunchul Oh, Michael Hirscher, Bettina V. Lotsch
Chem. Mater. **2015**, *27*, 8001-8010.

2. A tunable azine covalent organic framework platform for visible light-induced hydrogen generation,

Vijay S. Vyas, Frederik Haase, Linus Stegbauer, Gökçen Savasci, Filip Podjaski, Christian Ochsenfeld, Bettina V. Lotsch
Nat. Comm. **2015**, Art. No. 8508.

3. Synthesis of Triazine-Based Materials by Functionalization with Alkynes,

Nicole E. Braml, Linus Stegbauer, Bettina V. Lotsch, Wolfgang Schnick,
Chem.—European Journal **2015**, *21*, 7866–7873.

4. Enantioselective Desymmetrization of Prochiral Cyclohexanones by Organocatalytic Intramolecular Michael Additions to α,β -Unsaturated Esters

Adam D. Gammack Yamagata, Swarup Datta, Kelvin E. Jackson, Linus Stegbauer, Robert S. Paton, Darren J. Dixon
Angew. Chem. Int. Ed. **2015**, *54*, 4899–4903.

5. N-[3,5-Bis(trifluoromethyl)phenyl]-N'-(9R)-cinchonan-9-yl-thiourea,

Darren J. Dixon, Linus Stegbauer,
Encyclopedia of organic reagents (EROS) **2012**, doi: 10.1002/047084289X.rn01435.

6. Bifunctional organo/metal cooperative catalysis with cinchona alkaloid scaffolds,

Linus Stegbauer, Filippo Sladojevich, Darren J. Dixon,
Chem. Sci. **2012**, *3*, 942-958

7.3 Contributions to conferences

Oral presentations

1. Covalent organic frameworks as highly selective CO₂ capture materials.

Linus Stegbauer, Maximilian W. Hahn, Andreas Jentys, Johannes A. Lercher, Bettina V. Lotsch

25/2/15, 27. Deutsche Zeolith-Tagung, Oldenburg, Germany

2. TFPT-COF: A hydrazone-based covalent organic framework as a platform for solar energy conversion.

Linus Stegbauer, Katharina Schwinghammer, Bettina V. Lotsch

12/8/14, ACS 248th National Meeting, San Francisco, USA

3. TFPT-COF: A hydrazone-based covalent organic framework as a platform for solar energy conversion.

Linus Stegbauer, Katharina Schwinghammer, Bettina V. Lotsch

December 2013, Scholarship meeting FCI, Munich, Germany

Poster Presentations

1. TFPT-COF: A scaffold for solar energy conversion.

Linus Stegbauer, Katharina Schwinghammer, Bettina V. Lotsch

November 2015, Scientific Advisory Board Meeting of the Max Planck Institute for Solid State Research, Stuttgart, Germany

2. Covalent Organic Frameworks for renewable energy applications.

Linus Stegbauer, Maximilian W. Hahn, Andreas Jentys, Gökçen Savasci, Christian Ochsenfeld, Johannes A. Lercher, Bettina V. Lotsch

12/10/15, EUROMOF 2015, Potsdam, Germany

3. TFPT-COF: A scaffold for solar energy conversion.

Linus Stegbauer, Katharina Schwinghammer, Bettina V. Lotsch

26/02/14, Deutsche Zeolith-Tagung, Paderborn, Germany

4. Functional frameworks as scaffolds for solar energy conversion.

Linus Stegbauer, Katharina Schwinghammer, Bettina V. Lotsch

November 2013, Young Ideas in Nanoscience, Munich, Germany

5. A hydrazone based covalent organic framework designed for solar energy conversion.

Linus Stegbauer, Bettina V. Lotsch

July 2013, NIM Summer Retreat, Fall (Lenggries), Germany

6. A hydrazone based covalent organic framework designed for solar energy conversion.

Linus Stegbauer, Bettina V. Lotsch

July 2013, Nanosystems for Solar Energy Conversion, Munich, Germany

7. Covalent organic frameworks: Towards hierarchically structured nano architectures.

Linus Stegbauer, Bettina V. Lotsch

March 2013, NIM Winterschool, Kirchberg, Austria

8. Covalent organic frameworks: Towards ordered heterojunction architectures.

Linus Stegbauer, Vijay Vyas, Bettina V. Lotsch

November 2012, Scientific Advisory Board Meeting of the Max Planck Institute for Solid State Research, Stuttgart, Germany